

**Ultrafast linear and non-linear  
spectroscopy:  
From biological light-receptors to  
artificial light-harvesting systems**

**Dissertation**

zur Erlangung des Naturwissenschaftlichen Doktorgrades  
der Bayerischen Julius–Maximilians–Universität Würzburg

vorgelegt von

**Benjamin Dietzek**

aus Hildesheim

Würzburg 2005

Eingereicht am: .....  
bei der Fakultät für Chemie und Pharmazie

1. Gutachter: .....  
2. Gutachter: .....  
der Dissertation

1. Prüfer: .....  
2. Prüfer: .....  
3. Prüfer: .....  
des öffentlichen Promotionskolloquiums

Tag des öffentlichen Promotionskolloquiums: .....

Doktorurkunde ausgehändigt am: .....

# Contents

<b>1</b>	<b>Introduction and Motivation</b>	<b>1</b>
<b>I</b>	<b>Theory and Experiment</b>	<b>5</b>
<b>2</b>	<b>Femtosecond time-resolved spectroscopic techniques</b>	<b>7</b>
2.1	Pump-probe transient absorption spectroscopy . . . . .	7
2.1.1	Transient Absorption Spectroscopy . . . . .	8
2.1.2	Theoretical approach . . . . .	13
2.1.3	Experimental related aspects . . . . .	24
2.2	Four-Wave-Mixing Techniques . . . . .	25
2.2.1	Transient Grating spectroscopy . . . . .	26
2.2.2	Third order perturbation theory . . . . .	27
<b>3</b>	<b>Experimental Setup</b>	<b>30</b>
3.1	Generation of Femtosecond Laser Pulses . . . . .	30
3.1.1	100 kHz- System . . . . .	30
3.1.2	1 kHz- System . . . . .	32
3.2	White-light-probe transient absorption . . . . .	34
3.3	Transient grating spectroscopy . . . . .	36
3.4	Time-resolved fluorescence spectroscopy . . . . .	38
<b>II</b>	<b>Biological Systems</b>	<b>41</b>
<b>4</b>	<b>Exited State Dynamics of Phycocyanobilin</b>	<b>43</b>
4.1	The system Phycocyanobilin . . . . .	44
4.1.1	The biological relevance of Phycocyanobilin . . . . .	44
4.1.2	Photophysical model . . . . .	46
4.2	Experimental results . . . . .	48
4.2.1	Fitting procedure . . . . .	48
4.2.2	Pump-wavelength-dependency of the excited-state processes . . . . .	50
4.2.3	Pump-wavelength-dependency of the photoproduct formation . . . . .	53
4.2.4	Reaction dynamics of protonated Phycocyanobilin . . . . .	55

4.2.5	Conclusion	59
<b>5</b>	<b>Protochlorophyllide a</b>	<b>60</b>
5.1	The system PChla	61
5.2	Excited-State relaxation of MgOEt-porphyrin	63
5.3	Ultrafast Excited-State dynamics of protochlorophyllide a	74
5.3.1	A first transient absorption approach	74
5.3.2	Solvent and excitation energy dependence of excited-state processes	83
5.3.3	Picosecond time-resolved fluorescence	96
5.3.4	Proposed model	107
5.3.5	Conclusions	110
<b>III</b>	<b>Artificial Systems</b>	<b>111</b>
<b>6</b>	<b>Introduction and Motivation</b>	<b>113</b>
<b>7</b>	<b>Excited-State Processes in a Quasi-2D Light Harvesting Antenna</b>	<b>118</b>
7.1	Introduction to Ruthenium polypyridine complexes	119
7.2	Excited-State Dynamics in $(\text{tbbpy})_2\text{Ru}(\text{tmblH}_2)$	121
7.3	Excitation Dynamics in $\text{Ru}_2\text{Pd}_2$	138
7.4	Conclusion	147
<b>8</b>	<b>Conclusion - Zusammenfassung</b>	<b>149</b>
8.1	Conclusion	149
8.2	Zusammenfassung	152
<b>IV</b>	<b>Appendix</b>	<b>159</b>
	<b>Coherent Artifacts in Integrated Detection</b>	<b>161</b>
	<b>Bibliography</b>	<b>185</b>
	<b>Acknowledgements - Danksagung</b>	<b>198</b>
	<b>Lebenslauf</b>	<b>200</b>

# Chapter 1

## Introduction and Motivation

Light plays a fundamental role in biology. It triggers many complex biological processes such as photosynthesis, which is the basic reaction making life on earth possible, and light reception, transduction and interpretation on a molecular level, forming the basis of vision and of the photoreception of plants. For these functions to be highly efficient, the initial processes have either to occur on a time-scale much faster than statistical energy dissipation; or to take place in a specifically designed geometrically or chemically environment that steers the light-induced reaction along the biologically desirable pathway.

The molecules performing the functions of light reception, transduction and interpretation in biological systems are usually strong absorbers with well defined spectral properties. This fact makes optical spectroscopy a powerful tool in studying their molecular structure and reaction pathways. The role of light as a reactant in biological processes implies that the chemical reactions leading to physical geometry changes, ranging from an atomic to a mesoscopic scale and causing the actual biological response, are initiated by the absorption of light. This was the motivation for a great variety of experiments studying the photophysical and photochemical properties of biological photoreceptors with different time-resolved spectroscopic techniques. The earliest experiments on this subject were performed in the 1950s and 1960s using flash photolysis and various types of activation pulses, such as light and electron pulses or temperature and pressure jumps, for example. These early developments were awarded with the Nobel Prize in Chemistry to Manfred Eigen, Ronald G.W. Norrish and George Porter in 1967 "for their studies of extremely fast chemical reactions, effected by disturbing the equilibrium by means of very short pulses of energy" [1, 2]. Nevertheless, the upcome of the laser in the 1960s [3–5] and the rapid

technological progress in developing ultrashort laser pulses [6] extended the time-domain from about a microsecond ( $10^{-6}$  sec) [7], in which molecular reactions are observable by means of their spectral properties, to a few femtoseconds ( $10^{-15}$  sec) [8–10]. Very recently pulses on the order of 200 attoseconds ( $10^{-18}$  sec) have been reported. These are generated using high-harmonic generation and thus are centered in the soft X-ray region of the electromagnetic spectrum [11, 12]. - Nonetheless, time-resolved spectroscopy with a modest and routinely achievable time-resolution of ten to hundred femtoseconds provides a powerful tool and plays a dominant role in the studies of ultrafast dynamics [10]. This development was awarded with the Nobel Prize in Chemistry to Ahmed H. Zewail in 1999 "for his studies of the transition states of chemical reactions using femtosecond spectroscopy" [2]. The Nobel Prize to Ahmed H. Zewail stimulated even more research in this area. Even complex processes such as photosynthesis [13, 14] or the initial ultrafast steps in vision [15] are well characterized and a quite detailed understanding of light-induced reactions on model systems exists by now [13, 16–21].

The experiments on the photophysics and photochemistry of natural systems clearly reveal, that nature achieves extremely high efficiency and specificity in translating the information deduced from the absorbed photons (e.g. color, direction, photon density) into the biological response. This is done by specially designing the initial light receptors and implementing them into a specific environment; so that the desired molecular response occurs very fast - on the picosecond or sub-picosecond time-scale and thus, much faster than competing relaxation and energy dissipation processes - and directional, i.e. the molecular environment stirs the molecular response of the light absorbing moiety along the biologically favorable pathway. Therefore, the structure of the biological system critically influences the dynamics and the function requires a defined dynamic response of the system. Hence, in order to design artificial systems or so-called "molecular devices" with well defined characteristics and capable of mimicking biological functions it is crucial to have characterized the biological paradigm in great detail and to have understood the structure-dynamics and structure-function relationships in the natural archetype. Such molecular devices are designed to either mimic biological processes [16, 22–28] or to be used in molecular electronics [29, 30] or optical data-storage [31], for example. In turn, studying the properties of man-made systems with extremely well defined and at will interchangeable structural features leads to a better understanding and deeper insight into the structure-function and function-dynamics relationship in biological systems [13].

The experiments presented in this work utilize femtosecond time-resolved linear and non-linear spectroscopic techniques to address the light-induced excited-state processes in biological model systems and a particular molecular device that serves as a - structurally - very simple light-harvesting antenna or as a light-driven ultrafast catalysis-switch. The spectroscopic techniques employed to interrogate the light-induced processes in these systems are femtosecond time-resolved transient absorption and transient grating spectroscopy, the latter being a special case of four-wave-mixing spectroscopy. The combination of these techniques yields transient spectral information in concert with high quality, high signal-to-noise kinetic transients, which allow for precise fitting and therefore very accurate time-constants to be extracted from the data. The use of femtosecond time-resolved transient grating spectroscopy is relatively uncommon in addressing questions concerning the excited-state reaction pathways of complex (biological) systems [32]. Therefore the experiments presented in this work constitute, to the best of my knowledge, the first studies applying this technique to a metalloporphyrin (chapter 5) and an artificial light-harvesting antenna (see part III of this thesis).

This work is organized as follows: After giving a short theoretical overview over the spectroscopic techniques used and their relation to the systems characteristic density matrix in chapter 2, their experimental realization is briefly described (see 3). In part II the experiments performed on biological chromophores, prepared in the group of PD. Dr. Gudrun Hermann, Institute of Biophysics and Biochemistry at the University of Jena, are reported. In chapter 4 the excited-state relaxation processes in phycocyanobilin are investigated using pump-energy-dependent transient grating spectroscopy. In the subsequent chapter 5 experiments on photoexcited protochlorophyllide a and magnesium octaethyl porphyrin are presented. With the knowledge gained from these experiments, the light-induced excited-state processes in protochlorophyllide a are investigated using transient absorption and time-resolved fluorescence spectroscopy. In the third part of this thesis the focus is shifted to characterizing the light-induced processes in an artificially designed and structurally simple tetranuclear light-harvesting antenna, which is based on Ruthenium and Palladium chromophores, and its individual building groups. The complexes investigated here were synthesized in the group of PD. Dr. Sven Rau and Prof. Dr. Dirk Walther at the Institute for Inorganic Chemistry at the University of Jena. For this work a combination of transient absorption and transient grating spectroscopy has been chosen.

The experiments presented in the following chapters aim to provide detailed in-

sight into the ultrafast processes upon light absorption of two important biological photoreceptors, and address the photophysics of an artificially designed light-harvesting antenna system.



## Part I

# Theory and Experiment



## Chapter 2

# Femtosecond time-resolved spectroscopic techniques

The femtosecond time-resolved experimental techniques used in the course of this work are introduced in this chapter. First in section 2.1.1, the pump-probe transient absorption technique is discussed followed by a description of transient grating spectroscopy (in section 2.2.1), a special case of the general four-wave-mixing-scheme. For each of the techniques a pictorial picture is presented preceding a more detailed theoretical description. While the first approach should give an intuitive view on the physics of the various processes, the latter aims to correlated the time-evolution of the density matrix of the investigated system to the experimentally observed signal. The theoretical formalism presented is based on Liouville's theorem and the resultant time-dependent third order polarization, which acts as the microscopic source of the signal. To further elucidate the time-dependence of the system that is subjected to various sequences of laser-matter interaction, Feynman diagrams are used.

### 2.1 Pump-probe transient absorption spectroscopy

In a pump-probe scheme commonly used to investigate the excited state properties of molecular samples a single pump laser excites the sample at the time  $t=0$  and places individual molecules into the respective excited state of interest  $|i\rangle$ . The time evolution of the state  $|i(t)\rangle$  is interrogated with a second, the so called probe-, pulse that is delayed in time by  $\Delta t$  relatively to the pump pulse. The probe pulse projects the state  $|i(t)\rangle$  onto a target

state  $|j\rangle$ , which can be a continuum state as in time-resolved photo-electron spectroscopy or e.g. an energetically higher lying state as exploited in transient absorption spectroscopy. The result of this projection is detected as an electron or ion signal or an absorption change, respectively, and from this detection the time-evolution of the state  $|i(\Delta t)\rangle$  can be reconstructed. Within the overall pump-probe scheme a wide variety of different techniques has been developed including e.g. time-resolved resonance Raman [6], pump-CARS (Coherent anti-Stokes Raman Scattering) [33], fluorescence up-conversion (see for example [34]), macro-crystalline time-resolved Xray scattering [35], photo-electron spectroscopy [36] and - perhaps most commonly applied - time-resolved transient absorption [37].

### 2.1.1 Transient Absorption Spectroscopy

Transient absorption spectroscopy is used to monitor the absorption changes of a sample upon photoexcitation. As the absorption spectrum of a molecule, a cluster, etc. serves as a "fingerprint" of this species, changes in the absorption spectrum reflect the pass-way of relaxation and or photoreaction the system undergoes subsequent to the excitation. The principle of this method is shown in figure 2.1.

Panel A of figure 2.1 shows the ground-state absorption spectrum of a fictive molecule. As it is schematically indicated in panel C, the steady state absorption spectrum contains information about the dipole allowed transitions initiating from the  $S_0$ -state and their respective oscillator strength (schematically shown in panel D). If now the system is prepared in an excited state by absorbing light of a pump-pulse (see panel B), which here is assumed to be resonant with the  $S_0 \rightarrow S_1$ -transition, the absorption spectrum of the particular excited state can be measured by a supercontinuum pulse being delayed by  $\Delta t$  with respect to the pump. Thus, the spectrum contains not only spectral information, i.e. energetic position of dipole allowed  $S_1 \rightarrow S_n$ -transitions (see panel A) and the respective oscillator strengths but also temporal information by monitoring the absorption changes as a function of the delay-time  $\Delta t$ .

In order to obtain a clear but immediately intuitive picture of the information that can be gained with transient absorption spectroscopy one starts from the Lambert-Beer law, describing the absorption of light when passing through a sample:

$$I(\lambda, \Delta t) = I_0(\lambda) \cdot 10^{-OD(\lambda, \Delta t)} = I_0(\lambda) \cdot 10^{-\epsilon(\lambda) \cdot N(\Delta t) \cdot x}. \quad (2.1)$$

In this equation  $\epsilon(\lambda)$  denotes the wavelength dependent absorption coefficient,  $N(\Delta t)$  the

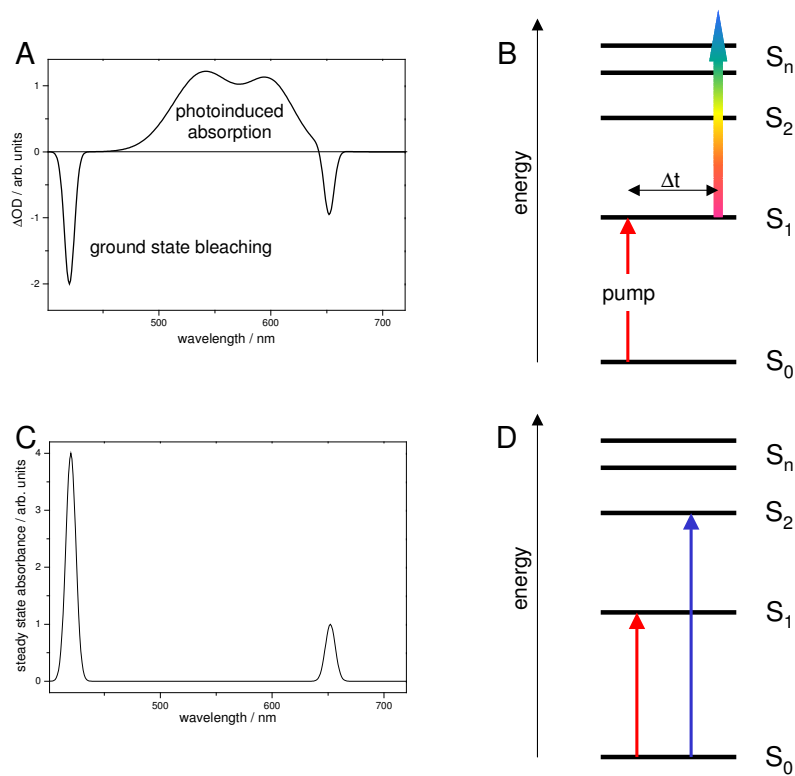


Figure 2.1: The principle of transient absorption in comparison with steady state absorption is shown.

number of molecules absorbing at the wavelength  $\lambda$  and  $x$  the length of the sample irradiated. With an experimental setup employing a pump-beam to excite the species of interest and a probe- (interacting with the same sample volume as the pump-beam) and a reference-pulse (interacting with unperturbed sample molecules) it is possible to measure  $I(\lambda, \Delta t)$  and  $I_0(\lambda)$  at the same time. (For a detailed description of the experimental setup please see chapter 3.) Thus, the quantity of interest, the change in optical density ( $\Delta OD$ ) of the sample can be extracted from the data according to the following equation

$$\Delta OD(\lambda, \Delta t) = -\log \frac{I(\lambda, \Delta t) - I_0(\lambda)}{I_0(\lambda)} = \epsilon(\lambda) \cdot N(\Delta t) \cdot x. \quad (2.2)$$

Spectral analysis of the absorption spectra for a given delay  $\Delta t$  between pump- and probe-pulse provides the absorption spectrum of the electronically excited state populated at the time  $\Delta t$  superimposed to the negative absorption spectrum of the photo-depleted ground state. This spectrum is governed by the wavelength dependent absorption coefficients  $\epsilon_{exc}(\lambda)$  and  $\epsilon_{ground}(\lambda)$ . In general a transient spectrum consists of contributions of different states and processes, in particular shows regions of negative  $\Delta OD$  (see in panel A of figure 2.1 at 420 and 650 nm) due to a bleaching of the ground-state absorption following photoexcitation. Since population is transferred from the ground- to an excited-state the supercontinuum probe will be absorbed less in the spectral region of  $S_0$ -absorption and therefore more light of the particular frequency enters the detector. Thus, a decrease in optical density ( $\Delta OD < 0$ ) is detected. The same argument applies for spectral regions, where stimulated emission occurs. This process as well leads to the detection of a decreased optical density as additional, stimulatedly emitted photons enter the detector. Positive changes of the optical density of the sample are observable in the spectral regions, where excited-states or photoproducts absorb. Thus these bands are assigned to  $S_i \rightarrow S_n$ -absorption ( $T_j \rightarrow T_n$ -absorption or photoproduct absorption, respectively), with  $i, j, n \in N$  and  $i \leq 1$ ,  $n > i$  and  $n > j$ , respectively. As in these spectral region less light passes the sample compared to the situation, in which all molecules are found in the ground-state, the optical density of the sample is observed to increase, i.e.  $\Delta OD > 0$ . Temporal analysis at a fixed wavelength  $\lambda$  yields the population dynamic ( $N(\Delta t)$ ) of the (electronic) state that shows absorption or bleaching, respectively, at this particular wavelength. Plots of  $\Delta OD_\lambda(\Delta t)$  are called *transients* at the particular probe wavelength  $\lambda$  from here on. These transients reflect the kinetic and dynamic behavior of the system. These transients are usually fit to a sum of exponentials describing the build-up and decay of the population placed in particular

states.

In order to further illustrate the capability of transient absorption on a model system, Figure 2.2 shows exemplary transient absorption data of the dye Nileblue, that was used in order to calibrate our transient absorption setup. Panel A shows a three dimensional plot of  $\Delta OD$  as a function of the probe wavelength and delay-time  $\Delta t$  following photoexcitation of the dye at 600 nm. Negative changes in optical density are shown as green and blue, while positive changes are color coded red. From the data displayed in panel A it is obvious, that the ground-state bleach near 600 nm manifests itself in slightly negative optical density changes is accompanied by an excited state absorption in the green spectral region at around 530 nm. Here,  $\Delta OD > 0$  is observed. The strong negative contribution to the transient absorption spectrum, which can also be clearly observed in the spectrum taken at 10 ps after photoexcitation, which is shown in panel B, is attributed to stimulated emission. Representative transients, reflecting the dynamics of the system monitored in the region of photoinduced absorption at 530 nm and in the region of ground-state bleach and stimulated emission at 630 nm are shown in panels C and D, respectively.

In order to be able to do a kinetic or dynamic analysis from transient absorption data the probe wavelength should be chosen to lie in a spectral region of absorption of at least one state involved in the decaying process or photoreaction. Thus if a two color pump-probe experiment is performed, some kind of knowledge about the excited state species has to be gained in advance to obtain information on the excited state electronic absorption spectrum. Nevertheless, the application of a white light continuum as a probe as shown in the data presented in figure 2.2 circumvents this problem and allows one to gain broadband spectral information simultaneously together with femtosecond-time resolution. The time-dependent electric field of the supercontinuum pulses used for white light probing can to a good approximation [38] be written as

$$E_{SC}(t) \propto \exp[-t^2/2\tau^2 + i(\omega_{SC}t + bt^2)] = \exp[-t^2/2\tau^2 + i\Phi(t)] \quad (2.3)$$

where  $\tau$ ,  $\omega_{SC}$  and  $b$  denote the probe pulse duration, its central frequency and the chirp rate, respectively. Thus, the *SC*-probe has a time-dependent instantaneous frequency  $\omega = \frac{d}{dt}\Phi(t) = \omega_{SC} + 2b \cdot t$ . Therefore, different frequency components of the *SC*-pulse interact at different delay-times  $\Delta t$  with the pump-pulse, which is assumed to be transform limited. In order to describe the situation quantitatively, the so called time-zero function

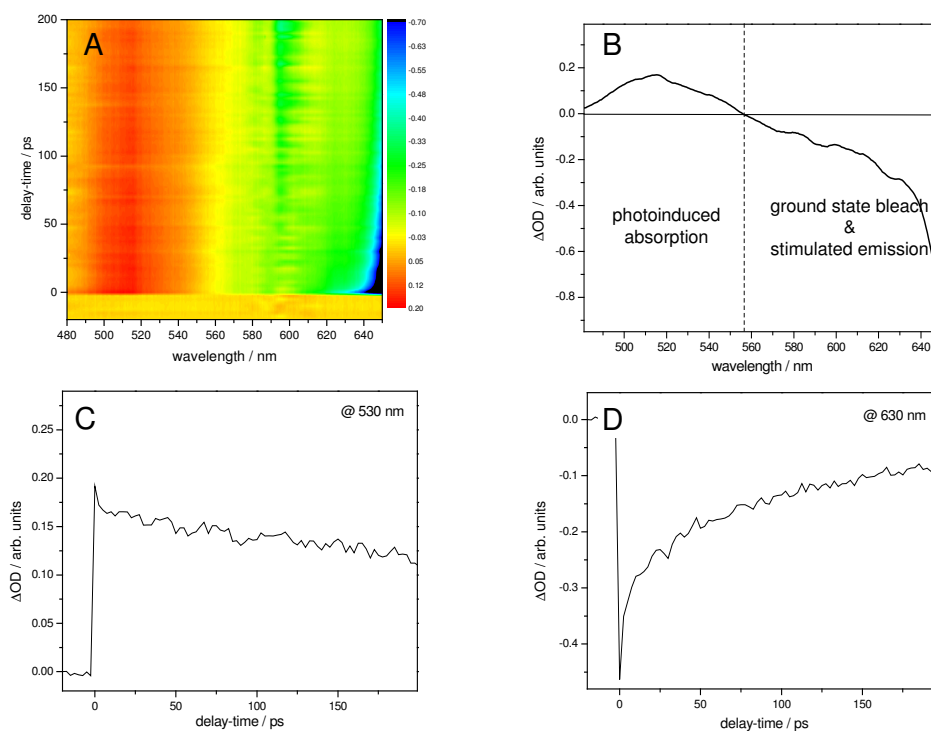


Figure 2.2: Exemplary transient absorption data of the dye NileBlue dissolved in methanol are shown. The excitation wavelength was chosen to be 600 nm. Panel A shows a three dimensional plot of the changes of optical density as a function of probe-wavelength and delay-time between pump- and probe-pulse. The transient absorption spectrum, i.e. a cut at a fixed delay-time through the data shown in panel A, is depicted in panel B. Here,  $\Delta t$  was chosen to be 10 ps. Panels C and D present transients taken at different spectral positions.



is defined as:

$$t_0(\omega) = \frac{\omega - \omega_{SC}}{2b}. \quad (2.4)$$

Assuming that the time-delay between pump and central frequency of the probe has been set to zero, i.e.  $t_0(\omega_{SC}) = 0$ , equation 2.4 provides the actual delay between the pump and the  $\omega$ -frequency component of the probe. In the more general case given by the second equality in equation 2.3 the time-zero function can be expressed as  $t_0(\omega) = -\frac{\partial}{\partial \omega} \Phi(\omega)$  [38]. The actual frequency dependent pump-probe delay  $\Delta t(\omega)$  then becomes  $\Delta t(\omega) = \Delta t(\omega_{SC}) + t_0(\omega)$ ; this time-zero correction necessary to account for the chirp of the supercontinuum probe light is usually achieved by fitting of the time-zero function to the experimental data. Besides the necessity for this chirp correction, it has been shown by Ernsting and coworkers [38] that probing with a transform limited pulse as well as with a chirped supercontinuum lead to the same kinetic information (see equations 2.31 and 2.32).

### 2.1.2 Theoretical approach

A theoretical approach to describe the signals obtained from pump-probe spectroscopy starts out from the density matrix  $\rho$  of the system, which reads for the case of a two level system:

$$\rho(t) = \begin{pmatrix} n & p \\ p^* & 1 - n \end{pmatrix} \quad (2.5)$$

where  $n$  and  $1 - n$ , the so called population terms, describe the probability of finding the system in the ground or excited state, respectively. On the other hand,  $p$  and  $p^*$  represent the coherences associated with a superposition of eigenstates of the system. The time evolution of the system is described by inserting the density matrix into the quantum mechanical Liouville equation and introducing a phenomenological damping term, which accounts for the coupling of the system to the bath. This leads to the the corresponding equation of motion [39]:

$$\frac{d}{dt} \rho(t) = \frac{1}{i\hbar} ([H_0, \rho(t)] + [V(r, t), \rho(t)]) + \frac{\partial}{\partial t} \rho(t)|_{damping}. \quad (2.6)$$

In this equation  $H_0 = |g\rangle \epsilon_g \langle g| + |e\rangle \epsilon_e \langle e|$  denotes the Hamiltonian of the unperturbed system, wherein  $|g\rangle$  describes the ground-state with the corresponding energy  $\epsilon_g$  and

$|e\rangle$  denotes the singly excited-state considered. (If the excited-state is considered to consist of a vibrational manifold  $|v\rangle$ , a similar treatment of the density matrix as outlined below can be performed yielding expressions capable to describe Resonance Raman cross-sections as well as pump-probe data (see for example reference [40]). Such a treatment is beyond the scope of this chapter, but the importance of describing the time-evolution of the systems density matrix has to be stressed here.) The interaction Hamiltonian  $V(r, t)$  is the product of the transition dipole moment operator  $\vec{\mu}$  and the total electric field and therefore reads  $V(r, t) = -\vec{\mu} \cdot \vec{E}(\vec{r}, t)$ . Despite of the relative orientation between the molecular dipole and the oscillating external field is of importance for the physics observed, and some experimental care has to be taken in order to avoid experimental artifacts due to unavoidable molecular orientation changes (see subsection 2.1.3), parallel polarizations are assumed here and the vector notation is dropped for simplicity. With *c.c.* referring to complex conjugation and the subscripts  $p$  referring to the pump- and  $t$  to the probe-test-field, respectively, the total electric field and the matrix elements of the dipole operator are written as:

$$E(r, t) = E_p(t) \cdot \exp[ik_p \cdot r - i\omega_p t] + E_t(t) \cdot \exp[ik_t \cdot r - i\omega_t t] + c.c. \quad (2.7)$$

$$\mu = \sum_v (|v\rangle \mu_{v0} \langle 0| + c.c.). \quad (2.8)$$

Here it is assumed, that the electric fields are in resonance with the corresponding molecular transitions. With this and assuming for simplicity only transitions involving the ground-state  $|0\rangle$  taking place, that is ignoring transitions within the excited state manifold, the equations of motion of the various components of the density matrix can be given within the rotating wave approximation (i.e. ignoring terms oscillating with the sum of two optical frequencies and keeping track of only such terms that involve the difference of two such frequencies):

$$\left( \frac{d}{dt} + i\omega_{ij} + \Gamma_{ij} \right) \rho_{ij}(t) = i \frac{E(t)}{\hbar} \cdot \sum_k (\mu_{ik} \rho_{kj} - \rho_{ik} \mu_{kj}). \quad (2.9)$$

In writing equation 2.9, that can be solved using a Green's function approach, the phenomenological damping rates  $\Gamma_{ij}$  have been introduced:

$$\frac{\partial}{\partial t} \rho_{ij}(t)|_{damping} = \Gamma_{ij} (\rho_{ij}(t) - \rho_{ij}^{(0)}). \quad (2.10)$$

For  $i = j$ , the damping rate describes the population relaxation between the two electronic states involved associated with the excited state lifetime  $T_1$ . On the other hand, for  $i \neq j$ ,  $\Gamma_{ij} = 1/T_2$  characterizes the total dephasing of the ensemble. It has to be noted, that the total dephasing time  $T_2$  is related to the population relaxation time  $T_1$  via

$$\frac{1}{T_2} = \frac{1}{T_2^*} + \frac{1}{2(T_{1g} + T_{1e})}, \quad (2.11)$$

wherein  $T_2^*$  is the pure dephasing due to inhomogeneous broadening, i.e. interaction of the system with the environment for example due to collisions with the solvent that lead to phase fluctuations experienced by the transition dipole [41, 42].

As mentioned above, the solution of the equation of motions of the system (equation 2.9) can be obtained by introducing the Green function, which can be thought of as the response of the system to an infinite short excitation (therefore it is often referred to as the response function of the system)

$$G_{ij}(t) = -\frac{1}{i\hbar} \exp(-i\omega_{ij}t) \cdot \exp(-\Gamma_{ij}t) \cdot \Theta(t), \quad (2.12)$$

with  $\exp(-i\omega_{ij}t)$  describing the free propagation of the system,  $\exp(-\Gamma_{ij}t)$  accounting for the damping processes and the Heaviside step-function  $\Theta(t)$  mathematically ensures, that the propagation of the system proceeds only subsequently to the interaction of the system with the electromagnetic field. Hence the formal solution of equation 2.9 reads:

$$\rho_{ij}(t) = G_{ij}(t) \otimes \left\{ E(t) \sum_k (\mu_{ik}\rho_{kj} - \rho_{ik}\mu_{kj}) \right\}, \quad (2.13)$$

where  $A \otimes B$  denotes the convolution of the functions  $A$  and  $B$ .

For weak excitation, standard perturbation theory can be employed in order to expand the density matrix into a perturbation series [43–45]. Pursuing this ansatz for a two level system leads to the following expressions for the time-dependent density-matrix elements:

$$\begin{aligned} \rho_{gg}^{(n)}(t) &= -\frac{1}{i\hbar} \exp(-i\omega_e t - t/T_{1g}) \otimes \left( \mu_{ge} E_n^*(t) \rho_{eg}^{(n-1)}(t) - \mu_{eg} E_n(t) \rho_{ge}^{(n-1)}(t) \right), \\ \rho_{ee}^{(n)}(t) &= -\frac{1}{i\hbar} \exp(-i\omega_e t - t/T_{1e}) \otimes \left( \mu_{ge} E_n^*(t) \rho_{eg}^{(n-1)}(t) - \mu_{eg} E_n(t) \rho_{ge}^{(n-1)}(t) \right), \\ \rho_{eg}^{(n)}(t) &= -\frac{1}{i\hbar} \exp(-i\omega_{eg} t - t/T_2) \otimes \left( \mu_{eg} E_n(t) (\rho_{gg}^{(n-1)}(t) - \rho_{ee}^{(n-1)}) \right). \end{aligned} \quad (2.14)$$

Herein  $\hbar\omega_{eg}$  denotes the energy difference between the unperturbed states  $|g\rangle$  and  $|e\rangle$ , whereas  $\hbar\omega_{e,g}$  refers to the energy of the respective state. It is interesting to note, that these equations couple coherence terms to population terms and vice versa according to the following scheme, which assumes that the initial unperturbed system solely occupies the ground-state:

$$\rho_{gg}^{(0)} \longrightarrow \rho_{eg}^{(1)} \longrightarrow \rho_{ee}^{(2)} \longrightarrow \rho_{eg}^{(3)} \longrightarrow \dots \quad (2.15)$$

Here it is necessary to remark, that the sequence of interactions schematically represented in equation 2.15 refers to a specific ordering of interactions between light field and matter, that has been chosen to stress the principle evolution of the density matrix. Nevertheless, there are other (namely in total  $2^n$  with  $n$  being the order of perturbation) possibilities of interaction sequences. In order to account for the complete quantum mechanical path of the system a summation over all possible interaction orders has to be performed.

In order to quantitatively evaluate the signals obtained from pump-probe spectroscopy the third order polarization has to be calculated. The first order polarization, and therefore the first order susceptibility  $\chi^1$  accounts for the stationary absorption ( $Im(\chi^1)$ ) and refraction properties ( $Re(\chi^1)$ ), while the second order polarization vanishes in media with inversion symmetry such as liquids [6, 38]. Therefore, the time-evolution of the density-matrix, which is correlated to the macroscopic polarization  $P(t)$  of an ensemble of  $N$  independent and identical systems per unit volume via

$$P(t) = N \langle \mu(t) \rangle = N Tr(\mu\rho(t)) = N \cdot \sum_{ij} \mu_{ji} \rho_{ij} \quad (2.16)$$

up to third order perturbation theory has to be considered. Again, assuming the equilibrated system to be in its ground-state, i.e.  $\rho_{gg}^{(0)} = 1$ , the density matrix in first order perturbation from equation 2.14 can be written as:

$$\rho_{eg}^{(1)}(t) = -\frac{1}{i\hbar} \exp(-i\omega_{eg}t - t/T_2) \otimes (\mu_{eg}E(t)) \equiv G_{eg} \otimes (\mu_{eg}E(t)), \quad (2.17)$$

which in turn is inserted again into equation 2.14 in order to determine the second order polarization (referring to the interaction ordering given in 2.15). Therefore, equation 2.14 reads:

$$\rho_{ee}^{(2)}(t) = G_{ee}(t) \otimes (\mu_{eg}^* E^*(t) [G_{eg}(t) \otimes \mu_{eg} E(t)]). \quad (2.18)$$

In writing equation 2.18 the explicit form of the Green function as given in equation 2.12 has been avoided for clarity. Pursuing this iteration, the third order density matrix can be written as:

$$\rho_{eg}^{(3)}(t) = G_{eg}(t) \otimes \{\mu_{eg} E(t) [G_{ee}(t) \otimes (\mu_{eg}^* E^*(t) [G_{eg}(t) \otimes \mu_{eg} E(t)])]\}. \quad (2.19)$$

In complete agreement with the expansion of the density matrix into a perturbation series the macroscopic polarization (see equation 2.16) determining the optical properties of the system can be expanded according to:

$$P(t) = P^{(1)}(t) + P^{(2)}(t) + P^{(3)}(t) + \dots \quad (2.20)$$

Therefore, in complete analogy to the density matrix, the  $n^{th}$  component of the polarization can be evaluated if the  $(n - 1)^{th}$  is known. And hence,

$$P^{(3)}(t) = \mu_{eg}^* \rho_{eg}^{(3)}(t). \quad (2.21)$$

As mentioned above, there are  $2^3 = 8$  terms contributing to  $P^{(3)}(t)$  differing in the order in which the pulses interact with the sample. But before describing the individual contributions to  $P^{(3)}(t)$  and the time dependence of the transient absorption signal in detail, it is instructive to look at the scheme given in equation 2.15 again. Figure 2.3 presents a pictorial view on this specific pulsed-light-system interaction in a two-level system.

Before interacting with the first laser pulse, the system is in its equilibrium state, which is assumed to be described by  $\rho_{gg}^{(0)} = 1$ . The first laser pulse centered at  $t_1$  excites a polarization proportional to  $\rho_{eg}^{(1)}$  (see equation 2.17), which propagates during the time-interval  $\tau_1$ . This propagation is characterized by an oscillation with the frequency  $\omega_{eg}$  and a damping of the modulation amplitude with the damping constant  $\Gamma_{eg} = 1/T_2$ . If the second laser pulse interacts with the sample at an instant  $t_2$  at which  $P^{(1)}(t)$  has not completely decayed, i.e.  $\tau_1 < T_2$ , the second interaction creates the population  $\rho_{ee}^{(2)}(t) \propto \exp(-t/T_1)$  (eqn. 2.18), which decays with the characteristic lifetime of the excited state,  $T_1$ , during the time-period  $\tau_2$ . The third laser pulse arriving at the sample at  $t_3$  excites the third order polarization  $P^{(3)}(t) \propto \rho_{eg}^{(3)}(t) \propto \exp(-i\omega_{eg}t) \cdot \exp(-t/T_2)$  (eqn. 2.19).

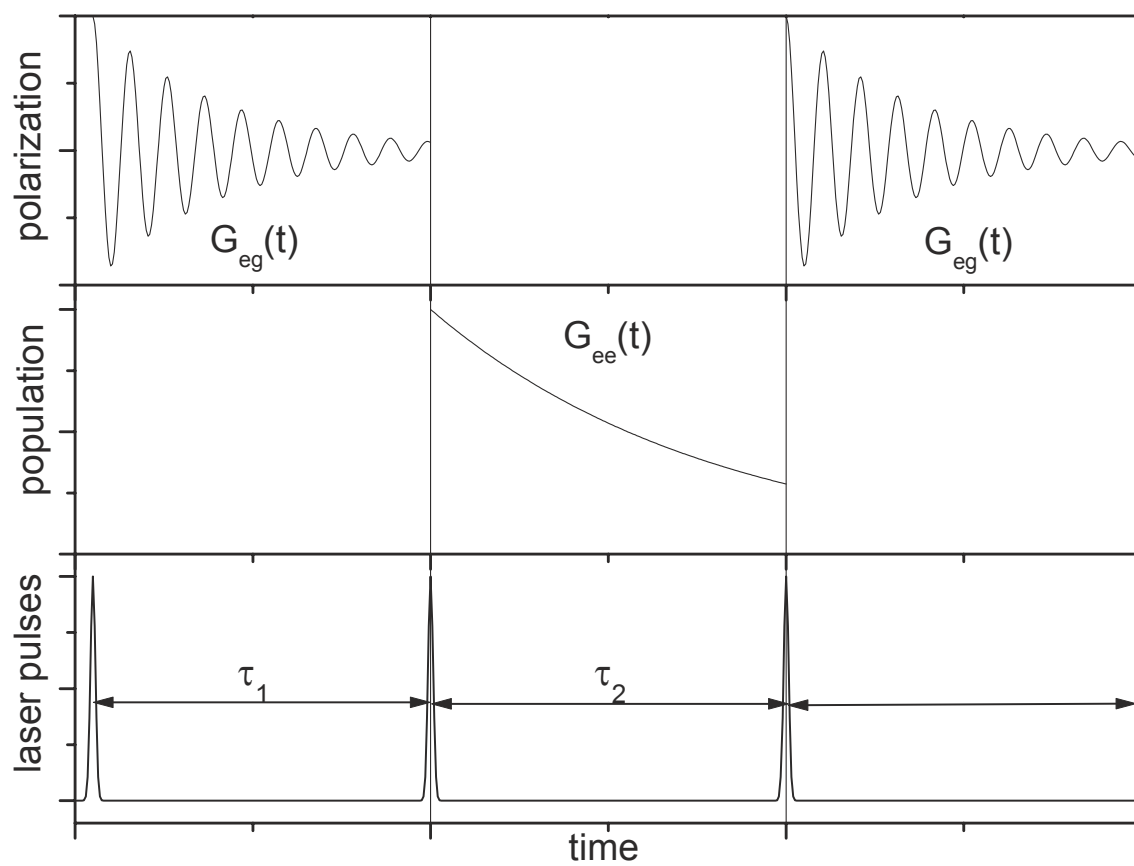


Figure 2.3: The polarization successively induced by three subsequent laser pulses is shown.

The corresponding Feynman diagrams schematically illustrating the light-matter interactions giving rise to  $P^{(3)}(t)$  are shown in figure 2.1.2. It has to be noted, that in each of the diagrams given in figure 2.1.2 the probe-pulse interacts only once with the system, while the pump-pulse interacts twice. This accounts for the fact, that the probe-pulse is assumed to be very weak compared to the pump pulse. Thus, the signals obtained, which result from the interactions given in figure 2.1.2, are independent of the probe power but linearly increasing with increasing pump intensity.

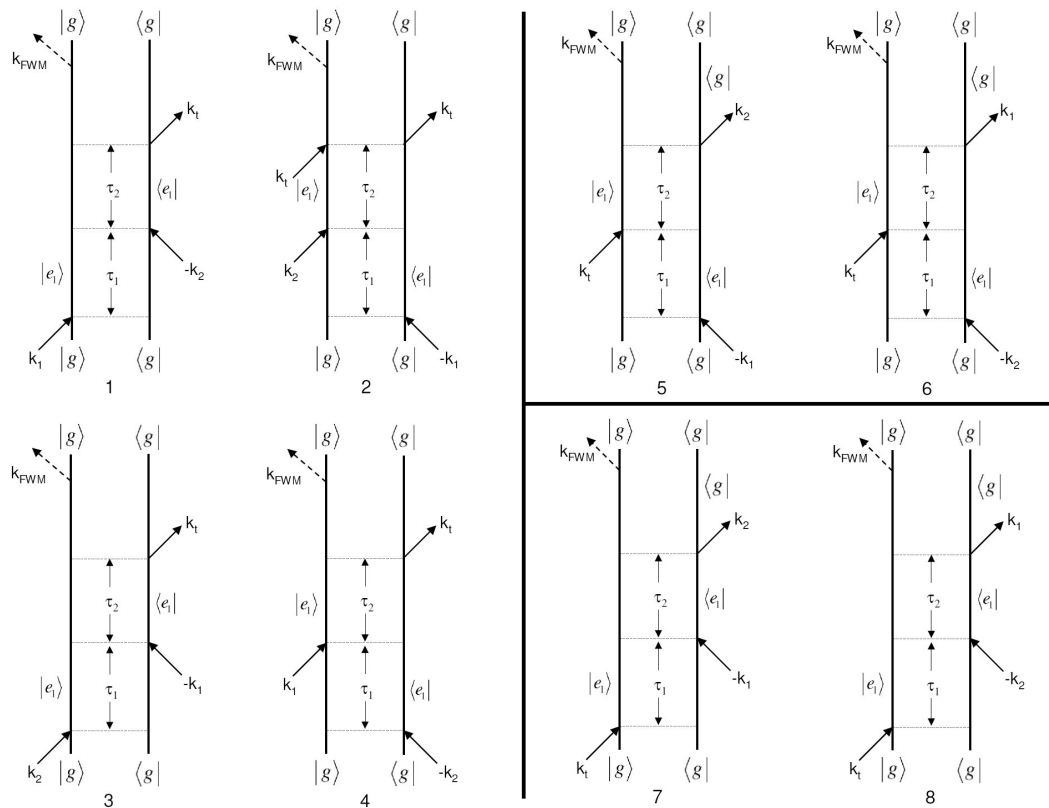


Figure 2.4: The Feynman diagrams representing the four different processes contributing to the third order polarization are shown. Note that a complete description of  $P^{(3)}$  involves the sum over all pathways shown here.

The first four terms, in which two pump photons interact with the system prior to the system-probe interaction, describe the so called *population contribution*, as the pump-pulse interactions transfers the system to a population state  $\rho_{ii}(t)$  before it is interrogated by the probe-pulse. These terms present the sequential absorption of pump and probe photons and are the only ones that contribute to the transient signal for long delay-times  $\Delta t$ . On

the other hand, the other diagrams represent the so called *non-sequential contributions*. These population contributions can be further classified. The first two terms are labeled *ground-state population contribution*, indicating that the time evolution of the ground-state population is affected by the first two interactions and subsequently monitored by the third one. The third and fourth terms are marked *excited-state population contribution*, as describing the time-evolution of  $\rho_{ee}(t)$ . As can be read from the corresponding Feynman diagram,  $\rho_{ee}(t)$  for the latter case can be written as:

$$\rho^{(3,ExSC)}(t) \propto G_{eg}(t) \otimes \left\{ \mu_{eg} \cdot E_t(t) \left[ \rho_{ee}^{(2)}(t) - \rho_{gg}^{(2)}(t) \right] \right\} \quad (2.22)$$

with the second order density matrix  $\rho^{(2)}_{ee}$  being expressed as:

$$\rho_{ee}^{(2)}(t) = G_{ee}(t) \otimes \left\{ \mu_{ge} \cdot E_p^*(t) [G_{eg}(t) \otimes \mu_{eg} \cdot E_p(t)] - \mu_{ge} \cdot E_p(t) [G_{eg}^*(t) \otimes \mu_{eg} \cdot E_p^*(t)] \right\}.$$

In contrast, the interaction sequence *pump-probe-pump* being counterintuitive with respect to the conventional transient absorption scheme gives rise to the fifth and sixth term in figure 2.1.2 describing the so called *pump-polarization coupling* (see ref. [46]).

$$\begin{aligned} \rho_{eg}^{(3,PPC)}(t) &\propto G_{eg}(t) \otimes \left\{ \mu_{eg} \cdot E_p(p) \left[ \rho_{ee}^{(2)}(t) - \rho_{gg}^{(2)}(t) \right] \right\} \\ &= G_{eg}(t) \otimes \left[ \mu_{ge} \cdot E_p(t) (G_{ee}(t) \otimes \left\{ \mu_{eg} \cdot E_t(t) [G_{eg}^*(t) \otimes \mu_{eg} \cdot E_p^*(t)] \right\}) \right]. \end{aligned} \quad (2.24)$$

These terms contribute most to the signal, when the pump and the probe beam are coincident in time. The last two contributions being due to the interaction sequence *probe-pump-pump* are labeled *perturbed free induction decay*-terms. These contributions dominate the signal, when the probe-pulse interaction with the sample volume proceeds the pump interactions. This contribution can be understood intuitively as the perturbation of the polarization caused by the probe pulse through the pump pulse.

$$\begin{aligned} \rho_{eg}^{(3,PFID)}(t) &\propto G_{eg}(t) \otimes \left[ \mu_{eg} \cdot E_p(t) \cdot (G_{ee}(t) \otimes \right. \\ &\quad \left. (\mu_{ge} \cdot E_p^*(t) \cdot (G_{eg}(t) \otimes \mu_{eg} \cdot E_t(t)))) \right]. \end{aligned} \quad (2.25)$$

Within the conventional scheme of a pump-probe experiment, two laser pulses are incident onto the sample: the strong pump-pulse (characterized by its electric field  $E_p(r) \propto \exp(ik_p r)$ ) and the usually much weaker probe-pulse (test-pulse, characterized by



$E_t(r) \propto \exp(ik_t r)$ ). Thus, in the case of non-collinear pulses a signal can be observed not only in a single direction. However, the possible directions of the signal pulses' wavevectors  $k_s$  are given by different phase matching conditions, which are schematically depicted in figure 2.5.

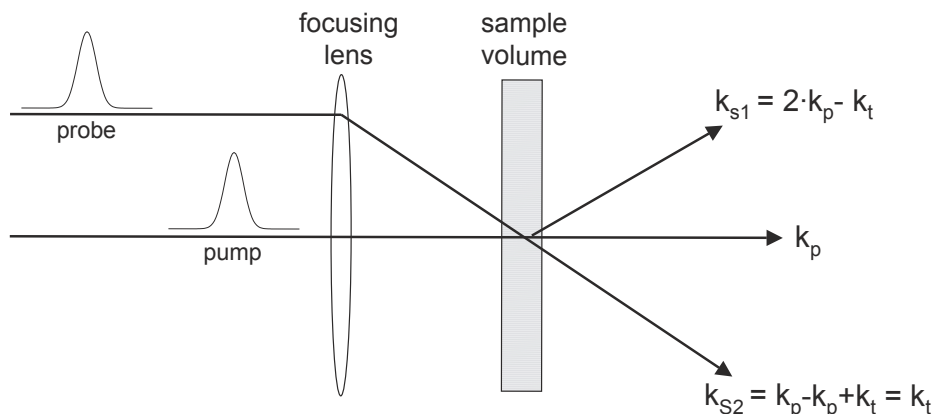


Figure 2.5: Experimental scheme employing two non-collinear laser pulse trains. The signal which is generated due to the excitation of the third order polarization can be observed in two distinct directions, which are given by the phase-matching conditions  $k_s = k_p - k_p + k_t$  and  $k_s = 2k_p - k_t$ .

As it is shown, a transient signal can be generated in either  $k_{s1} = 2k_p - k_t$  direction or in the direction of  $k_{s2} = k_p - k_p + k_t = k_t$ . The first phase-matching condition refers to a so called *two-pulse photon echo* experiment, while in the experiments performed in the course of this work the latter phase matching direction referring to conventional transient absorption experiments is employed.

The absorption cross section as measured by the probe-pulse can be related to the quantities discussed above by

$$\sigma_t(\omega) \propto -\omega \cdot \text{Im}(\chi(\omega)) = -\omega \cdot \text{Im}\left(\frac{P_t(\omega)}{E_t(\omega)}\right), \quad (2.26)$$

where  $E_t(\omega)$  describes the Fourier-transform ( $FT$ ) of the probe-envelope and thus the pulse spectrum of the probe-pulse:

$$P_t(\omega) = FT \left[ P_t^{(1)}(t) + P_t^{(3)}(t) \right]. \quad (2.27)$$

Thus, the detected differential optical transmission signal  $\Delta\alpha(\omega)$ , which is recorded in a conventional transient absorption measurement, is proportional to the imaginary part

of the third order polarization and reads

$$\Delta\alpha(\omega, \Delta t) \propto -\omega \cdot \text{Im} \left( \frac{FT [P_t^{(3)}(\Delta t)]}{E_t(\omega)} \right). \quad (2.28)$$

Therefore, the observed delay time-dependence of the differential transmission signal is determined by the time-evolution of  $P^{(3)}(\Delta t)$ , and thus depending on the experimentally controlled delay-time  $\Delta t$ .

In the following a second brief derivation of this time-dependence is outlined, which does not invoke an explicit treatment of the density matrix of the system and starts out from equation 2.28. This derivation follows the one given by Ernsting and coworkers in [38] and is presented here for the sake of giving a slightly different view on the theoretical basis of third-order non-linear spectroscopy and therefore further elucidating the underlying principles.

The third-order polarization which needs to be inserted in equation 2.28 can be split up in three parts according to the sequential contribution, the pump-polarization coupling and the perturbed free induction decay terms. Therefore,  $P^{(3)}(t)$  can be written within the rotating wave approximation:

$$\begin{aligned} P^{(3)}(t, \Delta t) = & 2 \cdot E_t(t - \Delta t) \int_{-\infty}^{\infty} dt' \chi_S(t - t') \cdot E_p^*(t') E_1(t') \\ & + 2 \cdot E_1(t) \int_{-\infty}^{\infty} dt' \chi_R(t - t') \cdot E_1^*(t') E_2(t' - \Delta t) \\ & + 2 \cdot E_1^*(t) \int_{-\infty}^{\infty} dt' \chi_{PFI}(t - t') \cdot E_1(t') E_2(t' - \Delta t). \end{aligned} \quad (2.29)$$

Assuming Gaussian time-dependence of the laser pulses, i.e.  $E_i(t) = A_i \cdot \exp(-t^2/2\tau_i) \cdot \exp(i\omega_i t)$ , and inserting equation 2.29 into 2.28 leads to a general expression relating the transient absorption signal to the response function of the system. In the case of well separated pulses, this expression reads [38]:

$$\Delta\alpha(\omega, \Delta t) \propto \int_{-\infty}^{\infty} d\Omega E_t^*(\omega) E_2(\omega - \Omega) \chi_S(\Omega) \cdot \exp(-\tau_1^2 \Omega^2 / 4) \cdot \exp(i\Omega \Delta t). \quad (2.30)$$

Other contributions characterized by the time-behavior of the terms  $FT[\chi_R(\omega)]$  or  $FT[\chi_{PFI}(\omega)]$  are neglected as they only contribute to the signal, when pump and probe pulse

are overlapping. In order to analyze above expression with respect to its dependence on  $\Delta t$  the response-function has to be specified. For population relaxation processes any arbitrary response function can be expressed as a sum over Lorentzian shaped functions, therefore equation 2.30 is evaluated using  $\chi_S(\Omega) = \frac{1}{i\Gamma_1 - \Omega}$ , where  $\Gamma_1 = 1/T_1$  is the characteristic population decay rate. Therefore, the response function used here can be thought of as the Fourier transform of the Green function  $G_{ee}(t)$  given in equation 2.12. Performing the integration leads to the expression

$$\begin{aligned} \Delta\alpha(\omega, \Delta t) &\propto \exp(-\Gamma_1 \Delta t) \exp(\Gamma_1^2 \tau_p^2 / 4) \cdot \text{erfc}(\tau_p \Gamma_1 / 2 - \Delta t / \tau_p) \\ &= \int_{-\infty}^{\infty} dt' \chi_S(t') \cdot F_{CC}(\Delta t - t') \end{aligned} \quad (2.31)$$

which is the well known expression for the convolution of the experimental response, i.e. the cross-correlation function  $F_{CC}(t)$ , and the exponential decay characterized by the time-constant  $T_1$ , written under the assumption that the pump-pulse duration is shorter than the probe-pulse  $\tau_p > \tau_t$ .

As this result was obtained for non-chirped pulses with a Gaussian envelope function, the question remains whether a similar expression holds for the delay-time-dependence of a transient absorption signal measured with a chirped supercontinuum. The derivation of a formula similar to 2.31 is much more complicated and not outlined here but can be found in reference [38]. The calculation results in

$$\Delta\alpha(\omega, \Delta t) = \int_{-\infty}^{\infty} dt' \chi_S(t') \cdot F_{CC}(\Delta t + t_0(\omega) - t'). \quad (2.32)$$

Thus, the transient signal measured with a chirped supercontinuum, which is corrected for the wave-length dependent zero-time (see equation 2.4) displays the same dependence on the pump-probe delay  $\Delta t$  as the signal obtained with non-chirped pulses. Therefore, it is obvious, that special care has to be taken during data evaluation in order to account for the chirp of the supercontinuum probe. In the experiments presented here, this is done numerically employing a routine that has been supplied by the group of PD. Dr. Gudrun Hermann, Institute of Biophysics and Biochemistry, University of Jena, and has been described elsewhere in detail [47]. With the approach a chirp compensation down to less than  $0.2 \text{ fs/nm}^{-1}$  could be reached (see reference [47] and chapter 5).

### 2.1.3 Experimental related aspects

The method of transient white light absorption, that is referred to as transient absorption spectroscopy (TA) from here on, has the advantage of providing spectral information over a broad range of wavelengths, the exact range depending on the specifications of the white light generation. A slight disadvantage of TA is the limited signal to noise ratio (S/N). This limitation originates in instabilities in the production of the probe white-light. Therefore two-color-pump-probe experiments or especially the coherent four-wave-mixing techniques described below provide much better S/N ratios.

If the sample is excited with a linearly polarized pulse having a wavelength resonant to an optical transition, those molecules will preferentially absorb whose transition dipole moments are oriented parallel to the field. This leads to an anisotropic spatial distribution of excited species. If now the probe pulse is polarized parallel to the pump beam, it will interact with only those molecules whose dipole moments are parallel to the laser polarization. Thus when the molecules aligned by the pump pulse change their orientation due to rotational redistribution their dipole moments are no longer parallel to the probe polarization. In a kinetic analysis this process gives rise to an additional signal decay describing the so called *rotational dephasing*. In contrast, if the probe beam is polarized perpendicular to the pump rotational dephasing will lead to a rise of the signal as additional molecular dipole moments are accessible for being probed. By measuring the kinetics for parallel ( $I_{\parallel}(\Delta t)$ ) and perpendicular laser polarizations ( $I_{\perp}(\Delta t)$ ) the time-constant describing this rotational reorientation or rotational dephasing process,  $\tau_{rd}$ , can be determined. This is done calculating the depolarization ratio, that is defined as:

$$R(\Delta t) = \frac{I_{\parallel}(\Delta t) - I_{\perp}(\Delta t)}{I_{\parallel}(\Delta t) + 2I_{\perp}(\Delta t)} \propto \exp(-\Delta t/\tau_{rd}). \quad (2.33)$$

The depolarization ratio is proportional to  $\exp(-t/\tau_{rd})$  and thus  $\tau_{rd}$  can be determined [48]. In contrast, the molecular kinetics can be measured free from rotational dephasing by setting the polarization of pump and probe at  $54.7^\circ$ , the so-called *magic angle* configuration. As the arguments given for the rotational dephasing also hold for two distinct non-parallel transitions within a non-rotating molecule the depolarization ratio also called *transient absorption anisotropy* gives information on the time-evolution and orientation of electronic or vibronic transitions involved in an intramolecular relaxation process.

Another experimental difficulty to be considered is caused by the group velocity

dispersion (GVD). GVD arises when a short pulse containing light of more than a single frequency travels through an optical transparent medium with non-flat dispersion relation. Thus, as a consequence of non-vanishing GVD, the pulses are broadened. Furthermore, as pulses used in a pump-probe scheme with different central frequencies travel with different speeds, experimental care has to be taken, to ensure that the pulses in a multicolor pump-probe (or four-wave mixing scheme see chapter 2.2.1) do overlap on the entire geometrical path through a sample. Therefore, the influence of GVD to the overall transient absorption signal can be kept negligible small by using samples being optically very thin. A further effect of GVD is the broadening of pulses while traveling through optical dense material such as cuvette windows, the solvent or optical elements such as lenses. The use of commercial cuvettes to hold a liquid sample causes the pulses to travel through 1.25 mm of fused silica before entering the actual sample region. This additional material causes the time-zero overlap to shift from what is usually measured for a thin glass plate and introduces additional chirp to the pulses.

A last experimental difficulty to be mentioned concerns non-resonant contributions to the observed short time dynamics of the system, which are usually summarized under the headline *coherent artifact*. Briefly, the main contribution of the coherent artifact arises from cross-phase modulation of the probe- in the presence of the strong pump-pulse. Thus, for delay-times, at which both pulses interact simultaneously with the sample or the cuvette windows, the probe frequency is shifted (the magnitude and sign of the shift depends on the actual overlap with the pump-pulse) and thus a loss or a gain of photons at a particular frequency is observed. This phenomenon gives rise to a peculiar time-zero behavior intrinsic to all pump-probe measurements. A detailed discussion of this interesting behavior, which arises from GVD and cross-phase modulation being present simultaneously, is far beyond the scope of this chapter but can be found in reference [49], for example. Experiments performed at the Department of Chemical Physics at Lund University to understand the appearance of a coherent artifact in an frequency integrated detection setup are presented in the appendix of this thesis.

## 2.2 Four-Wave-Mixing Techniques

In this section the general properties of time-resolved four-wave-mixing processes are described. The general discussion is applicable to techniques as degenerate four-wave-

mixing (DFWM), transient grating spectroscopy (TG spectroscopy), three pulse photon echo (TPPE) and CARS. These techniques have in common that three photons interact with a sample and a fourth signal photon is emitted in a well defined, phase-matched direction. By carefully controlling the pulse order, the photon energies and the phase-matching conditions a wide variety of molecular parameters can be interrogated specifically. The general features of four-wave-mixing will be discussed in this chapter on the example of transient grating spectroscopy. Before giving a theoretical approach to four-wave-mixing techniques in section 2.2.2, which is closely related to the theoretical description of transient absorption spectroscopy as outlined above, a pictorial view on transient grating spectroscopy is presented.

### 2.2.1 Transient Grating spectroscopy

Transient grating spectroscopy has been applied to address a wide variety of physical and chemical problems [50] such as diffusion in liquids [51], optical Kerr effect [52], electronic energy transfer [53], photoinduced electron transfer [54], non-adiabatic transitions [55] and excited-state relaxation dynamics [56].

In a transient grating experiment two laser pulses of the same color are incident on a sample in a non-collinear geometry. Thus, these pulses interfere and create a spatial modulation of the electric field. If the frequencies of these two pump-pulses are tuned to be in resonance with an optical transition within the species of interest, the sample will preferably absorb in the anti-nodes of the electric field pattern. The energy absorbed by the molecules leads to a local modulation of the index of refraction of the sample. Thus, periodic modulation of the index of refraction or an optical diffraction grating is formed with a grating period  $d = \frac{\lambda_p}{2 \cdot \sin(\theta/2)}$ , where  $\lambda_p$  denotes the wavelength of the pump-lasers and  $\theta$  is the angle under which the two pump-lasers are crossing. A third laser, the probe-laser, is then diffracted of the pump-induced transient grating. The scattering of the third pulse is greatly enhanced, if its frequency is tuned to fall into a molecular resonance (either a  $S_n \leftarrow S_1$ -transition, thus monitoring an excited state absorption or the  $S_1 \leftarrow S_0$ -transition and therefore monitoring the ground-state recovery dynamics). Under off-resonance conditions the scattering is solely due to the non-sequential contributions in figure 2.1.2 and persists only for delay-times  $\tau_2$  during which all three pulses interact simultaneously with the sample. The intensity of the scattered light is detected on a quadrature detector. As the transient

grating persists only during the presence of the sample excitation, its decay reflects the population dynamics of the ground-state hole or the excited state absorption created by the pump-pulse (see equation 2.35).

### 2.2.2 Third order perturbation theory

The third order perturbation theory used to describe four-wave mixing processes based on the description of the density matrix as derived by Mukamel and coworkers [57] is completely identical to the theory that can be used to describe transient absorption measurements as outlined above in section 2.1.2. The only but striking experimental difference is the use of a three-beam setup as schematically shown in figure 2.6 instead of a two-beam configuration sketched applied for transient absorption measurements as discussed in section 2.1.1 and sketched in figure 2.5.

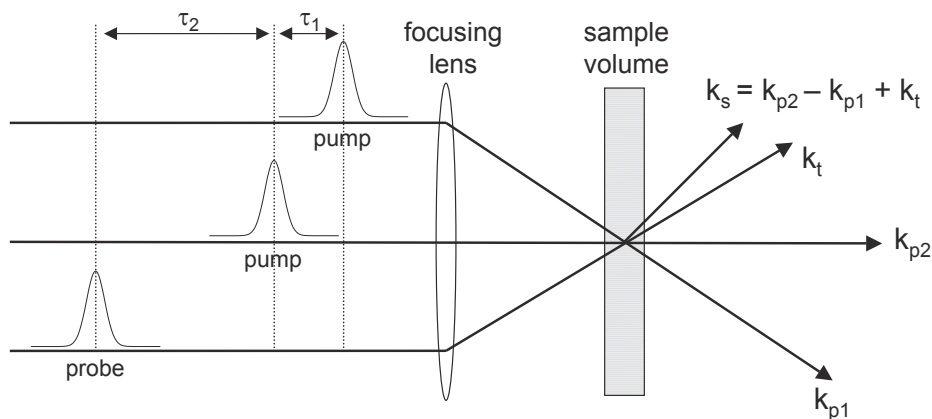


Figure 2.6: Experimental scheme used to perform four-wave mixing experiments with three beam excitation.

The inclusion of a third beam into the experimental scheme allows to fully control each of the time-intervals  $\tau_1$  and  $\tau_2$  given in figures 2.6 and 2.3. The separate experimental access to the delay-times allows for the investigation of a wider range of nonlinear phenomena occurring in the photoexcited system than in the case of using only two excitation pulses. In particular, inhomogeneous and homogeneous dephasing contributions can be separated (see e.g. [58] or [59]) and the coupling between vibronic (see e.g. [59–61]) and electronic states [62] can be investigated. The use of a non-collinear pulse geometry within the four-wave mixing scheme provides a further advantage: Since the signal, due to

the time-varying third order polarization  $P^{(3)}(t) = \mu_{eg}\rho_{eg}(t)$ , is emitted coherently in the phase-matched direction  $k_s = k_{p2} - k_{p1} + k_t$ , it can be aligned through an apparatus and therefore detected basically background free. Of course, there are other possible directions of the signal corresponding to a different combination of the incident wave vectors, but only the given one is of experimental interest for the experiments presented in this thesis. According to the given phase matching, the third order density matrix (and therefore  $P^{(3)}(t)$  as well) is proportional to  $E_{p1}^* E_{p2} E_t$ . The corresponding Feynman diagram leading to equivalent results as in a transient absorption experiment is presented in figure 2.7.

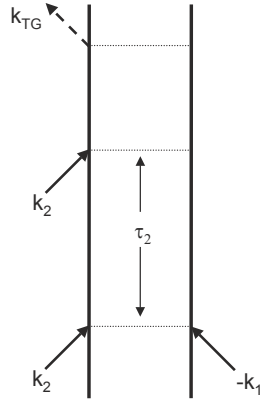


Figure 2.7: Feynman diagram relevant to the processes observed in a transient grating experiment.

The density matrix for this contribution, which can be identified to be a population contribution, is expressed as:

$$\begin{aligned} \rho_{e_1 e_2}^{(3)}(t) &\propto G_{e_1 e_2}(t) \otimes [\mu_{e_1 e_2} \cdot E_3(t) \{G_{e_1 e_1}(t) \otimes [\mu_{g e_1} \cdot E_2(t) (G_{e_1 g}^*(t) \otimes \mu_{e_1 g}^* \cdot E_1^*(t))]\}] \\ &= \frac{-i}{\hbar^3} \Theta(t - t_3) \Theta(t_2 - t_1) \cdot \exp(-\tau_2/T_1) \cdot \exp(-(t - t_3 + \tau_1)/T_2) \\ &\quad \cdot E_1^* E_2 E_3 \cdot \exp(-i\omega_{e_1 e_2}(t - t_3 - \tau_1)) \end{aligned} \quad (2.34)$$

In writing this equation, infinitely short pulses are assumed, i.e.  $E_i(t) = E_i \cdot \delta(t_i)$  with  $t_i$  being the incident at which the  $i^{th}$  pulse interacts with the sample, and the Heaviside step function  $\Theta(t)$  is introduced. Expression 2.34 can be easily related to the schematic pulse sequence given in figure 2.3. Thus, as it is readily seen from the expression in equation 2.34, the third order polarization, generating the coherent four-wave-mixing signal is generated at  $t = t_3$ . For times larger than  $t_3$  the signal reflects the temporal response of  $G_{e_1 e_2}(t) \propto$



$\exp(-i\omega_{e_1e_2} \cdot t - t/T_2)$ , depending on the polarization dephasing time of the sample  $T_2$ . Nevertheless, the time-dependence of the signal, that is the dependence on  $t$ , is not resolved in the experiments presented here, as the detection scheme employs a quadrature detector integrating over the full temporal response of the system, i.e. detecting [63–65].

$$I_{TG}(\tau_2) \propto \int_{t_3}^{\infty} dt \cdot |P_{e_1e_2}^{(3)}(t, \tau_2)|^2. \quad (2.35)$$

Therefore, the dependence of the FWM-signal on  $\tau_2$ , the time-interval between the two coincident pump-pulses ( $\tau_1 = 0$  see figure 2.3) and the probe, is recorded. In difference to the differential absorption signal recorded in a transient absorption experiment (equation 2.28) the four-wave-mixing signal intensity is proportional to the absolute square of the third order polarization. As  $P^{(3)}(\tau_2) \propto \exp(-\tau_2/T_1)$  and  $I_{TG}(t) \propto |P^{(3)}(t)|^2$ , the observed transient grating signal recorded with the quadrature detector will be  $\propto \exp(-2 \cdot \tau_2/T_1)$ , thus showing a different dependence on the experimentally controlled delay-time  $\tau_2$  compared to the  $\Delta t$ -dependence of the transient absorption signal.

## Chapter 3

# Experimental Setup

This chapter describes the laser systems, which were used to perform the experiments presented in this work. As the process of generating light pulses in the order of 80 fs is technological standard by now [66], no emphasis is put on the description of passive Kerr-lens mode-locking, the crucial experimental step in obtaining such pulses [66]. The presentation is limited to outline the essential technological features of the two laser systems employed. Having discussed the basic features of the laser setup, the experimental setup of the transient absorption and transient grating measurements will be presented. In particular, special attention will be paid to the phase-matching condition, which needs to be fulfilled for generating transient grating signals [67].

### 3.1 Generation of Femtosecond Laser Pulses

In this section the two laser systems used in the course of this work will be presented. One of the systems subsequently referred to as the *100 kHz- System* was applied to the measurements on Magnesium Octaethylporphyrin (see section 5.2). This system delivers laser pulses of relatively low pulse-energies at a repetition rate of 100 kHz. The second laser system used for the other experiments presented here, delivers higher pulse-energies but with a much lower repetition-rate of 1 kHz. It is therefore labeled *kHz-system*.

#### 3.1.1 100 kHz- System

The laser system is schematically presented in figure 3.1. It generates laser pulses of typically 60-80 fs duration (FWHM) with pulse energies of about 50-100 nJ. The system

consists of a Kerr-lens mode-locked femtosecond *oscillator* (MIRA Coherent) and a cavity dumped, cw-pumped *amplifier* (RegA 9000, Coherent), both being pumped by the output of an *argon ion laser* (Sabre, Coherent). The pump-laser is operated in the multi-line mode and its 25 W output is split into 8 W, used to pump the Ti:Sapphire based oscillator, and 17 W for pumping the RegA. The oscillator itself exploits passive Kerr-lens mode-locking to generate 60 fs pulses (FWHM) with pulse-energies of 10 nJ spectrally centered at 796 nm at a repetition rate of 76 MHz. The oscillator output is divided by means of a 30:70 beamsplitter and only 30% of the output is used to seed the regenerative amplifier. The in-coupling of a single, defined oscillator pulse into the amplifier-cavity is implemented by an acousto-optical modulator. In order to avoid independent lasing of the amplifier, a Q-switch opens the cavity exclusively for the period of time, in which the seed pulse is residing within it. Amplification of the pulses is obtained by multiple passing through the optical active medium of the amplifier (Ti:Sapphire). In order to avoid hardware damage from the successively amplified pulse traveling in the cavity, further dispersion is introduced to the pulse within each of its about 27 round-trips in the cavity. This dispersion leads to a spreading of the pulse and therefore keeps the peak intensity well below the damage threshold of the laser optics. Being amplified and stretched the pulse is out-coupled from the amplifier cavity by means of the acousto-optical modulator and compressed, by compensating for the chirp introduced in the amplification process with multiple reflection of a holographic grating. Having passed through the amplification stage the 796 nm-pulses show a FWHM of about 120 fs and have pulse energies of typically 8  $\mu$ J.

These amplified pulses are used to independently pump two white-light *optical parametric amplifiers* (OPA 9400, Coherent). For pumping the amplifier output is split by means of a 30:70 beamsplitter, thereby ensuring that the OPA, whose output is split in order to yield the two pump-pulses within the transient grating scheme, has about twice the output power of the other OPA. The OPAs allow for the pulses to be tuned in wavelength over the entire visible spectral range (430 - 730 nm). The light conversion in the OPAs is accomplished by super-continuum generation and frequency doubling using the fundamental output of the amplifier. Subsequently difference-frequency generation of the second harmonic radiation and variable infra-red components of the white-light continuum are employed in order to gain a high range of tunability. The OPA-output pulses are compressed using a double-pass prism-compressor in a standard configuration [66] with the dispersive medium being BK7. This yields laser pulses with typical pulse durations of 60-80 fs. The

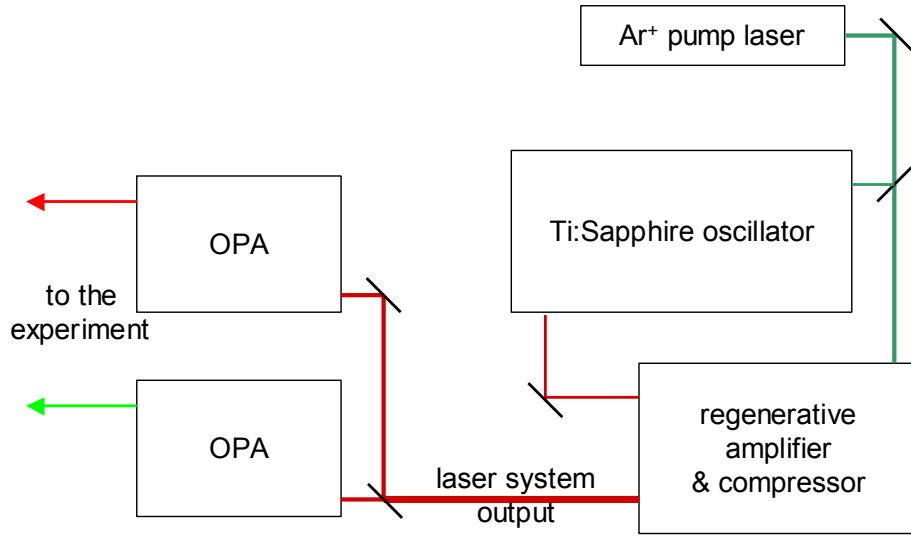


Figure 3.1: The 100 kHz-laser system is shown schematically. For details please see text.

pulses are temporally characterized with a commercial *auto-correllator* (Femtoscope MC-2, BMI), while their spectral profile is recorded by a CCD detector (LN/CCD512B, Princeton Instruments) in combination with a monochromator (SpectrPro 500, Acton).

### 3.1.2 1 kHz- System

The 1 kHz-laser system, shown schematically in figure 3.2, was used to perform the transient absorption measurements presented in this thesis (see section 5.3) and the transient grating experiments on phycocyanobilin (section 4) and the transition-metal complexes (see part III). It operates at a repetition rate of 1 kHz and delivers 70-80 fs (FWHM) laser pulses with pulse energies of some  $\mu\text{J}$  in the spectral range between 450 and 700 nm.

The key components of the system are a passive Kerr-lens mode-locked Ti:Sapphire based *oscillator* (MIRA, Coherent), which is pumped by the 8 W output of an *argon ion laser* (Innova 300, Coherent) operating in the multi-line mode. The oscillator produces pulses centered at 804 nm having a temporal FWHM of about 60 fs and pulse-energies of typically 10 nJ with a repetition rate of 76 MHz. Higher energy pulses are obtained by amplifying the oscillator output in an amplifier system (MXR/CPA 1000, Clark), which consists of a *stretcher*-, an *amplifier*- and a *compressor* unit. The *stretcher unit* lengthens the pulses to about 200 ps temporal duration by multiple reflections off a holographic

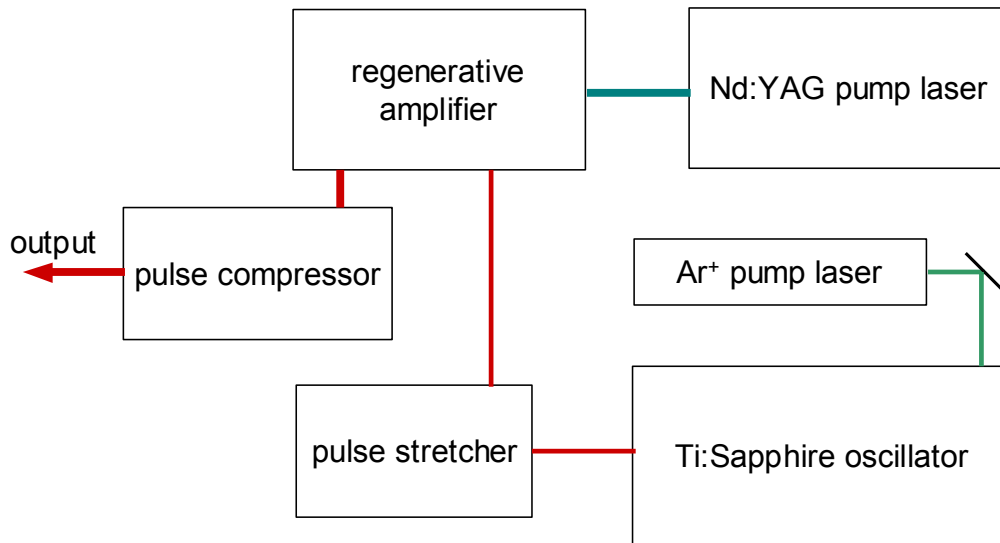


Figure 3.2: The 1 kHz-laser system is shown schematically. For details concerning the system please see text.

grating. This procedure introduces chirp to the pulses and greatly reduces the peak intensity and therefore ensuring that during the amplification process no damage is caused to the optical elements of the amplifier units. The *regenerative amplifier* is based on a Ti:Sapphire oscillator, which is pumped by the frequency doubled output of a Nd:YAG laser (MXR/ORC 1000, Clark) at 532 nm operating at a repetition rate of 1 kHz with approximately 10  $\mu\text{J}$  per pulse. Q-switching is achieved by means of a Pockels cell being triggered by the Nd:YAG-output at 1 kHz in order to avoid independent lasing of the amplifier cavity. The Pockels cell allows for in-coupling of a single, well defined and stretched oscillator pulse into the amplifier-cavity, where it resides for several round trips within the cavity. Having attained maximal amplification after multiple trips through the laser-active medium of the amplifier, the pulses are coupled out of the amplifier cavity by the Pockels cell. The amplified pulses are directed into a *grating compressor*, where the dispersion introduced by the stretcher unit is compensated for. This again is obtained by multiple reflections off a holographic grating, yielding 80 fs (FWHM) laser pulses centered at 804 nm with pulse energies of typically 800  $\mu\text{J}$ . The compressor output is used to pump two *optical parametric amplifiers* (TOPAS, Light Conversion) to generate tunable laser pulses. The operation of the TOPAS is based on a difference-frequency generation performed with the incoming pump-light. Photons of the fundamental frequency  $\omega_{\text{pump}}$  are subject to the non-linear process of parametric

down-conversion resulting in a signal,  $\omega_{signal}$ , and an idler photon,  $\omega_{idler}$ , with

$$\omega_{signal} + \omega_{idler} = \omega_{pump}. \quad (3.1)$$

Furthermore, the difference-frequency generation is combined with frequency doubling of the signal and idler frequency (yielding  $2\cdot\omega_{signal}$  and  $2\cdot\omega_{idler}$ , respectively) and signal-fundamental sum-frequency generation ( $\omega_{signal} + \omega_{pump}$ ). The combination of the various non-linear optical processes allows for laser pulses to be obtained within the spectral range of 450 to 700 nm. Beyond the visible spectrum, signal and idler allow for large regions of the IR spectrum to be covered, a spectral range that was not utilized in the course of this work. The additional dispersion introduced by the various non-linear processes taking place inside the TOPAS are compensated for by means of a double-pass prism (BK7) compressor in standard arrangement [66]. Being compressed the laser pulses are characterized to have a temporal FWHM of typically 90 fs and an energy of several  $\mu\text{J}$  per pulse. The temporal characterization of the pulses is done by means of a commercial autocorelator (MXR/AC 150, Clark), while their spectrum is recorded with the help of a CCD detector (SDS 9000, Photometrics) in combination with a monochromator (SpectraPro 500, Acton).

### 3.2 White-light-probe transient absorption

The experimental setup used to perform the white-light supercontinuum-probe transient-absorption experiments is sketched in figure 3.3. The output of one of the TOPAS is chirp compensated as mentioned above and used as the pump-pulse. The second part of the amplified 800 nm compressor output is attenuated and focused into in a 3 mm Sapphire window in order to generate the supercontinuum utilized as probe-pulse in the TA experiments.

The resulting supercontinuum is fairly smooth in the spectral region from 450 to about 720 nm and is re-focused with a short focal length lens ( $f=10$  mm). A wedge is used to split off part of the white light to be used as the reference beam. All three beams are focused into the sample with a focusing mirror ( $f=20$  cm). While the pump and the probe beam are aligned to be overlapping within the sample volume, the reference beam passes through the the sample without being overlapped with any other beam. The relative timing between the pump and the probe and reference pulse-trains is set by means of two computer controlled optical delay-lines. In order to avoid any rotational dephasing contribution to

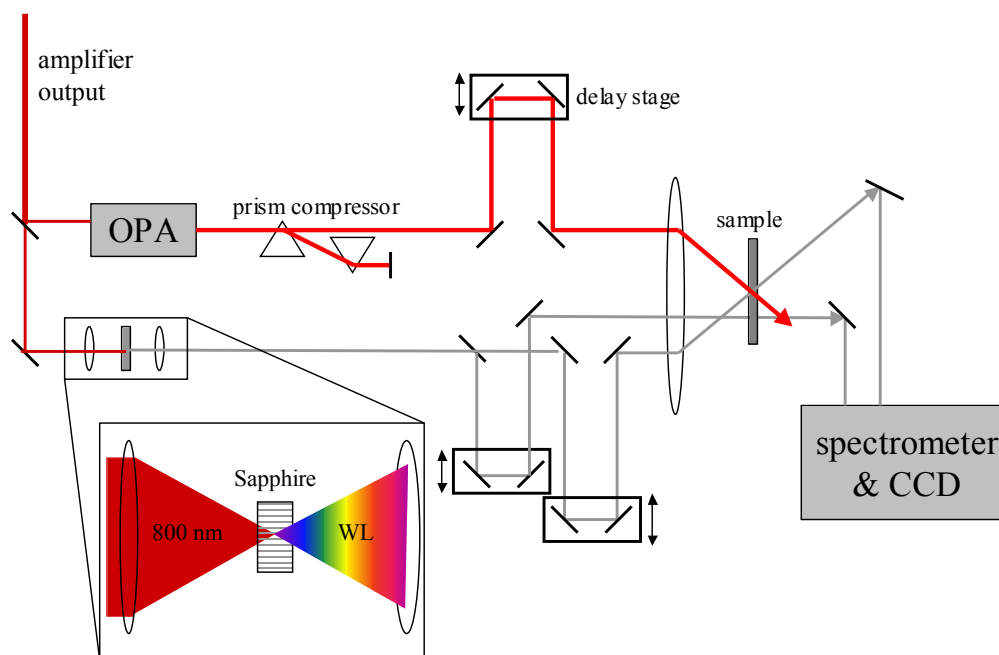


Figure 3.3: A schematic diagram of the pump supercontinuum-probe transient-absorption setup used for the experiments presented here is shown. For details please see text.

the transient absorption signal, the polarizations of the pump and probe beam were chosen to be at the magic angle of  $54.7^\circ$  (see section 2.1.3). Adjustment of the relative polarizations is achieved by means of Berek-compensators which are inserted in the beam pathes. While the probe beam is being blocked after the sample, the probe and the reference beam are made parallel and focused onto the entrance slit of the monochromator using a cylindrical lens ( $f=8\text{cm}$ ). The spectrometer is equipped with a CCD camera, whose CCD chip can be divided spatially into two parts that can be read out separately. Thus, the experimental setup allows for simultaneous spectrally dispersed detection of the probe and the reference beam. The chirp of the white light continuum was compensated numerically to  $\leq 0.2 \text{ fs/nm}$  by fitting the appropriate time-zero function (see eqn. 2.4) to the spectrally dispersed data. This was done with the help of a transient-absorption data analysis program provided by PD Dr. Gudrun Hermann (Institute for Biophysics and Biochemistry, University of Jena). For a detailed description of the program please see [47]. Thereby, the time resolution that can be obtained in the spectral region of our experiment is about 200 fs. Thus, as theoretically derived in section 2.1.2, by recording the transmission of the sample as a function of wavelength and delay-time between photo-excitation and probe-supercontinuum

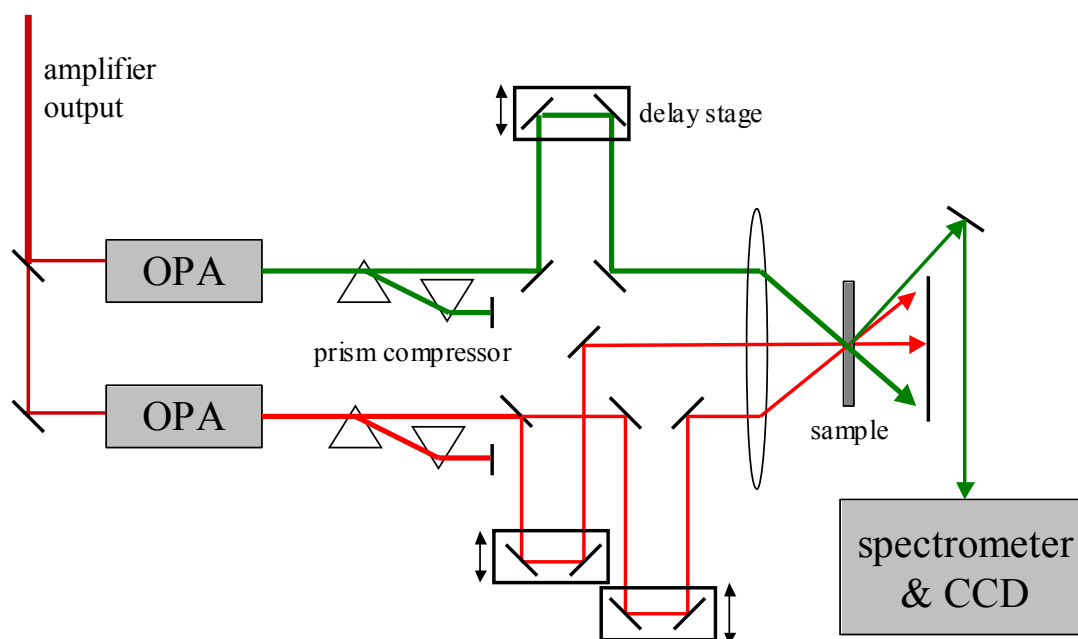


Figure 3.4: The experimental transient grating setup is shown. For details see text.

intermediate species can be characterized with respect to their absorption properties and lifetimes on a time-scale down to shorter than one picosecond.

### 3.3 Transient grating spectroscopy

Figure 3.4 schematically displays the setup used for performing the transient grating measurements. For these experiments each part of the amplified 800 nm light was used to separately pump two optical parametric amplifiers. These produce two independently tunable pulse trains, which were chirp compensated and re-compressed independently.

The pump- pulses ( $\mathbf{k}_1$  and  $\mathbf{k}_2$ ) within the transient grating scheme have the same color and are generated by dividing the output of one OPA (TOPAS when using the kHz-system) into two beams of approximately the same intensity by means of a 50:50 beam-splitter. The pulses produced by the second OPA (TOPAS) serve as the probe-pulses ( $\mathbf{k}_3$ ) within the experimental scheme and are delayed with respect to the pump-pulses by means of an optical delay line. In order to suppress any undesired anisotropy contributions to the TG-signal the polarization of the probe-beam was rotated by 54.7 with respect to the



polarization of the pump-beams, i.e. magic angle configuration was employed (see section 2.1.3). As in the case of transient absorption spectroscopy, Berek-compensators were used to align the polarization of each pulse-train. All beams were made parallel and focused into the sample with a 20 mm spherical mirror under a slight angle with respect to the optical axis. The pulse energies at the sample are typically 100 nJ, the sample itself is placed in a 1 mm path length rotating cell in order to avoid rapid photo-degradation of the sample and thermal effects for both transient grating and transient absorption measurements. The rotation speed is adjusted so that each set of pulses interacts with a fresh portion of the sample. Having passed the sample, the signal, which is generated in the phase matched direction

$$\mathbf{k}_{TG} = \mathbf{k}_1 - \mathbf{k}_2 + \mathbf{k}_3, \quad (3.2)$$

is recollected using a 50 mm focal length achromatic lens and sent to the detector (as described in sections 3.1.2 and 3.1.1), which allows to detect the transient absorption signal spectrally dispersed as a function of delay time between the pump-pulses and the probe-pulse.

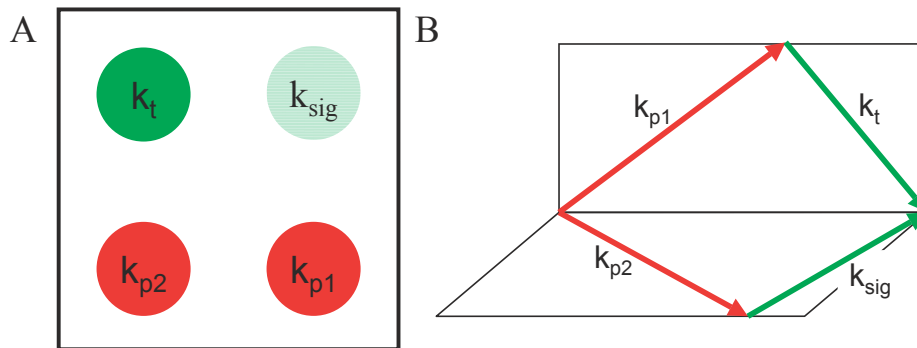


Figure 3.5: The arrangement of the laser beams within the experimental TG scheme is sketched. The specific realization of phase-matching corresponds to the so-called BOXCARS geometry. For details see text.

As transient grating spectroscopy is a coherent process not only energy but also momentum has to be conserved, that is - in the language of X-ray-scattering - the probe-light has to be incident onto the laser induced grating under Bragg-conditions in order for an elastically scattered signal to be observed (see also section 2.2.1): In a transient grating experiment the phase matching given in equation 3.2 has to be fulfilled. Figure 3.5 shows

a front view (a cut through the experimental beam alignment perpendicular to the optical axis) of the four beams involved in the transient grating process. The specific arrangement of beams is referred to as the BOXCARS geometry [68–70] and ensures, that the condition given in eqn. 3.2 is fulfilled. The wave-vectors of the probe-beam ( $\mathbf{k}_t$ ) and one of the pump-beams ( $\mathbf{k}_p^{(1)}$ ) lie in the same plane, while  $\mathbf{k}_p^{(2)}$  and the wave-vector of the signal are oriented in another plane perpendicular to the first one. Thus, the four-wave-mixing signal is generated in a spectrally distinct direction. Therefore, it can be very conveniently separated by the use of a simple pin-hole and thus, the signal can be detected background free. Hence, very high signal-to-noise ratios can be achieved with moderate experimental effort and it is this feature, that significantly contributes to the superior sensitivity of the grating detection compared to transmission measurements, which has been clearly demonstrated by Wild and coworkers for the case of spectral hole-burning [71].

### 3.4 Time-resolved fluorescence spectroscopy

Figure 3.6 schematically shows the experimental setup used for the time-resolved fluorescence measurements. A frequency doubled Nd:YAG laser is used to pump a Ti:Sapphire oscillator (Spectra Physics), whose output was tuned to 800 nm and frequency doubled in a BBO crystal to obtain the excitation wavelength at 398 nm. An acousto-optical modulator (AOM) is used as a pulse-picker in order to reduced the repetition rate, at which the sample is excited. The AOM allows for a reduction of the pulse rate from 82 MHz, the repetition rate of the oscillator, to 4 MHz. The polarization of the excitation light was controlled using a Berek compensator to be at the magic angle with respect to the polarization analyzer in the beam-path of the collected fluorescence. The fluorescence is detected in backward scattering direction and sent to the entrance slit of a grating spectrometer. The sample was placed in a rotating cuvette in order to avoid sample degradation and thermal effects and to ensure, that each pulse interacts with a fresh portion of the sample.

To detect the time-dependence of the fluorescence, a streak camera (Hamamatsu Photonics) was used. The basic operation principle of a streak camera is sketched in figure 3.7. Briefly, the fluorescence light is spectrally dispersed along the x-direction and focused onto the output slit of the spectrometer, which is aligned parallel to the x-axis of the system. In the streak camera itself, the light strikes a photocathode and releases electrons from the electrode with the number of electrons released at a given x-position being proportional to

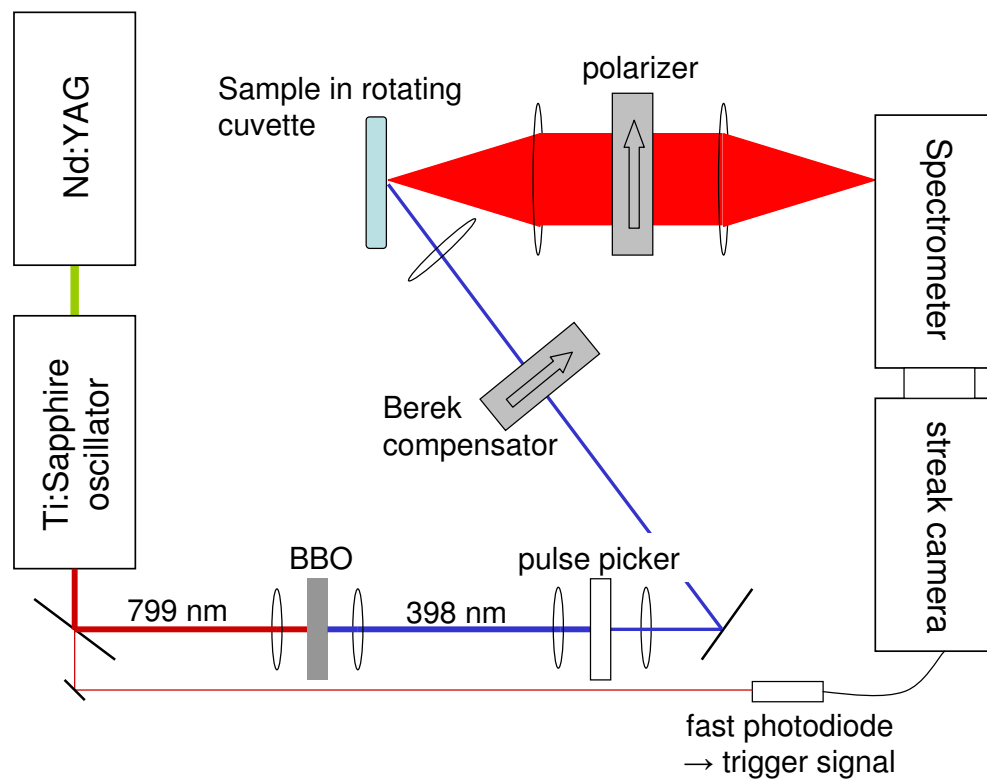


Figure 3.6: Schematic view of the experimental setup for the time-resolved fluorescence measurements.

the light intensity at the particular position. The released electrons are accelerated along the z-direction of the camera and pass an electric field region that deflects the electrons along the y-direction before being detected on a phosphor screen. As a linearly dropping voltage is applied on the deflecting electrodes, whenever a pulse laser pulse is detected by the trigger system, the electrons entering the field region first will be deflected most, whereas electrons entering at later times will be deflected less along the y-axis. Thus, the combination of spectrally resolving the fluorescence along the x-direction and temporal resolution along the y-axis gives rise to the two-dimensional data of a streak camera. The spectral range that can be monitored in a single experiment spans 100 nm, while the temporal window can be varied between 100 ps and 2 ns. In the latter measurement mode, the experimental time-resolution is about 20 ps, while in the first case it is as good as 1.5 ps.

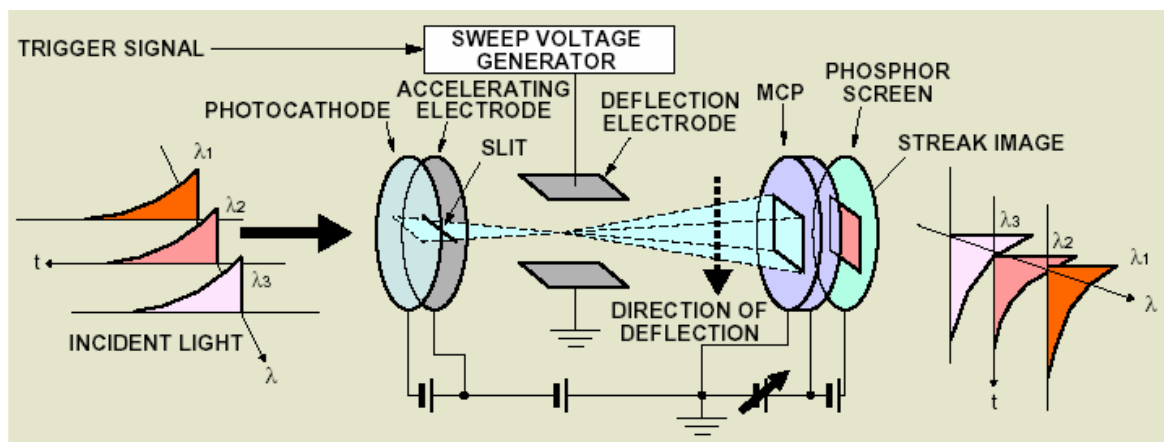


Figure 3.7: A schematic representation of the function of a streak camera. The figure is taken from the Hamamatsu Photonics web page.

**Part II**

**Biological Systems**



## Chapter 4

# Excited State Dynamics of Phycocyanobilin

The primary light-induced ultrafast relaxation processes of phycocyanobilin (PCB) were studied by means of femtosecond time-resolved spectroscopy. The system phycocyanobilin serves as a model chromophore for the enzyme phytochrome. By means of transient-grating (TG) spectroscopy where the excitation wavelength was varied over the spectral region of the ground-state  $S_0 \rightarrow S_1$ -absorption the ultrafast processes were studied upon excitation with varying excess energy delivered to the system. On the basis of the results obtained, both the rate of the photoreaction in PCB and the rate of the decay of different excited-state species via different decay channels depend on the excitation wavelength. Furthermore, the formation of the photoproduct is also dependent on the pump color. The data is in excellent agreement with a model for the primary photoprocesses in PCB established by Bischoff et al. [19]. Furthermore, it provides additional insight into the ultrafast light-induced processes in this system. Furthermore, transient absorption spectroscopy was employed to investigate the light-induced processes in the protonated form of phycocyanobilin suggested to be the product of the photoreaction observed for phycocyanobilin. Interestingly, no major changes in the overall decaying behavior have been observed. Therefore, the results presented in this chapter are aiming at understanding the photophysics of a model-system mimicing the photophysical behavior of a chromophoric unit of phytochromes.

## 4.1 The system Phycocyanobilin

### 4.1.1 The biological relevance of Phycocyanobilin

Phytochromes are pigments in plants, that are used to judge the environment of the plant by monitoring the electromagnetic spectrum in the visible and the infrared spectral region. Thus, phytochromes allow the plant to "see". Phytochromes are involved in such important processes as detection, interpretation and transduction of light signals, therefore allowing the plants to adapt to environmental conditions and to optimize their growth and development. [72] Phytochromes appear to exist in different types, which differ in their sensitivity to different parts of the electromagnetic spectrum. From their overall absorption spectrum it can be concluded that they are specialized for the detection of red and infrared light in the spectral regions 580 to 720 nm and 700 to 800 nm, respectively. (The absorption of blue light in the spectral region around 400 nm seems to be of less biological importance, especially due to the existence of additional photoreceptors in higher plants, the so called "cryptochromes", whose functionality is optimized for the absorption in this spectral region [73].) The range of biological responses triggered by phytochromes photoreceptors spans from shade avoidance over germination to flowering. At normal temperature all phytochromes exist in two stable forms referred to as Pr (Phytochrome red absorbing) and Pfr (Phytochrome far red absorbing), respectively. The chromophore in the Pr form exhibits an absorption maximum at about 670 nm, while the Pfr form of the chromophore absorbs best at 730 nm. Characteristic and critical for the photo-biological functionality of phytochromes is the light induced reversible interconversion of the Pr and the Pfr form of the chromophore. (The quantum efficiency of the Pr→Pfr transformation was measured to be  $\Phi_r = 0.16$ , while the quantum yield of the Pfr→Pr interconversion was determined to be  $\Phi_{fr} = 0.10$  [74].) Following light absorption in the characteristic spectral regions, the chromophoric group as well as the apoprotein change their geometrical structure and their interaction and in concert with these changes the biological response is triggered.

Thus, it is believed, that the first crucial part in the description of the mechanisms that lead from light absorption in a particular chromophore to a complex biological process such as seed germination is the thorough characterization of the photophysics of the chromophore itself. As the free chromophore of phytochrome is not stable in solution, the experiments done in the course of this dissertation were performed on phycocyanobilin (see figure 4.1), which is structurally very similar to the phytochrome chromophore and



therefore serves as a model compound. Protonated phycocyanobilin is included in these experiments presented here aiming to provide a detailed study of the phytochrome chromophoric photophysics.

Phycocyanobilin itself belongs to a class of open-chain tetrapyrroles playing a functional and vital role in nature [75]. Its structural form is displayed in figure 4.1. As a 2,3 dihydrobilindion chromophore (see 4.1) PCB constitutes the prosthetic group of the phycobiliproteins C-phycocyanin and allophycocyanin. Both proteins are involved in the light harvesting and energy transfer processes within the photosynthetic antenna complexes of cyanobacteria and red algae [76–78]. The structurally very similar system phytochromobilin (PΦB) constitutes the chromophoric group of the class of enzymes called phytochromes. PΦB differs from PCB only in the structure of the side chain connected to the Carbon atom C18, while in PΦB this particular side chain is a vinyl-group in PCB a ethyl group is attached to C18. Thus, PCB can be considered to be a suitable model for the phytochrome chromophore.

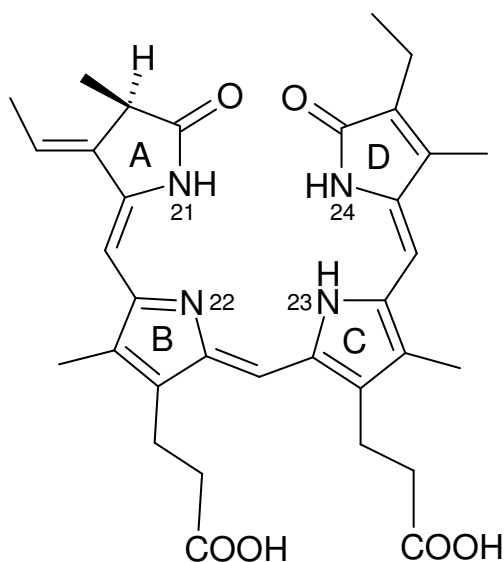


Figure 4.1: Structure of phycocyanobilin in the cyclic helical conformation. In the chromophore of phytochrome, the ethyl side chain at pyrrole ring D is replaced vinyl group.

### 4.1.2 Photophysical model

Previous time-resolved absorption and fluorescence up-conversion experiments [19] as well as  $^1\text{H-NMR}$  measurements [79] indicate that the ground-state of PCB consists of three different species.  $\text{PCB}_A$  represents the predominant species in thermal equilibrium at room temperature in alcoholic solution; dissolved in methanol 70% of the PCB molecules are found to persist in the  $\text{PCB}_A$  form. As  $^1\text{H-NMR}$  studies reveal, it adopts a cyclic-helical conformation [79] while the structural features that distinguish the other two species,  $\text{PCB}_B$  and  $\text{PCB}_C$ , from  $\text{PCB}_A$  remain still unknown. As the most stable structure,  $\text{PCB}_A$  is the lowest lying ground-state species with an absorption maximum at 580 nm solved in methanol.  $\text{PCB}_B$ , contributing to  $25 \pm 5$  % to the ground state population of PCB, absorbs best at 630 nm while  $\text{PCB}_C$ , which adds with about 3% least to the steady-state absorption, exhibits the highest ground-state energy with a maximum absorption at 710 nm (see figure 4.2).

Figure 4.2 schematically shows the model established by Bischoff et al. to account for the excited-state dynamics of PCB [19]. According to this model excitation of PCB at 610 nm, as in the experiments of Bischoff et al. [19], brings the species  $\text{PCB}_A$  and  $\text{PCB}_B$  into the corresponding excited-states  $A^*$  and  $B^*$ , respectively. Due to its longwave absorption maximum in relation to the pump pulse, species  $\text{PCB}_C$  is not excited. The population of  $B^*$  exclusively decays directly back into the corresponding ground-state resulting in a lifetime of  $B^*$  of  $\tau_1 = 3.2 \pm 1.0$  ps (referring to methanol as solvent).  $A^*$  returns back into its ground-state, while however simultaneously undergoing a photoreaction into the species  $\text{PCB}_B$  and  $\text{PCB}_C$  leading to a decay of the population in  $A^*$  with a time-constant of  $\tau_2 = 30 \pm 8$  ps. The photoreaction yields the species  $\text{PCB}_B$  and  $\text{PCB}_C$  in the respective ground-states. As a result of the photoinduced interconversion of  $\text{PCB}_A$  into  $\text{PCB}_B$  and  $\text{PCB}_C$ , the ground-state is not populated according to thermal equilibrium any longer. Thus, a thermally driven back-reaction from  $\text{PCB}_B$  and  $\text{PCB}_C$  into  $\text{PCB}_A$  takes place until thermal equilibrium is reached again. The time-constant of this back-reaction,  $\tau_3$ , is estimated to be  $\tau_3 = 350 \pm 100$  ps.

This model implies that the ratio of the decay amplitudes associated with the different decay channels is dependent on the excitation wavelength, i.e.  $\alpha_{\lambda_p}/\beta_{\lambda_p} = \Gamma(\lambda_{pump})$ . Furthermore excitation within the spectral coverage of only the ground-state absorption of  $\text{PCB}_B$  and  $\text{PCB}_C$  should not generate a photoproduct species.

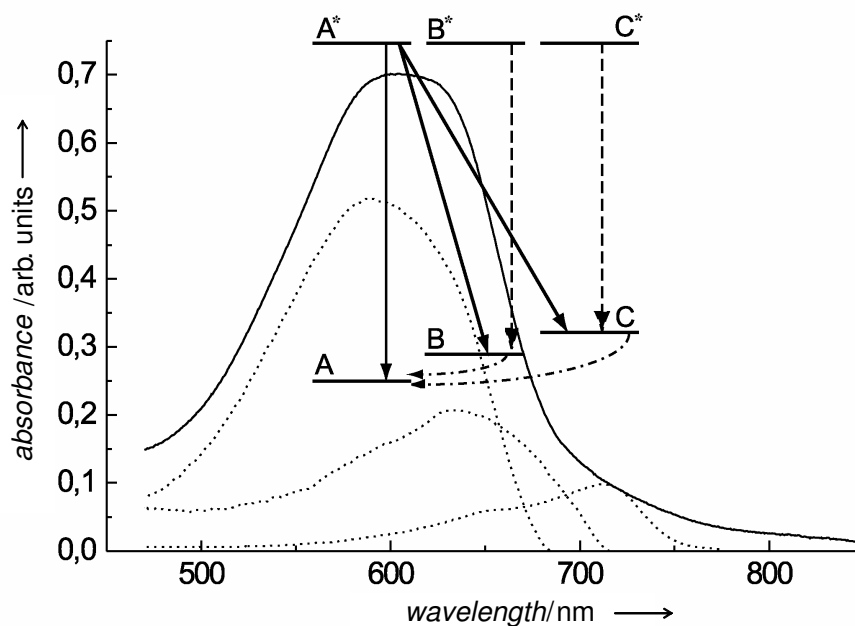


Figure 4.2: Steady-state absorption spectra of the individual species of phycocyanobilin and kinetic model of the reaction dynamics in photoexcited phycocyanobilin. The individual absorption spectra of the species  $PCB_A$ ,  $PCB_B$ , and  $PCB_C$  (dotted lines) are shown together with the stationary absorption spectrum of phycocyanobilin (solid line). The spectra refer to the solvent methanol and are calculated as reported by Bischoff et al. [19] In addition, a schematic drawing of the model suggested by Bischoff et al. to account for the excited-state reaction dynamics of phycocyanobilin is presented. [19]

## 4.2 Experimental results

As the model proposed by Bischoff et al. [19] is based on transient absorption (TA) spectroscopy data taken with a single excitation wavelength,  $\lambda_{pump} = 610$  nm, the experiments presented in this chapter were performed to test the validity of the model, i.e. to test the pump-wavelength-dependency of  $\Gamma(\lambda_{pump}) = \alpha_{\lambda_p}/\beta_{\lambda_p}$ . Furthermore, the pump-wavelength-dependency of the photoproduct formation was investigated by carrying out TG measurements. The excitation wavelength was varied between 600 and 670 nm, thus covering mainly the steady state absorptions of species  $PCB_A$  and  $PCB_B$ , while the absorption of species  $PCB_C$  is negligible in this wavelength region. Further, the probe wavelength was set to 500 nm, i.e. in a spectral region where an excited-state absorption of the species  $PCB_A$  and  $PCB_B$  can be observed [19]. In order to ensure that for all pump-wavelengths used the corresponding excited-state absorption was positioned at 500 nm, TA absorption measurements were done in advance.

Figure 4.3 shows some representative TG-data sets monitored at different pump wavelengths. In Figure 4.3A the absorption decays at pump wavelengths of 600 nm and 670 nm are compared. In figure 4.3B the absorption decay at an intermediate pump wavelength of 640 nm is presented together with a corresponding least square fit. As can be seen from the decays in Figure 4.3A, the absorption decline is steeper upon excitation at 600 nm than at 670 nm. This feature suggests a different time behavior for the processes associated with the time constants  $\tau_1$  and  $\tau_2$  at these two pump-wavelengths.

### 4.2.1 Fitting procedure

In order to extract the time behavior of the excited-state processes in photoexcited PCB dependent on the excitation wavelength, the experimentally obtained TG data were fitted using the following procedure: First the transient taken with the pump-wavelength at 610 nm were fitted using the time-constants published by Bischoff et al. [19]. Second, data taken with other pump-wavelengths were fitted the way that the time-constants were allowed to vary within the error margins given by Bischoff et al [19]. If the fits obtained were not satisfying the time-constants were allowed to vary in a wider range until good agreement of experimental data and fit was found. The function describing the population flow following photo-excitation of PCB according to the model schematically sketched in

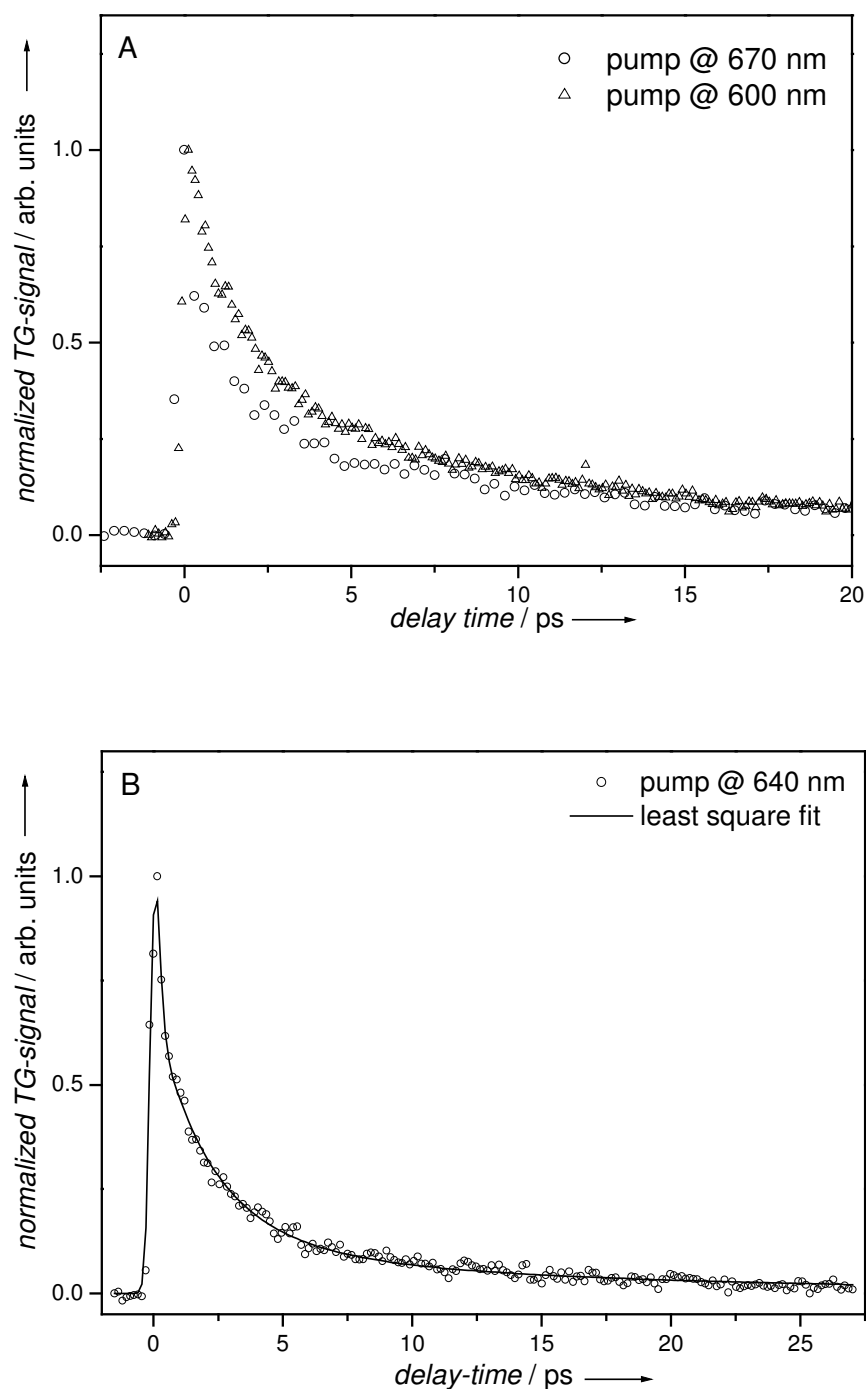


Figure 4.3: Kinetics of the absorption changes at 500 nm after excitation of phycocyanobilin at different pump wavelengths. A) Transient grating signal at 500 nm following excitation at 670 nm (circles) and 600 nm (triangles). B) Transient grating signal at 500 nm after excitation at 640 nm (circles) and the best-fit curve (solid line).

figure 4.2 can be written as:

$$f(\Delta t) = \alpha_{\lambda_p} \cdot \exp(-\Delta t/\tau_2) + \beta_{\lambda_p} \cdot \exp(-\Delta t/\tau_1) + \phi. \quad (4.1)$$

Equation 4.1 reflects the fact that the 350 ps-component observed by the authors of [19] is not explicitly taken into account during the fitting process because the scanning range in the experiments described here did not exceed 100 ps. Instead all contributions to the TG-signal with time-dependencies longer than our observation-time range are summarized by a constant  $\phi$ . As the polarization probed in a TG-experiment is proportional to the absolute square of the population, the TG-signal,  $I_{TG}$ , is proportional to  $|f(\Delta t)|^2$ . Thus, the complete function used for fitting is the convolution of our experimental response function  $R(t)$  and the absolute square of the function  $f(\Delta t)$  given in equation 4.1:

$$I_{TG}(\Delta t) = \int_0^\infty dt' R(t' - \Delta t) \cdot |f(t')|^2. \quad (4.2)$$

In case of a purely Gaussian response function, i.e.  $R(t)$  can be written as

$$R(t) = \frac{1}{\sqrt{\pi} \cdot w} \cdot \exp(-t^2/w^2), \quad (4.3)$$

equation 4.2 reduces to

$$I_{TG}(\Delta t) = \sum_j f_j^{\tau_j}(\Delta t) \cdot \frac{1 - \operatorname{erf}\left(\frac{w}{2\tau_j} - \frac{\Delta t}{w}\right)}{2}, \quad (4.4)$$

where  $f_j^{\tau_j}(\Delta t)$  denotes the part of the sum in  $|f(\Delta t)|^2$  that describes an exponential decay with the time-constant  $\tau_j$ . Equation 4.4 is then used for fitting the TG-data.

#### 4.2.2 Pump-wavelength-dependency of the excited-state processes

Figure 4.4 summarizes the estimates of the time constants  $\tau_1$  and  $\tau_2$  obtained from the fits of the data acquired over the whole range of the pump wavelengths covered by our measurements. As evident from figure 4.4A, the short decay-time,  $\tau_1$ , varies only very slightly with the excitation wavelength. Pumping at 600 nm results in a direct deactivation time of  $B^*$  and  $C^*$  molecules of 1.8 ps, while excitation at 670 nm leads to  $\tau_1 = 3.2$  ps. Thus, the majority of estimates conforms well with the value of  $\tau_1 = 3.2 \pm 1.0$  ps as determined by Bischoff et al. [19], the only exception being the estimate of 1.8 ps for pumping at 600 nm. In contrast, the longer decay-time  $\tau_2$ , reflecting the lifetime of the photoreactive species  $A^*$ , shows a pronounced dependence on the pump wavelength; it clearly increases with an

increased pump-wavelength. Nevertheless, all values of  $\tau_2$  measured here agree within the error-margins with the value of  $\tau_2 = 30 \pm 8$  ps, published by Bischoff et al. [19]; the estimates of  $\tau_2$  from our TG-experiments reach from 18 ps for excitation at 600 nm to 30 ps for pumping at 670 nm. Bischoff et al. [19] do not make any statement about a pump-wavelength-dependency of their observed time-constants. Due to the excellent signal-to-noise ratio of the coherent TG-detection scheme, the measurements presented here allow to observe the evolution of the time-constants  $\tau_1$  and  $\tau_2$  as a function of pump-wavelength within the error margins obtained from TA-measurements [19]. Thus, decreasing time-constants  $\tau_1$  and  $\tau_2$  with decreasing excitation wavelength could be observed; with increasing pump energy the reaction rate for the photoconversion of  $\text{PCB}_A$ , corresponding to  $1/\tau_2$ , is nearly doubled from about  $3.3 \cdot 10^{10}$  Hz at 670 nm to  $5.6 \cdot 10^{10}$  Hz at 600 nm. This finding is most likely due to an accelerated rate of the internal conversion process in the  $S_1$ -state, which may occur, when the excitation is initiated by pump-photons that deliver vibrational excess energy to the molecular system, a well known phenomenon [80]. Under this condition, a portion of the excess vibrational energy is transferred from the optically active modes into the photoreactive mode(s), the reaction then proceeds faster vs initialization from a vibrationally fully equilibrated  $S_1$ -excited-state. Accordingly, increasing the excess vibrational energy leads to an increased reaction rate.

Figure 4.4B shows the amplitude ratio  $\Gamma(\lambda_{pump})$  of the two lifetime components  $\tau_2$  and  $\tau_1$ , respectively, as a function of the excitation wavelength. The amplitude ratio is scaled the way that  $\Gamma(600)$  was set to be unity. It can be noted that  $\Gamma(\lambda_{pump})$  is strongly dependent on the excitation wavelength. It clearly drops off with increasing pump wavelength. At 670 nm the estimate for  $\Gamma$  is about 30% as compared to  $\Gamma(600)$ . This result fully agrees with the kinetic model. The pronounced drop of the amplitude ratio  $\alpha_{\lambda_p}/\beta_{\lambda_p}$ , which describes the relative contributions of  $A^*$  and  $B^*$  molecules to the initially prepared excited state population, can be understood considering the contributions of the different species to the overall ground-state absorption. Based on the species spectra shown in figure 4.2, at pump wavelengths between 600 nm and 670 nm both  $\text{PCB}_A$  and  $\text{PCB}_B$  are excited. However, on excitation with a short pump wavelength, the contribution of  $A^*$  to the initially produced excited-state population predominates over that of excited  $\text{PCB}_B$  ( $B^*$ ) yielding a higher amplitude ratio  $\alpha_{\lambda_p}/\beta_{\lambda_p}$  than at longer pump wavelengths. Pumping at longer wavelengths creates an increasing excitation of the species  $\text{PCB}_B$  which results in an increasing contribution of excited state  $\text{PCB}_B$  and thus in decreasing estimates for  $\Gamma(\lambda_{pump})$ .

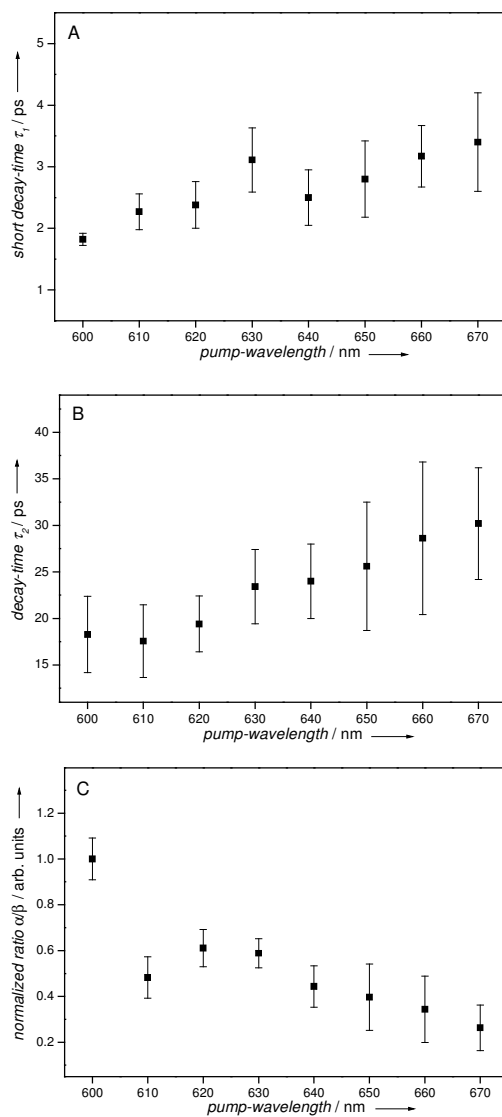


Figure 4.4: Pump-wavelength dependence of the decay-times and decay amplitudes in the kinetics of phycocyanobilin. The decay parameters were obtained from double-exponential fits to the changes in the excited-state absorption at 500 nm. Panel A: Plot of the short decay-time  $\tau_1$  as a function of pump wavelength. Panel B: Analogous plot for the intermediate decay-time  $\tau_2$ . Panel C: Ratio of the decay amplitudes of the intermediate- ( $\tau_2$ ) and short-component ( $\tau_1$ ) lifetimes  $\alpha/\beta$  as a function of pump-wavelength.



### 4.2.3 Pump-wavelength-dependency of the photoproduct formation

The reaction dynamics of phycocyanobilin was also probed by monitoring the kinetics in the region of the photoproduct absorption at different excitation wavelengths. The background of these experiments was as follows: The above kinetic model suggests that a photoconversion occurs from species  $\text{PCB}_A$  into species  $\text{PCB}_B$  and  $\text{PCB}_C$  while a photoreaction of the latter two species into a photoproduct, which is not species  $\text{PCB}_A$ , is not observable [19]. To verify the model in this respect, it was assessed whether the excitation into species  $\text{PCB}_B$  and  $\text{PCB}_C$  generates a photoproduct. For this purpose the kinetics of the photoproduct was analyzed by recording its transient absorption as a function of the pump-wavelength. The excitation was performed at 615 nm and 720 nm, i.e. in the absorption regions of  $\text{PCB}_A$  and  $\text{PCB}_B$  on the one hand and of  $\text{PCB}_B$  and  $\text{PCB}_C$  on the other. The kinetics of the photoproduct were analyzed by recording the transient absorption at 700 nm. [19] Of the two photoproducts,  $\text{PCB}_B$  and  $\text{PCB}_C$ , which normally arise on excitation of  $\text{PCB}_A$ ,  $\text{PCB}_C$  dominates the absorption at 700 nm (see figure 4.2). The reason for restricting the probe wavelength to 700 nm is that no contributions from excited  $\text{PCB}_A$  are expected there. Figure 4.5 compares the kinetics obtained from the TG-measurements at the two excitation wavelengths. The respective kinetics significantly differ from each other. The inset of figure 4.5 shows the decaying part of the signal on a logarithmic time-scale to stress the differences of the time-evolution of the signals. While on pumping at 615 nm the time evolution clearly exhibits longer-lived components, the TG-signal decays almost completely within 10 ps for pumping at 720 nm.

For the kinetic analysis of the data at 615 nm, a third lifetime component  $\tau_3$  is required in addition to  $\tau_1$  and  $\tau_2$  in the above fits. The three-exponential fit provides lifetimes of  $\tau_1 = 3.2 \pm 0.5$  ps,  $\tau_2 = 25 \pm 5$  ps and  $\tau_3 = 290 \pm 90$  ps which conform well with the estimates of Bischoff et al. determined from a global analysis of TA-data [19, 47]. While  $\tau_1$  originates from the excited-state decay of the non-photoreactive species  $\text{PCB}_B$ , the lifetimes  $\tau_2$  and  $\tau_3$  are correlated with the photoproduct kinetics. The 25 ps component is correlated to the rate of the photoreaction in excited  $\text{PCB}_A$  and the 290 ps component reflects the thermally driven back reaction of the photoproduct species into the educt to establish the initial thermally equilibrated mixture of all three species. Thus, the kinetics observed after excitation at 615 nm shows all the characteristic features of the photoreaction of  $\text{PCB}_A$  and the subsequent thermally driven back-reaction. In contrast, the kinetics upon

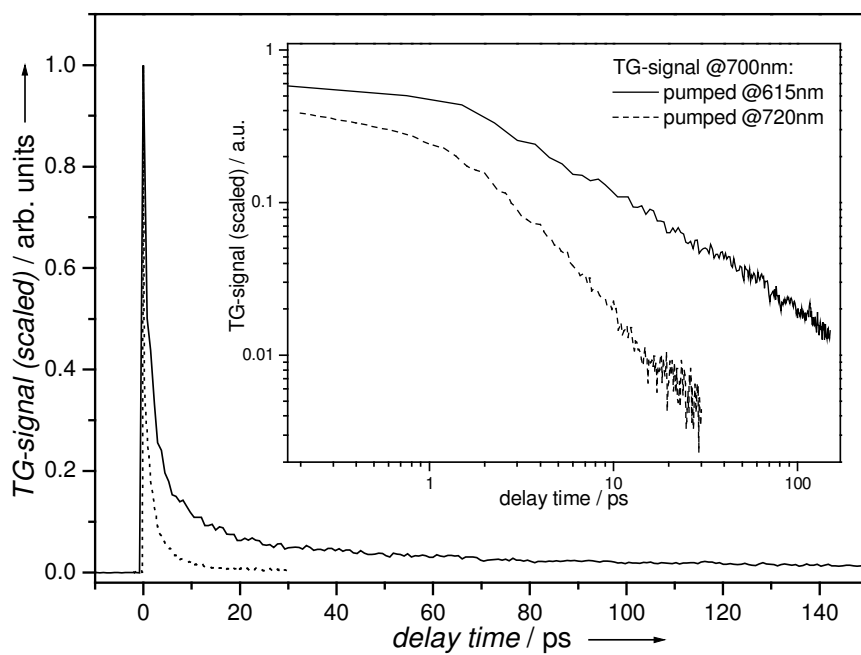


Figure 4.5: Kinetics of the absorption changes at 700 nm after excitation of phycocyanobilin at 615 nm (c) and at 720 nm (a). The scaled TG signals (normalized to unity at the maximum) are shown for the two pump wavelengths. A plot on a logarithmic scale is given in the inset.

excitation at 720 nm is composed of contributions from only two exponential components with lifetimes of  $2.4 \pm 0.5$  ps and  $3.7 \pm 0.7$  ps. Even though the difference in the two lifetimes is quite small, the absorption decay clearly deviates from a single exponential process. No distinct contribution from a longer-lived component indicative for the kinetics of a possible photoproduct appears concomitantly. It therefore seems very likely that no photoreaction yielding a product state with an absorption at around 700 nm occurs from the excited-state species  $\text{PCB}_B$  and  $\text{PCB}_C$ . The origin of the two fast kinetic components remains to be explained. Clearly, these belong to the excited-state decay of  $\text{PCB}_B$  and  $\text{PCB}_C$ . The fit results show that the  $3.7 \pm 0.7$  ps component contributes twice as much to the overall TG signal as the  $2.4 \pm 0.5$  ps component. Furthermore, at 720 nm  $\text{PCB}_C$  strongly dominates the ground-state absorption spectrum (see figure 4.2) and should become excited preferentially. Based on these considerations the lifetime of  $3.7 \pm 0.7$  ps can be attributed to the decay of excited  $\text{PCB}_C$  to the electronic ground-state. Accordingly, the lifetime of  $2.4 \pm 0.5$  ps can be related to the excited-state decay of  $\text{PCB}_B$ . The fact that this lifetime agrees well with the  $\tau_1$  values determined from the analysis of the excited-state absorption at 500 nm (see panel A of figure 4.4) corroborates this proposition as well. The sole occurrence of  $\text{PCB}_B$  and  $\text{PCB}_C$  in the region of the product absorption suggests that these two species are clearly the only photoproducts in the excited-state reaction of  $\text{PCB}_A$ . This result offers further validation of the kinetic model suggested by Bischoff et al. [19]

#### 4.2.4 Reaction dynamics of protonated Phycocyanobilin

Protonated phycocyanobilin ( $\text{PCB}\cdot\text{H}^+$ ) was included in the time-resolved spectroscopic investigations by performing femtosecond time-resolved transient-absorption experiments. Defining the reaction dynamics of  $\text{PCB}\cdot\text{H}^+$  has not been an objective of investigations thus far, despite the fact that protonated chromophores in the two photoreceptors phycocyanine and phytochrome are thought to be essential for their biological functionality [81–85]. Thus, the data presented here constitutes the first experimental approach to investigate the presumably biologically extremely relevant protonation effect. To study this effect, phycocyanobilin was transformed into its protonated form by titration with a strong acid, saturated HCl was used. Based on NMR studies, protonation takes place at the basic pyrrolic nitrogen atom ( $N_{22}$ ) of ring B (see figure 4.1) without a change of the overall structure [86,87]. Full protonation is indicated by a strong bathochromic and hyperchromic

shift in the  $S_0 \rightarrow S_1$ -absorption. These spectral features are illustrated in figure 4.6 which compares the absorption spectra of protonated vs. unprotonated phycocyanobilin.

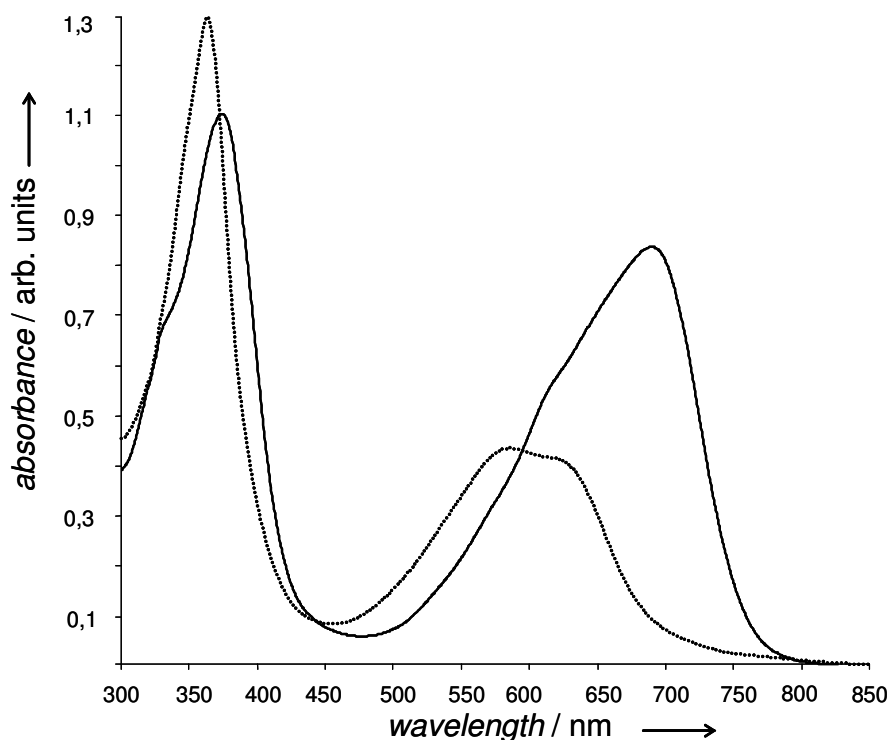


Figure 4.6: Figure 6. Steady-state absorption spectrum of protonated (solid line) and unprotonated phycocyanobilin (dashed line) in methanol.

TA-spectra of  $\text{PCB}\cdot\text{H}^+$  were taken up to 100 ps after excitation. The results obtained from these time-resolved TA measurements are summarized in Figure 4.7. Figure 4.7A displays the different absorption spectra of protonated as well as unprotonated phycocyanobilin, taken 2 ps after excitation at 700 nm and 620 nm, respectively. Figure 4.7B reflects the time evolution of these spectra over about the first 50 ps following excitation. Two significant spectral features dominate in the spectral range between 460 nm and 630 nm. At wavelengths longer than 560 nm, a negative band appears in the region of the ground-state absorption which is apparently due to the bleaching of the initial absorption. At wavelengths shorter than 560 nm a broad positive band with a maximum at  $\sim 490$  nm arises concurrent with bleaching. Due to the simultaneous appearance with excitation, this absorption quite obviously corresponds to an excited-state absorption. Over the time inter-

val of 50 ps, both the excited-state absorption and ground-state bleaching remain unchanged in their spectral position and decay in parallel, a behavior remarkably similar to the transient behavior of unprotonated phycocyanobilin. Completely analogous spectral features are developed when the excitation was set at 640 nm and 740 nm, i.e. at wavelengths localized at the blue and red wing of the steady-state absorption band. In comparison with the TA spectra of unprotonated PCB, in the spectra of the PCB·H<sup>+</sup> the excited-state absorption is blue-shifted from ~505 nm to ~490 nm and the intersection point of the difference spectra with the zero line is red-shifted from 530 nm to 560 nm (Figure 4.7A). While the latter effect correlates with the general red shift in the steady-state absorption spectrum of protonated phycocyanobilin, the former indicates that in addition to the energetic distance between the ground and first excited-state the distance between the first and higher excited-states is changed too.

In Figure 4.7C the kinetics recorded in the region of the excited-state absorption (520 nm) and the ground-state bleaching (618 nm) up to 100 ps after excitation is presented. At the two probe wavelengths the temporal behavior of the absorption signals is complex and non-mono-exponential. But as for unprotonated PCB, the kinetics is adequately fitted to a sum of three exponentially decaying functions. The lifetimes associated with the exponential components are  $\tau_1 = 4.0 \pm 0.7$  ps and  $\tau_2 = 35 \pm 7$  ps while  $\tau_3$  is in the order of a few hundred picoseconds, i.e.  $\tau_3 \geq 200$  ps. These lifetimes correlate quite well within the overall error with the estimates of unprotonated phycocyanobilin. The 4 ps and 35 ps lifetimes closely match the lifetimes of 2-3 ps and 18-30 ps, depending on the pump wavelength, as obtained for unprotonated PCB. Furthermore, the long-lifetime component ( $\leq 200$  ps) is related to the lifetime of about 290 ps of the product species generated in the excited-state reaction of unprotonated phycocyanobilin. From this and in addition from the close similarity in the spectral evolution both in PCB and PCB·H<sup>+</sup>, it seems very likely that the excited-state relaxations involve analogous kinetic components independent of the protonation state. It appears that despite the introduction of a positive charge and its influence on the electronic structure of the tetrapyrrole chromophore, the geometrical changes that might be associated with the reaction dynamics remains unaffected by protonation.

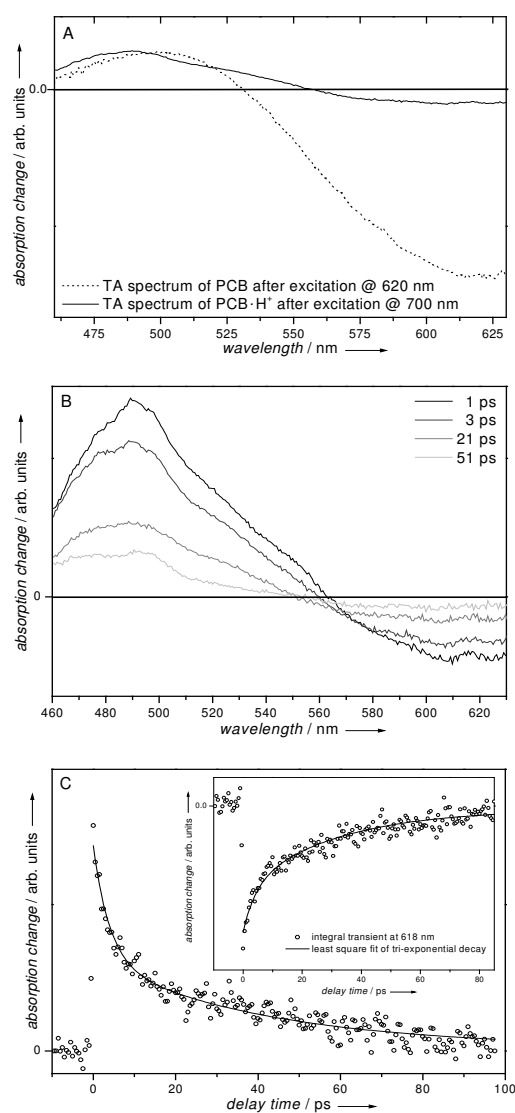


Figure 4.7: Transient absorption spectra of protonated phycocyanobilin (PCB-H<sup>+</sup>) and time dependence of the absorption changes in the region of the excited-state absorption (520 nm) and ground-state bleaching (618 nm). Panel A: Comparison of the light-induced absorption changes of protonated (dotted line) and unprotonated phycocyanobilin (solid line) monitored 2 ps after excitation at 700 nm and 620 nm, respectively. Panel B: Transient absorption spectra of protonated phycocyanobilin at different delay times following excitation at 700 nm. Panel C: Time evolution of the transient absorption changes at 520 nm; the inset shows the absorption decay at 618 nm. The data points (dots) are shown along with the best-fit function (solid line) obtained from a three-exponential analysis yielding decay-times of  $\tau_1=4.0\pm 0.7$  ps,  $\tau_2=35\pm 7$  ps, and  $\tau_3=200$  ps.

### 4.2.5 Conclusion

The results presented in the chapter show, that by using femtosecond time-resolved transient-absorption spectroscopy and, in particular, the technique of femtosecond time-resolved transient population gratings, further evidence was obtained for the complex reaction dynamics in phycocyanobilin. With excitation-wavelength-dependent TG measurements of the excited-state kinetics, the coexistence of three different ground-state species,  $\text{PCB}_A$ ,  $\text{PCB}_B$ , and  $\text{PCB}_C$ , could clearly be demonstrated. When exciting  $\text{PCB}_A$  and  $\text{PCB}_B$ , two kinetic components with lifetimes of  $\tau_1 \approx 2 - 3$  ps for the excited-state of  $\text{PCB}_B$  and  $\tau_2 \approx 18 - 30$  ps  $\text{PCB}_A^*$  were identified. The contributions of these two components to the overall kinetic vary with the excitation wavelength. Starting from excited-state  $\text{PCB}_A$ , a photoreaction forming  $\text{PCB}_B$  and  $\text{PCB}_C$  can be observed. The decay-time of  $\tau_2 = 18 - 30$  ps of excited  $\text{PCB}_A$  matches the ground-state appearance time of the photoproducts  $\text{PCB}_B$  and  $\text{PCB}_C$ . No photoreaction occurs when the pump laser is tuned outside the absorption of  $\text{PCB}_A$ , confirming the suggestion of Hermann and coworkers [19] that only  $\text{PCB}_A$  is photoreactive. Compared to  $\tau_1$ , the excited-state lifetime of  $\text{PCB}_B$  and  $\text{PCB}_C$ ,  $\tau_2$ , is significantly dependent on the excitation wavelength. It is remarkably shortened with decreasing pump wavelength, while  $\tau_1$  is scarcely affected. Most likely, if the exciting photons deliver an excess of vibrational energy, the internal conversion process is accelerated, which in turn leads to an enhanced photoreaction rate  $\tau_2^{-1}$ . These results in general verify the kinetic model suggested by Bischoff et al. for the excited-state processes of phycocyanobilin. [19] However, in detail, further significant insight was obtained due to the excitation-wavelength-dependent analysis of the excited-state dynamics. The time-resolved absorption measurements on phycocyanobilin protonated at the basic pyrroline nitrogen atom reveal kinetics that are very similar to those of the unprotonated form.

## Chapter 5

# Protochlorophyllide a

Having reported on a femtosecond time-resolved transient grating and transient absorption study on PCB, a model chromophore of phytochrome, that allowed further insight into the photophysics of the system and yielded a refinement of a recently suggested model [19] in chapter 4, this chapter presents transient absorption experiments illuminating the excited-state dynamics of protochlorophyllide a, a porphyrin like compound and precursor of the chlorophyll biosynthesis. As the experiments performed in this work constitute the first femtosecond time-resolved study on protochlorophyllide a, the approach of white-light probe transient absorption was chosen to allow for a full spectral and temporal characterization of the excited-state species involved in the overall relaxation process. In addition to pump-energy dependent measurements performed with protochlorophyllide a dissolved in methanol, the excited-state dynamics of protochlorophyllide a was interrogated in different solvents. These solvent dependent measurements revealed a drastically altered overall decay behavior when comparing the polar solvents methanol, acetonitrile, a mixture of glycerol and methanol on one side and the non-polar solvent cyclohexane on the other side. While in the latter solvent only a single 4.7 ps component is observed, the use of one of the more polar solvents results in a strongly non-exponential relaxation dynamics. Three kinetic components with time-constants of 4, 27 and 200 ps are found to be involved in the excited-state decay of protochlorophyllide a in methanol [56]. Furthermore, adding up to 60% glycerol to methanol used as solvent, and thus increasing the viscosity of the solvent, leads to an increase of the observed time-constants. In contrast, protochlorophyllide a dissolved in acetonitrile and methanol exhibits qualitatively and quantitatively identical relaxation dynamics involving three distinct kinetic components. In addition to the femtosecond



time-resolved absorption experiments the picosecond time-resolved fluorescence of the system was studied. The latter technique reveals clear signatures for two distinct fluorescence components differing in the spectral contributions to the overall emission spectrum and drastically altered lifetimes. The transient absorption and time-resolved fluorescence data allow to suggest a detailed model for the excited-state relaxation of protochlorophyllide a and to gain further insight into the characteristics of the states involved in the process. For further clarification the data is compared to measurements investigating the relaxational processes within the excited-state manifold of magnesium octaethyl-porphyrin, a structurally closely related system. The characteristic difference of protochlorophyllide a from the typical porphyrin structure of MgOEP is an additional cyclopentanone ring attached to the electronic  $\pi$ -system, thus from comparing the data obtained for the two systems the role and function of the cyclopentanone ring can be deduced. Finally, the model derived is related to models suggested to account for the reduction of protochlorophyllide a to chlorophyllide a within the natural enzymatic environment of POR.

## 5.1 The system PChla

Protochlorophyllide a (PChla) is a precursor in the biosynthesis of chlorophyll, the ubiquitous pigment of photosynthesis in plants, green algae and cyanobacteria [88,89]. The chemical structure of PChla is shown in figure 5.1. As can be seen, PChla is constituted by a Mg-tetrapyrrole made up of four pyrrole-type rings, which are linked together by four methine bridges. It is synthesized from  $\delta$ -aminolevulinic acid by enzyme catalysis via the cyclic tetrapyrrole uroporphyrinogen III that in turn is transformed into protoporphyrin IX. The insertion of  $Mg^{2+}$  and formation of the isocyclic ring yields PChla. The subsequent step in chlorophyll synthesis involves the reduction of PChla to the chlorin structure of chlorophyllide a and finally the esterification of the propionic acid side chain with the polyisoprene alcohol phytol which completes the structure of chlorophyll a [88,89].

The reduction of PChla is a light dependent process in all chlorophyll-containing organisms. It is catalyzed by the enzyme protochlorophyllide oxidoreductase enzyme, POR. The POR enzyme exists as a ternary complex with its substrate, PChla, and the coenzyme NADPH [90–92]. Light absorption by the substrate initiates the enzyme catalysis which ultimately results in the release of chlorophyllide a and  $NADP^+$ . Because of this light-induced photoreduction, the POR is of particular interest in that it is the only one of

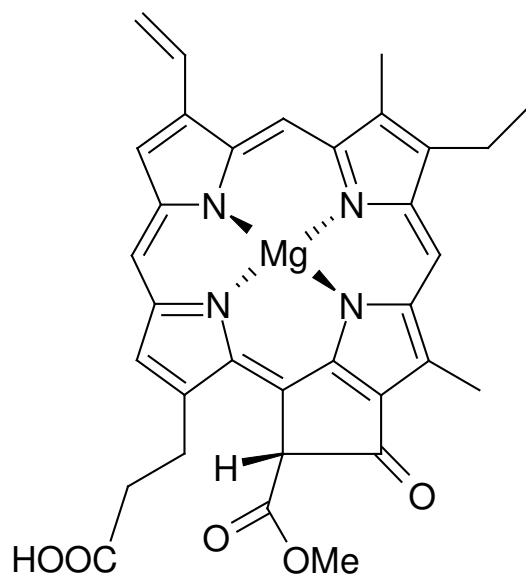


Figure 5.1: The chemical structure of protochlorophyllide *a* is shown.

two enzymes in nature, whose catalytic activity is switched on by the absorption of light. Therefore, the POR is ideally suited for visualizing the primary steps of enzyme catalysis in real-time by means of fs time-resolved spectroscopy [13,93,94]. Recently, a first fs time-resolved study on the initial dynamics of the primary light-induced events in the POR enzyme was reported [95].

In this chapter, a thorough characterization of the light induced processes in the isolated chromophor of POR, which are assessed by either fs excitation into the energetically lowest lying Q-band or ps Soret-band absorption, is presented. In the ternary POR complex, the time-dependent spectral features associated with ground-state depletion and excited-state absorption of the substrate as well as the product are most likely to be superimposed. Therefore, the study of the photochemistry and photophysics of isolated PChla should facilitate the interpretation of the intricate transient absorption changes in the whole ternary complex. Furthermore, the influence of the apoenzyme can thus be separated from the intrinsic properties of the substrate and the question of how specific substrate-apoenzyme interactions drive the catalytic process can efficiently be addressed.

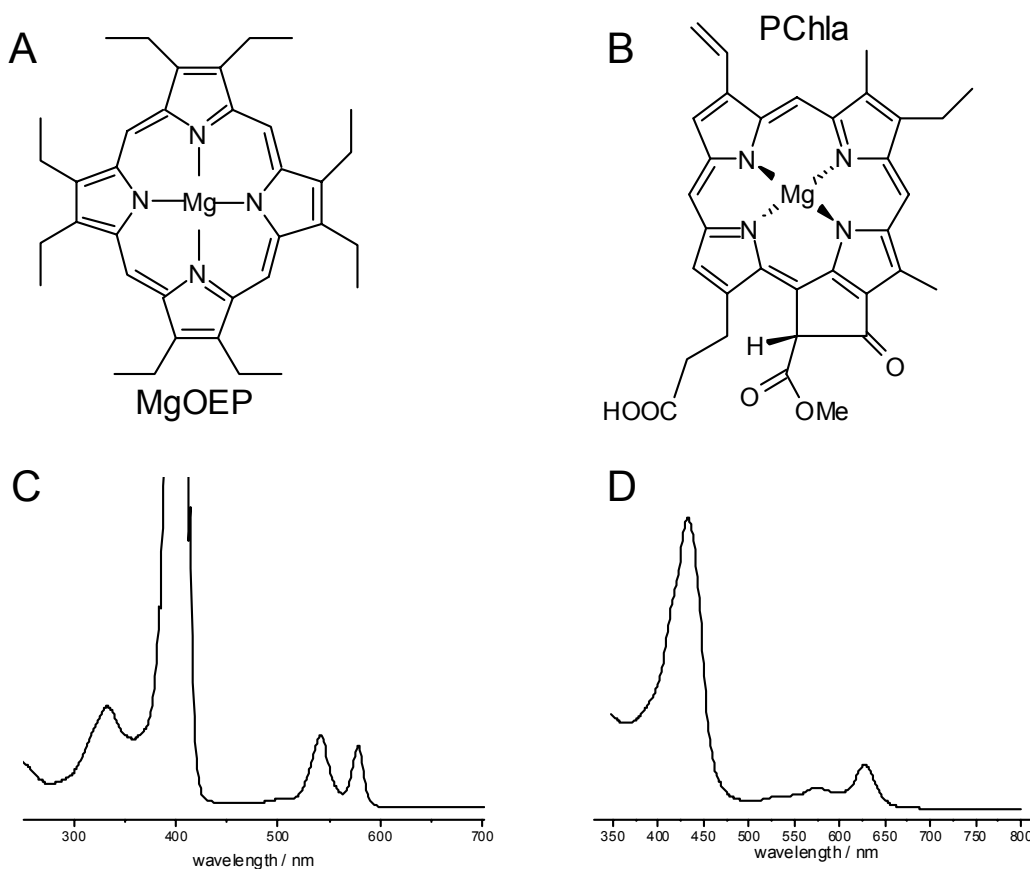


Figure 5.2: A comparison between the chemical structures of PChla (panel A) and MgOEP (panel B) is shown. In addition the respective steady state absorption spectra are opposed in panels C and D.

## 5.2 Excited-State relaxation of MgOEt-porphyrin

Before addressing the question of excited-state relaxation in PChla with transient absorption measurements, transient grating experiments on Magnesium-Octaethyl porphyrin (MgOEP) are presented. As shown in figure 5.2 the system is structurally similar to PChla and therefore should be an appropriate model system for being compared to PChla.

As can be seen from panel D of figure 5.2 the steady state absorption of MgOEP spectrum displays the typical features of a porphyrin absorption spectrum [96], a strong Soret-band centered at  $24600\text{ cm}^{-1}$  (407 nm) and two weaker Q-bands located at  $18450\text{ cm}^{-1}$  (542 nm -  $Q_{01}$ ) and  $17240\text{ cm}^{-1}$  (580 nm -  $Q_{00}$ ) can be distinguished. Due to the

reduced symmetry of PChla, three Q-bands are observed here (panel C of figure 5.2 (for a detailed description of the spectral features of PChla see section 5.3).

The experimental approach - schematically sketched in figure 5.3 - employed to investigate the relaxation processes within the excited-state manifold of MgOEP was realized on the 100kHz-laser-apparatus that has been described in section 3.1.1. According to literature, the experiments presented here constitute the first four-wave-mixing experiments on a femtosecond time-scale aiming to describe the light induced excited-state processes in a metal-porphyrin. So they are not only of interest in characterizing the excited-state relaxation in MgOEP and thus providing data, the PChla measurements can be compared to, but also of interest with respect to the power and applicability of fs time-resolved four-wave-mixing to investigate photoinduced relaxation in large biologically relevant molecules.

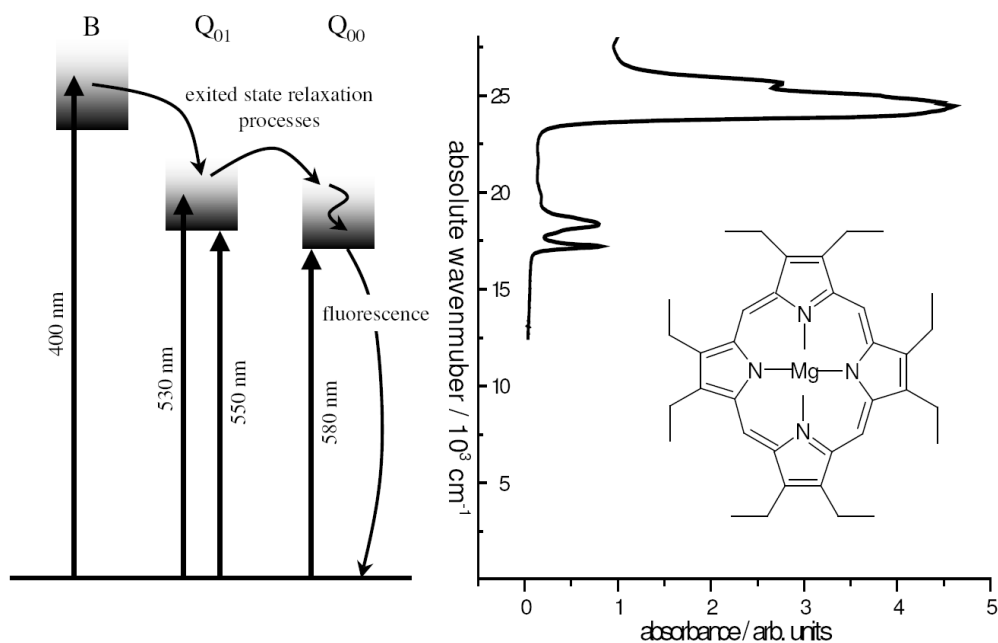


Figure 5.3: The experimental approach for investigating the relaxation processes within the excited-state manifold of MgOEP are shown. Panel B displays the ground-state absorption spectrum, while panel A represents the corresponding energy level diagram. The transitions among the various electronic states that are employed in the four-wave-mixing experiments are indicated as well as the electronic and vibronic relaxation paths in the photoexcited molecules.

In the experiments discussed subsequently, the excitation wavelength is varied in order to selectively promote the molecules into an experimentally chosen electronically ex-

cited state. The probe-wavelengths was set to monitor either the population in the state the molecules have been pumped into or in an energetically lower lying state. Therefore, relaxation pathways between the distinct electronic states can be monitored and characterized with respect to their respective time-constants.

MgOEP has been used as purchased from *Porphyrin products*. It was dissolved in dichloromethane. The concentration was adjusted to yield an optical density of typically 1.2 at 580 nm in a cuvette of 1 mm path length. Absorption spectra were taken with a Lambda 19 spectrophotometer (Perkin Elmer) in order to monitor the integrity of the sample. This is important because of the rapid sample degradation well-known for porphyrins dissolved in dichloromethane [97,98]. However, sample degradation can be efficiently suppressed by placing the sample in a rotating cell. The rotation speed is adjusted so that each set of pulses interacts with a fresh portion of the sample [97].

Figure 5.4 displays the results of the degenerate four-wave-mixing experiments, i.e. pump and probe pulses have identical color. Thus, the signals obtained reflect the kinetics of the originally photo-excited-state. In panel A of figure 5.4 the DFWM signal at 580 nm, at the maximum of the  $Q_{00}$ -band absorption, is presented depending on the delay-time  $\Delta t$ . The panels B and C show the DFWM signal at 530 and 550 nm, which is at the blue and red side of the  $Q_{01}$ -band, respectively. As can be seen, the kinetics obtained under the different experimental conditions vary significantly from each other (note the different time axis). Basically, the transient at 580 nm scarcely displays a kinetic change. It remains nearly constant with increasing  $\Delta t$  indicating a decay that is too slow to be measured with our apparatus. This finding is consistent with data from transient absorption measurements suggesting a lifetime on the nanosecond time scale for the energetically lowest lying  $S_1$ -state and with the  $Q_{00}$ -fluorescence lifetime of 9 ns as reported by Rodriguez et al. for metalloporphyrins [99]. It therefore seems quite reasonable that the long-lived transient signal is related to the relaxation of the lowest excited  $S_1$ - into the  $S_0$ -state of MgOEP.

In contrast to the transient at 580 nm, the transients measured across the  $Q_{01}$ -band exhibit a completely different time behavior. The signal at 530 nm has already disappeared within 200 fs after the non-resonant contribution of the overall signal has reached the maximum. Thus, the population placed into the  $Q_{01}$ -state obviously decays on a time-scale of less than 200 fs. However, when monitoring the decay of the  $Q_{01}$ -population at 550 nm, in addition to this short lifetime component a long-lived contribution, analogous to that with excitation at 580 nm, can be observed. From these results it seems very likely that

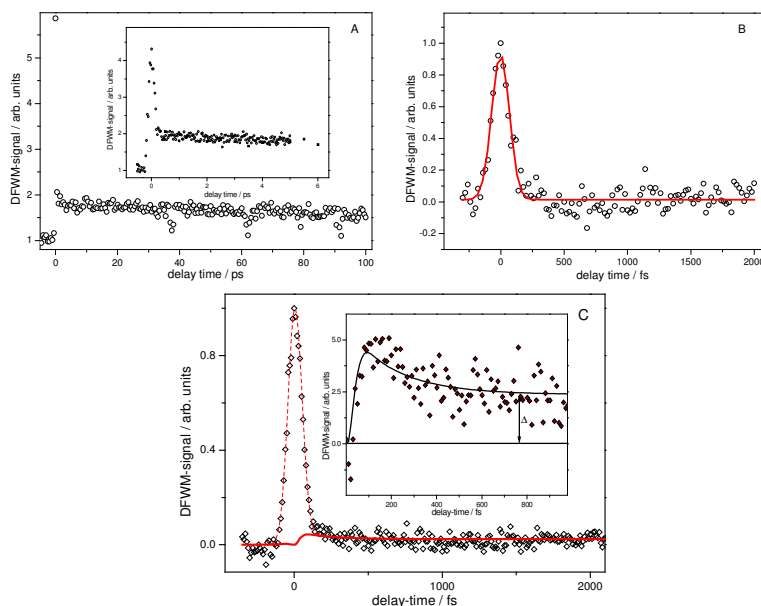


Figure 5.4: Degenerate four-wave-mixing signals of MgOEP dissolved in  $\text{CH}_2\text{Cl}_2$  are shown.

the slow nanosecond kinetics is due to the decay of an  $S_1 \rightarrow S_n$  excited-state absorption within the  $Q_{00}$ -band, while the fast sub-200 fs decay kinetics is related to the  $Q_{01} \rightarrow Q_{00}$  electronic relaxation [99, 100]. This explains why upon excitation in the long wavelength tail of the  $Q_{01}$ -band at 550 nm, the two processes can be seen in parallel, while excitation in the short wavelength tail at 530 nm yields only the fast lifetime component. To assess the  $Q_{01} \rightarrow Q_{00}$  population flow in a further experiment, the transient grating signal was measured across the  $Q_{00}$  band subsequent to excitation in the  $Q_{01}$  band at 530 nm. In Figure 5.5 the kinetics recorded under this condition are compared for distinct probe wavelengths within the overall profile of the probe pulse.

Panel A of figure 5.5 shows the kinetics following photo-excitation at 530 nm monitored at 580 nm. The peak at  $t = 0$  fs can be attributed to the so-called "coherent artifact", which is due to the non-resonant scattering of the probe pulse from the grating formed by the two pump pulses. This scattering is independent of any electronic resonance and persists for delay-times during which the three pulses interact simultaneously with the sample [42, 101]. Thus, the peak shows a temporal profile that is only described by the convolution of the three laser pulses. In contrast, the resonant scattering is dependent on the probe pulse tuned to be in resonance with the electronic transition in the  $Q_{00}$ -

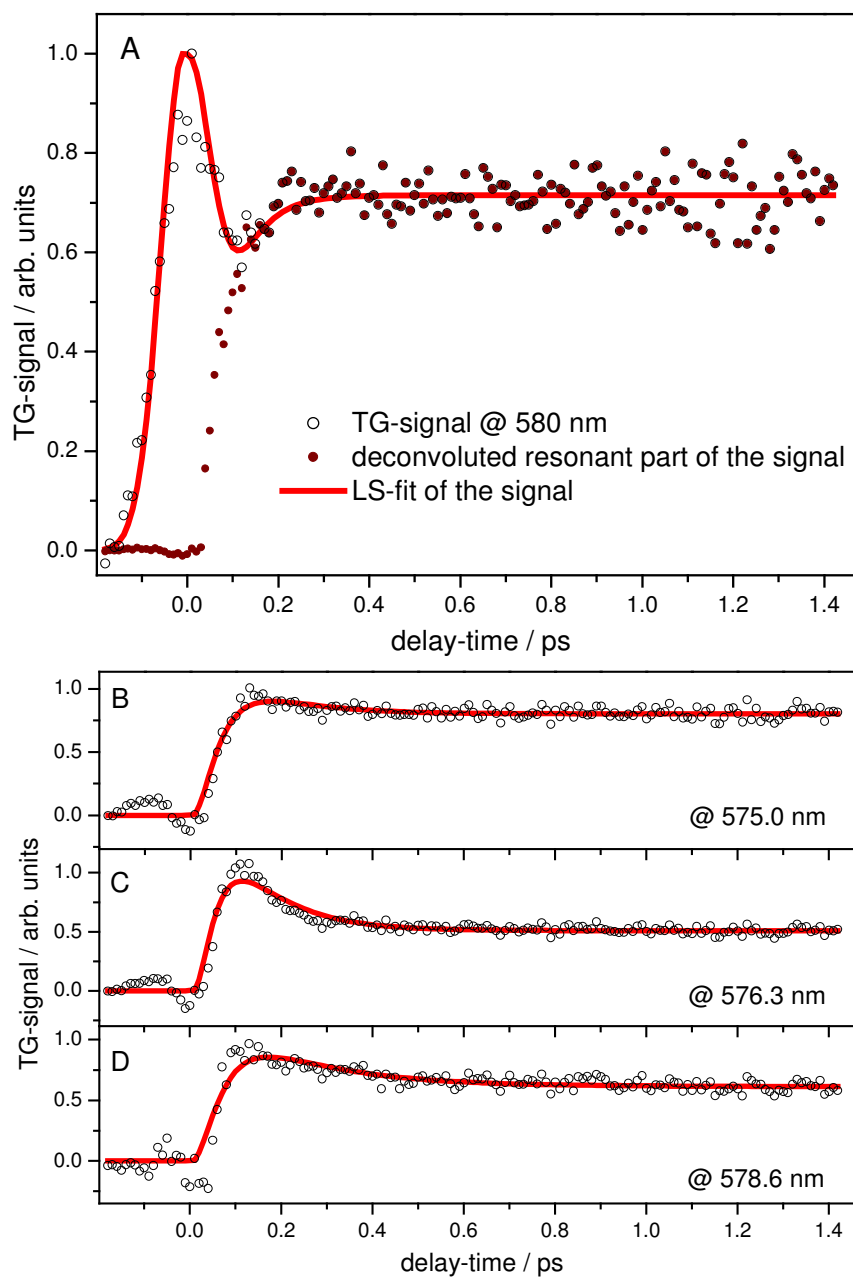


Figure 5.5: Panel A shows a TG-signal at 580 nm that was measured after photoexcitation at 530 nm. In addition to the experimental data (dots) LS-fits of the non-resonant part (dashed line) and the resonant part (solid line) are displayed. Panel B presents the resonant parts of signals taken at different spectral positions within the overall spectral profile of the probe pulse. Dots represent experimental data, while solid lines illustrate the corresponding LS-fits.

band. This resonant scattering can be clearly observed for delay-times longer than 100 fs. After this  $\sim 100$  fs time interval, the TG signal shows a rapid rise up to 200 fs, but then it remains nearly constant. These kinetics obviously reflect the flow of the population from the initially excited  $Q_{01}$ -state to vibrationally excited levels of the  $Q_{00}$ -band. When probing at wavelengths shorter than 580 nm (panels B-D), the rapid 200 fs rise kinetics can be further observed, but it is followed by a fast decay process before the long-lived decay component dominates the kinetics. For a quantitative kinetic analysis, the transient grating signals were fitted to the absolute square of the sum of the resonant and the non-resonant third-order non-linear response. This procedure gives rise to three distinct contributions to the fit function: the non-resonant contribution alone is given by the square of the experimental response function, which was approximated by a Gaussian centered at  $\Delta t = 0$  [102], while the pure resonant part of the non-linear response is given by the function  $f(\Delta t)$ :

$$f(\Delta t) = |p(\Delta t)|^2 = |A_0 \cdot (1 - \exp(-\Delta t/\tau_{rise})) \cdot (A \exp(-\Delta t/\tau) + B)|^2, \quad (5.1)$$

wherein  $p(\Delta t)$  itself describes the time-dependent population of the interrogated states [103]. Although, it is well established, that the square of the resonant contribution to the third-order polarization alone is capable of describing a transient grating signal for delay-times  $\Delta t$  larger than the cross-correlation width ( $T_{cc}$ ) of the pulses [102–104], the interference term between the non-resonant and resonant contribution is included in our fitting procedure in order to obtain more detailed information about the rise-kinetics for delay-times  $\Delta t \approx T_{cc}$ . This is done by adding the convolution of the experimental response and  $p(\Delta t)$  to the terms described earlier.

In equation 5.1  $\tau_{rise}$  denotes the time-constant of the  $Q_{01} \rightarrow Q_{00}$  population flow,  $\tau$  the time-constant of the fast decay and  $A$  the corresponding amplitude. The constant term  $B$  is added to simulate the long-living component arising from the nanosecond decay of the low-lying  $S_1$ -state. The multiplication with the factor  $A_0$  is done in order to account for the different absolute maximum intensities. The component lifetimes and amplitudes estimated by this fitting procedure are presented in figure 5.6.

Panel A of figure 5.6 shows the amplitudes  $A$  and  $B$  together with the amplitude ratio  $A/B$  depending on the probe wavelength. As can be seen, the relative contribution of the long-living decay amplitude  $B$  decreases for probe wavelengths set at the blue wing of the probe-pulse. For example, the value of  $B$  drops from 0.80 at 580 nm to 0.33 at



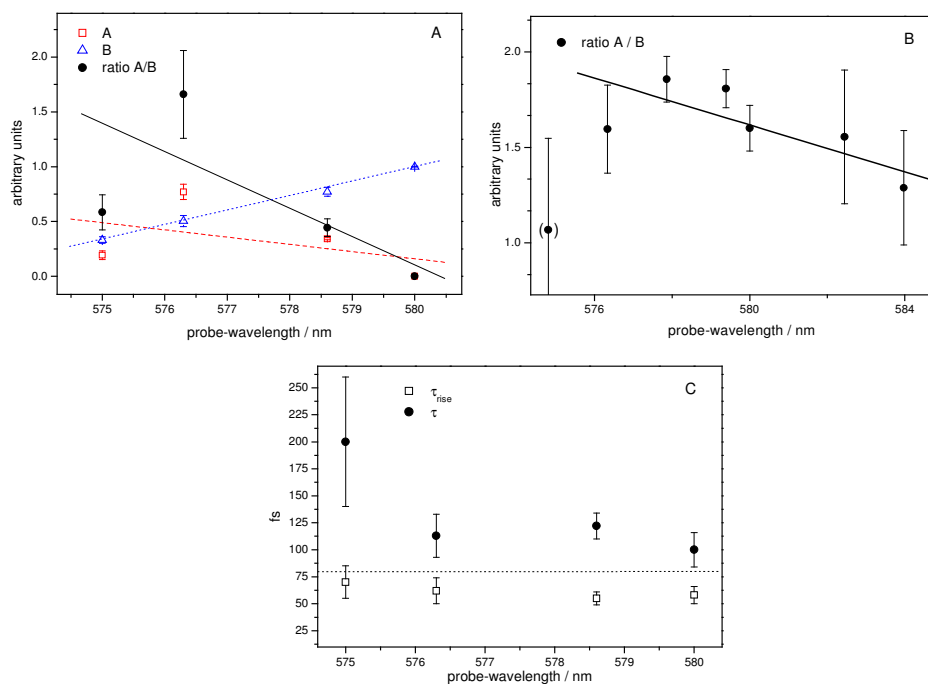


Figure 5.6: The parameter yielded by LS-fits of the experimental data are shown as a function of the probe-wavelength. Panel A displays the coefficients  $A$  (triangles) and  $B$  (squares), which result from a fit of the data presented in figure 3 panel B, together with the interpolation of the data. The ratio of the two coefficients  $A/B$  is shown as solid circles. Panel B presents the analogue ratio obtained from fitting the TG-signal at 580 nm following photo-excitation at 550 nm. The solid line illustrates a linear interpolation of the data points with the one at 574.6 nm omitted. Panel C presents the time-constants obtained from fitting the data shown in figure 5.5 panel B. The dashed line indicates the time-resolution of our experimental setup.

575 nm. Simultaneously the estimate of  $A$  increases. From 580 to 575 nm, the relative contribution of  $A$  increases from 0 to being larger than the value of  $B$  as can be judged from the amplitude ratio  $A/B$  depicted in panel A of figure 5.6. Pumping at 550 nm, the longwave instead of the shortwave side of the  $Q_{01}$ -band, and probing the kinetics in the  $Q_{00}$ -band, leads to similar results. Fitting this data to the above kinetic model yields the analogous probe-wavelength dependency of the amplitude ratio  $A/B$  with an increase of this ratio at the blue vs. the red wing of the probe pulse (figure 5.6 panel B). The origin of the fast decay associated with  $\tau$ , and the trend in the corresponding amplitude can be understood if it is taken into account that TG spectroscopy examines whether an electronic resonance at a definite spectral position exists. The observed decay therefore suggests that the  $Q_{01} \rightarrow Q_{00}$ -internal conversion populates energetically higher-lying levels within the  $Q_{00}$ -band, the subsequent intra-band relaxation of which then results in a partial loss of the electronic resonance and thus in a decay kinetics within the overall TG-signal. The time-constant for this fast decay,  $\tau$ , including the rise term,  $\tau_{rise}$ , in the kinetics, are shown in figure 5.6 panel C in dependence on the probe wavelength. The estimate for the rise time varies from 55 fs to 70 fs, both of which values fall into the time resolution of our apparatus. Nevertheless, with a pulse duration (instrumental FWHM) of  $\sim 80$  fs in our experiments, the upper limit of this rate can be approached by  $\sim 100$  fs. The fast decay-time,  $\tau$ , depends strongly on the probe-wavelength. While at 580 nm the fast decay is almost undetectable, it proceeds on a time scale of 120 and 110 fs at 576.3 and 578.6 nm, respectively, and at 574.8 nm, the blue wing of probe pulse, it takes as long as 250 fs. Based on the time scale of these decay kinetics, it seems to be due to an intramolecular vibrational energy redistribution (IVR) process. Vibrational cooling is not compatible with this time-constant, since it is not expected to proceed on the femtosecond time scale [105]. In contrast to cooling, vibrational redistribution is well known to occur in some hundreds of femtoseconds or even faster [106, 107]. Moreover, the time scale of 90-200 fs is very similar to those assigned to IVR within the lowest excited  $S_1$ -state in other femtosecond studies of porphyrin derivatives [98, 108, 109]. For these reasons the fast decay is ascribed to the intramolecular vibrational energy redistribution within the lowest excited  $S_1$ -state of MgOEP. Interestingly, the time-constant for IVR varies between 90 and 200 fs depending on whether lower or higher excited vibrational levels within the  $Q_{00}$ -band are involved in the IVR process. In a further experiment, the molecular relaxation processes following Soret-band excitation of MgOEP were investigated. Figure 5.7 shows a representative kinetic

trace, which was recorded at 572 nm, that is, within the  $Q_{00}$ -band, after excitation of the Soret-band at 400 nm. This kinetics is remarkably similar in appearance to that obtained by pumping the  $Q_{01}$ -band, as can be seen from a comparison with the data in figure 5.5 (panels B and C). The fit to the kinetic model presented above yields a time-constant of  $150 \pm 35$  fs for the rise term,  $\tau_{rise}$ , which refers to the rate of the  $B \rightarrow Q_{00}$  electronic relaxation. However, the  $\sim 100$  fs rise is instrument response limited, but with an instrumental FWHM of 350 fs for the pump wavelength of 400 nm, an upper limit of not more than 350 fs can be deduced for this rate. (The experimental response function for excitation carried out in the Soret-band is much broader than for excitation into one of the Q-bands, as presented above. This is due to the use of the uncompressed frequency-doubled fundamental light of one of the OPAs - see section 3 - for pumping the molecular system at 396 nm and thus within the spectral region of Soret-band absorption.) For the comparatively fast decay,  $\tau$ , corresponding to the intra-band relaxation in  $Q_{00}$ , a time-constant of  $650 \pm 180$  fs can be estimated. This time-constant is in reasonable agreement with that of  $250 \pm 50$  fs obtained for the IVR process from excitation of the  $Q_{01}$ -band considering the lower time-resolution for this experiment. It thus appears that Soret-band excitation strongly matches the intra-band relaxation in  $Q_{00}$  as observed for  $Q_{01}$ -band excitation. Further, the  $B \rightarrow Q_{00}$  electronic relaxation occurs with a time-constant shorter than a few hundred femtoseconds on a similar time scale as the  $Q_{01} \rightarrow Q_{00}$  internal conversion, although this relaxation is not as well determined due to the lower time resolution of our experimental set up for excitation at 400 nm versus 530 nm.

In this section a femtosecond time-resolved study on the ultrafast intramolecular relaxation dynamics of magnesium octaethylporphyrin in solution has been presented. With the use of spectrally resolved for-wave-mixing spectroscopy in the femtosecond time regime, the molecular relaxation processes following excitation in each of the Soret,  $Q_{01}$  and  $Q_{00}$ -bands have been investigated. The results presented show that the  $Q_{01} \rightarrow Q_{00}$  electronic transition occurs in less than 100 fs while the Soret  $\rightarrow Q_{00}$ -transition is instrument-limited and observed -due to the lower time resolution for excitation in the Soret-band- on the sub-350 fs time scale. Subsequent to the  $B \rightarrow Q_{00}$  and  $Q_{01} \rightarrow Q_{00}$  electronic transitions, an ultrafast intra-band relaxation within  $Q_{00}$ , the lowest excited singlet-state, takes place. Depending on the level of the  $S_1$  vibrational manifold that is probed, the intra-state relaxation decays with a time-constant between 90 and 250 fs. The 90-250 fs decay time is too fast for a molecular cooling process. Most probably, it corresponds to an intramolecular

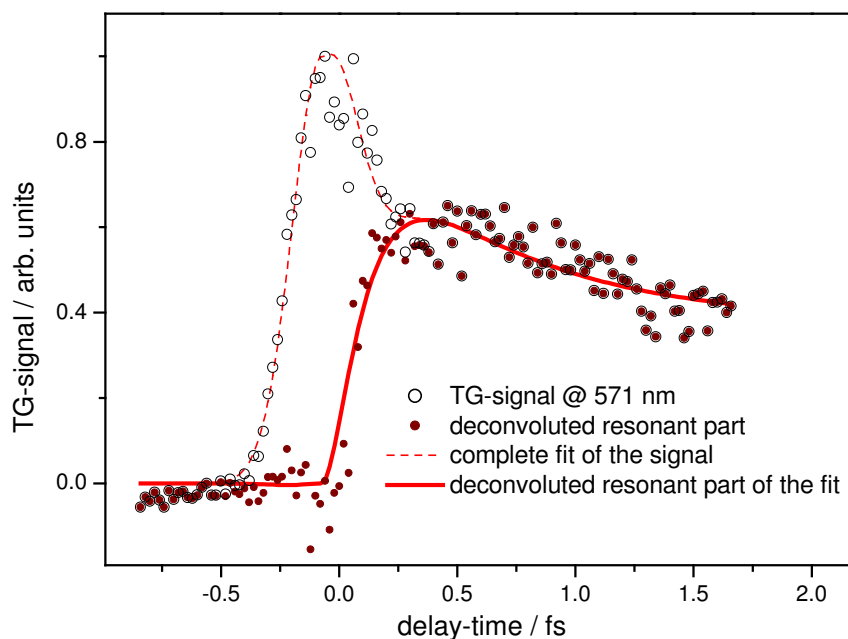


Figure 5.7: A transient grating signal excited at 400 and probed at 571.7 nm is shown (dots) together with a least square fit of the data (solid line).

vibrational redistribution process identified with a similar rate in other porphyrin derivatives [98, 108, 109]. The depopulation of the vibrationally relaxed  $S_1$ -state then proceeds on a significantly longer time scale, the exact estimate of which cannot be determined due to the femtosecond time resolution of the four-wave-mixing experiments.

The results presented here clearly reveal the various intermolecular relaxation processes, which can be consistently discussed in the framework of intra and interstate-relaxation commonly applied to understand the excited-state dynamics of porphyrins (for example see [98, 108, 109]). It has to be noted, that MgOEP does not display any excited state dynamics besides ultrafast IVR when being promoted directly to the lowest lying Q-band, which - as will be shown below - is very contrary to the behavior of PChla under similar experimental conditions. Thus, it may be speculated, that the distinguishing structural differences between MgOEP and PChla, plays a central role in the photophysics of the latter system. Therefore, the data constitute a valuable starting point for the discussion of the transient absorption measurements with the structurally similar PChla.

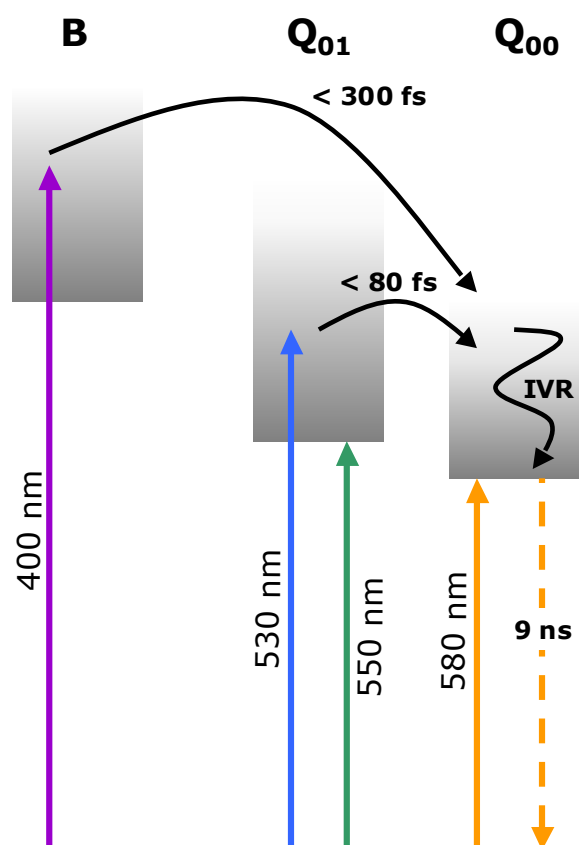


Figure 5.8: A comprehensive view on the relaxation processes within the excited-state manifold of MgOEP. Solid black lines indicate non-radiative transitions, while solid colored lines refer to the wavelength used for pumping and probing. The orange dashed line symbolizes fluorescence out of a thermalized  $S_0$  state.

## 5.3 Ultrafast Excited-State dynamics of protochlorophyllide

### a

Having discussed the relaxation processes in photoexcited MgOEP which can be thought of as a suitable model system for PChla, we shift our attention towards the investigation of the excited-state dynamics of the latter system. This section is organized as follows: In subsection 5.3.1 transient absorption data taken subsequent to excitation at 625 nm, i.e. in the center of the energetically lowest lying *Q*-band, is presented. This data leads to the tentative formulation of a model for the relaxation processes originating in the lowest lying excited-state of PChla dissolved in methanol. The data is compared to the results obtained by Heyes et al., who provided a first attempt to investigate the POR-PChla-catalytic reaction on a fs time-scale [95], and to the ultrafast photophysical behavior of MgOEP as discussed in section 5.2. In section 5.3.2 solvent and pump-energy dependent measurements are presented, which allow further insight into the suggested model. Based on this experiments and picosecond time-resolved fluorescence data (see section 5.3.3) the suggested model is refined.

### 5.3.1 A first transient absorption approach

Figure 5.9 depicts the steady state absorption, the fluorescence and the fluorescence excitation spectrum of PChla in methanol. The absorption spectrum exhibits the spectral features characteristic of porphyrins [96]. A strong Soret-band located at 434 nm is accompanied by three weaker *Q*-absorption bands at 534 nm, 576 nm and 629 nm. The Stokes shift between the maximum of the absorption band and the maximum of the fluorescence spectrum ( $\sim 300 \text{ cm}^{-1}$ ) is small indicating only a minor role of solvent reorganisation effects for excitation of PChla in methanol. Moreover, the excitation spectrum as shown in figure 5.9, is identical in shape to the steady state absorption spectrum, pointing to the presence of a single type of PChla species only in the ground-state thus signifying the high purity of the PChla samples used in this work. The spectroscopic properties given above for this PChla sample are in good agreement with the data reported in [110]. For examining the excited-state processes, excitation of PChla was conducted with pump-pulses of 90-fs FWHM at 625 nm, i.e. in the center of the energetically lowest lying *Q*-band. Following excitation, the transient absorption changes were recorded throughout the spectral region

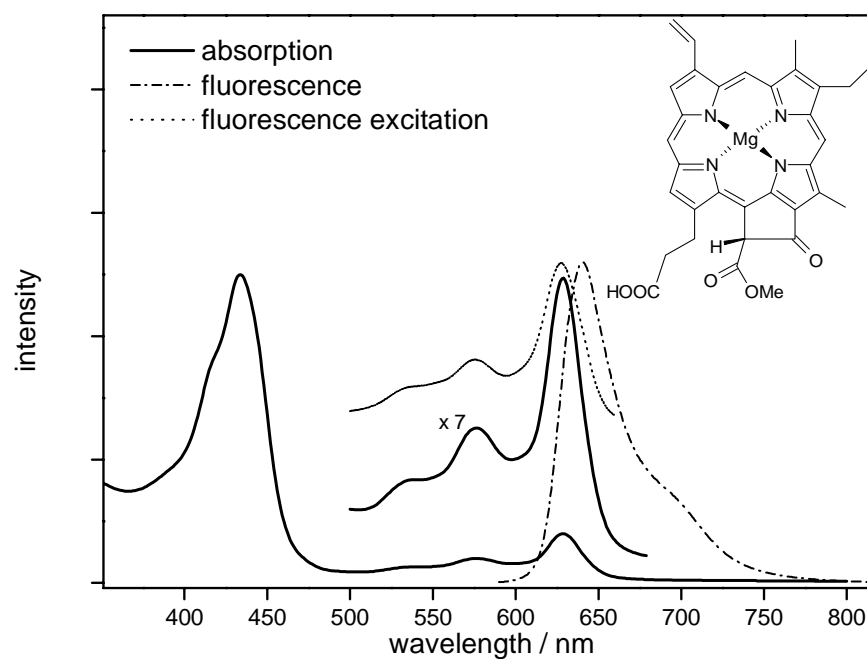


Figure 5.9: Steady-state absorption and fluorescence spectrum ( $\lambda_{exc} = 627$  nm) as well as fluorescence excitation spectrum ( $\lambda_{em} = 641$  nm) of PChla in methanol at room temperature. To demonstrate the close similarity between the steady-state absorption and fluorescence excitation spectrum, the visible absorption has been amplified by a factor of 7 in the region of the Q-bands.

between 500 nm and 700 nm up to 360 ps after excitation. In figure 5.10 time-resolved absorption difference spectra obtained upon photoexcitation are presented. The spectra are characterized by a strong negative band representing ground-state depletion and two broad positive bands extending at the blue and red sides of the ground-state depletion band. Figure 5.10 shows representative spectra acquired at delay-times between 0 and 10 ps.

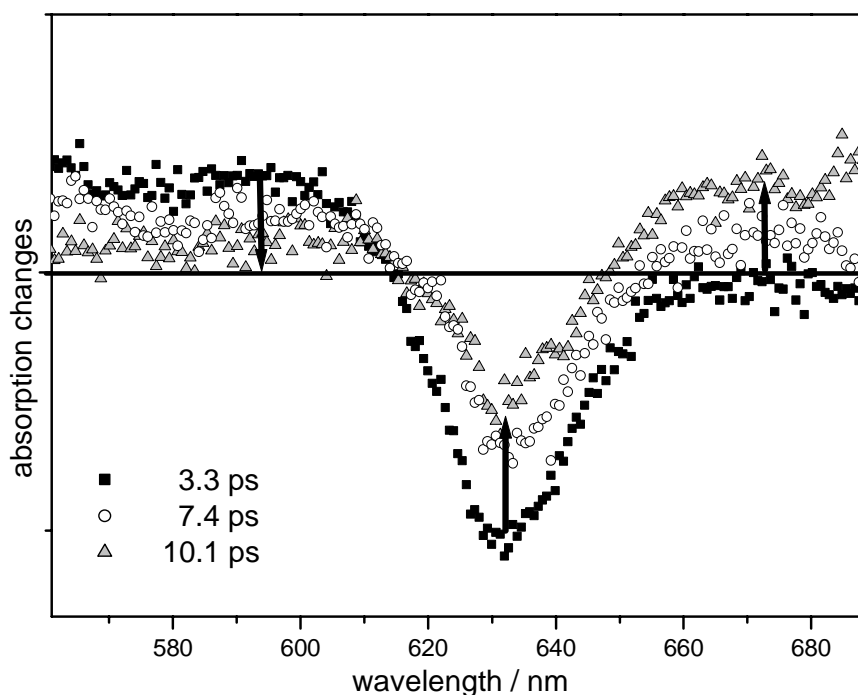


Figure 5.10: Transient absorption difference spectra of protochlorophyllide *a* in methanol recorded at various delay-times after excitation at 625 nm. The various delay-times are given in the inset. The arrows show the trend of the absorption changes in the respective spectral region.

While the photoinduced absorption to the blue side of the ground-state bleach spans the region from 500 to 610 nm, the latter extends from 650 to 700 nm, the red edge of the spectral range accessible to our measurements. Regarding the time evolution, the positive absorption changes between 500 and 610 nm appear with excitation and decay with the same overall time dependence as the adjacent ground-state bleaching. A slightly different time behavior may be observed for the positive absorption changes in the red spectral region above 650 nm. These occur as well with the excitation, i.e. within the time-resolution of our setup, but are subsequently further built up within the next few



picoseconds and their spectral position is shifted to the blue with time. In Figure 5.11 the difference absorption spectrum taken 8 ps after excitation is compared to the steady state absorption and fluorescence spectrum. As is evident, the difference spectrum looks similar to the steady-state absorption spectrum with the exception that the difference minimum is located at around 635 nm, i.e. slightly red-shifted from the ground-state absorption. This effect indicates contributions from stimulated emission which modify the shape of the main bleaching band. Furthermore, the transient absorption changes extending to the blue of this band show the shape of the absorption sub-bands at 534 and 576 nm, obviously due to a superposition of the excited-state absorption and ground-state bleaching in this spectral region.

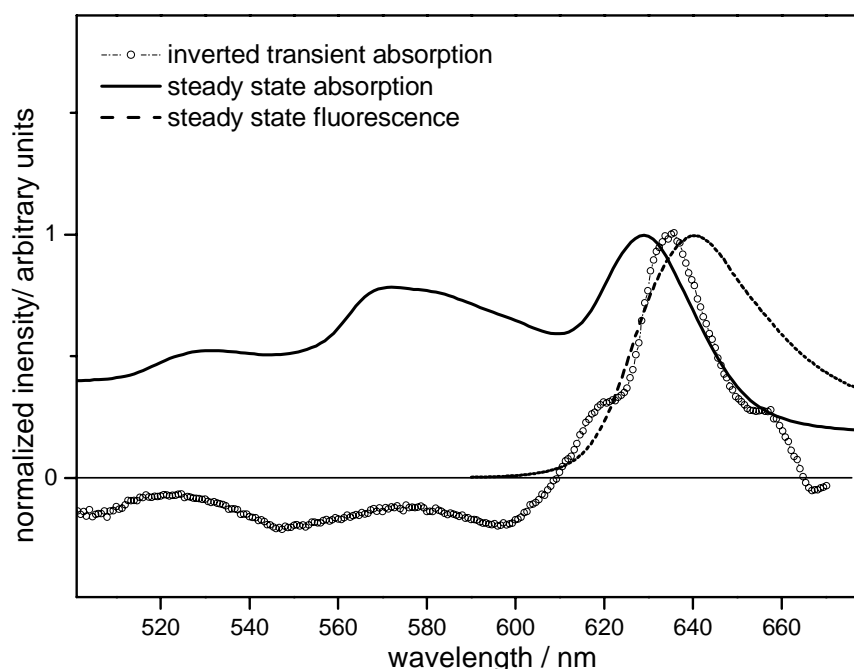


Figure 5.11: Comparison of the transient absorption difference spectrum of PChla in methanol taken 8 ps after excitation at 625 nm with the steady-state absorption (solid line) and fluorescence spectrum (dashed line), respectively. The transient difference spectrum is shown as inverted spectrum (dots).

For a more detailed kinetic analysis, the absorption changes at different probe wavelengths were subjected to a multi-exponential global fitting procedure [47]. Figure 5.12 shows the time evolution of the absorption changes at three representative probe wavelengths, 638, 624 and 578 nm, monitoring mainly ground-state bleaching, stimulated emis-

sion and the decay of the long-wave transient, respectively. The three kinetic traces represent integral kinetics being integrated over the intervals from 635 to 640 nm, 622 to 627 nm and 575 to 580 nm, respectively. Each kinetic could be fit to a sum of three exponentials and a constant term convoluted with the instrumental response function. The constant term was introduced, in order to simulate long-time absorption signals ( $\sim$ ns) which cannot be temporally resolved on the time scale of our measurements (see below). The global nonlinear least square fits of the transient absorption data yielded time-constants of  $\tau_1 = 4 \pm 1$  ps,  $\tau_2 = 27 \pm 9$  ps,  $\tau_3 = 200 \pm 60$  ps and, in addition, the afore-mentioned long decay time that exceeds the 360 ps window of our measurements. Figure 5.13 shows the wavelength-dependency of the amplitudes (decay-associated spectra, DAS) obtained from the three-exponential fits for these kinetic components.

The 4 ps and 200 ps components show very similar spectral features, i.e. broad induced absorptions extending from the blue and red wings of the ground-state depletion region. However, in the 200 ps component spectrum, the absorption extending at the blue side of the bleaching band mimics the shape of the absorption sub-band at 576 nm indicating a contribution of ground-state bleach in this spectral region. In contrast, the 27 ps component spectrum does not show any contribution to the overall ground-state bleach but is mainly dominated by strong negative amplitudes in the spectral region above 650 nm, indicating that the 4 ps process populates levels within the  $S_1$ -excited-state which may undergo decay by stimulated emission. Contributions from this stimulated emission lead to the observed increase in the long-wave photoinduced absorption within the first 10 ps after excitation. On the other hand, the significantly lower amplitude of the 27 ps component vs. the 4 and 200 ps components below 610 nm results in an overall decay of the short-wavelength transient absorption over the first 10 ps (see figure 5.10). Which types of dynamical relaxation processes might be associated with the above kinetic components? The 4 ps component agrees reasonably well with the relaxation lifetimes of 1 - 2 ps as reported for porphyrins [48,98,109,111]. They also correspond with the  $\sim$ 3 ps kinetic component as determined for chlorophyll a and b in pyridin [112,113] as well as the  $\sim$ 10 ps component measured for bacteriochlorophyll a in methanol [114]. In the porphyrins, the rates observed on the time scale of picoseconds to tens of picoseconds are attributed to solvent-induced vibrational relaxation processes of the  $S_1$ -state population. In our experiments, the overall spectral similarities between the 4 ps and the 200 ps component spectrum suggest that the 4 ps process is due to an  $S_1 \rightarrow S_n$ -transition. The 4 ps process should therefore be related

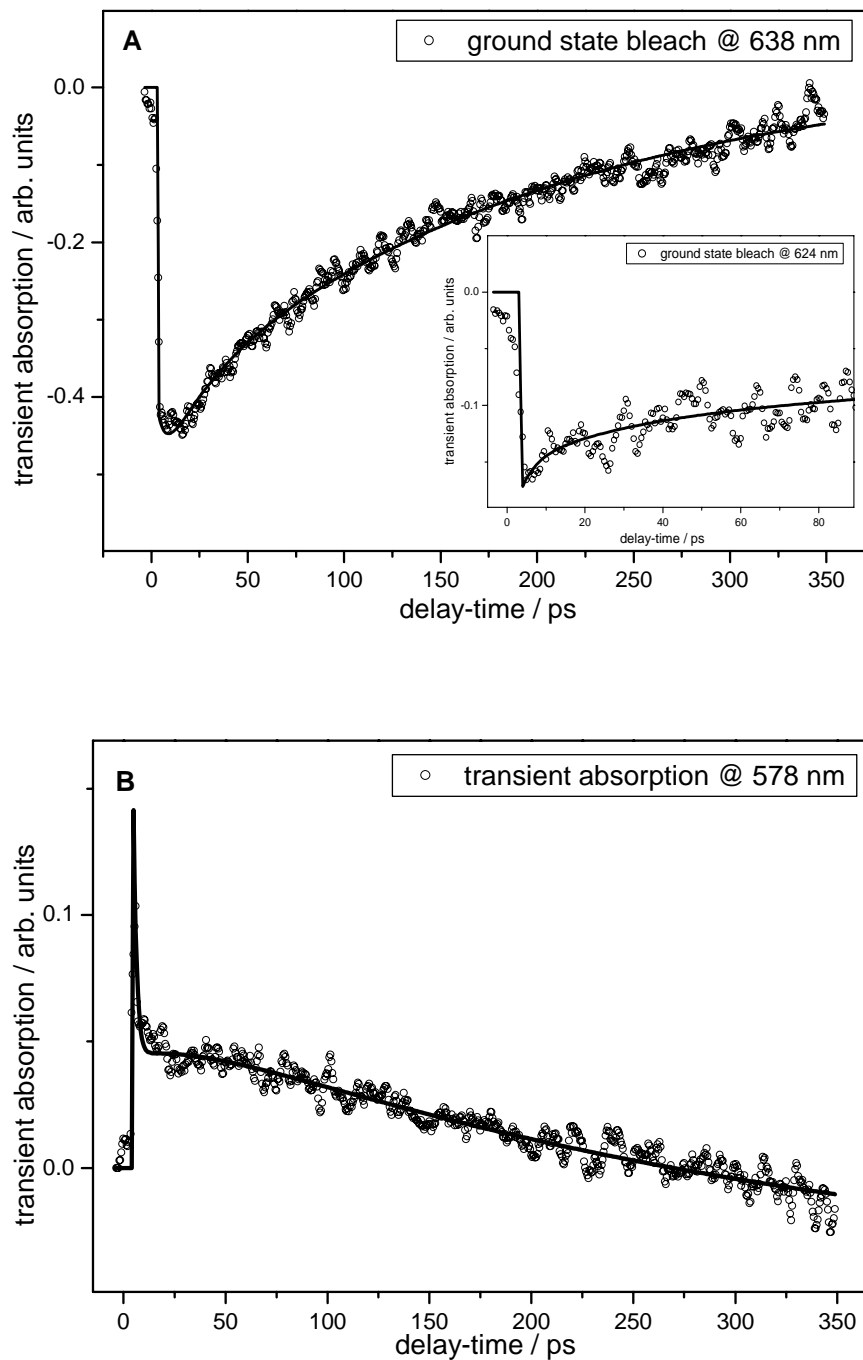


Figure 5.12: Transient absorption kinetics observed at 638 nm (panel A) and 578 nm (panel B) after excitation of PChla at 625 nm. PChla was dissolved in methanol. The kinetics shown at 638 nm and 578 nm was integrated over the absorption changes in the interval from 635 to 640 nm and 575 to 580 nm, respectively. The experimental data (dots) and the fit function resulting from the best fit parameters are shown (solid line). The inset in panel A gives the kinetic absorption changes at 624 nm (integration from 622 to 627 nm), a different spectral position within the region of the overall ground-state bleach.

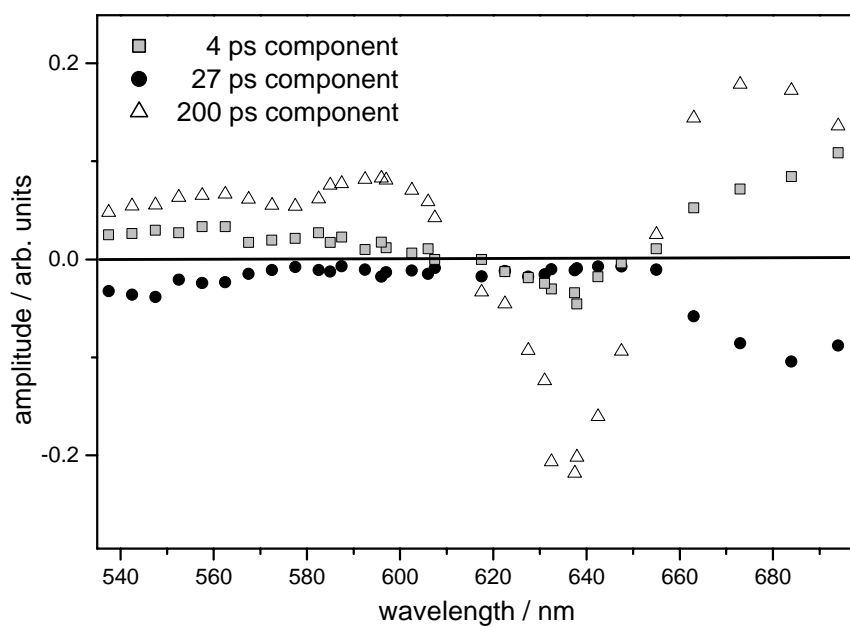


Figure 5.13: Wavelength-dependency of the amplitudes for the individual kinetic components with the time-constants of 4 ps, 27 ps and 200 ps, estimated from the tri-exponential fits.

to vibrational relaxation and the solvent-induced vibrational energy redistribution of the initially excited  $S_1$ -state, a relaxation process characteristic for porphyrins [48,98,109,111]. Up to this point of the investigations, the origin of the 27 ps relaxation step is unclear. The question remains whether the solvent-induced vibrational relaxation may occur over a range of time scales (picoseconds to tens of picoseconds) and thus include the 27 ps relaxation time, too. However, considering the 27 ps relaxation step along with the 200 ps process, another model may account for these two kinetics. This model suggests that the 27 ps process may reflect a motion out of the initially populated Franck-Condon region into an intermediate state that is subsequently depopulated back into the ground-state in 200 ps. On the basis of the results so far, a severe assignment of the 27 ps component cannot be made. Therefore, additional work was performed and is presented in sections 5.3.2 and 5.3.3 in order to further specify the processes associated with the 27 and 200 ps components. But in contrast to the uncertainty in the interpretation of these two components, the long lifetime component that persists for times far beyond the 360 ps window of our measurements, is obviously associated with the nanosecond decay from the fully equilibrated  $S_1$  population as recently observed in fluorescence lifetime measurements on PChla [110]. Picosecond time-resolved fluorescence decay data obtained in the course of this work (see section 5.3.3 also revealed a long lifetime component of  $3.5 \pm 0.1$  ns ( $\Phi_{fluorescence} = 0.06 \pm 0.01$ ) for excitation at 620 nm. In particular, no 200 ps component was found in the fluorescence decay. The absence of a 200 ps process further supports the model suggested above for the excited-state processes in PChla, i.e. that the 200 ps component is most likely due the ground-state recovery via a second decay channel. Based on these considerations, the model schematically presented in figure 5.14 is tentatively suggested to account for the excited-state excitation dynamics observed in photoexcited PChla and serves as the basis and starting-point for the further discussions.

Following excitation with 80-fs (FWHM) pulses at 625 nm, three relaxation processes can clearly be discerned in the decay of the initially excited population in the  $S_1$ -state, when PChla is dissolved in methanol. These relaxation processes occur on time-scales of 4, 27 and 200 ps, respectively. Among these, the fastest relaxation time is very similar to those generally observed in porphyrins and chlorophylls, while the longest time is in the order of the  $(400 \text{ ps})^{-1}$  reaction rate determined for the photoreduction of protochlorophyllide *a* in the NADPH:POR-complex. Taking into account that excitation was carried out into the Q-absorption band with only a small surplus of vibrational energy and that interference

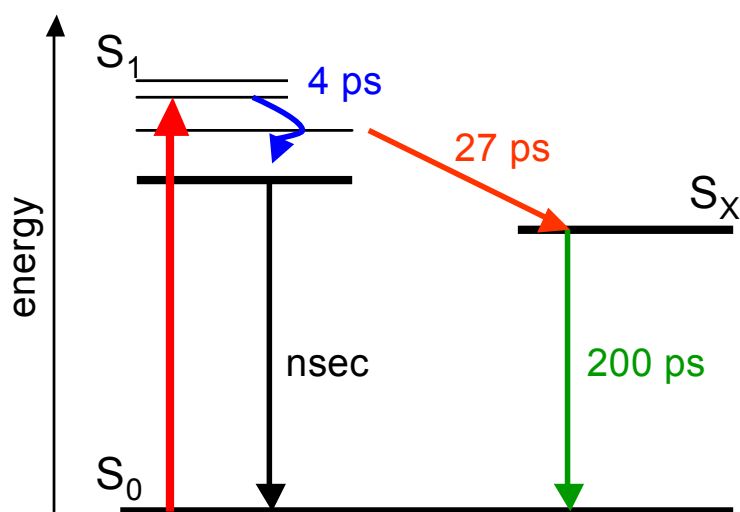


Figure 5.14: A model suggested to account for the transient absorption and fluorescence data obtained for PChla dissolved in methanol is presented schematically.

from solvent rearrangement is insignificant, the fast observed kinetic process is attributed to solvent-induced vibrational redistribution and cooling while the 27 ps is assigned to the formation of an intermediate state that subsequently is depopulated into the ground-state with a time-constant of 200 ps.

Interestingly, there is rich excited-state dynamics to be observed when photopopulating the  $S_1$ -state of PChla compared to transferring MgOPE molecules into its lowest lying and very long lived excited- $S_1$  state. This surprising difference leads to the conclusion that the cyclopentanone attached to the overall porphyrin structure and its electronic system might be of significant relevance in interpreting the ultrafast reaction dynamics of PChla (see section 5.3.2).

From a comparison of the ultrafast reaction dynamics of PChla alone in the alcoholic solvent and PChla in the oxidoreductase complex [95] it becomes apparent that there are, with respect to the 4 ps and 200 ps kinetics in the solvent as well as the 3 ps and 400 ps kinetics in the complex, generally very similar relaxation time scales within the  $Q$ -state. Further, the DAS of these components clearly show that the region of the ground-state

depletion and photoproduct absorption in the oxidoreductase complex is overridden by the excited-state absorptions of PChla. Thus, in the complex, an increase in the amplitudes at the blue wing of the main bleaching band upon evolution of the 400 ps component is observed. A similar trend also appears in the DAS of PChla in solution (see figure 5.13), whereby these spectra might offer an explanation for this effect. Most likely, the increase in amplitudes is caused by the decline of the excited-state absorption of PChla positioned at the blue side of the bleaching region. After 10 ps, i.e.  $2.5 \cdot \tau_1$ , this excited-state absorption has undergone nearly complete decay so that the ground-state bleaching is no longer supplanted by the excited-state absorption and therefore in effect increases.

### 5.3.2 Solvent and excitation energy dependence of excited-state processes

Having obtained a first impression of the richness of the excited-state relaxation pathways in PChla, the aim of the experiments presented in this chapter is to further elucidate the individual processes and states involved in the scheme shown in figure 5.14. More specifically, the influence of the solvent on the observed processes will be investigated. Here it is of particular interest to what extent the nature of the solvent influences the decaying behavior of photo-excited PChla. Therefore, instead of using methanol to dissolve PChla acetonitrile, a 60:40 mixture of glycerol and methanol and cyclohexane were used in order to selectively interrogate the influence of the solvent's acidity (meant as the ability of donating protons), viscosity and polarity, respectively. In addition, pump-energy dependent measurements of PChla dissolved in methanol were performed.

Figure 5.15 depicts an enlarged view on the region of Q-band absorption of PChla dissolved in the three different solvents used in this study in addition to methanol; a mixture of 60% glycerol and 40% methanol, the polar but aprotic solvent acetonitrile and cyclohexane serving as a unpolar and aprotic environment. The absorption spectrum of PChla in methanol is shown again for direct comparison. The absorption spectrum obtained for the glycerol-methanol mixture shows Q-bands at 538, 580 and 631 nm and therefore matches the Q-band structure of PChla in pure methanol very well. Thus, it is concluded that adding glycerol to methanol does not effect the electronic structure of the dissolved PChla but solely changes the viscosity of the solvent. In contrast, using acetonitrile to dissolve PChla leads to a significant blue shift of the entire Q-band structure with the lowest lying band being shifted to 626 nm. Furthermore, the width (FWHM) of this band is narrowed

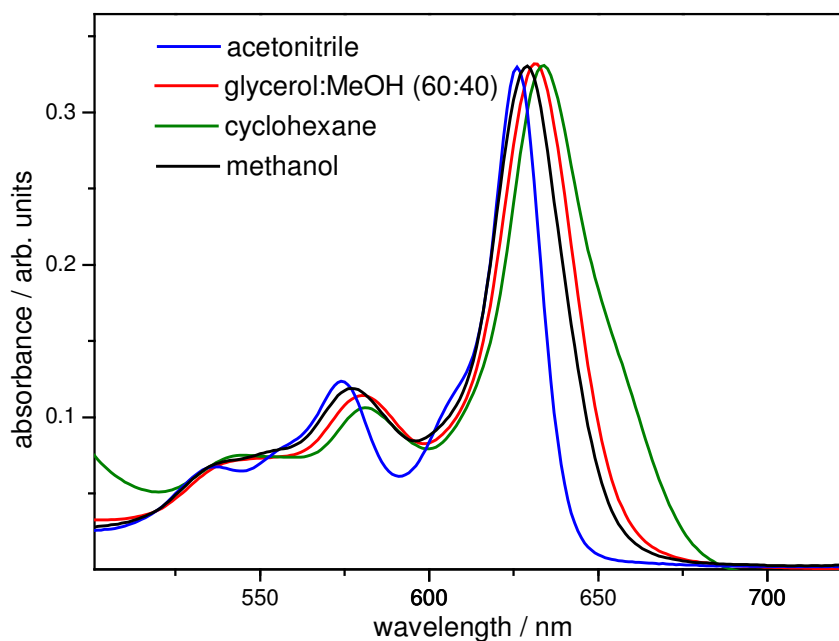


Figure 5.15: Steady-state absorption spectra of protochlorophyllide *a* dissolved in methanol, acetonitrile, cyclohexane and a mixture of 60% glycerol and 40% methanol at room temperature are shown. An enlarged view on the Q-band absorption region is depicted. The spectra are normalized.



from 28 nm in methanol and in the glycerol-methanol mixture to 20 nm in acetonitrile. In addition, two shoulders unobserved in methanol show up in the absorption spectrum recorded in acetonitrile at 555 and 606 nm. The contrary effect is observed for PChla dissolved in cyclohexane, wherein the energetically lowest lying Q-band appears red shifted with a maximum at 634 nm possessing a FWHM of 34 nm. Therefore, having observed the influence of the solvent to the electronic structure of PChla as mirrored in the steady state absorption spectra, it is to be expected that these changes are reflected in the transient absorption behavior of PChla as well. This subject will be discussed in the subsequent section.

### Solvent Acidity Dependence

Figure 5.16 compares the spectral and temporal features of the lowest lying excited-state of PChla dissolved in methanol and acetonitrile. Panels A and B present the transient absorption spectra taken at 3 and 22 ps subsequent to initial photo-excitation within the short wavelength flank of the lowest lying Q-band at 600 nm. All spectra are characterized by a strong ground-state bleach (GSB) centered at around 630 nm. The region of negative differential optical density is flanked by regions of broad and basically featureless photoinduced absorption, extending throughout the spectral range accessible for the experimental setup. The photoinduced absorption (PIA) observed to the red side of the GSB exhibits significantly higher oscillator strength than the photoinduced absorption extending to the blue side of the spectrum, which, as well as the GSB, exhibits a spectral shape that is in excellent accordance with the steady state absorption features, e.g. note the shoulder showing up at 615 nm in the spectrum taken for PChla dissolved in acetonitrile (PChla-acetonitrile). Furthermore, the reduced optical densities at 575 nm in PChla-acetonitrile and at 640 nm in the PChla-methanol spectrum are due to a bleaching of the  $Q_v$  ← ground-state absorption bands at these spectral positions superimposed to the broad and featureless PIA band. Panels C and D of figure 5.16 display transient absorption kinetics monitored within the region of photoinduced absorption to the red side of the GSB. As can be seen, both transients exhibit nearly identical decay characteristics. The initial ultrafast rise is followed by a slower rise component leading to an increase of the optical density up to about 50 ps after photoexcitation. Subsequently, a slow decay of the photoinduced absorption signals is observed. In order to evaluate the data quantitatively, they were fitted to the convolution

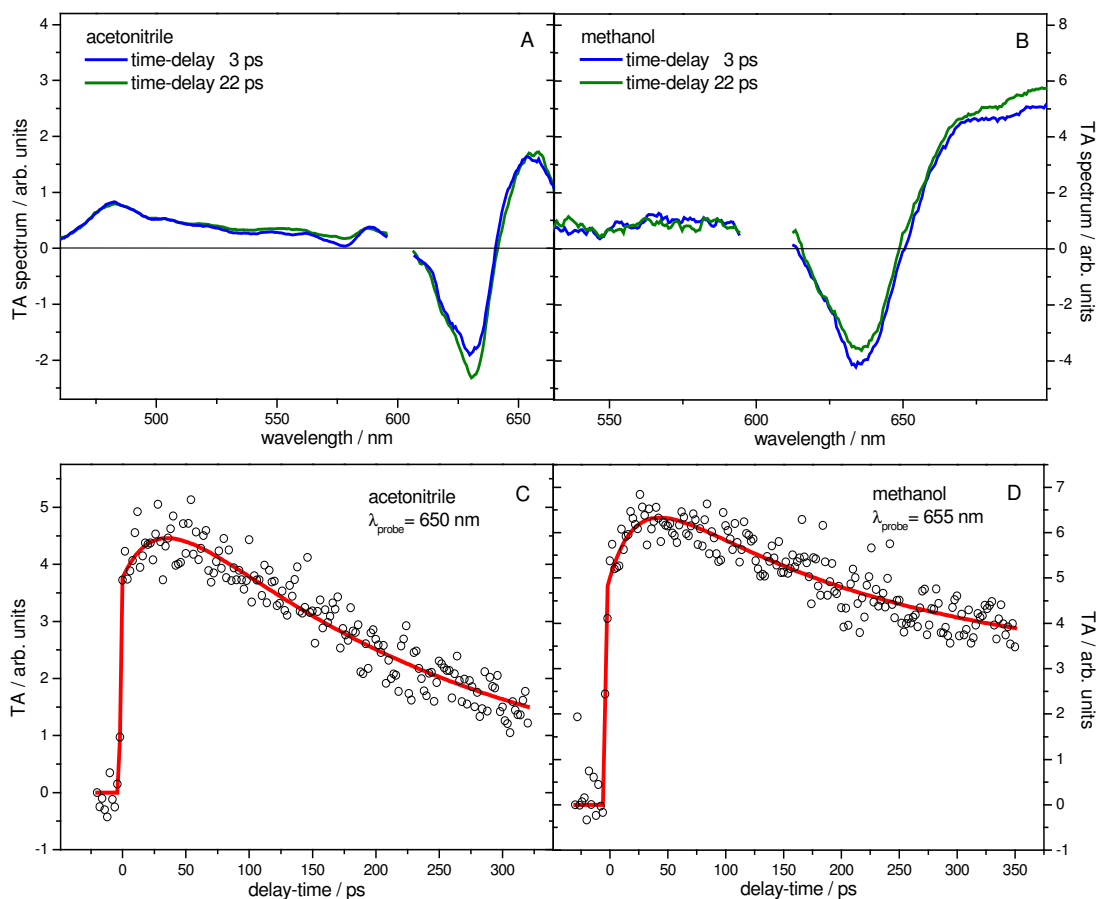


Figure 5.16: The transient absorption features of protochlorophyllide *a* dissolved in methanol and acetonitrile are compared. The respective transient absorption spectra taken 3 and 22 ps after photoexcitation are shown in panel A (acetonitrile) and B (methanol). Transient kinetics monitoring the transient absorption adjacent to the red side of the ground-state bleach is depicted in panels C (acetonitrile probed at 650 nm) and D (methanol probed at 680 nm). Dots represent experimental data, while the results of fits are shown as solid lines.

of the experimental response function, determining the shape of the initial ultrafast rise, and a sum of three exponentials and a constant. The latter was introduced in order to simulate any time-dependence beyond the delay-time range accessible in our experimental setup. This approach leads to the description of the excited-state relaxation processes of PChla-acetonitrile with time-constants of  $\tau_1 = 4.7$ ,  $\tau_2 = 22$  and  $\tau_3 = 205$  ps. These values are in excellent agreement with the values obtained for PChla dissolved in methanol as reported in the preceding section 5.3.1 [56], where kinetic components of  $\tau_1 = 4$ ,  $\tau_2 = 27$  and  $\tau_3 = 200$  ps following photo-excitation at 625 nm are reported. The solvents methanol and acetonitrile mainly differ in their ability of donating protons, while their polarities and viscosities are very similar. Therefore, from the close proximity of the observed overall decay characteristics and the characteristic time-scales, it has to be concluded that changing the acidity of the solvent does not influence the excited-state relaxation of PChla. Thus, the absence of a protonation step within the relaxation mechanism can be deduced. This is of particular interest for the correlation of the decay pattern observed for the free chromophore in solution to the reduction mechanism of protochlorophyllide a to chlorophyllide a in the enzymatic PChla-POR-NADPH complex. Inhere a keto-enol-tautomerization at the cyclopentenone ring has been suggested to be involved in this reaction of PChla in the POR matrix [115, 116]. This proposed reaction mechanism is depicted in figure 5.17.

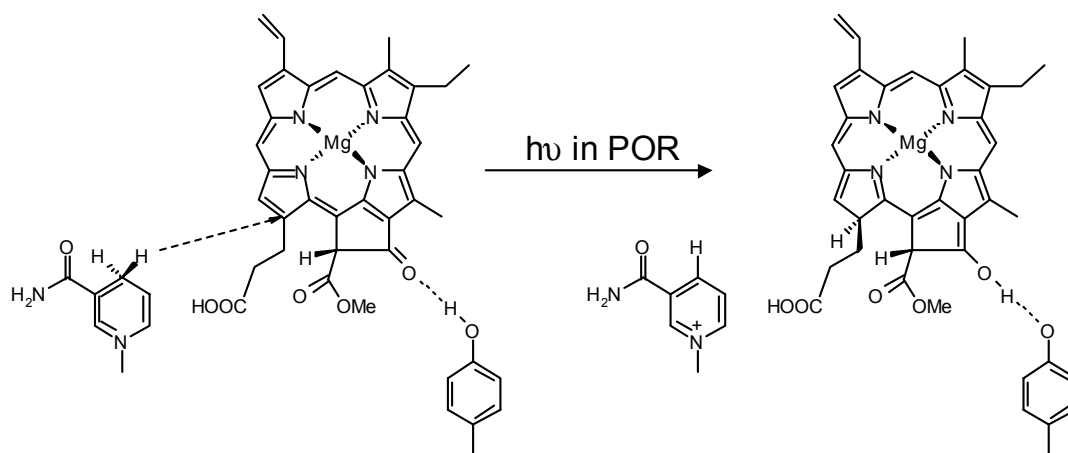


Figure 5.17: The reaction mechanism proposed by Klement et al. [115, 116] leading to the reduction of protochlorophyllide a to chlorophyllide a within the ternary POR complex is shown.

Though the reaction conditions within the enzymatic structure may differ com-

pletely from the environment the free chromophore is objected to in solution, it is highly interesting to note, that no keto-enol-tautomerization is involved in the relaxation dynamics of the free chromophore, as can be deduced from the absence of a solvent acidity dependence.

### Solvent Polarity Dependence

In contrast to the relaxation dynamics of PChla observed in ethanol and acetonitrile, the disposal of cyclohexane to dissolve PChla leads to a drastic change of the overall transient absorption kinetics upon photoexcitation into the lowest lying Q-band.

Panel A of figure 5.18 depicts the transient absorption spectra of PChla-cyclohexane taken 1.5 and 5 ps after photo-excitation into the lowest lying Q-band at 620 nm. It clearly exhibits features closely related to those observed for PChla in the other solvents; a strong GSB covering the spectral region of the ground-state absorption is accompanied by a broad and featureless positive  $\Delta OD$ -bands extending to the blue and the red side of the spectrum. The maximum negative absorption band shifts from 640 nm at 1.5 ps after light absorption to 630 nm at 5 ps. This is due to excited state cooling, while energy is dissipated and the population within the  $S_1$ -state declines the vibrational ladder the strong photoinduced absorption on the red side of the spectrum due to the  $S_1 \rightarrow S_n$ -transitions appears blue shifted. Thus, it overlaps with the GSB and therefore causes the blue shift of the overall GSB feature. A time-constant of  $\tau_1 = 4.7$  ps can be assigned to characterize the cooling process. In the spectral regions adjacent to the GSB the cooling process manifests itself as an overall decay of the PIA. Panel B shows transient kinetics taken at 685 nm and thus monitoring the time-dependence of the PIA on the red side of the spectrum. The transients clearly indicate that a single exponential plus a constant term is sufficient to describe the experimental data. Subsequent to the initial ultrafast rise of the signal, being limited by the pulse width of our experimental setup ( $\text{FWHM} \leq 100$  fs), only one kinetic component associated with  $\tau_1$  is observed throughout the time-range accessible with our experimental setup. This finding is in contrast to the results obtained for PChla dissolved in the more polar solvents acetonitrile and methanol. This strikingly different decaying behavior deserves some thorough considerations.

The experimental findings discussed so far might be explained on the basis of a split  $S_1$ -state in analogy to arguments given by Zigmantas et al. [117] and Bautista et al. [118] to account for the observed excited-state dynamics of peridinin, a highly substituted

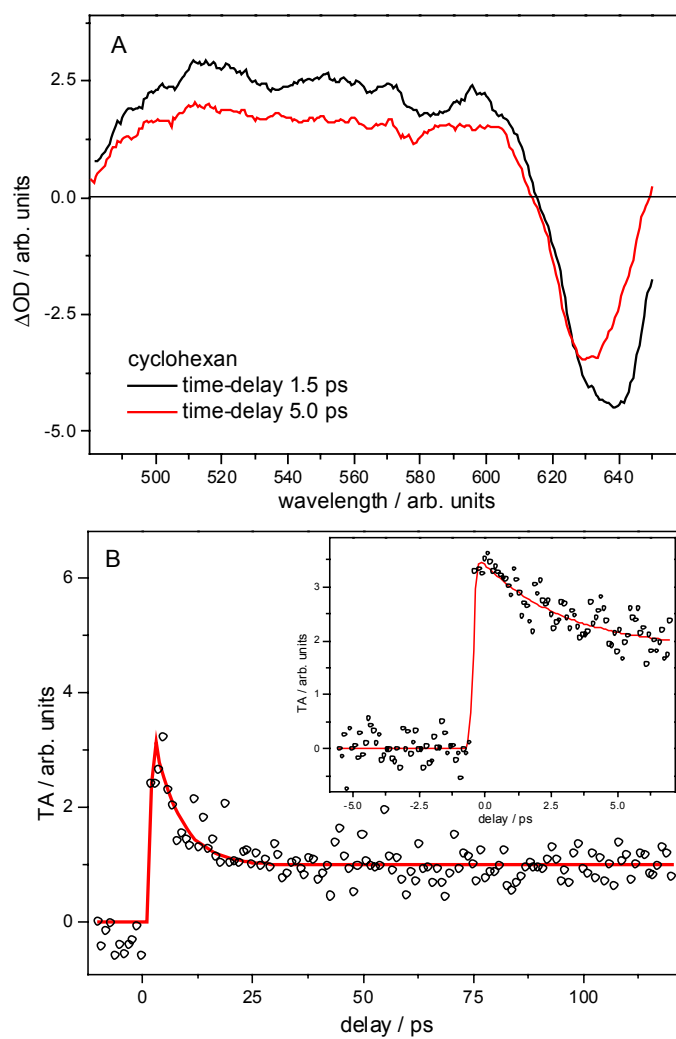


Figure 5.18: Panel A. Transient absorption spectra of protochlorophyllide *a* dissolved in cyclohexane taken 1.5 and 5 ps after photo-excitation at 620 nm. Panel B. Transient reflecting the transient absorption changes in the red spectral region after photo-excitation at 620 nm. The inset shows an enlarged view on the short time-range. Dots represent experimental data, while the results of fits are shown as solid lines.

carotenoid. The second state involved would most likely possess intermolecular charge-transfer (ICT) character and is therefore stabilized in more polar solvents and - in turn - destabilized in a non-polar environment. Thus, these authors observe an  $S_1 \rightarrow S_{ICT}$  transfer rate, that is controlled by a solvent polarity dependent barrier. They show, that in *n*-hexane the barrier is high enough to prevent the population of the  $S_{ICT}$ -state to take place and only the  $S_1 \rightarrow S_0$  internal conversion is observed. These authors report on a decreasing barrier in parallel with increasing solvent polarity resulting in a quenching of the  $S_1$  state by means of the  $S_1 \rightarrow S_{ICT}$  relaxation [117].

The results obtained in the course of this work, might be explained in analogy to the arguments given above; in the polar solvents acetonitrile and methanol the intramolecular charge-transfer state lies below the initially photo-populated  $S_1$ -state and is therefore accessible for population to flow into it. In the non-polar solvent cyclohexane this state is destabilized and the rise of its potential minimum above or close to the  $S_1(v=0)$ -state leads to a high barrier between the two states inhibiting  $S_1$ -molecules to be depopulated into the intermolecular charge-transfer state ( $S_{ICT}$ ). Since the barrier is constituted by the energy difference between the minimum of the potential energy surface of the  $S_1$ -state and the crossing point of the  $S_1$  and the  $S_{ICT}$  electronic potentials, the barrier increases with decreasing solvent polarity, i.e. increasing destabilization of  $S_{ICT}$ . The absence of a 200 ps-component in the transient signals of PChla-cyclohexane indicates that this time is due to the relaxation of the  $S_{ICT}$ -state into the ground-state, therefore, occurring subsequently to the population of the charge-transfer state characterized by  $\tau_2$ . The further discussions are devoted to shed more light onto the nature of the states involved and the processes promoting population between the distinct excited-states. As stated above, the  $S_{ICT}$ -potential minimum can be shifted by the use of solvents of different polarity. Thus, it is concluded that the  $S_{ICT}$ -state itself is most likely to possess a large dipole moment. Therefore, the electronic excitation cannot be spread over the entire aromatic system, because this would mean a delocalized excitation. Thus, it is deduced that the excitation should become localized within the  $S_1$  potential and therefore the decay-constant  $\tau_2$ , ascribed to the population of the  $S_{ICT}$ -state, corresponds to a charge-localization within the excited-state manifold. It can be speculated that the cyclopentanone ring is involved in this localization step. This assumption is likely because other groups having observed a decay pattern very similar to the one reported here made their observations in peridinin, a carotenoid highly substituted and possessing a *cyclopentanone ring* as well [117–120]. This assumption is further cor-

robored by the experimental results obtained on MgOEP as presented in chapter 5.2, as MgOEP, in contrast to the structurally similar PChla, which in addition has an attached cyclopentanone ring to the porphyrin macrocycle, does not exhibit any significant excited state dynamics, when directly being promoted into the Q<sub>00</sub> band. Correlating the presence of two distinct decay channels, one of which involving a charge-separated state, with the presence of the cyclopentanone ring would be of particular interest, because all models proposed to understand the reduction of the C17=C18 double bond of PChla in the PChla-NADPH-POR complex [115,116,121] suggest a H<sup>-</sup>-attack at the C18 atom of PChla. This process should be facilitated by a decreased local electron density at the particular molecular position. Despite the fact that - as stated above - the environmental and thus the reaction conditions within the protein matrix might be completely different from those in solution, it is again remarkably interesting that the excited-state charge-localization observed in the free chromophore might lead to an electronic configuration that favors the reduction of a particular double bond within the porphyrin-conjugated system of PChla.

### Solvent Viscosity Dependence

In order to address the question whether the excited-state charge-localization discussed above involves large nuclear motions or occurs in the quasi-static molecule, the excited-state relaxation of PChla was interrogated by monitoring the TA of a sample dissolved in a 60% glycerol-40% methanol mixture (hereafter referred to as *glycerol* for simplicity). This way the influence of the sample viscosity on the kinetic behavior can be investigated while keeping the polarity of the solvent approximately unchanged. Transients reflecting the short time behavior of PChla dissolved in glycerol and of PChla-methanol are shown in figure 5.19.

Although the transients are monitored at different spectral position the important difference can be clearly seen. While the signal taken in glycerol shows an primary decay (subsequent to the ultrafast initial rise) that can be characterized by a time-constant of  $\tau_1 = 12.1$  ps, the corresponding process in methanol occurs on a faster time-scale with a time-constant of only 4 ps (see section 5.3.1 and reference [56]). Therefore, focusing on the dynamics occurring within the first 12.1 ps after photo-excitation PChla-methanol exhibits a rise component in addition to the primary decay, while the kinetics of PChla-glycerol can be accounted for by the 12.1 ps decay only. The complete transient behavior observed in

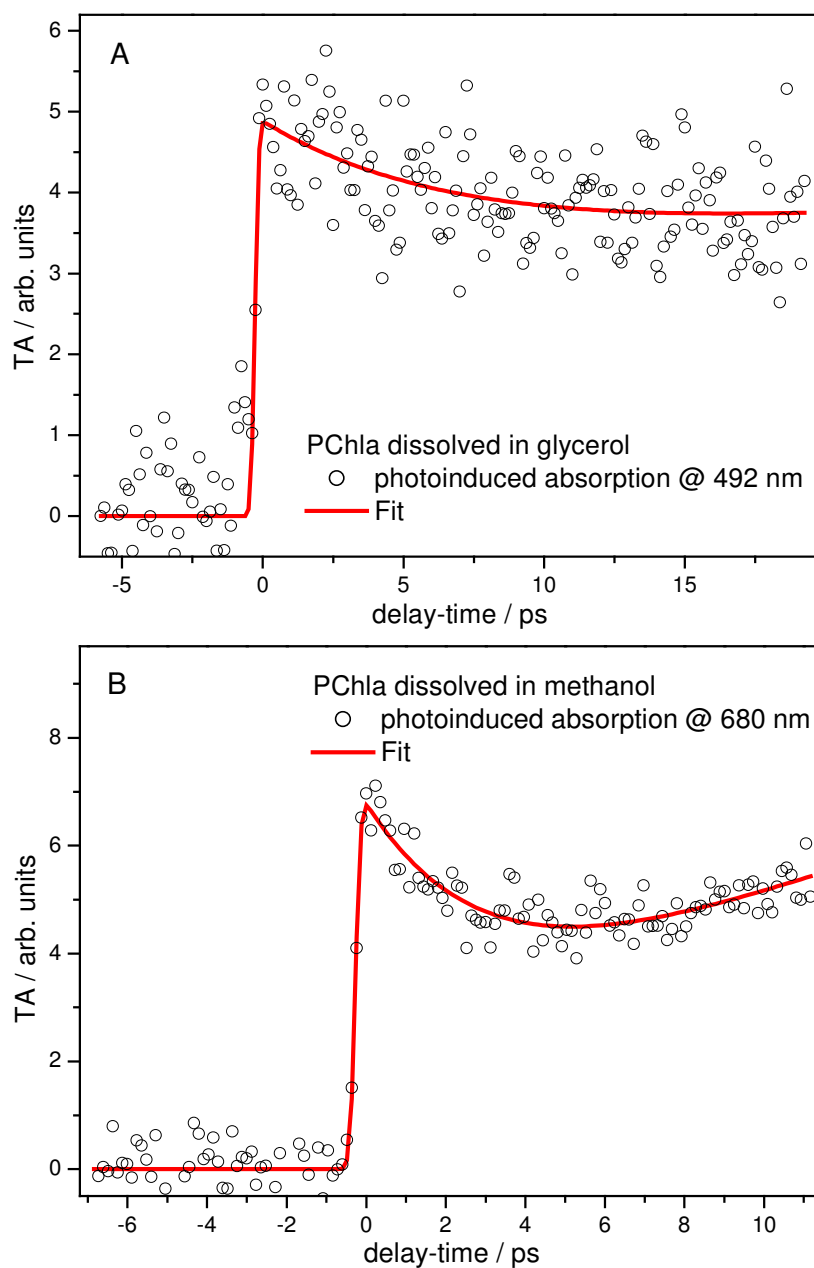


Figure 5.19: Transient absorption kinetics of protochlorophyllide *a* dissolved in glycerol (panel A) and methanol (panel B). Panel A shows a transient data taken at 495 nm, thus reflecting the transient absorption in the blue spectral region. The data shown in panel B was taken at 680 nm and thus within the spectral region of the red transient absorption. Dots represent experimental data, while the results of fits are shown as solid lines. Protochlorophyllide *a* was excited at 630 nm in both cases.



glycerol, methanol and acetonitrile can be described by three distinct kinetic components characterized by the time-constants  $\tau_1$ ,  $\tau_2$  and  $\tau_3$ . The time-constant obtained from fitting the various experimental data are summarized in table 5.1.

Solvent	$\tau_1$ /ps	$\tau_2$ /ps	$\tau_3$ /ps
Methanol	$4.0 \pm 1.0$	$27 \pm 6$	$200 \pm 60$
Acetonitrile	$3.5 \pm 1.2$	$22 \pm 4$	$200 \pm 60$
Glycerol	$12.1 \pm 2.6$	$40 \pm 7$	$270 \pm 70$
cyclohexane	$4.5 \pm 1.8$	—	—

Table 5.1: Summary of the time-constant obtained from fitting the experimental data. All data were taken with the pump-wavelength to fall in the absorption maximum of the lowest lying Q-band. For details see text.

From the characteristic time-scales of PChla-glycerol being significantly longer than the corresponding time-constants obtained for PChla-methanol, it can be inferred that the increased viscosity affects the rate of the corresponding relaxation processes [19,120,122–126]. As the nuclear motion of the vibrating molecule is slowed down in the highly viscose solvent the rate of energy dissipation associated with the shortest time-scale decreases. In addition to the primary decay, the kinetic component associated with  $\tau_2$  is also slowed down considerably in glycerol compared to methanol as solvent, while  $\tau_3$  remains almost unaffected within the experimental errors. Thus, it can be concluded that not only cooling but also the process of charge-localization is associated with significant nuclear motion.

### Pump-energy Dependence

In this section the discussion will focus on the influence of the pump-energy on the observed relaxation dynamics. In order to address this question, TA measurements of PChla-methanol in the spectral region extending to the low energy side of the overall GSB were performed with different pump-energies. The excitation wavelength was varied from 655 nm, thus falling in the red flank of the lowest lying Q-band, to the high-energy side of the absorption feature at 600 nm. Figure 5.20 shows two representative transients recorded at 670 nm under the experimental conditions mentioned above.

As can be clearly seen, for delay-times larger than about 60 ps the normalized data match very well; however, the transients differ significantly in their short time behavior. The primary decay visible in the transient pumped at 600 nm is not observed for excitation at 655 nm. This kinetic component can be ascribed to a characteristic decay-time of  $4 \pm 1$  ps and

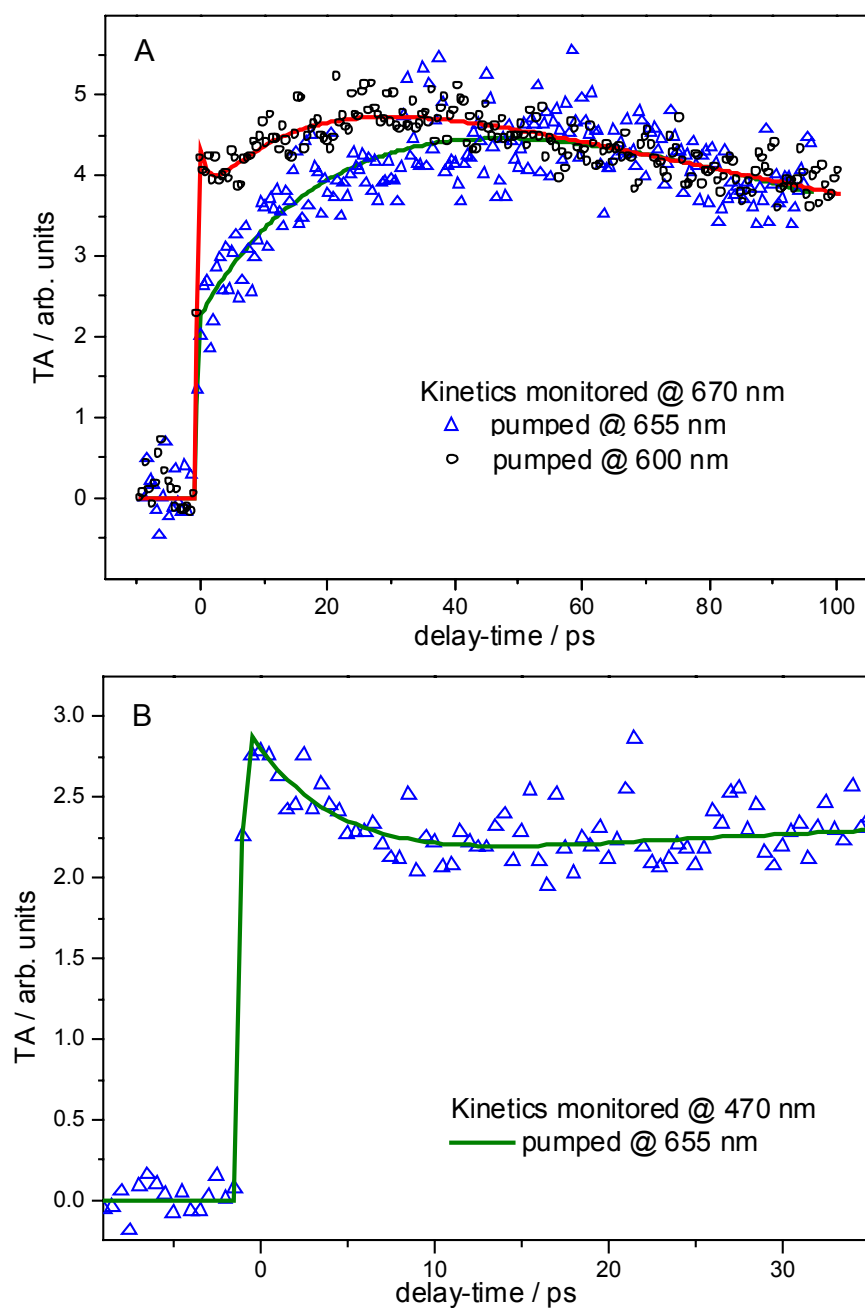


Figure 5.20: Transient absorption kinetics of protochlorophyllide *a* dissolved in methanol taken at 670 nm for two different pump-wavelengths are shown. Open circles represent data taken subsequent to photo-excitation at 600 nm, while data taken after light absorption at 655 nm are displayed as hollow triangles. Solid lines represent the corresponding least square fits.

is therefore associated with cooling. Thus, it is obvious that energy dissipation is observed with a much smaller amplitude (and consequently not visible in the transient presented here) following excitation into the red flank of the ground-state absorption band. In the latter case barely any vibrational excess energy is delivered to the molecular system that therefore is prevented from undergoing a clearly observable cooling process. But obviously, the transients differ not only in the short time behavior but also in the time-range extending up to 60 ps. It can be seen, that the rise of the PIA signal associated with  $\tau_2$  is considerably slower when pumping at 655 nm compared with the transient monitored subsequent to excitation at 600 nm. A quantitative analysis involving a fitting function as described above yields the value of  $\tau_2 = 19 \pm 2$  ps when pumping at 600 nm and  $27 \pm 3$  ps when the pump wavelength is set to 655 nm. In contrast to the observed pump-wavelength dependence of  $\tau_2$ ,  $\tau_1 = 4 \pm 1$  ps and  $\tau_3 = 200 \pm 60$  ps are found to be independent of the pump-wavelength in the spectral range from 600 to 655 nm, thus covering the lowest lying Q-band absorption. The acceleration of the excited-state charge-localization process associated with  $\tau_2$ , when delivering  $7100 \text{ cm}^{-1}$  excess energy into the molecular system, can be understood on the basis of three distinct arguments outlined in the following: First of all, the  $S_{ICT}$ -state is separated from the initially populated  $S_1$ -state by a barrier, which originates from the displacement of the corresponding potential minima along the reaction coordinate. In addition, the height and width of the barrier are influenced by the solvent-induced energetic position of the potential surface minima. Despite of not knowing the precise height and shape of the barrier preventing quasi-instantaneous population of the  $S_{ICT}$ -state, it is important to consider, that the rate of molecules crossing the barrier will increase exponentially with the vibrational excess energy delivered to the system in the  $S_1$ -state. Second, the coupling of the two states  $S_1$  and  $S_{ICT}$  involved in the process of intramolecular charge transfer will increase with increasing vibrational excess energy in the  $S_1$ -state. In general, the absolute value of non-adiabatic coupling matrix elements of the form  $\left\langle f(v_f) \left| \frac{\partial^{(2)}}{\partial x^{(2)}} \right| i(v_i) \right\rangle$  increases with increasing vibrational quantum numbers,  $v_{i,f}$ , in the states involved in the transition. Furthermore, the rate of the non-adiabatic crossing between the potentials of two distinct states depends not only on the coupling matrix elements but also on the density of states in the final potential. As the density of states in the  $S_{ICT}$ -potential increases with increasing energy, this effect further accelerates the rate of  $S_1 \rightarrow S_{ICT}$ -transition and - in turn - shortens the associated time-constant  $\tau_2$ .

### 5.3.3 Picosecond time-resolved fluorescence

In order to further corroborate the suggested model for the excited state relaxation processes and to add to a detailed description of the light induced ultrafast processes of PChla, the results of picosecond time-resolved fluorescence measurements are presented. The picosecond time-resolved fluorescence measurements were performed in the laboratory of the group of Prof. Villy Sundstrom at the Department for Chemical Physics at Lund University. The experimental setup employed for the experiments is described in section 3.4. The time-resolution obtained was as good as  $\leq 2$  ps and thus being sufficient to observe the processes associated with  $\tau_1$ ,  $\tau_2$  and  $\tau_3$ . For the measurements, that were performed in backward scattering geometry, the sample was placed into a rotating cuvette in order to avoid sample damage. The integrity of the sample was checked repeatedly by measuring steady-state absorption spectra. Excitation into the Soret-band at 398 nm was chosen for technical reasons as the Q-band absorption was not accessible with the experimental setup used. Nonetheless, a number of studies focusing on the ultrafast light-induced processes in porphyrins and porphyrin-like systems have consistently shown ultrafast relaxation from the initially populated Soret- into the Q-band manifold (see chapter 5.2 and references [98, 109, 127–131]), thus with will have relaxed into the  $S_1$  state manifold within the best accessible time-resolution of the streak camera.

The experimental data clearly reveals two fluorescence components with emission maxima at 640 and 655 nm, respectively. While the first component appears within the time-resolution of the experiment and decays with a time-constant of 27 ps, the latter contribution exhibits a 4 ps-rise prior to a 3.5 ns lifetime. In agreement with the transient-absorption measurements presented above, the fastest 4 ps-component is assigned to cooling within the lowest lying Q-band, while the 27 ps-component is associated with the depopulation of a distinct, rapidly populated blue-emitting state; the latter state being in turn deactivated into the  $S_{ICT}$ -state, which is found to be non-fluorescing.

#### Results of time-resolved fluorescence measurements

Figure 5.21 displays the fast time-evolution of the fluorescence spectrum of PChla dissolved in methanol. The times given in the inset refer to the relative delays with respect to the fluorescence maximum at 641 nm. An initial rise of the spectra was found to within the time-resolution of the streak camera settings used in this experimental run. Nonetheless,

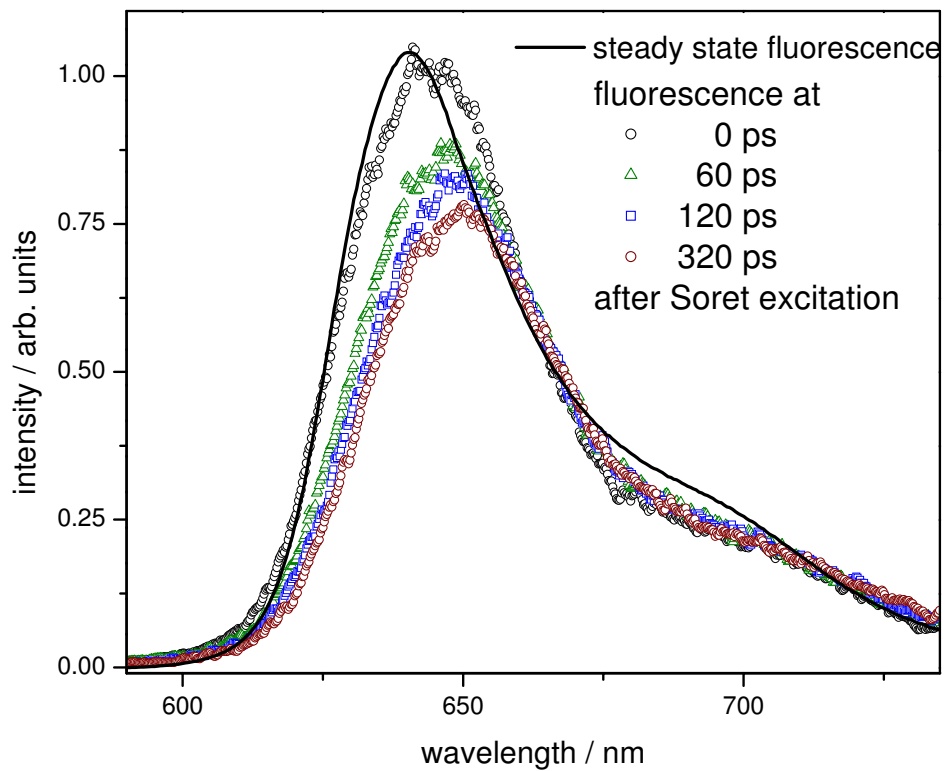


Figure 5.21: Fluorescence spectra upon photo-excitation into the Soret-band ( $\lambda_{exc} = 398$  nm) are shown for various waiting times after light absorption. The corresponding times are indicated in the legend. For comparison the steady-state fluorescence spectrum is shown as well.

the shift of the spectral maximum to the red for increasing waiting time can clearly be observed. While the maximum of the fluorescence at 0 ps is found to be at 644 nm, it gradually shifts towards lower absolute wavenumbers and is observed at 651 nm at 320 ps. It should be noted, that on the other hand, the shoulder at around 700 nm does not diminish in concert with the observed decrease of the fluorescence at 640 nm. This is surprising, if one assumes that the shoulder is due to a vibrational progression of the principal emission. In this case, it should be expected to decrease proportionally with the principal transition. However, unlike the blue side of the fluorescence band, the fluorescence intensity on the red flank of the band does not change over the time-interval of the first 320 ps indicating that its appearance is not due to a simple progression of the main transition.

In order to quantitatively evaluate the time-evolution of the fluorescence, spectral cuts along the time-axis of the three dimensional streak camera data are shown in figure 5.22. The kinetics reflecting the time-evolution of the red flank of the fluorescence peak at 695 nm displays a short instrumentation limited (FWHM of experimental response 40 ps) rise-time and a subsequent quasi-constant signal reflecting the long-lived fluorescence with a time-constant larger than 3 ns. In contrast, transients monitoring the blue side of the fluorescence peak exhibit a short decay-component. This finding reflects the observation of an initial red-shift of the overall fluorescence spectrum as present in the spectra shown in figure 5.21.

In order to gain insight into the excited state relaxation pathways as mirrored in the time-dependent fluorescence spectra the transients presented in figure 5.22 were fitted to the convolution of the experimental response and a sum of two exponential-functions. The quantitative analysis of the transients resulted in two well separated time-constants  $\tau_1 \leq 40$  ps and  $\tau_2 \geq 3.0$  ns. The relative contribution of the fast  $\tau_1$ -process increases from zero at 695 nm to about 64% at 625 nm. While the value of  $\tau_1$  given here is limited by the time-resolution of the streak camera in the particular operation mode employed, the accuracy of  $\tau_2$  can be enhanced by measuring time-resolved fluorescence in a larger time window. This approach using data acquisition up to 20 ns after photo-excitation yields values of  $\tau_2$  ranging from 3.32 to 3.50 ns depending on the particular spectral position within the fluorescence band. Thus, these values are in good agreement with the fluorescence lifetime of PChla in methanol as reported in [110]. To obtain a precise value of the short fluorescence component we measured the fluorescence in the blue part of the spectrum (600 to 630 nm) with a time-resolution of 2 ps (FWHM of the experimental response). The resultant trace

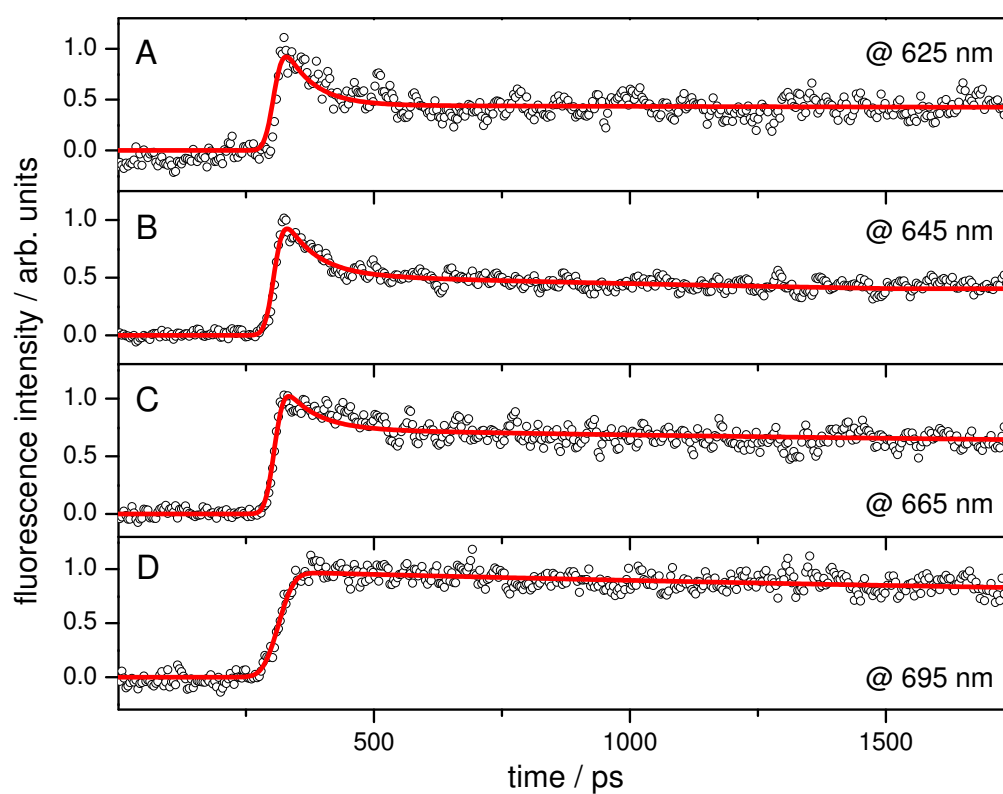


Figure 5.22: Time-resolved fluorescence traces of protochlorophyllide a dissolved in methanol are depicted for various spectral positions. Symbols represent data points while solid lines refer to fits.

is plotted in panel A of figure 5.23: An instrumentation limited rise is followed by a decay, whose characteristic time-constant is fitted to 27 ps. This fast component contributes to 67% to the overall fluorescence signal and is accompanied by a 3 ns-component.

In contrast, when monitoring the red part of the fluorescence in the spectral region 660 to 700 nm the approach to fitting the data as outlined above fails. Panel B of figure 5.23 shows the corresponding time-resolved fluorescence data together with the experimental response function and two different fit results. The blue line refers to a fit employing the function used for fitting the data shown in panel A of figure 5.23, i.e. an instrumentation limited rise is followed by a 27 ps-decay. Though this approach holds for the blue part of the fluorescence, in the red part of the spectrum the fluorescence seems to appear delayed. In order to account for this qualitative finding an exponential rise of the form  $1 - \exp(-t/\tau_{rise})$  is included into the fitting function, leading to the fit shown as black line in figure 5.23B. As can be seen, when implementing an additional rise-component with  $\tau_{rise} = 3.5$  ps, the agreement between data and fit is excellent. Thus, the red part of the fluorescence occurs delayed by approximately 4 ps and shows a lifetime of  $\sim 3$  ns, while the blue fluorescence appears within the time-resolution of the streak camera in its fastest mode ( $\leq 2$  ps) and exhibits a fast 27 ps-component in addition to the long lived ns-fluorescence.

The component spectra of the 27 ps- and the ns-component are shown in panel A of figure 5.24, while the panels B to F display representative cuts at particular wavelengths employed to construct the component spectra. The overall features reflected in the component spectra can yet be seen easily when comparing the time-resolved traces. While in the red part of the spectrum no 27 ps component is present, the short component dominates the time-behavior for example at 621 nm with a relative contribution of 60%. This qualitative examination translates into the component spectra shown in figure 4A. It can be seen clearly that two distinct fluorescence bands can be assigned to the decay components. The ns-component shows a fluorescence maximum at 655 nm and extends from the blue side of the fluorescence band to the red side of the spectral range of our measurement, while the 27 ps-component exhibits its emission maximum at 640 nm and is therefore  $358\text{ cm}^{-1}$  blue shifted compared to the ns-component. The absence of any short decay in the time-resolved red fluorescence traces is reflected by the amplitudes of the 27 ps-component to be zero for wavelengths longer than approximately 670 nm. It should be mentioned, that in agreement with other literature on porphyrin fluorescence (see e.g. [98]) an additional fluorescence band was present in the data. This additional band was found to have its



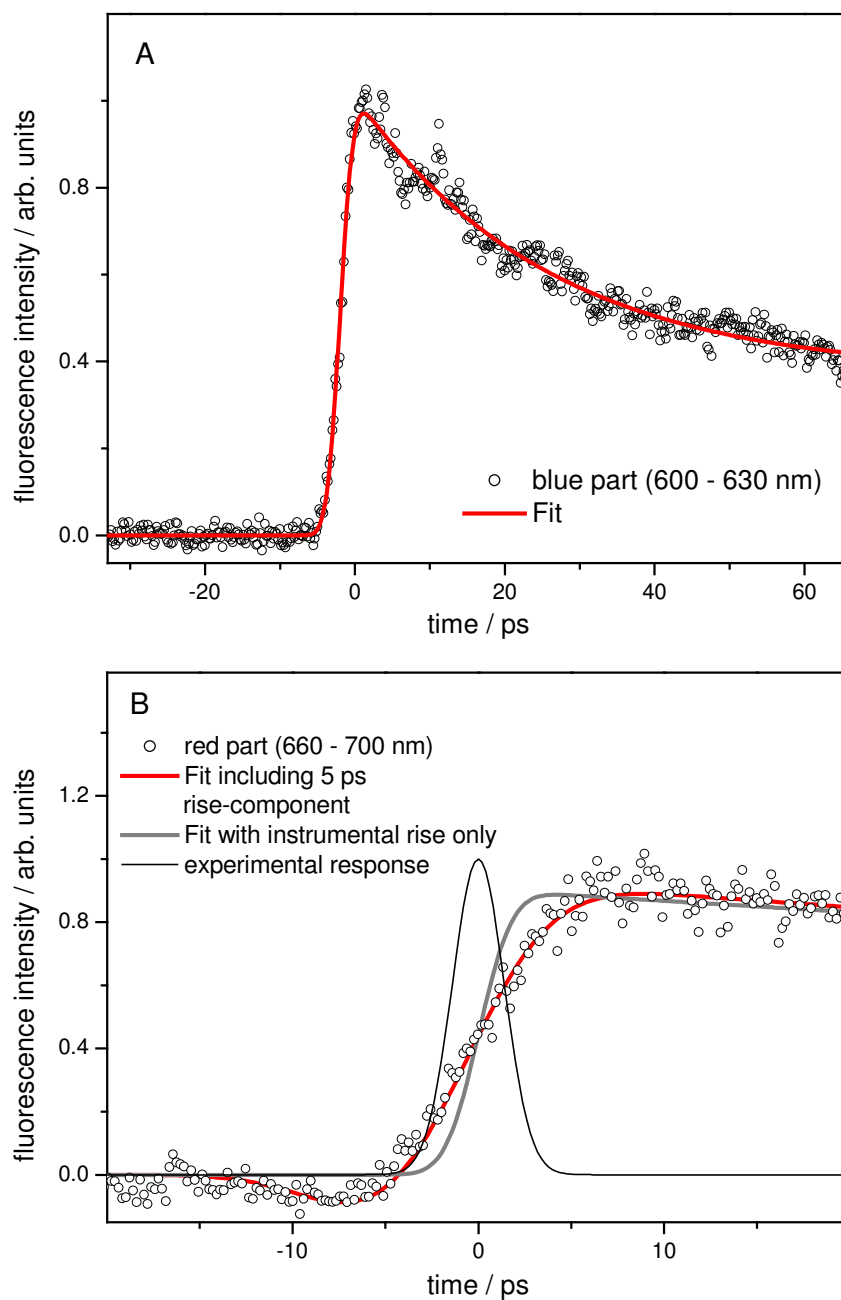


Figure 5.23: Panel A. Fluorescence decay integrated over the spectral region 600 to 630 nm is shown as symbols together with the result of a least square fit (solid line). Panel B. displays the time-resolved fluorescence integrated from 660 to 700 nm (circles) together with the result of a fit including a ps-rise component (red line). For comparison the instrumental response function is shown (thin black line) together with a fit that excludes an additional exponential rise-term (blue line). For details see text.

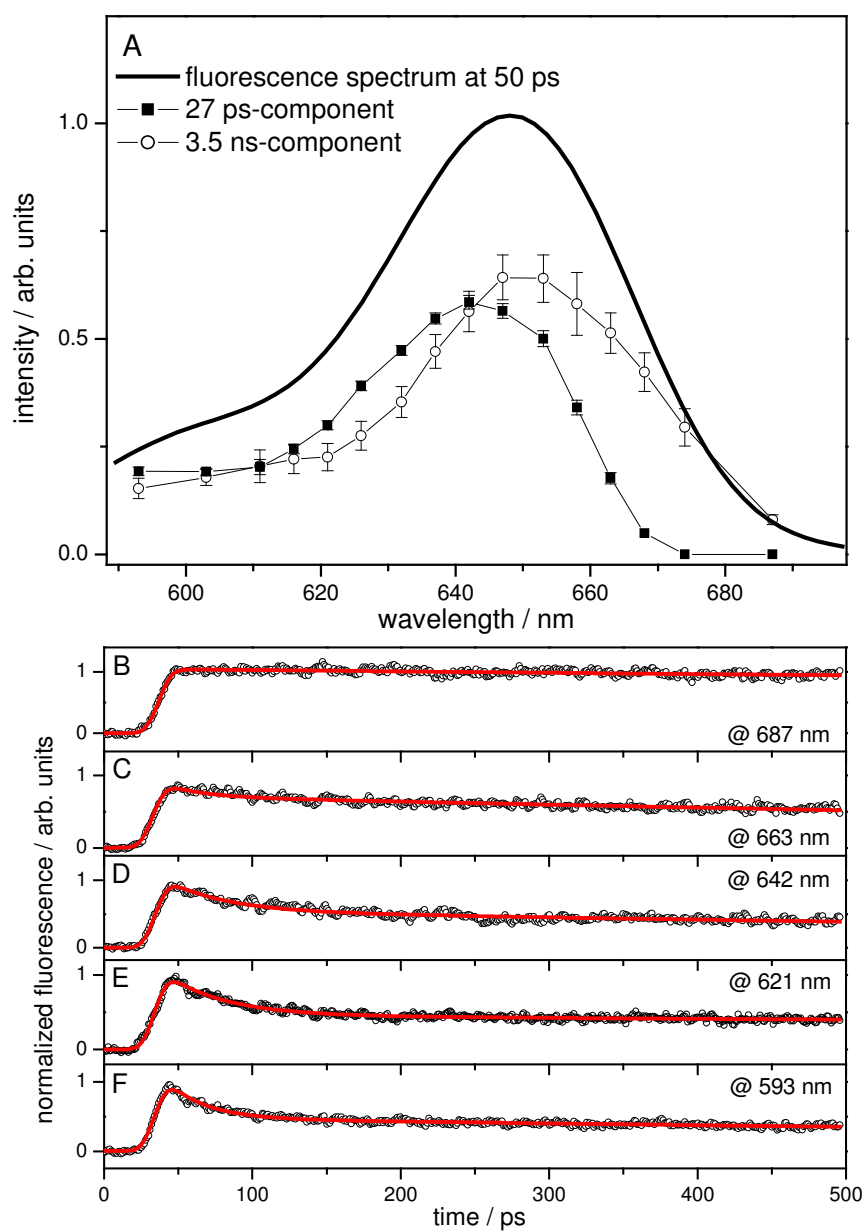


Figure 5.24: Panel A shows the individual fluorescence component spectra of the 27 ps- and the ns-component of protochlorophyllide *a* dissolved in methanol. Panels B to F present exemplary transients used to construct the component spectra displayed in panel A.

emission maximum at 560 nm and displays a time-dependent behavior identical to the one of the fluorescence in the spectral region 600 to 630 nm (see also figure 5.25).

In excellent agreement with the data presented in chapter 5.3, the time-constants associated with the 4 ps-rise and the 27 ps- as well as the 3.5 ns-decay components have been found in the femtosecond time-resolved transient absorption data reflecting the excited-state relaxation processes of PChla dissolved in methanol as well [56,132]. In these measurements PChla was excited into the lowest lying Q-band. Nonetheless, the same time-constants are observed indicating that the processes associated with these time-constants can be assigned to the  $S_1$ -state manifold. However, in order to obtain a full description of the transient absorption measurements, the inclusion of a 200 ps-component into the model is necessary. The absence of the latter component in the time-resolved fluorescence data is striking. When monitoring the excited-state relaxation processes in PChla as a function of solvent, it was found that the overall relaxation pattern is strongly solvent polarity dependent (see section 5.3.2 and [132]). While in the polar solvents methanol, acetonitrile and glycerol a multi-exponential fit yields the above listed time-constants, PChla dissolved in the unpolar solvent cyclohexane displays a mono-exponential decay-pattern upon photo-excitation into the lowest lying Q-band. In the unpolar environment the 27 ps- and 200 ps-components are absent and only two processes associated with the 4 ps- and the ns-time-constant are observed (see section 5.3.2). Therefore, we investigated the time-dependence of the PChla-cyclohexane fluorescence upon excitation into the Soret-band in order to deduce the influence of the solvent polarity on the overall fluorescence appearance. Representative fluorescence transients obtained for PChla-cyclohexane are presented in figure 5.25.

Panel A of figure 5.25 compares the time-dependent fluorescence intensity integrated from 600 to 640 nm with the fluorescence observed in the red flank of the overall emission spectrum together with the results of the respective fits. While the blue part of the fluorescence rises instantaneously within the instrumental response of the streak camera, the red fluorescence appears delayed and stays constant within the entire time-window of 100 ps employed in the measurement. The delayed rise was simulated by a 3.5 ps-component in addition to the experimental response. Based on the transient absorption data (see sections 5.3.1 and 5.3.2) it is expected to observe a 4 ps component only, when recording the time-evolution of the PChla-cyclohexane fluorescence. However, when monitoring the decay of the blue part of the fluorescence a 26 ps-decay component followed by a ns-contribution is observed. The latter manifests itself as a constant signal within the range of times ac-

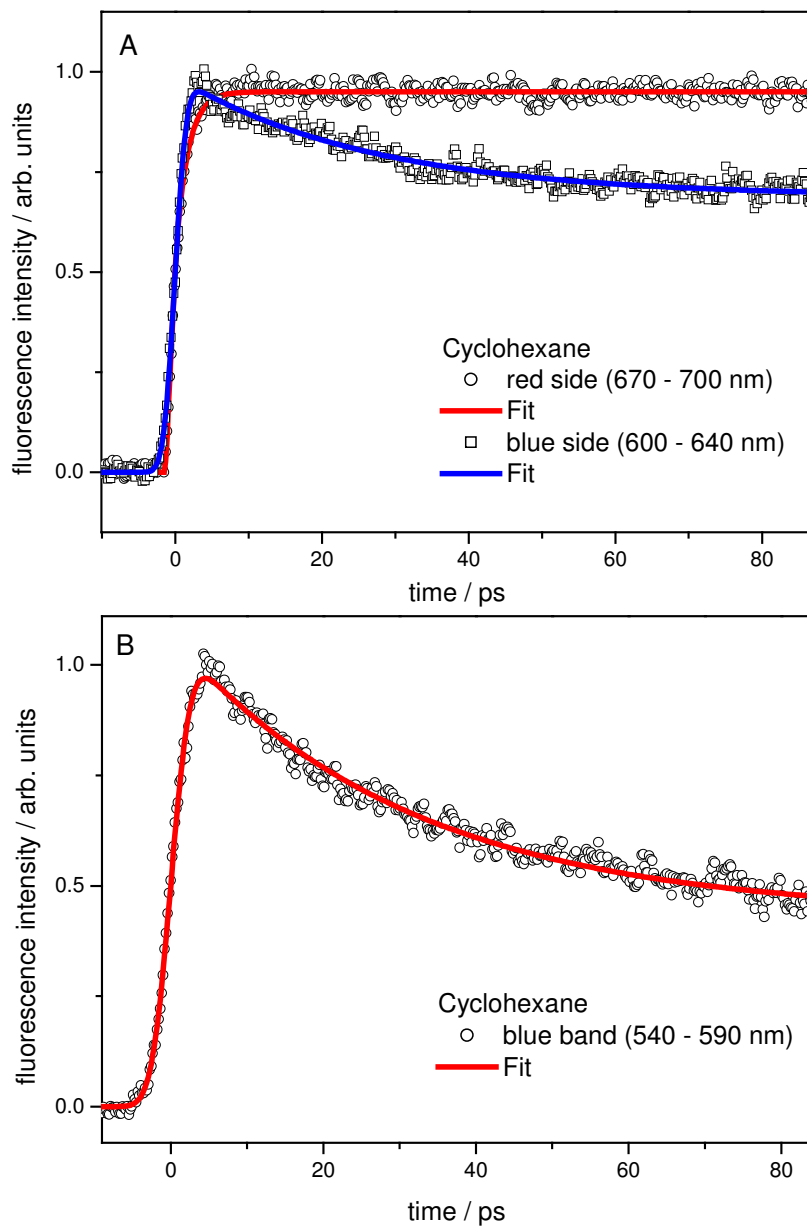


Figure 5.25: Time-resolved fluorescence data for protochlorophyllide *a* dissolved in cyclohexane. Symbols represent data and solid lines refer to results of fits. Panel A compares the short time behavior of the fluorescence spectrally integrated from 670 to 700 nm and from 600 to 640 nm. Panel B. The time-evolution of the < 600 nm fluorescence band is shown.

cessible in this measurement and its characteristic time-constant was fitted to be 3.11 ps from measurements within a larger time-window. Thus, the data presented in figure 5.25 resembles identical features as the data shown in figure 5.25 obtained for PChla dissolved in methanol. Hence, the use of cyclohexane to dissolve PChla leads to overall identical time-resolved fluorescence data as for the solvent methanol. This is particularly interesting when recalling that the excited-state relaxation pathway upon photo-excitation into the lowest lying Q-band was found to be drastically altered in the unpolar cyclohexane environment [132]. The fact, that the PChla-cyclohexane fluorescence exhibits the same overall decay features as PChla-methanol is due to the fact, that for the fluorescence experiment excitation was performed at 398 nm and thus within the  $S_0 \rightarrow S_2$  transition. Therefore, 1.13 eV of additional energy are deposit into the molecular system leading to different decay channels available for the molecules and resulting - after internal conversion - in vibrational highly excited  $S_1$  molecules. The excess energy delivered to the molecular system is enough to overcome the solvent induced barrier and thus population flow into the  $S_{ICT}$  state can be observed in the fluorescence kinetics of PChla-cyclohexane. (Panel B of figure 5.25 displays a trace reflecting the time-evolution of the above mentioned additional fluorescence band at 560 nm. The time-dependence of the fluorescence exhibits the same characteristics as the blue part of the main fluorescence band ( $\geq 600$  nm): An initial instrumentation limited rise is followed by a fast decay ( $\tau_1 = 31$  ps) and long-lived fluorescent component.)

### Discussion and refined model

The interpretation of the time-resolved fluorescence data in the context of the transient absorption data presented above starts from the finding of different decay characteristics of the red and the blue part of the fluorescence. As mentioned, the long wavelength part of the emission (see figure 5.21) cannot be explained by means of a progression of the principal transition, because following this assignment one fails to explain why the progression does not decay proportionally to the fundamental transition. This result leads to the conclusion that the observed fluorescence originates from two distinguished excited singlet states, referred to as *blue-emitting* and *red-emitting* state from here on. These states are energetically separated by approximately  $360\text{ cm}^{-1}$ , the difference of the emission maxima of the 27 ps- (at 640 nm) and the ns-component spectrum (at 655 nm). While the population of the blue-emitting state occurs within the time-resolution of the measurements presented

here ( $\leq 2$  ps), the population flow into the red-emitting state can be time-resolved and manifests itself as the 3-4 ps rise-component present in the traces reflecting the evolution of the red-part of the fluorescence. In contrast to the blue-emitting state, which has a lifetime of only  $\sim 27$  ps, the red-emitting state decays with about 3.5 ns.

Based on transient absorption data presented above (see also [56, 132]) the 4 ps-component is assigned to cooling within the  $S_1$ -state. As the 4 ps-process proceeds the longwave fluorescence the red-emitting state is associated with the  $S_1$ -state being initially photo-excited in the transient absorption experiments [56, 132]. Therefore, the initial build-up of the red fluorescence is assigned to energy dissipation within the lowest lying Q-band. In contrast to the transient absorption measurements, in which direct Q-band excitation is employed, the data presented in this contribution was obtained upon photo-excitation into the Soret-band. Nonetheless as shown for MgOEP (see section 5.2), it is known for porphyrin systems that Soret  $\rightarrow$  Q-band relaxation occurs on an ultrafast time scale [21, 98, 109] and therefore occurs within the time-resolution of our streak camera response. Thus, the ultrafast relaxation from the higher lying  $S_2$ -state into the  $S_1$ -manifold is not visible in the time-resolved fluorescence data and all processes being evident in the data presented here are assumed to take place within the  $S_1$ -manifold. As the blue-emitting state displays distinct spectral and decay features that cannot be explained based on a simple emission progression, it has to be deduced that the population of this state has to be complete within the ps-time resolution of the streak camera. Furthermore, as the formation of the blue-fluorescence proceeds the 27 ps-component, which is assigned to the decay of the respective emission component and is seen in the transient absorption data as well [56, 132], the population of the blue-emitting state should be visible in the transient absorption data, if it occurs on a sub ps time-scale. As no such component is visible in the transient absorption data, it must be concluded, that the formation of the blue-emitting state does not only occur faster than the resolution of the streak camera but also within the time-resolution of the transient absorption measurements and thus within the first 100 fs after photo-excitation.

The 27 ps-component was assigned to the population of a state possessing intramolecular charge transfer characteristics ( $S_{ICT}$ -state) [117, 118, 132]. As the origin of this component a keto- enol- tautomerization can be ruled out based on the finding, that the acidity of the solvent does not influence the excited-state relaxation (see section 5.3.2). As the 27 ps-component also correlates with the deactivation of the blue-emitting state, this state is assigned to be the parent-state of the  $S_{ICT}$ -state, which was found to have a

lifetime of about 200 ps according to the transient absorption results [56, 132]. As no 200 ps-component is present in any of the time-resolved fluorescence data, it is concluded that the  $S_{ICT}$ -state of PChla does not fluoresce but is deactivated back into the ground state via an internal conversion process instead. The origin of the 27 ps fluorescence component in the case of the solvent cyclohexane remains to be considered, because its appearance is noticeable recalling the absence of this component in the transient absorption measurements. Nonetheless, the excitation for the fluorescence measurements was carried out into the Soret-band unlike in the transient absorption measurements, in which the molecules were photo-excited into the lowest lying Q-band. Therefore, it is assumed that the molecules upon photoexcitation into the  $S_2$ -state relax into higher lying vibrational levels within the blue-emitting state, thus possessing enough energy to further relax into the  $S_{ICT}$ -state and not being hindered by its energetically increased potential minimum.

### 5.3.4 Proposed model

Thus, in combining the results of femtosecond time-resolved transient absorption spectroscopy and the fluorescence data, the following model is suggested to account for the observed photophysics: Photo-excitation of PChla into the Soret-band leads to an ultrafast relaxation of the  $S_2$  state into the  $S_1$ -manifold. The rapid internal conversion populates the high lying vibrational levels of the lowest lying  $S_1$  state and - most likely - simultaneously places molecules into the blue-emitting  $S_1$  state, that is referred to as  $S_x$  in figure 5.26. In the  $S_1$  potential, part of the molecules undergo cooling in the Q-band and subsequent fluoresce back to the ground state. In contrast, the majority of the molecules is promoted out of the vibrational excited states of the  $S_1$  potential into the blue-emitting state ( $S_x$ ) within the first 100 fs after light absorption. (The upper limit for the relaxation time can be estimated from the fact that no build up of the absorption of this state could be observed within the time-resolution of the transient absorption measurements.) The characteristically blue-shifted fluorescence of this state decays within 27 ps reflecting the population flow into the non-emitting intramolecular charge transfer state, which in turn internally converts back into the ground state with a time-constant of 200 ps as determined from transient absorption measurements [56, 132]. Therefore, two relaxation pathways within the  $S_1$ -manifold of PChla can be distinguished: The first one containing a 4 ps and a 3.5 ns-step, which we refer to as the non-reactive pathway for reasons that will be discussed below. The second channel,

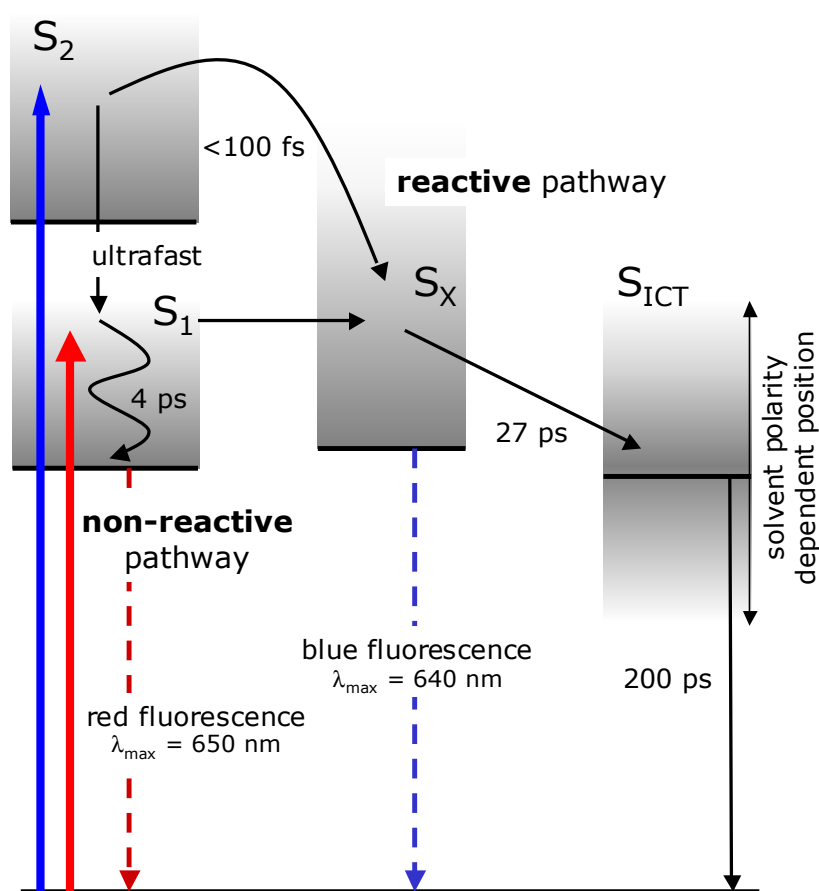


Figure 5.26: The model suggested to account for the excited state relaxation processes in protochlorophyllide *a* upon photo-excitation is presented.



we refer to as reactive channel, comprises a multi-step relaxation with a sub-100 fs initial step and subsequently a 27 ps- and 200 ps-component. The latter component shows a close kinetic similarity with the 400 ps component observed in the light induced enzymatic reduction of protochlorophyllide a to chlorophyllide a [95]. This leads to the speculation that the  $S_{ICT}$ -state, whose characteristics are observed, is involved in the natural enzymatic reaction. This would explain the close proximity of the observed lifetimes for this state depending on the environment; i.e. 400 ps in the enzymatic environment leading to the biologically favored reaction product chlorophyllide a (Chla) on the one hand and 200 ps for the free chromophore in alcoholic solution on the other hand. Therefore, we assign the term reactive pathway to the relaxation channel involving the  $S_{ICT}$ -state and label the Q-band relaxation followed by fluorescence as non-reactive pathway. This assignment might be further corroborated by the decisive role the cyclopentanone ring seems to play in the photophysics of PChla [132]. When investigating the light-induced excited state processes in the model substance MgOEP, in contrast to the structurally similar PChla, no significant excited-state dynamics are found when directly exciting the porphyrin into the  $Q_{00}$ -band (see section 5.2 and [21]). This finding is contrary to the rich photophysics of PChla upon excitation into the lowest lying Q-band, which as the decisive structural feature has an attached cyclopentanone ring to the porphyrin macrocycle. This might lead to the conclusion that possibly the cyclopentanone ring is of significant relevance for the ultrafast reaction dynamics of PChla. Furthermore, if the charge in the  $I_{SCT}$ -state is localized on the cyclopentanone ring, thus giving rise to the large dipole moment of the state required to be destabilized in non-polar solvents, this feature would well coincide with reaction mechanisms proposed to account for the enzymatic reduction of PChla to Chla. Klement et al. suggested an  $H^-$  attack at the porphyrin macro cycle [115, 116, 121], which would be facilitated, if the electron density in the cyclic  $\pi$ -system would be reduced by a relaxation step resulting in a charge localization on the cyclopentanone ring. Thus, it seems to us, that  $I_{SCT}$ -state might play a crucial role in understanding the biophysical properties of the enzymatic chlorophyllide a formation and thus the photophysics of the free educt PChla.

### 5.3.5 Conclusions

This chapter presented femtosecond time-resolved pump-probe data and time-resolved fluorescence measurements on protochlorophyllide a upon excitation into the lowest lying Q and the energetically much higher lying Soret-absorption band. The time-resolved experiments allow to suggest a detailed model of the excited state relaxation processes in photo-excited protochlorophyllide a. The overall relaxation pattern could be separated into two distinct relaxation pathways, one of which includes cooling within the Q-band and subsequent red fluorescence, which decays with a 3.5 ns time-constant. In contrast, the reactive pathway includes the rapidly populated blue-emitting state and a state possessing intramolecular charge transfer character. The latter state is populated within 27 ps and decays non-radiatively within 200 ps back to the ground state.

By comparison of the model explaining the light induced excited state processes of protochlorophyllide a to the models suggested to account for the enzymatic reduction of protochlorophyllide a to chlorophyllide a in the enzyme protochlorophyllide-oxidoreductase [115,116,121], the 4 ps-relaxation followed by ns-fluorescence is assigned to be a non-reactive relaxation pathway. In contrast, it can be supposed that the formation of an intramolecular charge transfer state proceeds the product formation in the naturally abundant reaction and thus label the excited state relaxation pathway, which includes ultrafast preparation of the blue-emitting state and subsequent population of the non-fluorescent intramolecular charge transfer state, as reactive pathway. Therefore, the time-resolved fluorescence and transient absorption data presented in this chapter allowed to gain detailed insight into the light-induced relaxation processes of protochlorophyllide a and suggest a detailed model of the excited state processes of this particularly interesting biologically relevant chromophore.

## Part III

# Artificial Systems

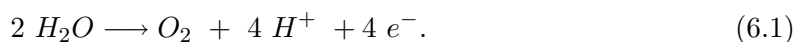


## Chapter 6

# Introduction and Motivation

Today fossil materials such as oil and gas are the main sources of energy, keeping the world's economy running. Nevertheless, the world's oil resources will be exploit in a time-frame of about 100 years. If nothing else, this fact constitutes the urgent necessity to search for alternative sources of energy. Ideally, a new widely used energy source should not rely on limited but on renewable resources and furthermore should be clean to the environment. Flowing water and wind are - by now - quite commonly used to produce electricity, but neither of these sources directly provides energy to be used directly as fuel for cars or aircrafts, for example. Nevertheless, sunlight, the third natural source of renewable energy, might be able to not only produce electricity in photovoltaic cells but also hydrogen in a photosynthetic process, which subsequently might be used as a replacement for conventional gas. Therefore, immense and growing effort is taken to understand the functionality of natural photosynthetic reaction centers and to design and characterize artificial photosynthetic systems.

Natural photosynthesis is a sunlight driven process, in which water and carbon dioxide are converted into oxygen and organic compounds in a series of complex reaction steps involving such fundamental processes as energy and electron transfer. A key step in photosynthesis is the splitting of of water, resulting in oxygen, protons and electrons,



In natural photosynthesis occurring in green plants both hydrogen ions and electrons produced are re-used in the complex process of producing organic material, whereas

oxygen is not and released from the plants. The basic idea of artificial photosynthesis is not to produce oxygen or organic material but to provide hydrogen in a water splitting reaction.

In order to outline the demands for a man-made system to be related to artificial photosynthesis, the initial steps in natural photosynthesis are briefly outlined. As stated above, natural photosynthesis is a sunlight driven process, which initiates with the absorption of light in the leaves of plants. To spatially direct the absorbed energy to the geometrical point, where the chemical reaction takes place, the so called *reaction center*, light harvesting (LH) antennas are employed. The functionality of LH antennas is closely related to their structure, which was published in 1996 for the model antenna systems of purple bacteria [133,134]. As this system, whose schematic structure is shown in figure 6.1, is well characterized and understood, the following brief outline of the principle functionality of LH antennas is oriented on the light-harvesting system of purple bacteria.

The structure of the peripheral antenna complex LH2 as reported for *Rhodospseudomonas acidophila* [134] consists of two bacteriochlorophyll (BChl) rings of different lengths and nine carotenoids, which mainly fulfill a photoprotective function though a minor part of the incident sunlight is absorbed by them. The main part of the light harvesting function is carried by the BChl-rings, one of which consisting of nine BChl units (called B800 - due to its strong absorption maximum centered at 800 nm) while the other one is constituted by 18 BChls. The latter one exhibits maximum absorbance at 850 nm and therefore is referred to as B850. The energy absorbed by B800 travels around in the ring for about 500 fs before it is transferred to the B850 ring. This step is characterized by a time-constant of 1.3 ps. From there the energy migrates to the central LH1 complex within 3-5 ps. The LH1 complex itself is centered around the reaction center to which the energy is finally transferred in less than 50 ps [135]. The cyclic arrangement of the BChls in the LH2 systems ensures that disregarding, where in the ring the initial light-absorption takes place, the energy is always directed toward the center of the complex, where the photosynthetic reaction takes place.

In order for an artificial system to be viewed as an artificial photosynthetic system or functional part within such a system, some requirements can be formulated:

- light has to be absorbed, preferably over a wide spectral range and with high efficiency,
- the excitation resulting from light absorption has to be transferred to a reaction center within the molecule,

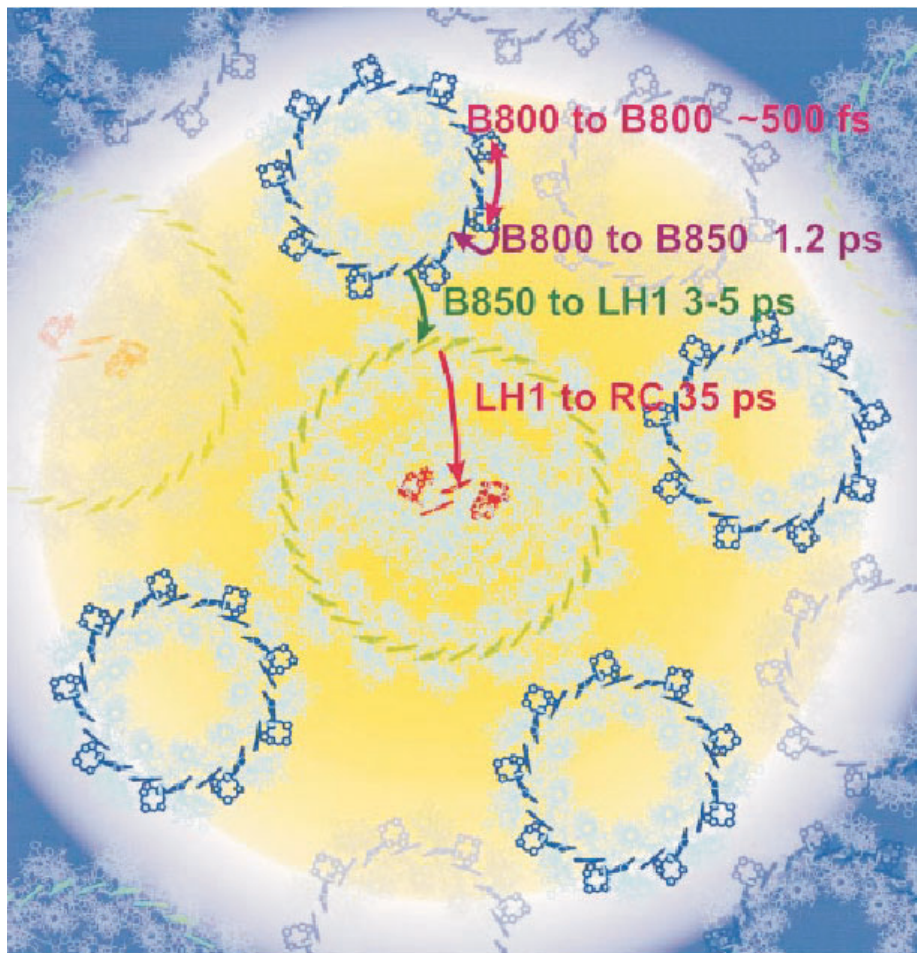


Figure 6.1: The schematic structure of the light-harvesting complex of purple bacteria based on the known structural data of is shown. The bacteriochlorophyll molecules of LH2 (B800 and B850), LH1 and reaction center are blue, green and red, respectively. The structural diameter of about 230 Å is indicated by the background ring. (Figure taken from [14].)

- subsequently the energy is used in the reaction center to initiate a chemical reaction, ideally resulting in the production of hydrogen.

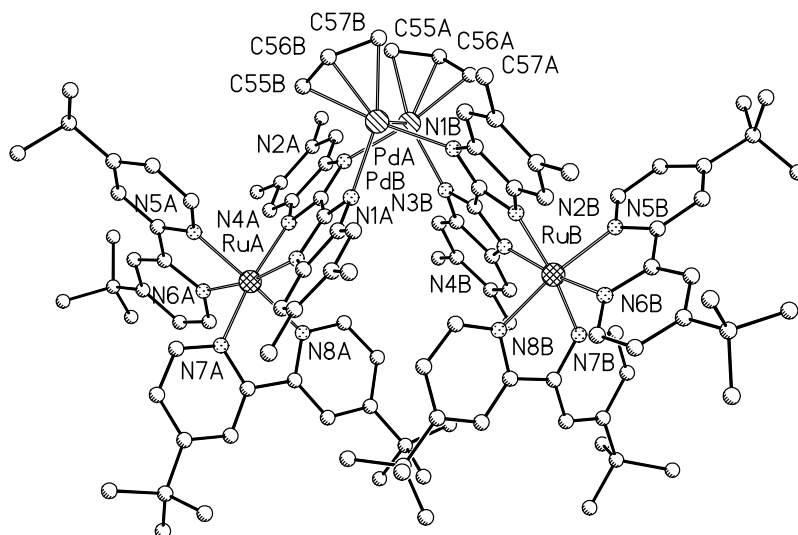


Figure 6.2: The chemical structure of  $[(\text{tbbpy})_2\text{Ru}(\text{tmbi})]_2[\text{Pd}(\text{allyl})]_2 (\text{PF}_6)_2$  as taken from reference [136] is shown.

The system investigated in the course of this work,  $[(\text{tbbpy})_2\text{Ru}(\text{tmbi})]_2[\text{Pd}(\text{allyl})]_2 (\text{PF}_6)_2$ , is much smaller than the natural light-harvesting apparatus outlined above (see figure 6.2) and does not occur to have the characteristic cyclic structure of LH1 and LH2 of purple bacteria. Nevertheless, as will be shown and discussed in detail in the following sections

- the system's absorption spectrum is characterized by a strong absorption in the green part of the visible spectrum,
- the excitation is initially located on the peripheral Ru-units of the complex and subsequently migrates to the central part of the system within 40 ps, where it is located on the Pd centers,
- the excited Pd-centers are speculated to be capable to catalyze the production of hydrogen.



Thus,  $[(\text{tbbpy})_2\text{Ru}(\text{tmbi})]_2 [\text{Pd}(\text{allyl})]_2(\text{PF}_6)_2$  matches the characteristics of a photosynthetic system stated above and can be thought of a small inorganic light-harvesting antenna or as a catalytic switch for the production of hydrogen.

## Chapter 7

# Excited-State Processes in a Quasi-2D Light Harvesting Antenna

A detailed study on the excited-state excitation migration taking place within the tetranuclear complex  $[(\text{tbbpy})_2\text{Ru}(\text{tmbi})]_2[\text{Pd}(\text{allyl})]_2(\text{PF}_6)_2$  is presented in this chapter. The charge transfer is initiated by the photoexcitation into the lowest metal-to-ligand charge-transfer ( $^1\text{MLCT}$ ) band of one of the peripheral Ru(II) chromophores and terminates on the central Pd-subunits. The kinetic steps involved in the overall process are inferred from femtosecond time-resolved transient-grating kinetics recorded at various spectral positions within the spectral regions of ground-state bleach and photoinduced absorption. The kinetics display a complex non-exponential time-behavior and can be fitted to a bi-exponential rise and a mono- or bi-exponential decay, depending on the experimental situation. In order to facilitate the interpretation of the rather complex transient data obtained for this system, transient grating experiments on the peripheral building blocks of the antenna,  $(\text{bbpy})_2\text{Ru}(\text{tmbiH}_2)(\text{PF}_6)$ , and a closely related Ru(II)-complex,  $\text{Ru}(\text{tbbpy})_3^{2+}$ , are presented. In order to extend the time-range during which information can be gained on the excited-state processes to times within the instrumental response of our fs laser system (about 100 fs), resonance Raman (RR) measurements were performed in the group of Professor Popp in Jena. This data provides valuable insight into the role of individual ligands within the peripheral Ru(II)-unit and is cited here. The experimental results lead to the

formulation of a model for the intra-molecular excitation hopping that ascribes intersystem crossing and subsequent cooling to the two fastest among the recorded processes. Following these initial steps charge transfer from the Ru- to the one of the Pd-chromophores is observed. A 220 ps-component that is observed in the ground-state recovery only is attributed to excitation hopping between the two identical Pd-chromophores.

## 7.1 Introduction to Ruthenium polypyridine complexes

The substantial interest in the excited-state-properties of transition metal polypyridine complexes, in particular those that are built of  $d^6$  metals such as Ru(II), is largely motivated by their potential use in photovoltaic devices [137]. Besides their potential applicability in dye-sensitized solar cells, optical data-storage or in molecular devices these systems play a central role in addressing a wide variety of fundamental questions concerning the mechanisms of inter- and intramolecular energy and electron transfer, charge localization, supramolecular chemistry and inorganic light-harvesting [138–143]. The generally accepted frame, in which the excited-state properties of transition metal polypyridine complexes are explained, exploits a very rapid light-induced population of the lowest lying excited triplet-state. Inter system crossing (ISC) from the originally excited singlet state ( $^1\text{MLCT}$ ) to the lowest lying metal-to-ligand charge transfer triplet state ( $^3\text{MLCT}$ ) was found to be extremely fast in most transition metal complexes; in  $\text{Ru}(\text{bpy})_3^{2+}$  (bpy=2,2'-bipyridine) ISC takes place as fast as in sub-100 fs. Thus, the spin-forbidden process of ISC proceeds with unitary efficiency and thus occurs in concert with spin-allowed processes such as internal conversion (IC) and intramolecular vibrational energy redistribution (IVR) in these systems [144–147]. The ultrafast intersystem crossing is due to the pronounced heavy-atom effect in the presence of the central transition metal ion, that induces strong spin-orbit coupling, and a relatively large number of unoccupied excited-states that are available for excitation [144,148,149]. All photophysics of Ru-complexes subsequent to the ultrafast ISC is usually discussed starting from the rapidly populated  $^3\text{MLCT}$  state. However, important exceptions from the above outlined picture have recently been found; Browne et al. have reported on a Ru(II) system, in which the formation of the  $^3\text{MLCT}$  state occurs on a 100 ps time-scale and with a efficiency lower than unity, which is ascribed to the perdeuteration of the polypyridine ligands in the particular species [150]. Another important deviation from this generally accepted picture was found by Sundstrom and coworkers [151]; they report

on the light-induced processes in a multi-centered Ru-Os complex, in which the ISC within the photo-excited Ru-subunit occurs in concert with an extremely rapid ( $\leq 60$  fs) singlet-singlet Ru-to-Os energy transfer. Similar recent results were obtained by Campagna, see reference [152].

Despite the exceptions outlined above, it can be assumed that a description of the photophysical behavior of supramolecular devices based on transition metal polypyridine subunits starting out from a rapid populated  $^3\text{MLCT}$ -state is valid in most cases [145, 153]. The issue of intramolecular charge and energy transfer from one subunit of the system to another is of particular interest in systems that are designed to serve as metal-based light-harvesting antennas [154–158]. Such systems containing more than one metal ion, which are connected via covalently bound aromatic bridges, that can be designed to be quite extended for some systems. These multi-center complexes can be described as basically independent centers between which charge transfer can occur [159, 160], this leading to the intuitive indication of the aromatic bridges as *molecular wires* [161]. In the studies cited above transient absorption spectroscopy, fluorescence up-conversion and time-resolved fluorescence spectroscopy as well as transient anisotropy decay measurements have been exploited to gain a rich variety of information about the excited-state properties of transition metal complexes and the light induced processes in these substances. In the present work, according to literature the first fs-time-resolved four-wave-mixing study on the excited-state processes in Ru-bipyridine based complexes is presented. Transient grating spectroscopy was chosen for this study as it is well established that this coherent technique yields excellent signal-to-noise ratios and thus allows for a very precise fitting of the transient data [20, 136, 162]. In order to facilitate the interpretation of the kinetic data gained by the transient grating method, we performed transient absorption data first. This data was taken with a poor time-resolution and is solely used to obtain spectral information about the excited-states of the investigated complexes. The species under investigation [Bis-(4,4'-Di-tert.butyl-2,2'-bipyridin)-Ru (II)-(5,6,5',6'-Tetramethyl- 2,2'-bibenzimidazol)] as well as [Tris-(4,4'-Di-tert.butyl- 2,2'-bipyridin)-Ru] and the bi-metallic four-center complex Bis-[Bis-(4,4'-Di-tert.butyl-2,2'-bipyridin)- Ru(II)-(5,6,5',6'-Tetramethyl-2,2'-bibenzimidazolyl)]- Bis- [1,3 -Allyl]-Pd(II)Bis-hexafluorophosphat, hereafter referred to as the Ru-complex and Ru<sub>2</sub>Pd<sub>2</sub>-complex respectively, are shown schematically in scheme 1. (tbbpy)<sub>2</sub>Ru(tmbiH<sub>2</sub>)(PF<sub>6</sub>)<sub>2</sub> and the structure of the reference compound Ru(tbbpy)<sub>3</sub><sup>2+</sup> are displayed in panel A, while the peripheral building block of the tetranuclear antenna [(tbbpy)<sub>2</sub>Ru(tmbi)]<sub>2</sub>[Pd(allyl)]<sub>2</sub>(PF<sub>6</sub>)<sub>2</sub>

is sketched in panel B. The substances under investigation were synthesized in the group of PD Dr. Sven Rau and Prof. Dr. Dirk Walther in the Institute of Inorganic Chemistry at the University of Jena [163–165].

The discussion of this chapter is organized as follows: First, the data obtained for the Ru-complex, which constitutes one of the chromophoric centers of the Ru<sub>2</sub>Pd<sub>2</sub>-complex is presented and discussed. It is investigated in order to facilitate the interpretation of the data obtained for the Ru<sub>2</sub>Pd<sub>2</sub>-complex, which is done subsequently. In order to supplement the discussion transient kinetics observed for Ru(tbbpy)<sub>3</sub><sup>2+</sup>, which structurally differs from [(tbbpy)<sub>2</sub>Ru(tmbiH<sub>2</sub>)]<sup>2+</sup> by the replacement of the bridging tmbiH<sub>2</sub>-ligand with the tbbpy-ligand, is added to the argument. To address the question which particular ligand is involved in the process of photo-excitation, it is referred to the RR measurements performed in the group of Prof. Popp at the Institute for Physical Chemistry in Jena. The discussion of the photophysical properties of the Ru<sub>2</sub>Pd<sub>2</sub>-complex focuses on the multi-exponential charge transfer process that moves the excitation originally located on the Ru-chromophore to the Pd-center. Thus, as mentioned, the complex can be viewed as a model system for a small inorganic antenna system, as the excitation initially located on the peripheral Ru-chromophore is effectively transferred to the central Pd-groups. However, in contrast to other inorganic or natural light-harvesting-systems the energy trap, the Pd-subunit, is not surrounded by the light-harvesting, the Ru-subunits, in three dimensions but rather placed in the middle and therefore quite accessible (the X-ray data shows that the complex is not flat its more like the roof of a house with the palladium unit being the roof ridge [164]). Thus, the system [(tbbpy)<sub>2</sub>Ru(tmbi)]<sub>2</sub>[Pd(allyl)]<sub>2</sub>(PF<sub>6</sub>)<sub>2</sub> is considered to be an extremely interesting model of an inorganic-antenna system.

## 7.2 Excited-State Dynamics in (tbbpy)<sub>2</sub>Ru(tmbiH<sub>2</sub>)

First, as a basis for the discussion of the photophysical processes occurring in the Ru<sub>2</sub>Pd<sub>2</sub>-complex the excited-state processes observed in the Ru-complex, that constitutes the peripheral building blocks of the larger tetranuclear complex, will be discussed.

The absorption spectrum of the Ru-complex is shown in figure 7.2 together with its fluorescence and the fluorescence excitation spectrum. The complex spectral properties observed in transition metal complexes are due to the fact that a number of both singlet and triplet states contribute to the spectral characteristics of these species. The strong

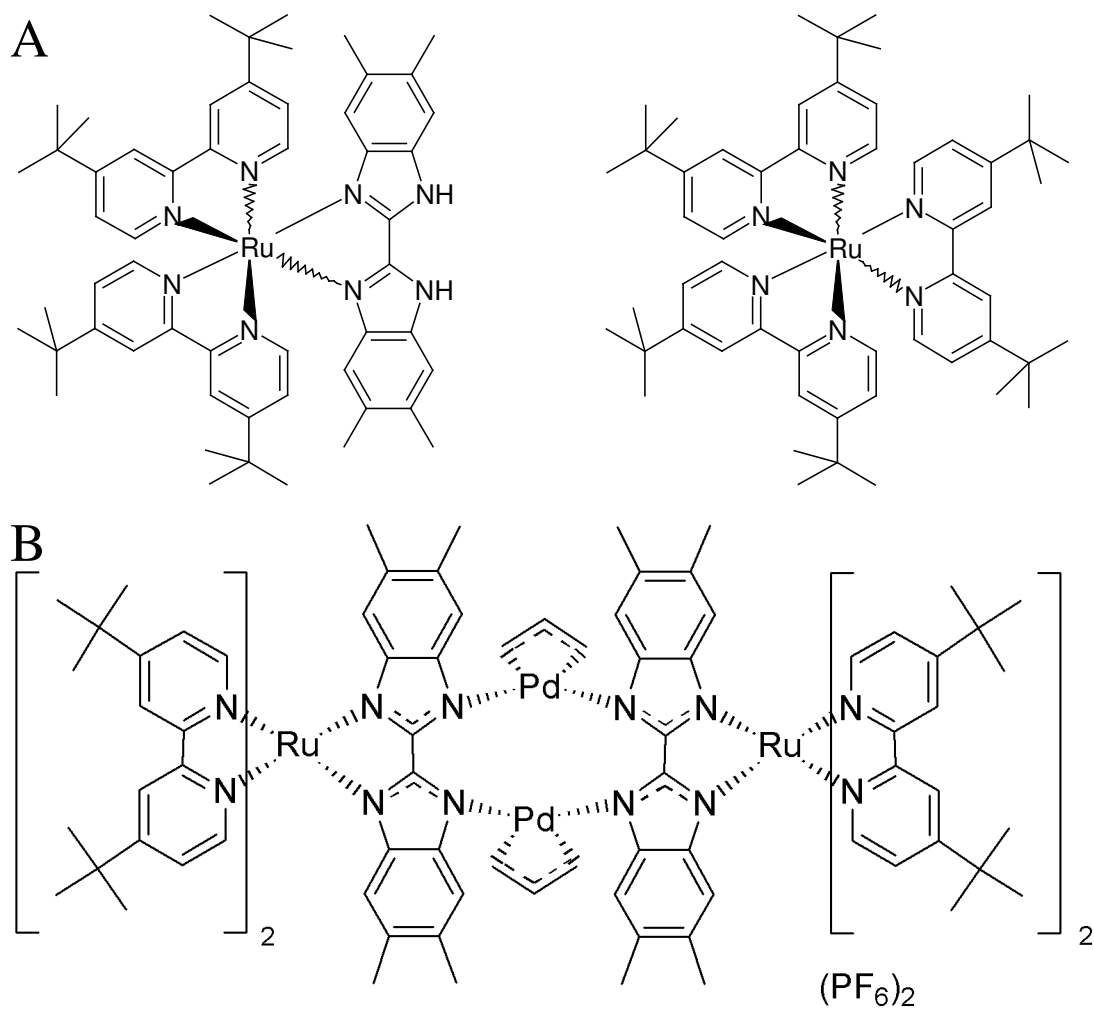


Figure 7.1: The chemical structures of the investigated species are compared. Panel A displays  $(tbbpy)_2Ru(tmbiH_2)(PF_6)_2$ , the peripheral building block of the antenna, in comparison with  $Ru(tbbpy)_3^{2+}$ . The structure of  $[(tbbpy)_2Ru(tmbi)_2[Pd(allyl)]_2](PF_6)_2$  is shown in panel B.

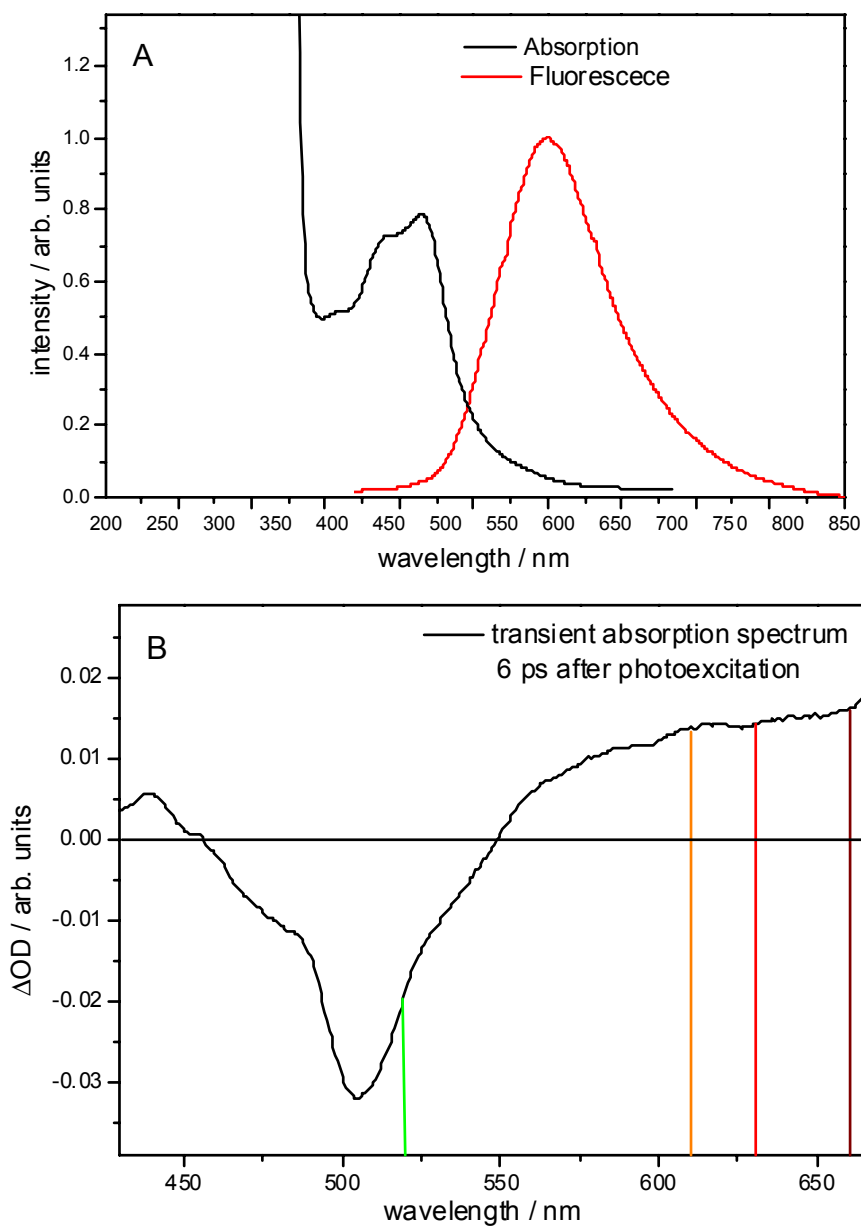


Figure 7.2: Panel A displays the steady state absorption-, fluorescence- and fluorescence excitation spectrum of  $(\text{tbbpy})_2\text{Ru}(\text{tmbiH}_2)$ . The fluorescence was excited at 460 nm and when recording the excitation spectrum the fluorescent intensity was monitored at 650 nm. Panel B shows the transient absorption spectrum of  $(\text{tbbpy})_2\text{Ru}(\text{tmbiH}_2)$  taken 5 ps after photoexcitation into the  $^1\text{MLCT}$  band at 500 nm. The wavelengths used in the following to probe the transient grating kinetics are indicated as vertical lines.

absorption band centered at 490 nm is due to the optical allowed transition that promotes a metal  $d^6$ -electron into a  $^1\text{MLCT}$ -state located on one of the aromatic ligands. The fluorescence occurs considerably red shifted with respect to the excitation spectrum with a maximum at 650 nm corresponding to a Stokes-shift of about  $5020\text{ cm}^{-1}$ . In the transient grating experiments as well as for recording the transient absorption spectra the complex was excited at 500 nm and thus within the  $^1\text{MLCT}$ -band. Therefore on the basis of the generally accepted picture used to describe the photophysics of Ru-polypyridine complexes, it is expected to observe a rapid formation of the long-lived  $^3\text{MLCT}$  state. The transient absorption spectrum taken 5 ps after photo-excitation into the  $^1\text{MLCT}$  band is shown in panel B of figure 1. It exhibits the typical transient absorption features for this class of molecules; a strong ground-state bleach (GSB) in the spectral region of ground-state absorption is accompanied by a broad and featureless photoinduced absorption (PIA) to the red of the ground-state bleach originating from excited singlet and triplet states. We ascribe the slight red shift of the bleach maximum with respect to the maximum of the  $^1\text{MLCT}$  band to minor contributions from stimulated emission. The probe-wavelengths exploited for our TG-measurements were chosen on the basis of the transient absorption spectrum and are indicated in panel B of figure 7.2. In order to probe the dynamics of the photoexcited complex the probe laser was tuned to 600, 630 and 660 nm, thus monitoring the time-evolution of the excited-state absorption. The implicit assumption that the transient absorption spectrum shown in figure 7.2 (panel B) reflects the absorption properties of the entirely thermalized lowest excited-state of the Ru-complex will be justified by considering the TG-kinetics displayed in figure 7.3. Panels A and B of figure 7.3 are recorded within the spectral region of excited-state absorption at 630 and 660 nm, respectively. All data presented in figure 7.3 were acquired using dichloromethane as solvent. The transients presented here exhibit a common feature: At zero delay-time a highly peaking and rapidly decaying intensity is observed. Following this spike the signals presented in panels A and B rise within the first 5 ps and subsequently the TG-signal is found to be constant.

The peak at  $t = 0$  fs, that is a common feature to all the transients presented in this chapter, is attributed to the so called *coherent artifact*, whose origin is described in section 5.2. As the coherent artifact signal is only observed for delay-times at which all three incident pulses interact simultaneously with the sample, it provides the "internal clock" that allows to define the starting point of the lightinduced dynamics with high accuracy. In contrast, the resonant contribution to the TG-signal depends on the probe laser wavelength



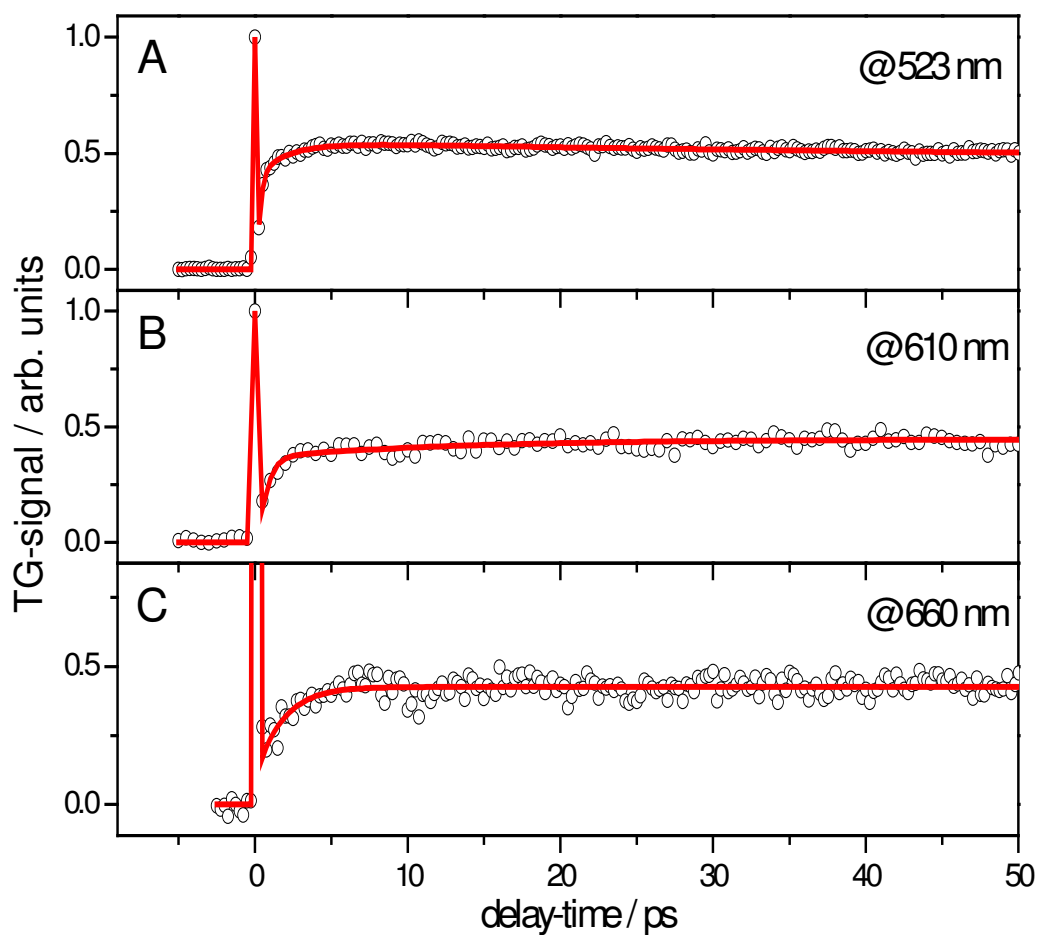


Figure 7.3: Transient grating kinetics of  $(\text{tbbpy})_2\text{Ru}(\text{tmbiH}_2)$  dissolved in dichloromethane recorded in the spectral regions of ground-state bleach and transient absorption following excitation at 500 nm are shown. The probe-wavelengths are indicated in the individual panels. Data are shown as symbols, while solid lines represent the results of LS-fits.

to be tuned to a molecular resonance, i.e. an absorption of the transiently populated state or a ground-state absorption. In figure 7.3 the resonant part of each of the signals displayed in panels A and B can be clearly observed for delay times larger than approximately 150 fs. It manifests itself as an initial rise of the signal that after approximately 5 ps remains constant over the range of delay-times accessible in our measurements (350 ps). In order to evaluate the data quantitatively, the transients were fitted to a bi-exponential rise and a Gaussian that was used to account for the non-resonant scattering contribution. This procedure leads to a fast rise-time of about 200 fs and a long time-constant of about 2.5 ps. The process associated with the 200 fs time-constant contributes to approximately 80% to the overall increase, while the 2.5 ps-component is responsible for the remaining 20%. (The values obtained from fitting the individual transients taken at different wavelength range from 180 to 325 fs and 1.5 to 3.5 ps, respectively, and are summarized together with the values for the relative amplitudes in tables 7.1 and 7.2.) Considering these time-constants for the build-up of the transient absorption and relating them to initial light-induced molecular relaxation processes, it becomes obvious that the transient absorption spectrum taken 5 ps after the initial photoexcitation reflects the absorption properties of the lowest excited-state of the complex. Thus, the bi-exponential rise observed can easily be explained with the formation of the energetically most favorable  $^3\text{MLCT}$  state.

In order to gain better insight into the processes that finally result in this lowest  $^3\text{MLCT}$  state, TG-measurements in the more polar solvent acetone were performed. A representative transient of these measurements is shown in figure 7.4 in comparison with a transient taken under the same experimental conditions with the Ru-complex dissolved in dichloromethane.

As it is obvious from the data shown the transients differ significantly from each other. The initial ultrafast rise, that can be fitted with a time-constant of typically 190 fs for acetone used as solvent, occurs on a time-scale that is very similar to the one observed for  $\text{CH}_2\text{Cl}_2$  as solvent. Nonetheless, the ultrafast component contributes more to the ultrafast rise compared to  $(\text{tbbpy})_2\text{Ru}(\text{tmbiH}_2)^{2+}$  dissolved in dichloromethane. The ultrafast increase of the signal is accompanied by a slower contribution described by a time constant of approximately 7.5 ps. The latter time-constant turns out to be roughly three times larger than the corresponding time-constant obtained from fitting the transient recorded with the solvent dichloromethane. However, the relative contribution of the slower rise-component to the overall signal increase is reduced compared to the observations in dichloromethane.

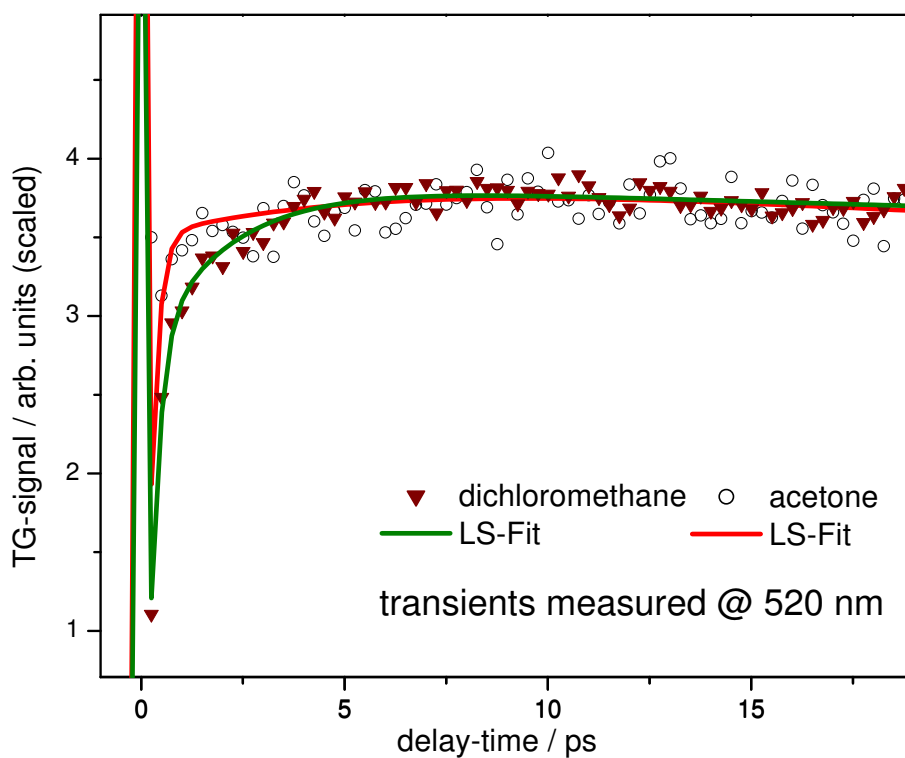


Figure 7.4: A comparison between the transient grating kinetics measured at 520 nm of  $(\text{tbbpy})_2\text{Ru}(\text{tmbiH}_2)$  dissolved in acetone and in dichloromethane is shown. Symbols represent data, results of LS-fits are shown as solid lines. (The transient are scaled for convenient presentation.)

(The values obtained from fitting the individual transients taken at different wavelength dissolved in both acetone and dichloromethane are summarized in tables 7.1 and 7.2.) Furthermore, it has to be mentioned, that the data taken with the probe-wavelength at 480 nm and thus being resonant with the GSB feature displays a bi-exponential decay instead of the ultrafast rise observed in the PIA band. This finding corroborates the bi-exponential nature of the ground-state recovery dynamics. On the basis of the results presented, the processes that finally place the complex in its energetically most favorable  $^3\text{MLCT}$  state will be discussed. Basically three different scenarios will be considered and discussed.

Dichloromethane				
		@ 520 nm	@610 nm	@630 nm
@660 nm				
$\tau_1$ / fs	215	180	325	200
$A_1$	.80	0.78	0.79	0.65
$\tau_2$ / ps	2.1	3.5	3.0	1.5
$1-A_1$	0.20	0.22	0.21	0.35

Table 7.1: The parameter obtained from fitting the TG-data of  $[(\text{tbbpy})_2\text{Ru}(\text{tmbiH}_2)]^{2+}$  dissolved in dichloromethane are summarized. The typical absolute errors of both time-constants and amplitudes range from 10 to 25 %.

Acetone				
	@480 nm	@520 nm	@610 nm	@630 nm
$\tau_1$ / fs	195	185	190	195
$A_1$	—	0.95	0.80	0.82
$\tau_2$ / ps	7.0	5.0	10.6	9.3
$1-A_1$	—	0.05	0.20	0.18

Table 7.2: The parameter obtained from fitting the TG-data of  $[(\text{tbbpy})_2\text{Ru}(\text{tmbiH}_2)]^{2+}$  dissolved acetone are summarized. The typical absolute errors of both time-constants and amplitudes range from 10 to 25 %.

The ultrafast rise-time is attributed to the very rapid intersystem crossing (ISC) observed in Ru-bipyridine complexes [8,35] that brings the system from its initially photoexcited  $^1\text{MLCT}$  into the corresponding  $^3\text{MLCT}$  state. This ascription seems to be very obvious considering the enormous amount of work published in the literature on similar molecular systems, that is consistently discussed in the frame work of an initial ultrafast  $^1\text{MLCT} \rightarrow ^3\text{MLCT-ISC}$ .

The finding of a bi-exponential build-up of the  $^3\text{MLCT}$  state, i.e. the presence of

a second rise component in the order of 2.5 ps using dichloromethane as solvent, might be interpreted in terms of two closely spaced but distinct  $^1\text{MLCT}$  states that are both populated by the pump-pulse and show different decaying behavior. Thus, the deactivation times of the initially populated states and therefore the build-up characteristics of the  $^3\text{MLCT}$  state might be extremely different and result in the observed transient kinetics. A similar model was proposed by Zewail and coworkers in order to account for the transient absorption signals observed in a zinc porphyrin [98]. Despite the model being straight forward, it is not obvious how to account for the significant solvent dependence of the decay constant  $\tau_2$ . The change from the non-polar solvent  $\text{CH}_2\text{Cl}_2$  to acetone might give rise to a more stable  $^3\text{MLCT}$  state, as the extended charge separation in this state leads to a stronger complex-solvent interaction. But a priori, this should not affect the rate of ISC from one of the initially populated  $^1\text{MLCT}$  states and leave the singlet to triplet transition starting from the other  $^1\text{MLCT}$  state unaffected. Thus, from the comparison of the data taken for the different solvents we conclude that this approach, though leading to good results in the interpretation of the transient absorption data of zinc tetraphenylporphyrin, is unlikely to be successful in describing the photophysics of  $(\text{tbbpy})_2\text{Ru}(\text{tmbiH}_2)(\text{PF}_6)_2$ .

The phenomenon of inter-ligand charge transfer (ILCT) has been discussed in the vast literature on transition metal complexes and is typically associated with time-constants ranging from about 1 ps for structurally different ligands involved in the process of ILCT to about 100 ps for identical ligands but typically being in the order of 10 ps (see [166] and references therein, [167]). Benko et al. investigated ILCT between the two bipyridine ligands in  $\text{RuN3}$  ( $\text{Ru}(2,2'\text{-bipyridine-4,4'\text{-dicarboxylate}})_2(\text{NCS})_2$ ) [168]. These authors found the ILCT to take place on a 20 ps time-scale. Thus, it seems very unlikely that our observation of a 2.5 ps time-constant can be attributed to an ILCT between the  $\text{tbbpy}$ -ligands, which are structurally very similar to the bipyridine-dicarboxylate ligands. Furthermore, as the process observed in our experiments appears as a time-dependent change in the TA of the system, it cannot be associated with ILCT between identical ligands. Thus, the possibility of ILCT between the structurally different ligands  $\text{tbbpy}$  and  $\text{tmbiH}_2$  has to be taken into account. Shaw et al. reported recently on an ILCT between two structurally different ligands [167]; their findings show that ILCT can occur as fast as on a ps-timescale, thus, being faster than the process observed in our experiments. However, when considering the solvent sensitivity of the process, this picture leads to an inconsistency, as in the more polar environment of acetone the lowest  $^3\text{MLCT}$ -state should more stabilized than in  $\text{CH}_2\text{Cl}_2$ .

This would give rise to an increase in driving force for the ILCT and consequently lead to a higher rate for this process [160] and therefore leads to a shorter time-constant associated with it.

Before continuing with the discussion of the processes giving rise to the observed decay-behavior, the RR measurements performed by Ute Uhlemann in the group of Prof. Popp in Jena are cited, in order to further reveal the role of the individual ligands tbbpy and tmbiH<sub>2</sub> within the overall excited-state relaxation of photoexcited (tbbpy)<sub>2</sub>Ru(tmbiH<sub>2</sub>). The RR measurements were performed on the reference compound Ru(tbbpy)<sub>3</sub><sup>2+</sup> and the peripheral building block of the tetranuclear antenna (tbbpy)<sub>2</sub>Ru(tmbiH<sub>2</sub>) (see panel 7.1). The results of the resonance Raman measurements show, that light absorption in the <sup>1</sup>MLCT band of either complex results in an enhancement of the vibrational modes associated with the tbbpy-ligands. Thus, the data indicates, that the initially populated MLCT-state is located on this particular ligand(s) rather than on the tmbiH<sub>2</sub> ligand in the case of (tbbpy)<sub>2</sub>Ru(tmbiH<sub>2</sub>)<sup>2+</sup>.

The question, whether this finding is reflected in the transient behavior of the photo-excited complexes was addressed by performing TG-measurements on Ru(tbbpy)<sub>3</sub><sup>2+</sup>, which is not only structurally related to [(tbbpy)<sub>2</sub>Ru(tmbiH<sub>2</sub>)]<sup>2+</sup> but also to Ru(bpy)<sub>3</sub><sup>2+</sup>, the "work-horse" of fundamental Ru-bipyridine- physics. Therefore, the data presented here not only allows to address the issue, which ligand is predominantly involved in the excited-state relaxation of [(tbbpy)<sub>2</sub>Ru(tmbiH<sub>2</sub>)]<sup>2+</sup>, but furthermore can be related to well established experimental results of Ru(bpy)<sub>3</sub><sup>2+</sup>. As, to the best of my knowledge, the data presented here constitute the first TG-approach to investigate the excited-state processes in transition metal complexes on a fs time-scale, the latter comparison is of great value in order to establish fs time- and spectrally-resolved four-wave-mixing as a valuable tool to address the fundamental photo-physics in transition metal complexes.

Figure 7.5 shows the absorption spectrum of Ru(tbbpy)<sub>3</sub><sup>2+</sup> dissolved in CH<sub>2</sub>Cl<sub>2</sub>. The strong absorption feature centered at 460 nm is due to the promotion of a metal 6<sup>d</sup>-electron into a <sup>1</sup>MLCT-state located on one of the tris-(4,4'-di-tert-butyl-2,2'-bipyridine)-ligands. The longwave shoulder of the absorption peak centered at 469 nm is assigned to direct photoexcitation of the <sup>3</sup>MLCT state. This transition, that is strictly speaking spin forbidden, occurs in the spectrum - as already state above - due to the strong heavy atom effect introduced by the presence of the Ruthenium ion. The fluorescence with a maximum at 605 nm is found to be considerably red-shifted with respect to the excitation spectrum

indicating that significant excited-state effects as outlined above have to be considered in the interpretation of the spectra.

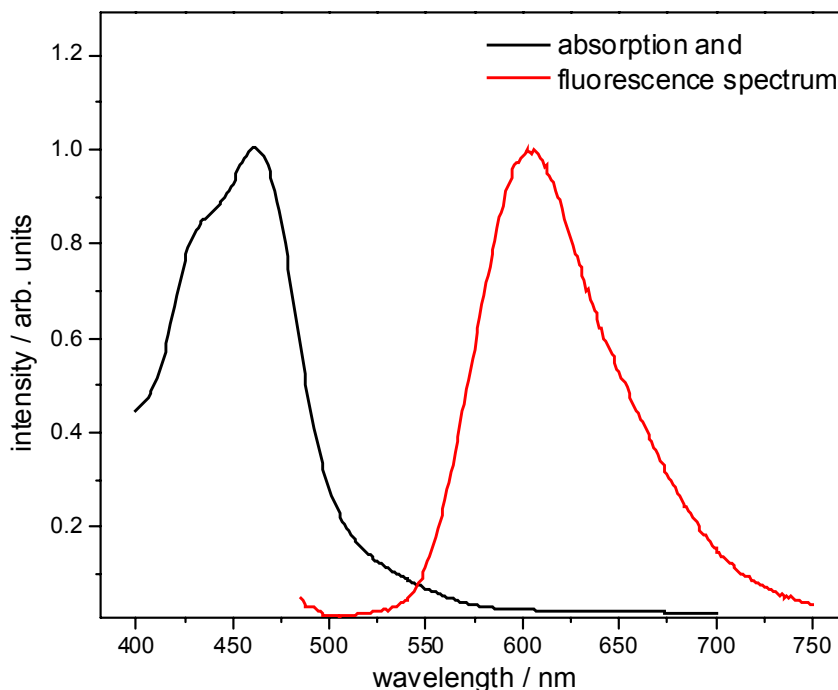


Figure 7.5: The steady state absorption spectrum is shown together with the fluorescence spectrum of  $\text{Ru}(\text{tbbpy})_3^{2+}$ . All spectra are normalized to unity at their respective maximum. The fluorescence spectrum was excited at 470 nm, while the fluorescence was monitored at 600 nm in order to record the excitation spectrum.

In the fs time-resolved experimental-runs the  $\text{Ru}(\text{tbbpy})_3^{2+}$  complex was excited with 110 fs laser pulses spectrally centered at 500 nm and thus tuned to be within the spectral range of the  $^1\text{MLCT}$  absorption band. In part of the experiments the probe-wavelength was chosen to be resonant with the transient absorption, which (for Ru(II) bipyridine complexes typically) extends into the infra-red, and set to 600, 625, and 650 nm. In addition to this wavelength arrangement, the transient behavior of the ground-state bleach was monitored by setting the probe laser to 492 nm and thus overlapping with the spectral region of overall ground-state bleach. A typical three dimensional plot obtained from our spectrally resolved TG- measurements with the probe wavelength tuned to 492 nm (thus being resonant with the ground-state absorption) is displayed in figure 7.6. As it is clearly visible the signal intensity peaks at a delay-time of 0 fs between the two pump-pulses

and the probe-pulse. The peak at  $\Delta t = 0$  fs shows all features of the coherent artifact. In figure 7.6 the resonant scattering observed subsequently to the coherent artifact is clearly apparent for delay times larger than about 200 fs. It manifests itself in the rise of the overall TG signal during the first picoseconds after light absorption and the consecutively constant signal - in complete analogy to the kinetic traces obtained for  $(\text{tbbpy})_2\text{Ru}(\text{tmbiH}_2)$ , as discussed above. A more detailed picture of the underlying process can be gained by fitting two-dimensional cuts of the three dimensional data at a fixed probe-wavelength. Such transients measured at different spectral positions are shown in panel B of figure 7.6 and for the probe laser tuned to be in resonance with the broad TA extending on the longwave side of the ground-state absorption in figure 7.7.

As can be seen clearly all transients show an increase of the resonantly scattered intensity over the first 5 ps after photo-excitation. Furthermore, this increase is found to be non-exponential but can be fitted to a sum of two different exponential rise-components; therefore

$$I_{TG} = A_0 [(A \cdot \exp(-t/\tau_1) + (1 - A) \cdot \exp(-t/\tau_2))]^2. \quad (7.1)$$

In this equation, that is used for fitting the resonant part of the experimental data, the time-constants  $\tau_1$  and  $\tau_2$  refer to two distinguishable processes leading to the overall rise of the TG-signal; this finding being in complete analogy to the data obtained for  $(\text{tbbpy})_2\text{Ru}(\text{tmbiH}_2)$ . Yet, the two processes are assumed to be identical to those being responsible for the very identical transient grating kinetics observed for  $(\text{tbbpy})_2\text{Ru}(\text{tmbiH}_2)$ .  $A$  and  $(1 - A)$ , respectively, describe the amplitudes of each of the two processes. The rather phenomenological amplitude  $A_0$  is introduced in order to account for the maximum constant value of the resonant signal at long delay times. This approach leads to a fast rise time  $\tau_1$  of less than 200 fs and a rise time  $\tau_2$  in the order of 2 ps (the values obtained from fitting individual transients are summarized in table 7.3.) Following the initial rise, the TG-signal intensities remain constant over the time-range accessible in our measurements (see figure 7.7).

In analogy to the interpretation of the TG-data obtained for  $(\text{tbbpy})_2\text{Ru}(\text{tmbiH}_2)$ , the ultrafast sub-200 fs rise is explained in terms of the extremely rapid ISC typically observed in Ru-bipyridine complexes [144, 169]. The extremely good agreement between the data sets obtained for  $(\text{tbbpy})_2\text{Ru}(\text{tmbiH}_2)$  and  $\text{Ru}(\text{tbbpy})_3$  is illustrated in figure 7.8.



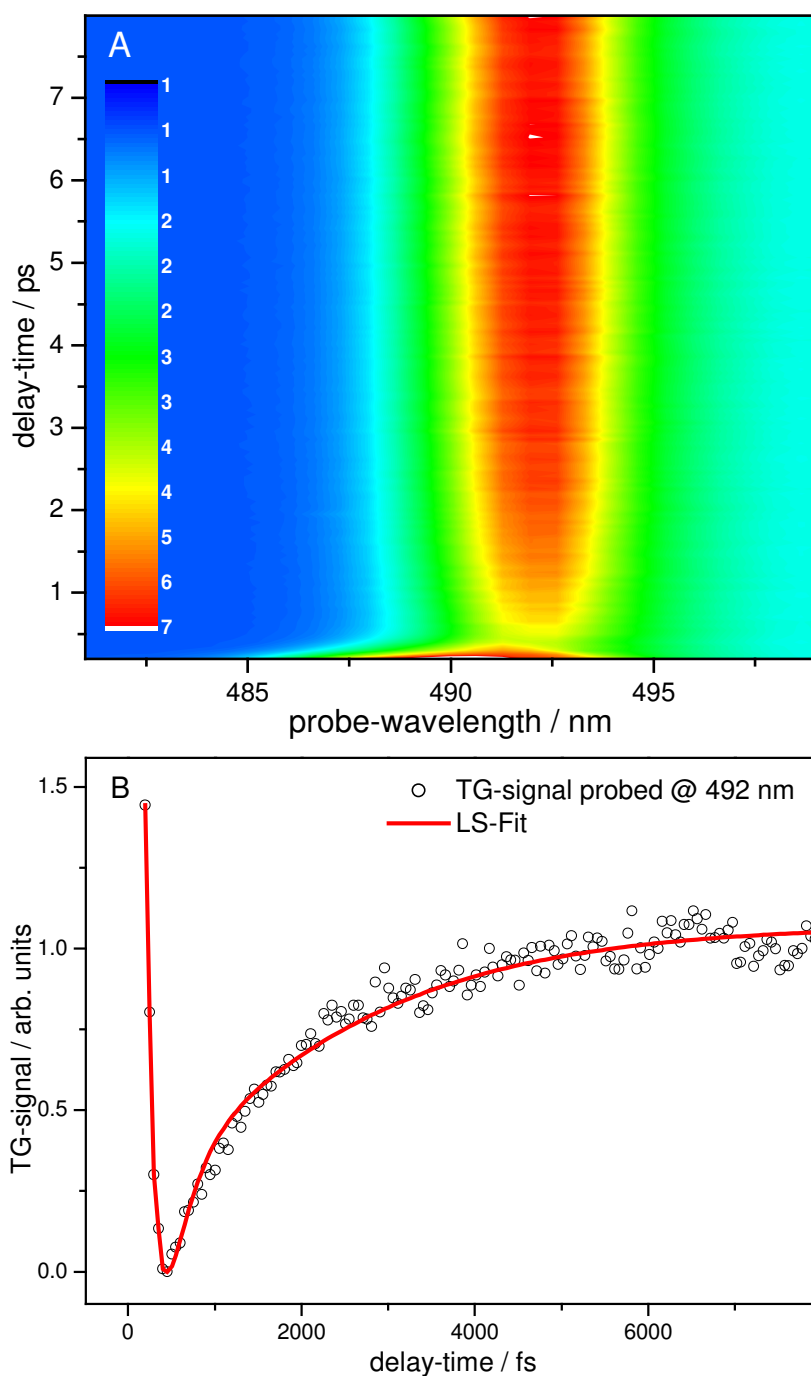


Figure 7.6: A three dimensional plot of the spectrally resolved TG-signal taken at 492 nm is shown. The interrogated molecular dynamics was initiated by photon absorption at 500 nm. Blue regions indicate low TG-signal intensities, while red or white ones mark high scattered intensity. Panel B displays a time-trace at 492 nm.

	GSB	photoinduced absorption		
	@ 495 nm	@ 600 nm	@ 625 nm	@ 650 nm
$\tau_1$ / fs	$200 \pm 50$	$175 \pm 75$	$195 \pm 45$	$140 \pm 90$
A	$0.62 \pm 0.03$	$0.63 \pm 0.08$	$0.59 \pm 0.04$	$0.63 \pm 0.04$
$\tau_2$ / ps	$2.0 \pm 0.2$	$2.1 \pm 0.2$	$2.0 \pm 0.1$	$2.3 \pm 0.3$
(1-A)	$0.38 \pm 0.03$	$0.37 \pm 0.08$	$0.41 \pm 0.04$	$0.27 \pm 0.04$

Table 7.3: The constants obtained from fitting the transient kinetic traces at various probe wavelengths to the absolute square of the function given in equation 6 are listed.

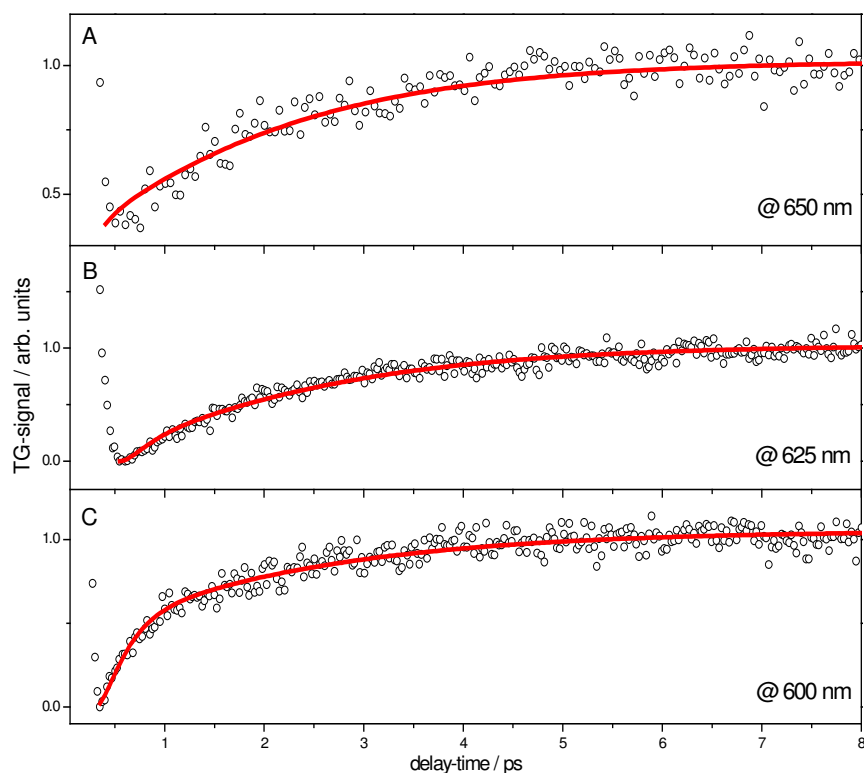


Figure 7.7: Transient grating signals taken at various spectral positions within the broad transient absorption band extending to the longwave side of the ground-state absorption. All transients were taken after photoexcitation at 500 nm. Experimental data is shown as circles, while solid lines represent the corresponding least square Fits of the resonant part of the signal.

Here the transient grating kinetics as monitored in the spectral region of the photoinduced absorption at 600 nm are shown. Both transients display the characteristic bi-exponential rise-behavior and subsequently a constant signal on the ps-time-scale.

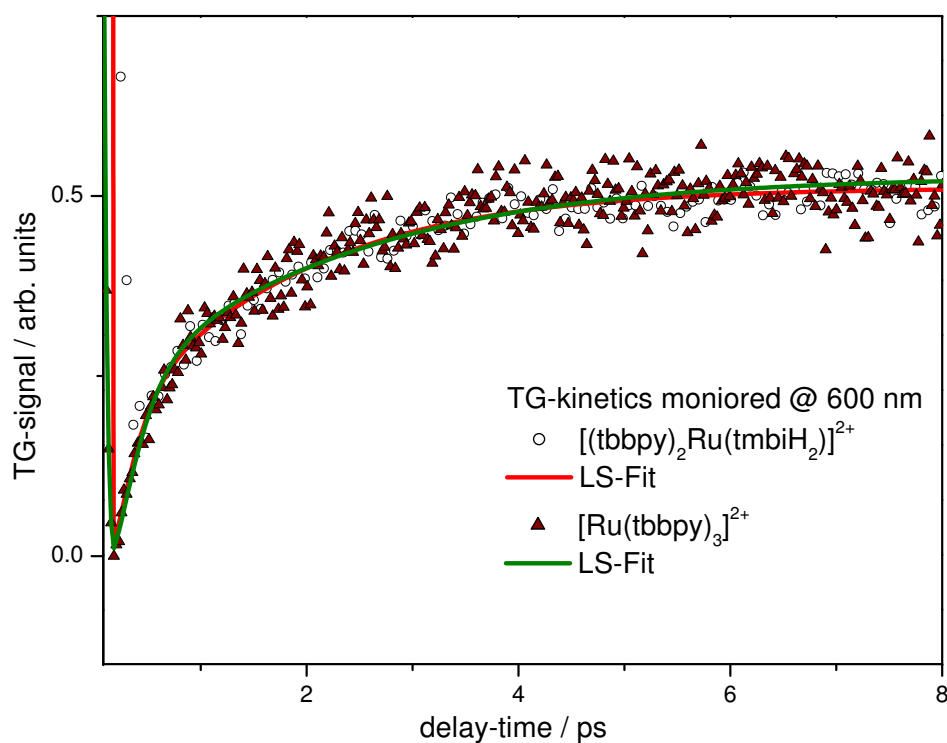


Figure 7.8: Transient grating kinetics reflecting the time-evolution of the transient absorption are shown as measured for  $[(\text{tbbpy})_2\text{Ru}(\text{tmbiH}_2)]^{2+}$  and  $[\text{Ru}(\text{tbbpy})_3]^{2+}$  dissolved in dichloromethane.

The data evaluation clearly shows that a bi-exponential rise has to be fitted to the data. The second rise-component in the order of 2 ps observed for either of the two complexes (see table 7.3) can be interpreted in terms of cooling and solvent reorganization within the  $^3\text{MLCT}$  state. This process has been suggested in several articles dealing with the photophysics of Ru(II)-complexes structurally similar to  $\text{Ru}(\text{tbbpy})_3^{2+}$  [143, 167, 169–171]. In these studies the energy dissipation process was found to proceed as fast as in about 1 ps [170], while Damrauer et al. [171] report on energy dissipation dynamics taking place in Ru(II) complexes structurally very similar to the ones being investigated here. These

authors report on a 5 ps relaxation time in Ru[tris-(4,4'-di-methyl-2,2'-bipyridine)]<sup>2+</sup> and a 2 ps component in Ru[tris-(4,4'-diphenyl-2,2'-bipyridine)]<sup>2+</sup>, which is assigned to rotational motion of the peripheral aryl rings that is accompanied with vibrational cooling. Thus, the time-scale observed in our experiments is in excellent agreement with cooling times observed for structurally very similar systems. Therefore, it is concluded, that fs time-resolved four-wave-mixing spectroscopy is a powerful tool to investigate the transient dynamics of complex structures taking place immediately after photoexcitation. Furthermore, the time-scale observed in these experiments matches cooling times observed not only for structurally very similar systems but also is in excellent agreement with the fitting parameter obtained from the analysis of the corresponding (tbbpy)<sub>2</sub>Ru(tmbiH<sub>2</sub>) data. The fact that the 2 ps-component is observed as a contribution to the overall rise only and not as a decaying component, as one might have expected for a cooling-process, can be understood when considering that the photoinduced absorption band on the longwave side of the ground-state absorption extends far into the infra red. Thus, any red-shift that is associated with energy dissipation from the Franck-Condon active modes of the complex into the solvent or non-Franck-Condon active modes of the molecule will not be visible in our TG-signals recorded in the spectral region up to 660 nm. Thus, ISC taking place on a sub-200 fs and cooling on a 2 ps time-scale result in an equilibrated energetically lowest lying excited triplet state of Ru(tbbpy)<sub>3</sub><sup>2+</sup> as summarized schematically in figure 7.9. The remarkable agreement of time-scales observed in the initial ultrafast dynamics in photoexcited Ru(tbbpy)<sub>3</sub><sup>2+</sup> and (tbbpy)<sub>2</sub>Ru(tmbiH<sub>2</sub>) leads to the conclusion that in both systems identical ligands are involved in the relaxation processes. This finding is completely coherent with the results of the RR measurements cited above, that show that the initial excitation is located on one of the tbbpy-ligands present in either complex. Therefore, it can be concluded:

- photo-excitation at 500 nm leads to a <sup>1</sup>MLCT-state located on a tbbpy-ligand in both complexes,
- identical processes contribute to the initial ultrafast rise of the TG-signals in both complexes.

Ruling out the possibility of two individual photo-populated states and ILCT contributing to the experimental signals and based on a comparison with literature [143, 167, 169–171], we suggest, that the long rise-component should be attributed to cooling and solvent reorganization effects following the rapid <sup>1</sup>MLCT → <sup>3</sup>MLCT-ISC. The absence of

a blue shift within the TA, coherently observed for  $(\text{tbbpy})_2\text{Ru}(\text{tmbiH}_2)$  and  $\text{Ru}(\text{tbbpy})_3^{2+}$ , is attributed to the interplay of the very broad TA extending far into the infrared and the experimental conditions, which allow us to measure TA spectra up to 700 nm only. Thus, a red shift typically associated with cooling is not observed. However, the observed solvent dependence is in agreement with the assignment of cooling to the ps-process. In contrast to the plain energy dissipation observed in dichloromethane, the charge separation in the lowest lying  $^3\text{MLCT}$ -state forms a molecular dipole, which in turn triggers orientational changes in the polar solvent acetone. Therefore, not only inner-shell de-excitation but also outer-shell reorganization and relaxation has to be taken into account. This additional molecular motion causes the relaxation process to take place in about 6.5 ps and thus on a longer timescale than in the less-polar solvent dichloromethane.

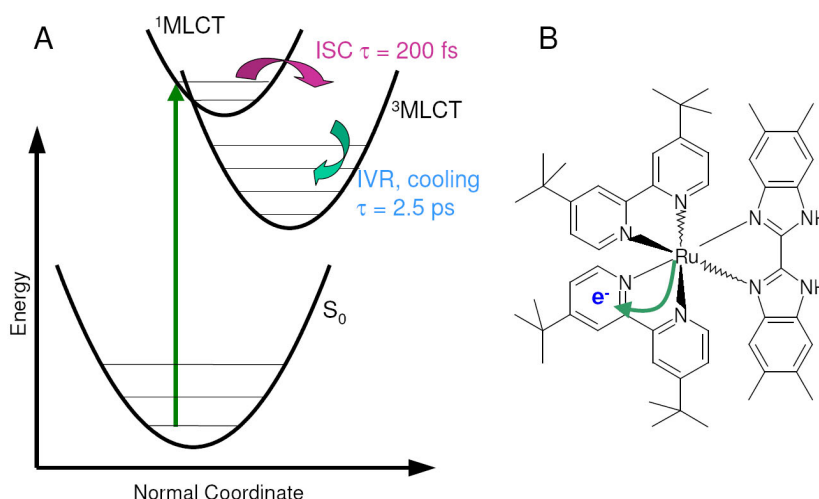


Figure 7.9: The ultrafast processes observed in  $(\text{tbbpy})_2\text{Ru}(\text{tmbiH}_2)$  are schematically summarized. Panel A presents a scheme involving the different states involved in the process, whereas panel B shows a local picture of the charge excitation. The relaxation in  $\text{Ru}(\text{tbbpy})_3^{2+}$  is found to proceed in an analog scheme. In both systems the initially excited  $^1\text{MLCT}$  state is located on the tris-butyl bipyridine ligand. (For details please see text.)

In conclusion the data is interpreted as a rapid sub-200 fs ISC followed by a cooling and solvent reorganization process that takes place on a ps timescale. The interplay of both processes finally places the molecular system in its lowest excited-state as schematically depicted in figure 7.9. And hence, all light-induced ultrafast dynamics in  $[(\text{tbbpy})_2\text{Ru}(\text{tmbiH}_2)]^{2+}$  and  $\text{Ru}(\text{tbbpy})_3^{2+}$  dissolved in dichloromethane is completed within

the first 10 ps after photoexcitation. The resulting lowest lying excited-state was found to have a lifetime of 260 ns in acetonitrile by performing ns-time-resolved fluorescence spectroscopy [164].

### 7.3 Excitation Dynamics in $\text{Ru}_2\text{Pd}_2$

Having discussed the ultrafast dynamical processes following initial photo-excitation of the  $(\text{tbbpy})_2\text{Ru}(\text{tmbiH}_2)(\text{PF}_6)$  forming the peripheral building blocks of the four center complex  $[(\text{tbbpy})_2\text{Ru}(\text{tmbi})]_2[\text{Pd}(\text{allyl})]_2(\text{PF}_6)_2$  and the reference compound  $\text{Ru}(\text{tbbpy})_3^{2+}$ , we will now shift our focus to the tetranuclear antenna system. The steady state absorption and fluorescence spectrum of the  $\text{Ru}_2\text{Pd}_2$ -complex are shown in panel A of figure 7.10.

The strong absorption band at 530 nm is due to a  $d^6 \rightarrow {}^1\text{MLCT}$ -transition within one of the Ru-chromophores. The fact, that this absorption feature is red shifted compared with the absorption spectrum of the simple Ru-complex as shown in 7.2, reflects the interaction of the Pd-moieties with the Ru-centers [172]. The longwave flank of the absorption peak at 530 nm again is attributed to direct excitation of lower lying  ${}^3\text{MLCT}$  states. The overall luminescence shows a maximum intensity at 658 nm and decays with a lifetime of 244 ns. Panel B of figure 7.10 displays the TA spectrum of the  $\text{Ru}_2\text{Pd}_2$ -complex taken 15 ps after photo-excitation of the system at 520 nm. The spectrum is dominated by a strong GSB in the region of ground-state absorption. In the adjacent spectral regions photoinduced absorption bands can be observed; the one located on the blue side of the GSB is centered at 450 nm. As found for the Ru-complex, whose TA resembles the spectrum displayed in figure 7.2, the photoinduced absorption of the  $\text{Ru}_2\text{Pd}_2$ -complex manifests itself in a broad basically featureless band extending to the red of the ground-state bleach. For the TG-experiments, which were performed on the  $\text{Ru}_2\text{Pd}_2$ -complex dissolved in dichloromethane, we chose the probe-wavelengths to be either resonant with the photoinduced absorption, i.e. the probe-laser tuned to 600, 630, 636 and 660 nm, or the GSB, i.e. the probe-wavelength was set to be 480 or 520 nm, respectively.

The transients following excitation at 520 nm reflecting the time-dependence of the photoinduced absorption are shown in figure 7.11. The data exhibit a coherent artifact as discussed previously and a subsequent rise of the resonant part of the signal followed by a slower decay. For delay times larger than approximately 120 ps the signal intensity stays constant within the time-range of 400 ps accessible with our experimental setup. For

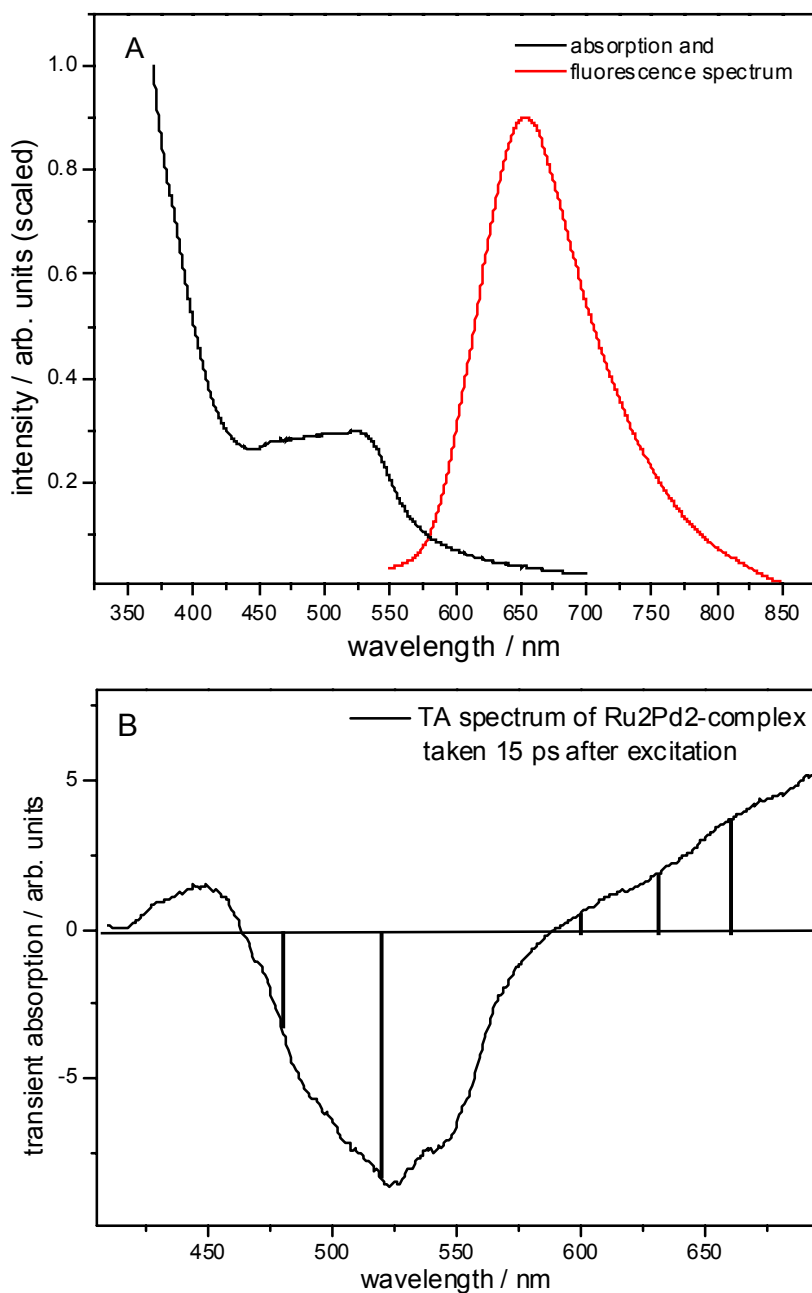


Figure 7.10: The steady state absorption- and fluorescence spectrum of  $[(\text{tbbpy})_2\text{Ru}(\text{tmbi})_2][\text{Pd}(\text{allyl})_2](\text{PF}_6)_2$  are shown in panel A. The fluorescence was excited at 520 nm. Panel B shows the transient absorption spectrum of  $[(\text{tbbpy})_2\text{Ru}(\text{tmbi})_2][\text{Pd}(\text{allyl})_2](\text{PF}_6)_2$  taken 20 ps after photoexcitation into the MLCT band at 500 nm. The wavelengths used in the following to probe the transient grating kinetics are indicated as vertical lines.

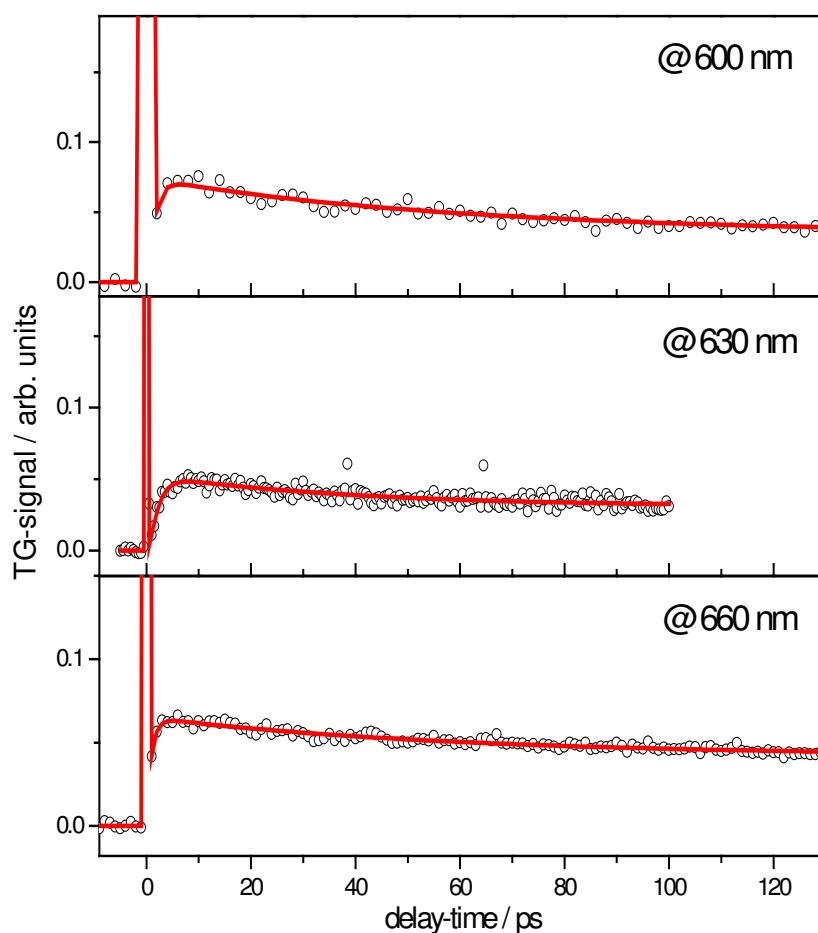


Figure 7.11: Transient grating kinetics of  $[(\text{tbbpy})_2\text{Ru}(\text{tmbi})]_2[\text{Pd}(\text{allyl})]_2$  dissolved in dichloromethane recorded in the spectral regions of transient absorption following excitation at 520 nm are shown. The probe-wavelengths are indicated in the individual panels. Data are shown as symbols, while solid lines represent the results of LS-fits. The details concerning the fitting procedure and results are given in the text.



a quantitative analysis of the data the resonant parts of the transients were fitted to a bi-exponential rise multiplied with a sum of a mono-exponential decay and a constant that is used to account for the long-lived constant signal. Nanosecond time-resolved luminescence spectroscopy was used to characterize the lifetime of the long-lived state to be 244 ns. Therefore, the function used to fit the non-resonant part of the signal reads:

$$I_{TG} = A_0 \cdot [(1 - A \cdot \exp(-t/\tau_1) - (1 - A) \cdot \exp(-t/\tau_2)) \cdot (B \cdot \exp(-t/\tau_3) + \text{const})]^2. \quad (7.2)$$

A Gaussian curve centered at  $t = 0$  fs simulates the coherent artifact. This approach leads to the time-constants for the individual probe-wavelengths that are summarized in table 7.4; the values of the long rise-times range from 1.4 to 2.2 ps while the ultrafast rise-component can be characterized by a time-constant  $\leq 180$  fs. In order to clearly demonstrate the bi-exponential nature of the initial rise, an enlarged view on the transient taken at 636 nm is presented in figure 7.12A, while panel B of figure 7.12 shows a direct comparison of kinetic traces obtained for the Ru- and the Ru<sub>2</sub>Pd<sub>2</sub>-complex.

The decay observed for all probe-wavelengths within the spectral range of the photoinduced absorption can be described by a time-constant  $\tau_3$  with values ranging from 50 to 58 ps. For the transients probed within the photoinduced absorption band the process described by  $\tau_3$  contributes to approximately 27% to the overall non-rising signal, while the remaining 73% are attributed to the long-lived component, which appears as a constant in our measurements. Having discussed the experimental data measured within the spectral region of photoinduced absorption we shall shift the discussion to transients monitoring the time-evolution of the GSB. Table 7.4 also contains the values of the fitting parameters obtained from fitting the TG-signals with the probe-wavelengths being resonant with the overall GSB; the corresponding transients are plotted in figure 7.13. As it is qualitatively obvious, in an experimental situation, in which the probe-laser is tuned to examine the ground-state recovery dynamics, the approach of fitting a bi-exponential rise followed by a mono-exponential decay to the data fails. Instead a multi-exponential decay following the coherent artifact has to be employed in order to model the data. In order to obtain sufficiently satisfactory fits a long decay constant  $\tau_4$  in the order of 220 ps has to be taken into account in addition to the time-constants used to fit the data taken for probe-wavelengths  $\geq 600$  nm. The additional slow process, which is only present in the data when monitoring the kinetics reflecting the time-dependence of ground-state recovery, contributes to about

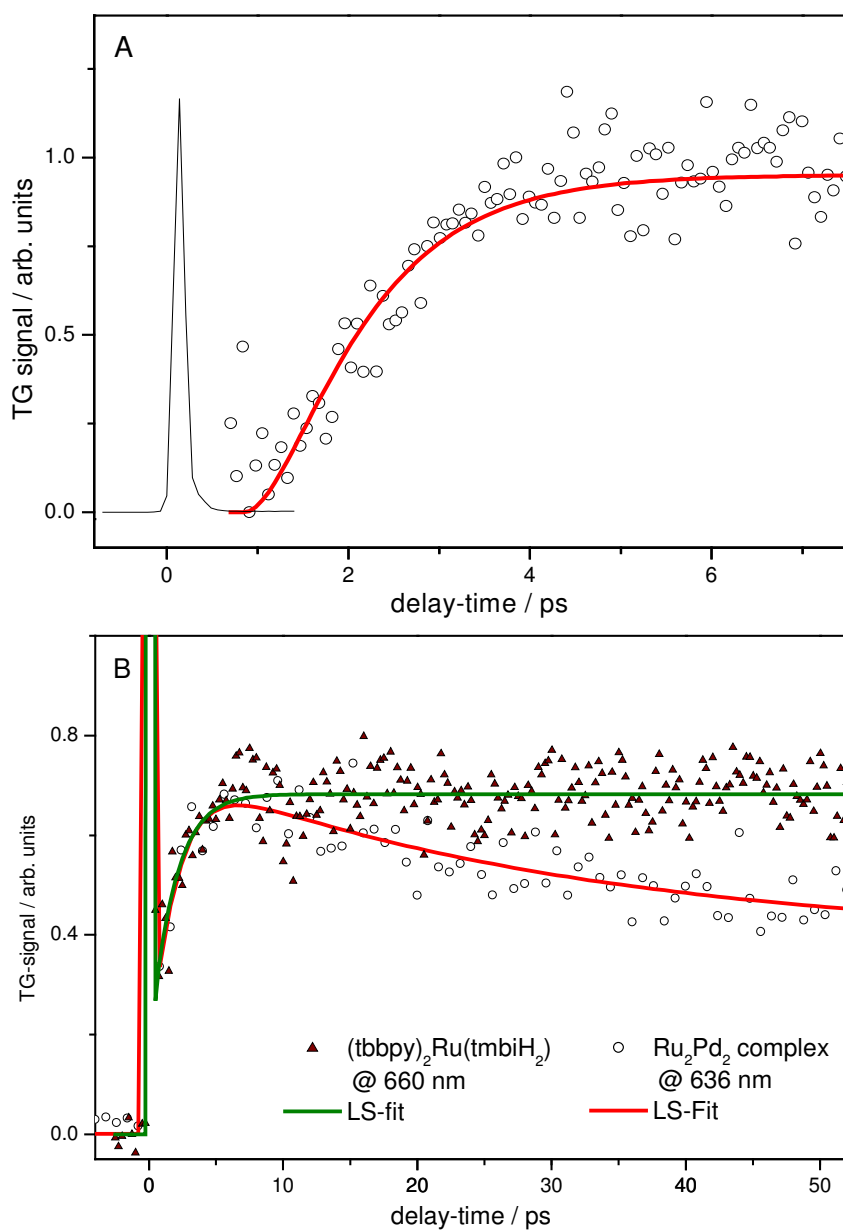


Figure 7.12: Transient grating data of  $[(\text{tbbpy})_2\text{Ru}(\text{tmblH}_2)]_2[\text{Pd}(\text{allyl})]_2$  recorded at 636 nm are shown. While the inset displays a long-time scan, the main panel exhibits an expanded view on the ultrafast bi-exponential rise of the resonant part of the signal. This part of the signal was enlarged with respect to the signal recorded around  $t = 0$  fs to better emphasize the rising-characteristics of the signal.

69%, the process associated with  $\tau_3$  to 22% and the process that appears as a constant within our time-resolution to 9% to the overall signal.

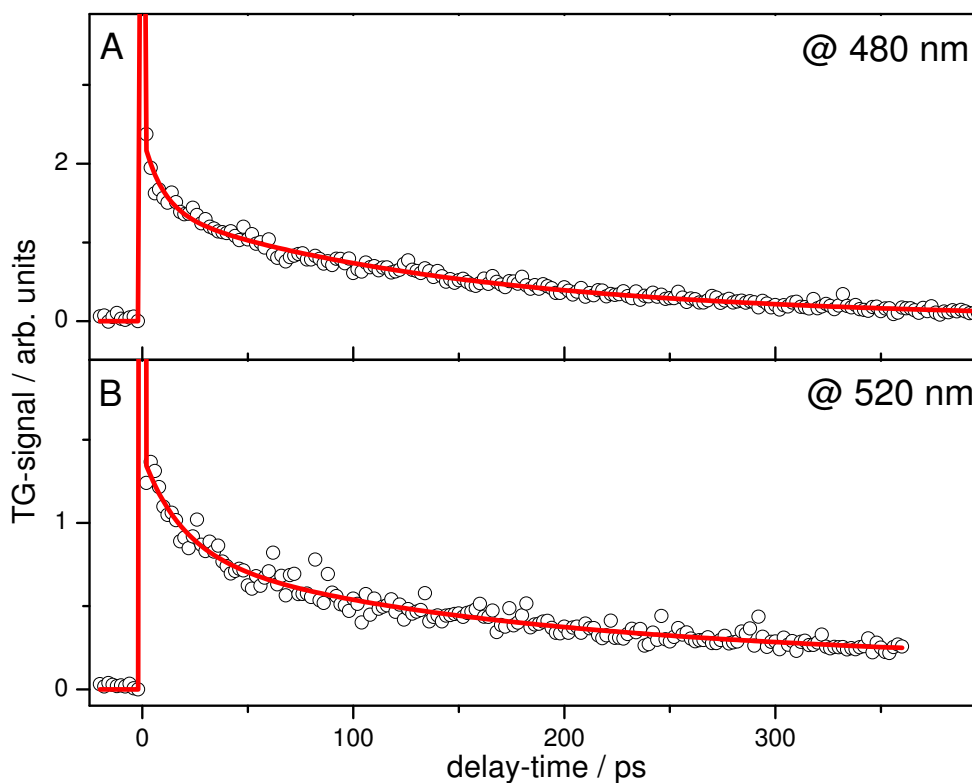


Figure 7.13: Transient grating kinetics of  $[(\text{tbbpy})_2\text{Ru}(\text{tmbi})]_2[\text{Pd}(\text{allyl})]_2$  dissolved in dichloromethane recorded in the spectral regions of ground-state bleach following excitation at 520 nm are shown. The probe-wavelengths are indicated in the individual panels. Data are shown as symbols, while solid lines represent the results of LS-fits. The details concerning the fitting procedure and results are given in the text.

Now, the focus will be shifted to the discussion of the results of the TG-measurements on the  $\text{Ru}_2\text{Pd}_2$ -complex that are summarized in table 7.4. In order to obtain a complete picture of the photoinduced processes in the  $\text{Ru}_2\text{Pd}_2$ -complex the results of our considerations about the relaxation processes in  $(\text{tbbpy})_2\text{Ru}(\text{tmbiH}_2)$  will be added to the argument.

The striking similar values of the short time-constants  $\tau_1$  and  $\tau_2$  obtained for Ru and the  $\text{Ru}_2\text{Pd}_2$ -complex (as well as for  $\text{Ru}(\text{tbbpy})_3^{2+}$  used as a reference system) lead to the conclusion that these time-constants are associated with the overall same processes in

	Ru <sub>2</sub> Pd <sub>2</sub>					Ru
	@480 nm	@520 nm	@600 nm	@630 nm	@660 nm	average
$\tau_1$ / fs	180	200	$\leq 150^*$	180*	150*	200*
$\tau_2$ / ps	1.2	0.8	1.3*	1.7*	1.1*	2.1*
$\tau_3$ / ps	42.6	50.2	57.5	50.1	55.1	—
A <sub>3</sub>	0.17	0.26	0.30	0.32	0.20	—
$\tau_4$ / ps	218	216	—	—	—	—
A <sub>4</sub>	0.73	0.65	—	—	—	—
const	0.10	0.09	0.70	0.78	0.80	1.00

Table 7.4: The parameter obtained from fitting the TG-data of  $[(\text{tbbpy})_2\text{Ru}(\text{tmbi})]_2[\text{Pd}(\text{allyl})]_2$  dissolved in dichloromethane are summarized. Time constants that appear as a rise of the TG-signal at the given probe-wavelengths are indicated with an asterisk. The amplitudes correspond to relative contributions to the non-rising part of the signal. For comparison averaged values of the fitting parameters of  $(\text{tbbpy})_2\text{Ru}(\text{tmbiH}_2)$  are given in the last column. The asterisk refers to kinetic components that manifest themselves as a rise in the overall TG signal. The typical absolute errors of both time-constants and amplitudes range from 10 to 25 %.

all systems. This ascription is further supported by the fact that poly-center- transition-metal-complexes can successfully be described based on the assumption of two (or more) independent chromophores that are only weakly coupled. Furthermore, the initial excitation is located on one of the peripheral Ru-chromophores. Thus, in accordance with our previously discussed results, we ascribe all dynamics observed for delay-times  $\leq 10$  ps to relaxation processes within the peripheral Ru-subunits. Thus, we ascribe  $\tau_1$  and  $\tau_2$  to the processes of rapid ISC, promoting the system from a  $^1\text{MLCT}$  to the  $^3\text{MLCT}$ -state located on the Ru-chromophore, and subsequent cooling and IVR within this state. (From here on states located on one of the chromophores are labeled as Ru- or Pd-states, respectively. Thus, in this nomenclature the process associated with  $\tau_1$  reads as Ru- $^1\text{MLCT} \rightarrow$  Ru- $^3\text{MLCT-ISC}$ .) Hence, the processes associated with  $\tau_1$  and  $\tau_2$  lead to the build-up of the photoinduced absorption of the Ru- $^3\text{MLCT}$  state. When investigating the photoinduced dynamics of the Ru-complex dissolved in  $\text{CH}_2\text{Cl}_2$  no kinetic component with a characteristic time-constant larger than 3.5 ps has been observed. Thus we conclude, that the existence of slower components in the dynamical processes of Ru<sub>2</sub>Pd<sub>2</sub> is due to the presence of multiple chromophores within the complex and relaxation processes associated with charge transfer in between these centers. Therefore, we ascribe the process that shows up as a  $\sim 50$  ps decay in the photoinduced absorption to an excitation transfer from a Ru- $^3\text{MLCT}$ -state to

one of the Pd-chromophores. This Ru-<sup>3</sup>MLCT  $\rightarrow$  Pd-excitation hopping manifests itself in the spectral region of the overall GSB as well. The values of  $\tau_3$  obtained from fitting the data within the excited-state absorption band correlate well with those used for fitting the transients monitoring the ground-state recovery kinetics. This leaves us with the discussion of the slow decay, which takes place on a 220 ps-timescale and is solely observed when monitoring the ground-state recovery. Recalling the lifetime of the Ru<sub>2</sub>Pd<sub>2</sub>-complex to be 244 ns might lead to the speculation that the 220 ps time corresponds to a non-fluorescent transition back to the ground-state, that is too fast to be visible within the time-resolution of the ns-experiment. Nevertheless, such a process should be visible in the photoinduced absorption as well as in the GSB of the complex. But as the transients taken in the spectral region of excited-state absorption do not exhibit any evidence for the presence of a 220 ps component, we discard this model. Instead we suggest, that the slow dynamical component is due to an excitation transfer between the two Pd-chromophores, thus leading to a situation in which the excitation is equally distributed over both palladium centers. In this scenario one would expect to observe no spectral changes in the excited-state absorption of the system, as corresponding states of either Pd-center exhibit identical absorption properties. However, the process of inter-center excitation transfer (ICET) (see figure 7.3) is evident in the GSB-kinetics as it leads to the fully equilibrated excited-state and thus proceeds complete ground-state recovery. The lifetime of the fully equilibrated excited-state has been measured to be 244 ns using time-resolved luminescence spectroscopy. This model of ICET following excitation transfer from the Ru-subunits to the Pd-moieties is consistent with the relative contributions of the components visible in our data as summarized in table 7.4. Within the GSB the process associated with  $\tau_4$  and the constant contribute to approximately the amount of the constant within the photoinduced absorption band, while the contributions of  $\tau_3$  are about the same in both spectral regions; for example  $A_4$  and the constant resulting from a fit of the data taken at 520 nm sum up to 0.74, which is consistent with the average value of the constant obtained from fitting the transients taken in the spectral region of excited-state absorption 0.76 (for details see table 7.4). This finding implies the presence of a sequential process - instead of concurring relaxation pathways - with the slow contribution just being not visible when monitoring the kinetics of the excited-state absorption band. In contrast to ILCT, which involves two distinguished ligands within the same chromophoric center, the ICET as apparent in the data presented here takes place between two identical chromophoric centers, which have the same energetic

positions of their excited-states. Hence, the driving force of ICET cannot be associated with the energetically different structures of two structurally distinct ligands. In order to shed light onto the principles underlying the ICET, consider the two palladium centers, which are in close spatial proximity (the distance was found to be as small as 3.8 Angstrom [136]), as two potential energy wells forming a double-well potential as schematically depicted in figure 7.14.

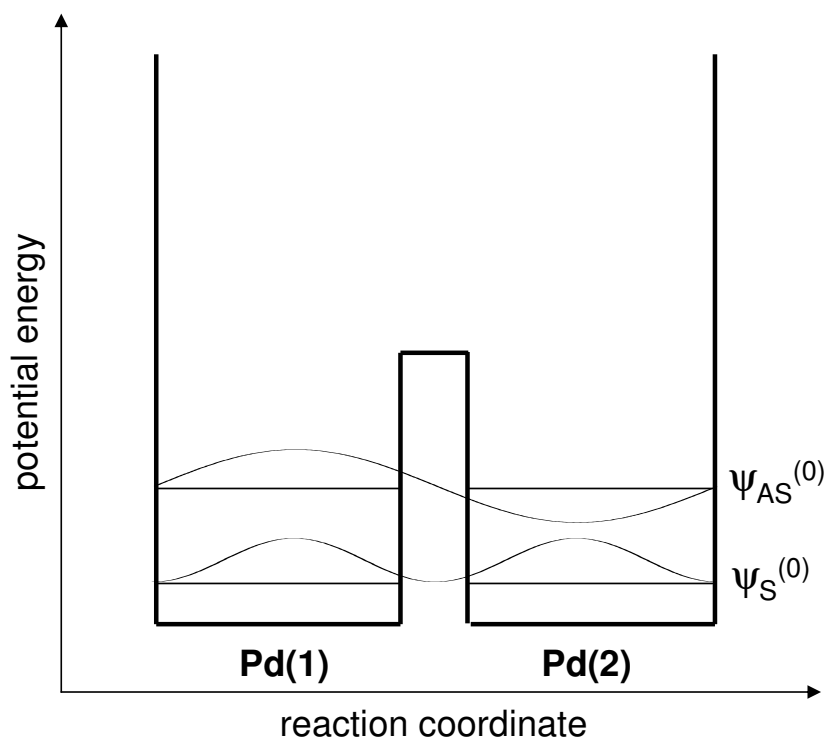


Figure 7.14: The energetic principles underlying inter-center excitation transfer are schematically illustrated.

It is well known from textbook quantum mechanics, that the coupling between the two potential wells results in a splitting of the energetically otherwise degenerate states. This splitting results in a symmetric ( $\psi_S^{(0)}$ ) and an anti-symmetric wavefunction ( $\psi_{AS}^{(0)}$ ) associated with the state of a state, that would be degenerate in the absence of electronic coupling, with  $E_{AS} > E_A$ . Here  $E_{AS(S)}$  denotes the energy of the state described by the anti-symmetric (symmetric) wavefunction. Following the Ru-<sup>3</sup>MLCT  $\rightarrow$  Pd(1)-electron transfer, in the schematic representation given in figure 7.14 the charge is located solely in the potential minimum of Pd(1). Thus, the situation is described by the wavefunction

$\frac{1}{2} \cdot (\psi_S^{(0)} + \psi_{AS}^{(0)})$ . As the energy of the system in this state,  $E_{Pd(1)}$ , is larger than  $E_S$ , which corresponds to the situation of equally populating both the potential minima of Pd(1) and Pd(2), the system will relax into the state described by  $\psi_S^{(0)}$ . Hence, the excitation originally located on Pd(1) will be distributed equally over palladium centers. Thus, a strong driving force for a ICET due to the existence of an energetically favorable state located on one of the chromophoric centers is absent [160] and the observed relatively long time-constant becomes reasonable. Figure 7.3 schematically resembles the kinetic processes observed in the Ru<sub>2</sub>Pd<sub>2</sub>-complex.

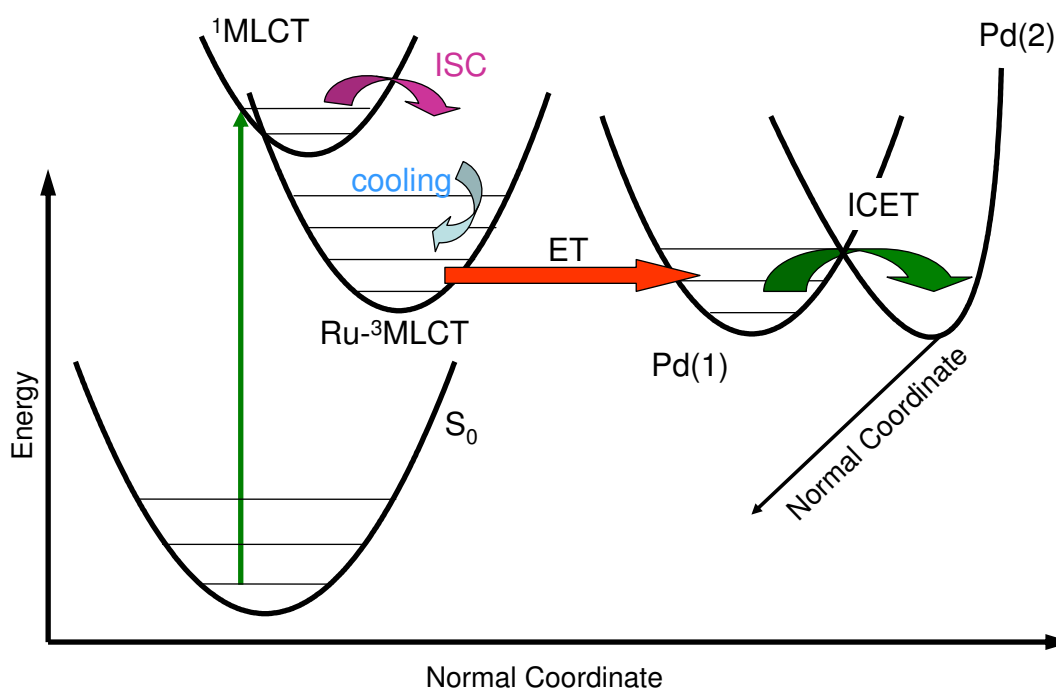


Figure 7.15: The kinetic processes initiated by photoexcitation at 520 nm observed in the tetranuclear light-harvesting antenna  $[(tbbpy)_2Ru(tmbi)]_2[Pd(allyl)]_2$  are depicted schematically.

## 7.4 Conclusion

In this chapter a detailed kinetic study on the excitation migration processes in the tetranuclear transition-metal complex  $[(tbbpy)_2Ru(tmbi)]_2[Pd(allyl)]_2(PF_6)_2$ , that may serve as a model system for a small inorganic-light-harvesting antenna or simple model of a photosynthetic reaction center, was presented. To facilitate the interpretation of the com-

plex kinetic data  $(\text{tbbpy})_2\text{Ru}(\text{tmbiH}_2)$ , the peripheral building block of the former complex, was included in our studies. By exploiting fs-time-resolved transient-grating spectroscopy we have probed the ultrafast excited-state relaxation processes that lead to the equilibrated lowest lying excited-state of the complexes. Recording the TG-kinetics in the spectral regions of ground-state bleach and transient absorption in combination with solvent dependent measurements allowed us to assign a distinct kinetic process to each of the observed time-constants. In isolated  $(\text{tbbpy})_2\text{Ru}(\text{tmbiH}_2)$  a rapid  $\leq 200$  fs  $^1\text{MLCT} \rightarrow ^3\text{MLCT-ISC}$  is followed by cooling and solvent reorganization leading to a fully thermalized excited-state on a ps-timescale. Time-resolved luminescence-spectroscopy with ns time-resolution reveals that the lowest lying excited-state in the Ru- complex decays with a characteristic time-constant of 260 ns. In  $[(\text{tbbpy})_2\text{Ru}(\text{tmbi})]_2[\text{Pd}(\text{allyl})]_2(\text{PF}_6)_2$  additional time-constants are observed; one being in the order of 50 ps, is attributed to a charge transfer from an excitation centered at a Ru-chromophore to one of the Pd-centers of the complex. The slowest process apparent in the data is characterized by a time-constant of 220 ps. As it is observed only in the ground-state recovery kinetic but not in the excited-state absorption, it is concluded that this component is due to an inter-center excitation hopping. This process finally leads to an excitation that is equally distributed between both Pd-centers of the four-center transition-metal-complex. The lifetime of this lowest lying state was found to be 244 ns. Finally, from a technical point of view, the studies presented here constitute to the best of my knowledge the first femtosecond time-resolved four-wave-mixing study on transition metal complexes. Thus, it has been shown that fs-time-resolved transient-grating spectroscopy is a powerful tool to illuminate relaxation processes even in complex systems and to address questions concerning the ultrafast photophysical mechanisms in charge transfer systems.



## Chapter 8

# Conclusion - Zusammenfassung

### 8.1 Conclusion

In the experiments presented in this work, linear and non-linear femtosecond time-resolved spectroscopy were applied to investigate the structure-function and function-dynamics relationship in biological and artificially designed systems. The experiments presented in this work utilize femtosecond time-resolved transient absorption and transient grating as well as picosecond time-resolved fluorescence spectroscopy to investigate the photophysics and photochemistry of biological photoreceptors and address the light-induced excited-state processes in a particular molecular device that serves as a - structurally - very simple light-harvesting antenna and potentially as a catalysis-switch for the production of hydrogen in solution. The combination of white-light probe transient absorption and coherent transient grating spectroscopies yields spectral information about the excited state absorption in concert with high quality, high signal-to-noise kinetic transients, which allow for precise fitting and therefore very accurate time-constants to be extracted from the data. The use of femtosecond time-resolved transient grating spectroscopy is relatively uncommon in addressing questions concerning the excited-state reaction pathways of complex (biological) systems, and therefore the experiments presented in this work constitute according to the literature the first studies applying this technique to a metalloporphyrin (see chapter 5) and an artificial light-harvesting antenna - see part III.

A short theoretical overview over the spectroscopic techniques used and their relation to the system's characteristic density matrix is presented in chapter 2, their experimen-

tal realization was briefly described in section 3. In part II of this thesis the experiments performed in the course of this work on biological chromophores, that are prepared in the group of PD. Dr. Gudrun Hermann, Institute of Biophysics and Biochemistry at the University of Jena, were reported. In chapter 4 the excited-state relaxation processes in phycocyanobilin were investigated using pump-energy-dependent transient grating spectroscopy. The data obtained validate a recently suggested model to account for the photophysics of phycocyanobilin and provided further and more detailed insight into it. In particular, the role of vibrational excess energy disposed in the excited-state manifold could be clarified: With increasing vibrational excess energy the rate of photoexcited phycocyanobilin molecules internally converting back to the ground-state increases as well as the photoreaction rate. Having covered a great part of the steady-state absorption spectrum by the excitation laser, it could be shown that only one of three at room-temperature abundant phycocyanobilin species undergo a light-triggered reaction. These results not only prove the model suggested by Hermann and coworkers but yield further insight into the excited-state processes of the phytochrome model chromophore.

In chapter 5 femtosecond and picosecond time-resolved experiments on photoexcited magnesium octaethylporphyrin and protochlorophyllide a were presented. The relaxation processes occurring within the excited-state manifold of magnesium octaethyl porphyrin, which is structurally very similar to protochlorophyllide a and should therefore be an appropriate model and reference for the latter system, were investigated using transient grating spectroscopy. By varying the excitation and probe wavelength the molecules were selectively promoted into an experimentally chosen state, and the population flow out of the initially excited state or into a lower lying excited-state was monitored. Thereby, relaxation pathways between the distinct electronic states can be monitored and characterized with respect to their respective time-constants, giving rise to a detailed mapping of the relaxation processes within the excited-state manifold. With the knowledge gained from these experiments, the light-induced excited-state processes in protochlorophyllide a are investigated. As the study presented here is the first approach to characterize the excited-state relaxation in this system, the approach of femtosecond time-resolved transient-absorption was chosen in order to allow for a full temporal and spectral characterization of the excited-state intermediates observed. On the basis of the data obtained for protochlorophyllide a dissolved in methanol a first model for the excited-state processes was tentatively assigned, which

was further specified with respect to solvent and pump-energy dependent measurements. Furthermore, picosecond time-resolved fluorescence data obtained from streak-camera measurements are added to the argument. The experimental data, yielding three distinct decay-constants (ranging from 4 to 200 ps) for a polar solvent environment and only a single relaxation-time (4.7 ps) in the non-polar solvent cyclohexane is explained in terms of the presence of an intramolecular charge-transfer state, whose potential minimum is shifted as a function of solvent polarity. Besides, the absence of a keto-enol-tautomerization step in the overall kinetics can be deduced from the very similar transient data obtained for two distinct polar solvents with differing proticity. This finding is of particular interest, as the reaction mechanisms proposed to account for the reduction of protochlorophyllide a to chlorophyllide a in the natural enzymatic environment suggest such tautomerization should take place. The rich dynamics observed upon photoexcitation of protochlorophyllide a was compared to the long lived fluorescent  $S_1$ -state of reference porphyrin. From this comparison it was concluded that the cyclopentanone ring, the distinguishing structural difference between protochlorophyllide a and magnesium octaethyl porphyrin, might play a crucial role in the formation of the intramolecular charge transfer state and thus in the overall photophysics of the system. The data and the resultant model are compared to reaction schemes suggested to account for the mechanism involved in the reduction of protochlorophyllide a to chlorophyllide a in the enzymatic environment of the protochlorophyllide oxido reductase enzyme.

In the third part of this thesis (see part III) the focus was shifted to characterize the light-induced processes in the system  $[(\text{tbbpy})_2\text{Ru}(\text{tmbi})]_2[\text{Pd}(\text{allyl})]_2(\text{PF}_6)_2$ , artificially designed in the group of Dr. Sven Rau and Prof. Dr. Dirk Walther at the Institute for Inorganic Chemistry at the University of Jena to serve as a catalysis-switch and a structurally simple light-harvesting antenna. For this work a combination of transient absorption and transient grating spectroscopy has been chosen. The discussion of the experimental approach starts with presenting data obtained for the peripheral building block,  $(\text{tbbpy})_2\text{Ru}(\text{tmbiH}_2)(\text{PF}_6)$ , of the antenna. The experimental results can be explained by invoking ultrafast intersystem crossing, a process typical for this class of transition metal complexes, promoting the system from the initially photexcited singlet metal-to-ligand charge-transfer (MLCT) to a long-lived triplet MLCT-state, in which relaxation on a picosecond time-scale can be observed. The question, which of the structurally distinct ligands in  $[(\text{tbbpy})_2\text{Ru}(\text{tmbiH}_2)]^{2+}$  is involved in the excited-state processes, is addressed by transient

grating measurements of the reference compound  $[\text{Ru}(\text{tbbpy})_3]^{2+}$ . These measurements and resonance Raman data, that were obtained in the group of Prof. Dr. Jürgen Popp at the Institute for Physical Chemistry at the University of Jena, reveal that the initial excitation and relaxation dynamics takes place on the tbbpy-ligand of the complex. With this knowledge gained, the entire tetranuclear antenna system is investigated yielding three or four characteristic time-constants depending on the spectral position chosen for probing. Among these the two fastest processes are assigned to relaxation within the initially excited terminal Ru-chromophore, while a 50 ps process is attributed to Ru  $\rightarrow$  Pd-excitation transfer. Subsequently, a 220 ps process is observed solely in the spectral region monitoring ground-state bleach and being not visible in recording photoinduced absorption kinetics. This process leading to a finally equilibrated excited-state is associated with excitation transfer between the two palladium centers in the complex. Thus, the results presented here constitute the first experimental observation of a Ru  $\rightarrow$  Pd-excitation transfer using femtosecond time-resolved spectroscopy. Furthermore, they provide profound insight into the reaction dynamics of a small inorganic light-harvesting antenna  $([(\text{tbbpy})_2\text{Ru}(\text{tmbi})_2][\text{Pd}(\text{allyl})_2]_2)(\text{PF}_6)_2$ .

The experimental work presented in this thesis was aimed to present the combination of femtosecond time-resolved transient absorption and transient grating spectroscopy as a powerful tool in addressing the photoinduced excited-state processes in biological photoreceptors and artificially designed systems. Furthermore, detailed insight into the structure-dynamic and dynamic-function relationships of the investigated systems could be obtained from a careful analysis of solvent and pump-energy dependent measurements and comparisons with previously suggest reaction models were established.

## 8.2 Zusammenfassung

In der hier vorliegenden Arbeit wurden die Struktur- Funktions- und Funktions-Dynamik- Beziehungen in biologischen und künstlich synthetisierten Systemen untersucht. Hierfür wurden Femtosekunden zeitaufgelöste lineare und nicht-lineare spektroskopische Techniken verwendet. Mittels transientser Absorptions- und transientser Gitterspektroskopie sowie Pikosenkunden zeitaufgelöster Fluoreszenzmessungen wurden ausgewählte pflanzliche Photorezeptoren untersucht und die Relaxationsprozesse im angeregten Zustand einer

artifiziellen Lichtsammelantenne charakterisiert. Die Kombination aus Femtosekunden-zeitaufgelöster transientser Absorption unter Verwendung eines Weisslichtsuperkontinuums als Probepuls und kohärenter Vier-Wellen-Mischungs-Spektroskopie erlaubt es, breitbandige spektrale Informationen über einen photo-angeregten Zustand zu gewinnen und gleichzeitig Kinetiken mit einem sehr hohen Signal-Rausch-Verhältnis zu messen. Letztere erlauben einen präzisen Fit, und somit können sehr präzise charakteristische Zerfallskonstanten aus den zeitaufgelösten Daten rekonstruiert werden. Durch den komplexeren Versuchsaufbau eines Vier-Wellen-Mischungs-Experiments verglichen mit dem transienter Absorptionsspektroskopie ist die Verwendung von zeitaufgelöster transientser Gitterspektroskopie zur Untersuchung licht-induzierter Prozesse in komplexen biologischen Systemen noch immer relativ unüblich. Daher stellen die hier präsentierten Ergebnisse die ersten Experimente dar, in denen diese Technik zur Untersuchung von angeregter Zustandsrelaxation in einem Metalloporphyrin und einem künstlichen photosynthetischen Reaktionszentrum eingesetzt wurde.

Im ersten Teil der Arbeit wurde eine kurze theoretische Übersicht über die hier verwendeten spektroskopischen Techniken und ihre mathematische Relation zu der Dichtematrix des untersuchten Systems gegeben und ihre experimentelle Realisierung diskutiert (siehe Kapitel 2 und 3). Im zweiten Teil der vorliegenden Dissertation wurden die Experimente, die zum Ziel hatten, die Photophysik von ausgewählten biologisch relevanten Chromophoren zu charakterisieren, vorgestellt. Die Proben, die in diesem Teil der Arbeit untersucht wurden, wurden von Privatdozentin Dr. Gudrun Hermann, Institut für Biophysik und Biochemie an der Friedrich-Schiller Universität Jena, isoliert und aufgereinigt. Eine detaillierte Charakterisierung der ultraschnellen Relaxationsprozesse des photo-angeregten Zustandes in Phycocyanobilin gelang mittels Femtosekunden-zeitaufgelöster transientser Gitterspektroskopie. Die Ergebnisse bestätigen ein Modell für die lichtinduzierten Prozesse in Phycocyanobilin, das von Dr. Hermann und ihren Mitarbeitern aufgestellt wurde. Darüber hinaus konnten aber deutlich weitergehende, detailliertere Einblicke in die angeregte Zustandsphysik dieses Systems gewonnen werden. Insbesondere konnte der Effekt von überschüssiger Schwingungsenergie im angeregten Zustand quantifiziert werden. Ein Ansteigen der durch Lichtabsorption im angeregten Zustand deponierten Schwingungsenergie führt zu einer Beschleunigung sowohl der internen Konversion zurück in den Grundzustand als auch zu einer beschleunigten Photoreaktion der angeregten Phycocyanobilinspezies. Indem in Pumpwellenlängen-abhängigen Messungen ein grosser Teil des Grundzustandsab-

sorptionsspektrums abgedeckt wurde, konnte gezeigt werden, dass nur eine der drei bei Raumtemperatur vorhandenen Grundzustandsspezies von Phycocyanobilin eine Photoreaktion eingeht. Die hier gewonnenen Ergebnisse erlauben weitergehende Einblicke in die Photophysik des Phytochrom-Modellchromophores Phycocyanobilin und stellen eine exzellente experimentelle Bestätigung eines von Dr. Hermann und Mitarbeitern vorgeschlagenem Reaktionsmodells dar. Die hier zusammengefassten Ergebnisse wurden in Kapitel 4 im Detail diskutiert.

Im folgenden Kapitel (Kapitel 5) wurden die Ergebnisse der Untersuchungen an photoangeregtem Protochlorophyllid A und dem strukturell verwandten Magnesium-Oktaethylporphyrin vorgestellt. Die Relaxationsprozesse auf der angeregten Zustandsoberfläche des Magnesiumporphyrins wurden mittels transients Gitterspektroskopie untersucht. Magnesium-Oktaethylporphyrin wurde gewählt, da es aufgrund seiner hohen strukturellen Ähnlichkeit mit Protochlorophyllid A ein sehr gutes Modellsystem für Protochlorophyllid A darstellt. Indem die Anregungs- und die Probewellenlängen systematisch variiert wurden, konnte der Populationsfluss zwischen verschiedenen und experimentell kontrollierten angeregten Zuständen abgefragt und charakterisiert werden. Mit der Kenntnis dieser Ergebnisse wurden dann die lichtinduzierten Primärprozesse in Protochlorophyllid A untersucht. Dieses Molekül ist als Zwischenstufe in der enzymatisch katalysierten Chlorophyllsynthese in grünen Pflanzen von besonderem Interesse, da seine Reduktion zu Chlorophyllid A in dem Enzym NADPH:Protochlorophyllid-Oxidoreduktase eine von nur zwei bekannten lichtgesteuerten enzymatischen Reaktionen darstellt. Da es sich bei den hier präsentierten Ergebnissen um die erste Studie zu der ultraschnellen Photophysik dieses Systems handelt, wurde die Technik der Superkontinuums- Probe transienten Absorption gewählt, um eine breitbandige spektrale und zeitliche Charakterisierung der angeregten Zustandsintermediaten zu gewährleisten. Auf der Basis erster Messungen, in denen Protochlorophyllid A in Methanol gelöst wurde, konnte ein vorläufiges Modell für die angeregten Zustandsprozesse formuliert werden. Dieses Modell wurde dann mit den Ergebnissen von Pumpwellenlängen- und Lösungsmittel-abhängigen Experimenten weiter verfeinert. Zusätzlich zu den Femtosekunden-zeitaufgelösten transienten Absorptionsexperimenten wurden Pikosekunden-zeitaufgelöste Fluoreszenzmessungen durchgeführt, um das vorgeschlagene Modell zu erhärten. Drei charakteristische Zeitkonstanten im Bereich von 4 bis 200 ps konnten in den transienten Absorptionsdaten gefunden werden, wenn Protochlorophyllid A

in polaren Lösungsmitteln wie Methanol oder Acetonitril gelöst wurde. In dem unpolaren Lösungsmittel Cyclohexan wurde nur eine einzige kinetische Komponente (4.7 ps) identifiziert, während die Fluoreszenzdaten unabhängig vom gewählten Lösungsmittel keinen Beitrag der 200-ps-Komponente zeigen.

Das auf der Grundlage dieser Daten verfeinerte Modell, basiert auf der Anwesenheit eines intramolekularen ladungsseparierten nicht-fluoreszierenden Zustand, dessen Potentialminimum als Funktion der Lösungsmittelpolarität stabilisiert bzw. in unpolarer Umgebung destabilisiert wird. Darüber hinaus kann auf die Abwesenheit einer intermolekularen Keto-Enol-Tautomerisierung in der Relaxation von photo-angeregtem Protochlorophyllid A in alkoholischer Lösung geschlossen werden, da die transienten Absorptionsdaten für Protochlorophyllid A in Methanol nicht von denen in Acetonitril abweichen. Dies ist von besonderem Interesse, da einige Reaktionsmechanismen, die für die enzymatische Reduktion von Protochlorophyllid A zu Chlorophyllid A vorgeschlagen wurden, eine solche Tautomerisierung in Verbindung mit der Enzymmatrix beinhalten. Die nicht-exponentielle Relaxationsdynamik von Protochlorophyllid A wurde verglichen mit dem langlebigen und fluoreszierenden  $S_1$ -Zustand des Magnesium-Oktaethylprophyrins. Dieser Vergleich legt nahe, dass dem Cyclopentanonring, der das charakteristische strukturelle Unterscheidungsmerkmal zwischen den beiden Systemen darstellt, eine entscheidende Rolle in der Bildung des intramolekularen ladungsseparierten Zustandes und damit in der Photophysik von Protochlorophyllid A zukommt. Abschliessend wurden die experimentellen Ergebnisse von Protochlorophyllid A in Lösung mit den Reaktionsmechanismen verglichen, die vorgeschlagen wurden, um die enzymatische Reduktion von Protochlorophyllid A zu erklären.

Nach den Untersuchungen an ausgewählten biologischen Photorezeptoren wurden im dritten Teil dieser Arbeit Experimente vorgestellt, die die Licht-induzierten Prozesse in einem tetranuklearen organometallischen Komplex charakterisieren. Der untersuchte vierkernige Ruthenium-Palladium-Komplex stellt eine strukturell einfache künstliche Lichtsammelantenne mit einem zentral integrierten und sterisch leicht zugänglichen Reaktionszentrum dar. Dieses System und die monomeren Rutheniumkomplexe, die in Ergänzung zu dem vierkernigen Ruthenium-Palladium-Komplex untersucht wurden, wurden in der Arbeitsgruppe von Dr. Sven Rau und Prof. Dirk Walther am Institut für Anorganische Chemie der Friedrich-Schiller-Universität in Jena synthetisiert. Für die in diesem Teil der Arbeit durchgeführten Experimente wurde eine Kombination aus transientser Absorptions- und

transienter Gitterspektroskopie gewählt, um eine breitbandige spektrale Charakterisierung des angeregten Zustandes zu gewährleisten und eine sehr präzise Bestimmung der charakteristischen Zeitkonstanten zu ermöglichen. Nach einer kurzen Einführung in artifizielle Photosynthese beginnt das Kapitel III mit der Diskussion der Ergebnisse von zeitaufgelösten Messungen an  $[(\text{tbbpy})_2\text{Ru}(\text{tmbiH}_2)]^{2+}$ . Dieser Komplex bildet die peripheren Teile der vierkernigen Gesamtantenne. Die experimentellen Ergebnisse können mit einem für diese Art von Übergangsmetallkomplexen typischen Modell erklärt werden: Lichtabsorption in einen Singulett- Metall- Liganden- Ladungstransferzustand führt zu einem ultraschnellen Übergang in einen Triplett- Ladungstransferzustand, in dem auf einer Pikosekundenzeitskala Energieabgabe an das Lösungsmittel und intramolekulare Schwingungsenergieumverteilung beobachtet wird. Die Frage, auf welchem der beiden strukturell verschiedenen Liganden in  $[(\text{tbbpy})_2\text{Ru}(\text{tmbiH}_2)]^{2+}$  die beobachteten Relaxationsprozesse ablaufen, wurde mit Hilfe von transienten Gittermessungen an der Referenzsubstanz  $[\text{Ru}(\text{tbbpy})_3]^{2+}$  diskutiert. Diese Messungen und zusätzliche Resonanz-Raman-Spektren, die in der Arbeitsgruppe von Prof. Jürgen Popp am Institut für Physikalische Chemie der Friedrich-Schiller-Universität in Jena aufgenommen wurden, zeigen eindeutig, dass die photo-induzierte Anregung und die unmittelbar darauffolgende ultraschnelle Relaxation auf dem Tertbutylbipyridin-Liganden lokalisiert ist. Nach den Experimenten an dem Referenzkomplex  $[\text{Ru}(\text{tbbpy})_3]^{2+}$  und der peripheren Baueinheit,  $[(\text{tbbpy})_2\text{Ru}(\text{tmbiH}_2)]^{2+}$ , wurde die Photophysik der tetranuklearen Lichtsammelantenne untersucht. Die kinetischen Daten zeigen in Abhängigkeit von der Probewellenlänge ein nicht-exponentielles Abklingen der Anregung mit drei bzw. vier charakteristischen Zeitkonstanten. Die beiden kürzesten Abklingzeiten stimmen ausgezeichnet mit den kinetischen Konstanten überein, die für die beiden vorher untersuchten Komplexe gefunden wurden. Eine zusätzlich auftretende 50-ps-Komponente wird durch einen Elektronentransfer von den Ru-Einheiten auf eines der Pd-Zentren erklärt. Der langsamste (220 ps) Prozess wird nur in der Grundzustandsbleichung und nicht in der angeregten Zustandsabsorption beobachtet. Daher wurde vorgeschlagen, diesen Prozess mit einer Equilibrierung der Anregung zwischen den beiden Pd-Zentren zu korrelieren. Die hier präsentierten Ergebnisse stellen die erste experimentelle Beobachtung eines Ru  $\rightarrow$  Pd-Anregungstransfers mittels Femtosekunden-zeitaufgelöster Spektroskopie dar. Darüber hinaus geben sie einen detaillierten und weitreichenden Einblick in die angeregte Zustandsdynamik einer kleinen, strukturell sehr einfachen künstlichen Lichtsammelantenne mit sterisch sehr leicht zugänglichen Reaktionszentren.



Die experimentelle Arbeit dieser Dissertation zielte darauf hin, die Kombination aus Femtosekunden-zeitaufgelöster transientser Absorptions- und transientser Gitterspektroskopie als Methode zur Charakterisierung von lichtinduzierten Primärprozessen in biologischen Photorezeptoren und komplexen künstlich synthetisierten Systemen zu etablieren. Darüber hinaus konnten insbesondere durch Lösungsmittel- und Pumpwellenlängen abhängige Messungen und Vergleiche mit vorgeschlagenen Reaktionsmechanismen detaillierte Einblicke in die Struktur-Eigenschafts- und Dynamik-Funktions-Beziehungen der untersuchten Systeme gewonnen werden.



**Part IV**

**Appendix**



# Appendix - Coherent Artifacts in Integrated Detection

This appendix contains the manuscript of a publication that is based on experiments performed during a three-months research visit at the Department of Chemical Physics of Lund University. The work presented in this chapter was done under the supervision of Dr. Arkady Yartsev in the group of Prof. Villy Sundstrom and deals with the particular appearance of coherent artifact signals (see section 2.1.3) in an integrated detection scheme. The manuscript given in the following section is submitted for publication to the journal *Physical Review A*.

## Coherent artifacts in femtosecond time-resolved transient absorption spectroscopy employing spectrally integrated detection

We study the appearance of coherent artifact signals in transient absorption spectroscopy employing an spectrally integrated detection system, i.e. an experimental situation in which the entire probe-pulse spectrum is detected on a single photodetector. It is shown, that despite the fact that this detection is not sensitive to the color of a single probe-photon, the emergence of dispersion shaped coherent artifact signals in this detection scheme can be attributed to cross-phase modulation. Experimental evidence for contributions other than cross-phase modulation and two-photon absorption to the artifact signal is presented. We introduce a very simple phenomenological model to account for the delay-time dependence of the artifact signal even for very large sample thickness. After discussing the influence of the particular detector design on the appearance of the artifact, we will consider an ex-

perimentally very important case, in which the shape of the coherent artifact is strongly influenced by the presence of the sample itself; thus leading to a situation, in which the artifact signal cannot be accounted for by simple comparison of the kinetics obtained for the solvent only. Finally, an estimate of the relative contribution of the artifact to the overall transient absorption changes is presented that is meant to facilitate the interpretation of short time transients in the present of artifact contributions. Furthermore, this approach allows to estimate the excited state absorption cross section for the case of known pump-intensity dependence of the artifact signal.

## Introduction

Femtosecond time-resolved transient absorption spectroscopy has been proven to be a powerful tool for addressing questions of molecular relaxation and chemical reaction pathways on an ultrafast time-scale. [8–10]. In a typical transient absorption experiment the reaction is initiated by absorption of a strong pump-pulse and interrogated by the interaction of a weak probe-pulse with the photoexcited molecular system. The probe-pulse is commonly tuned to be resonant with a molecular transition and is variably delayed in time with respect to the pump-pulse. The observed signal is directly related to the lowest order non-linear susceptibility  $\chi^{(3)}$ . [57] If the two pulses do overlap within the sample volume at around zero delay-time, non-resonant contributions give rise to signals, which are not related to molecular dynamics of the solute. These contributions are commonly summarized under the term coherent artifact. (Though the nomenclature indicating undesired, unexplainable and uncontrollable signal contributions is somewhat misleading we will adopt it here and use it throughout this publication.) The presence of coherent artifacts is intrinsic to all time-resolved measurements employing ultrashort pulses and special care has to be taken to account for them. This is - as discussed below - of special importance when measuring ultrafast dynamics on a time-scale comparable to the pulse-widths and involving weak optical transitions in the systems under investigation. It is necessary to recall that coherent artifacts are observed in media completely transparent for both pump- and probe-beam. Therefore, an additional complication arises from the fact that in a common liquid phase transient absorption experiment contributions not only from the overlap of the pulses in the solvent but also in the cuvette windows have to be taken into account. This is of particular interest as a typical experimental setup involves a flow-cell with two 1.25

mm thick quartz-windows and a sample thickness of about 100 to 500 mm, thus the total thickness of the cuvette material exceeding the thickness of the sample volume. Several experimental approaches might be exploit in order to reduce the contribution of the coherent artifact to the signal. Generally, but not in any experimental situation applicable, reducing the pump-power results in a minor contribution of the coherent artifact to the overall signal as well as arranging laser-pulse polarizations such that pump- and probe-pulse are polarized perpendicular. If non-standard fused silica cuvettes are to be used, Assel et al. suggest the use of  $\text{CaF}_2$  windows [173] in order to reduce the coherent artifact signal in their measurements. Nevertheless as shown below, this approach might induce different complications by itself and it might be easier to compensate for the coherent artifact during data processing than putting much experimental effort into the avoidance of this contribution. The standard and most commonly employed procedure to account for the coherent artifact is to measure the response of the cuvette filled with the solvent solely under experimentally identical conditions to those used to perform the measurement on the system of interest. The artifact-free signal is obtained subsequently by subtracting the trace measured for the solvent only from the experimental data obtained when measuring the dye in solution.

Several contributions to the so-called coherent artifact have been discussed in the literature. Rasmusson et al. showed that two-photon absorption can account for the time-zero signal in a wide variety of solvents under special experimental situations. [174] In media with instantaneous electronic response the coherent artifact can be used to distract the real and imaginary part of the third order non-linear susceptibility and thus separate the contributions to the signal due to two-photon absorption - related to  $\text{Im}(\chi^{(3)})$  - and cross-phase modulation - associated with  $\text{Re}(\chi^{(3)})$ . [175,176] Both the net energy loss from the probe-pulse (two-photon absorption) and the phase change (cross-phase modulation) of the probe-field induced by the presence of a strong pump-beam modify the transmission of the probe pulse. Nevertheless, cross-phase modulation (XPM) is solely related to a shift of frequency of the probe light and does not lead to any loss of photons when integrated over the full spectral widths of the probe-pulse. Though the main part of this effect giving rise to the typical dispersion-shaped signal [177–180] is due to the third order optical non-linearity, contributions to cross-phase modulation arising from even higher terms of non-linear susceptibility have been reported. [181] These authors used numerical fitting of their data to extract the real and imaginary parts of  $\chi^{(5)}$  for fused silica. Ripoche et al. [182,183] and Lange et a. [184] have employed XPM in fused silica and ionized air to

determine the derivative of the auto-correlation function of their experimental pulses and thus demonstrated that the spectral shift induced to the weak probe- in the presence of a strong pump-pulse can be used to measure autocorrelations in experimental situations, in which commonly used sum-frequency generation is not applicable. The basic physics behind XPM is the pump-induced time-dependent change of the refractive index "experienced" by the weak probe-pulse due to the intensity dependence of the materials susceptibility:

$$n(\omega_{probe}) = n_1 + \frac{n_2}{2} \cdot I_{pump}(t) = \frac{1}{2} \cdot Re(\chi^{(3)}) \cdot |E_{pump}(t)|^2. \quad (8.1)$$

In equation 8.1  $n(\omega_{probe})$  denotes the index of refraction that is experienced by the probe-field, while  $n_1$  refers to the static index of refraction, which is related to the first order non-linear susceptibility  $\chi^{(1)}$  of the medium, and  $n_2$  is the intensity dependent second order index of refraction related to the third order non-linear susceptibility  $\chi^{(3)}$ . In writing this equation, it is assumed that the intensity of the pump-beam is much higher than the probe-intensity, thus  $|E_{pump}(t)| \gg |E_{probe}(t)|$ . In this limit the index of refraction experienced by the probe is not influenced by the presence of the probe itself. Therefore, the presence of the strong pump-beam leads to a modulation of the local index of refraction as "seen" by the pump and therefore in turn to a phase modulation of the probe-field and hence to a time-dependent spectral shift of the probe-spectrum, when overlapping with the pump-pulse. This effect is linear in pump-energy; therefore, as stated above, the overall contribution of the coherent artifact to the transient kinetics can be reduced by reducing the pump-power. The spectral changes induced to the probe-spectrum by the intensity dependence of the refractive index of the material in the presence of the strong pump-beam can easily be detected if the probe-pulse is spectrally dispersed after having passed the sample. [178,179,185] It is important to recall that the spectrally resolved detection is essential to observe XPM-signals as the effect only redistributes photons between different colors. Therefore, it leads to a spectral shift of the probe- but does not cause a net loss or gain of photons in the pulse. For a delay-time chosen such that the probe-pulse overlaps with the leading edge of the pump-pulse a red-shift of the probe-frequencies is observed. This situation results in positive differential absorption signals on the blue side of the probe spectrum and negative signals on the red-side of the probe spectrum. If in contrast the probe-pulse overlaps with the trailing edge of the pump, negative differential absorption signals are observed on the blue side and positive signals on the red side of the probe-



---

spectrum due to the blue-shift imprinted on the probe-frequencies. In other words, XPM preserves the overall number of photons in the weak probe but redistributes the energy over different frequencies instead, thus the effect is not visible when employing an integrated detection scheme. Hence, the literature dealing with a mathematical description of cross-phase modulation and coherent artifacts based on this process aims at a description of single wavelength-kinetics obtained from spectrally dispersed detection of the probe-pulse having passed through the sample. [38,175–177,181–187] Two different approaches have been implemented and reported in literature in order to mathematically derive the actual shape of the coherent artifact signals. Ernsting and coworkers [38] derived in an extended study analytical expressions for the transient absorption signal on the basis of formal expressions of the third order non-linear susceptibility. [57] As Ekvall et al. have shown, [186] those results are in excellent agreement with results obtained from their numerical calculations for thin samples. Among others [175, 176, 181, 185, 188–190], the latter authors employ an approach based on Maxwell's equations leading to two coupled scalar equations that govern the amplitudes of the copropagating pump- and probe-pulse. By numerically integrating these equations Ekvall et al. [186] calculate the amplitudes and phases of the two pulses and thus derive the shape of cross-phase modulation induced signals for samples as thick as 3 mm and thus for thickness that cannot be accounted for by the approach of Ernsting and coworkers [38], who intrinsically assume thin samples. Both derivations are able to explain the characteristic dispersion-like shapes of the coherent artifact signals pointing out that cross-phase modulation leads to the redistribution of probe-photons between different colors preserving the overall energy of the pulse. Thus, if the transmission of the probe-pulse is detected with a single photo-diode and therefore integrating over the full spectral width of the pulse no contribution of cross-phase should be visible in the signal.

Nevertheless, as will be shown and discussed in detail below, under particular but still not uncommon experimental conditions strong coherent artifact signals can be observed even employing integrated detection. This publication focuses on the influence of the detection system on the appearance of the coherent artifact signal in a femtosecond pump-probe experiment, an issue that is only very briefly addressed in literature to the best of our knowledge. [185] Nonetheless, we will show that the design of the detection critically influences the manifestation of coherent artifact signals in the kinetic traces recorded. The following of this contribution is organized as follows: After giving a brief introduction to our experimental setup, we will present our results on coherent artifacts in an integrated

detection scheme. We will discuss in some detail the emergence of the signal under experimental conditions, under which no contribution of cross-phase modulation is supposed to be seen, and show the correlation between detector design and the actual shape of the artifact signal. In addition to the experimental findings, the effect of the spectral sensitivity of the detector is modeled using the analytical expressions derived by Kovalenko et al. [38] to describe cross-phase modulation in very thin samples. Furthermore, the effect of propagation and group-velocity mismatch to the timing of the signal for very thick samples is described on the basis of rather simple equations rather than numerical integration of Maxwell's equations based pulse-propagation equations. [186] Before concluding, we finally want to draw the attention to particular experimental arrangements that can give rise to strong and completely unexpected coherent artifact contributions to the overall transients. Under the experimental conditions discussed the coherent artifact signal cannot be accounted for by simply subtracting the solvent response measured under otherwise identical conditions. Thus, the resulting signal might be easily confused with coherent oscillations excited in the sample. Finally, we present an estimation aiming to approximate the cross-section of the coherent artifact signal and compare it to transient absorption signals of dyes for typical concentrations and average absorption cross-sections. This view aims to provide a guidance to estimate the coherent artifact signal to be expected in ones experimental data.

## Experimental

The setup used to perform the experiments presented here consists of a Clark MXR CPA-2001 regeneratively amplified oscillator system that produces light pulses at 775 nm with pulse durations of 150 fs at 1 kHz repetition rate. The pump pulses were generated in an TOPAS-white (Light Conversion) and used without further compression. The probe wavelength was tuned by an two stage noncollinear optical parametric amplifier (NOPA); the probe pulses were externally compressed to about 20 fs (FWHM of autocorrelation) using a double pass prism compressor in standard geometry. A typical crosscorrelational width (FWHM) measured at the sample position is 30 fs. Berek compensators inserted in into each beam in combination with Glan polarizers ensured the probe to be parallel with the pump polarization. Having passed the sample, detection of the transmitted probe light was done by a Si photodiode. This detection averages over all different colors intrinsically being present in the ultra short probe pulses.

## Results and Discussions

### Coherent Artifact Signals in Integrated Detection

The work presented in this publication was stimulated by the observation of strong coherent artifacts in the transient absorption kinetics monitoring the phot-induced absorption of tetranuclear transition metal [(osmium)<sub>1</sub>(ruthenium)<sub>3</sub>] complexes at 1000 nm (see panel A of figure 1). As these particular systems show an extremely fast ( $\approx 60$  fs) kinetic component [151, 191], it is of great importance to understand the origin of the specific appearance of coherent artifacts under the experimental conditions employed. Nonetheless, the signals clearly displayed the dispersion-like shape reported for spectrally resolved XPM-signals even in the case of spectrally integrated detection and thus under experimental conditions, under which the effect of time-dependent spectral shift of the probe-spectrum is not observable. [192] Therefore, the question arises, if XPM is the right process to account for the observed signals under this experimental conditions or if else a completely different mechanism is the origin of the observed features? A straight forward indication of the boundaries necessary to describe this different mechanism is gained from monitoring the overall timing, i.e. peak-to-peak distance, of the transient traces. Varying the solvent in the cuvette and thus the effective optical length of the sample leads to a change of the peak-to-peak distance (tptp) (data not shown), thus hinting, that the signals observed are related to the step in refractive index experienced by the light pulses at the entrance and exit surfaces of the cuvette windows and the sample volume. In order to test the assumption that such surface-contribution to the coherent artifact is observed and to simplify the evaluation of the data, a series of measurements on fused silica windows of various but well defined thicknesses was performed. The results of these experiments are shown in figure 8.1. All transients observed show a clear two-peak structure that is related to the overlap of the pump- and probe-pulse on the entrance and exit surface of the fused silica window. While the signal recorded for the 0.5 mm thick quartz plate shows the derivative-like shape characteristic for spectrally resolved detected cross-phase modulation signals [177–180, 182–184], the two peaks get increasingly separated due to propagation effects in the thicker samples. [186] The reduced amplitude of the second peak in the 10mm fused silica window can be assigned to propagation induced pulse-spreading but is not discussed further here. As can be seen for delay-times later than the second peak an oscillatory contribution to the signal is observed, [38, 185] which is shown enlarged in the inset of figure 8.1A for 0.5 and 2

mm quartz plates. The origin of this contribution in the particular experimental situation is discussed below.

It is qualitatively obvious, that an increase of the sample thickness leads to a prolongation of the artifact signal over a larger range of delay-times, i.e. an increasing value of the peak-to-peak time  $\tau_{ptp}$ , as the group-velocity difference between pump- and probe-pulse leads to an increasing timing-mismatch on the exit surface with increasing sample thickness. In order to quantify the effect of group-velocity mismatch, the group-velocities of the pump- and probe-pulses are calculated according to:

$$v_g(\lambda) = \frac{c_0}{n(\lambda)} - \lambda \frac{dn}{d\lambda}. \quad (8.2)$$

The only quantity that needs to be known a priori in order to perform this simple calculation is the dispersion relation  $n(\lambda)$ , which is tabulated for most materials used for optical elements. Given the group-velocity dispersion  $v_g(\lambda)$ , the propagation time  $T$  of each pulse through the medium of the thickness  $x$  can be calculated as  $T = x/v_g(\lambda)$  and thus  $\tau_{ptp}$  can be deduced according to  $\tau_{ptp} = T_{pump} - T_{probe}$ . Panel B of figure 8.1 comprises the experimentally determined peak-to-peak distances for the various quartz windows with values calculated based on the group-velocity dispersion in fused silica. The very good agreement between calculation and experiment indeed indicates that the artifact signal appears when the two pulses overlap on each surface of the quartz window. To corroborate this finding further we shifted the probe-wavelength from 1  $\mu\text{m}$  to 870 nm, thus reducing the group-velocity mismatch from  $3.88 \cdot 10^6$  to  $3.40 \cdot 10^6$  m/sec ( $0.013$  to  $0.011 \cdot c_0$ ) keeping all other experimental parameters especially the pulse duration of the probe-pulse (30 fs) constant. Hence, we expect to observe peak-to-peak distances to be reduced compared to the data presented in figure 8.1B.

Figure 8.2 shows the transients measured at 870 nm in a 0.5 and in a 2 mm thick fused silica window upon pumping at 505 nm. As it is obvious, both signals are qualitatively completely different from the signals obtained for probing at 1  $\mu\text{m}$  with all other experimental parameters kept unchanged (compare to transients displayed in figure 8.1). Instead of showing dispersion-like features and presenting a peak with positive and one with negative differential absorption changes, the signals can be characterized by a single feature with negative absorption changes. Note that the amplitude of this signal is about an order of magnitude smaller than the amplitude of the signals shown in figure

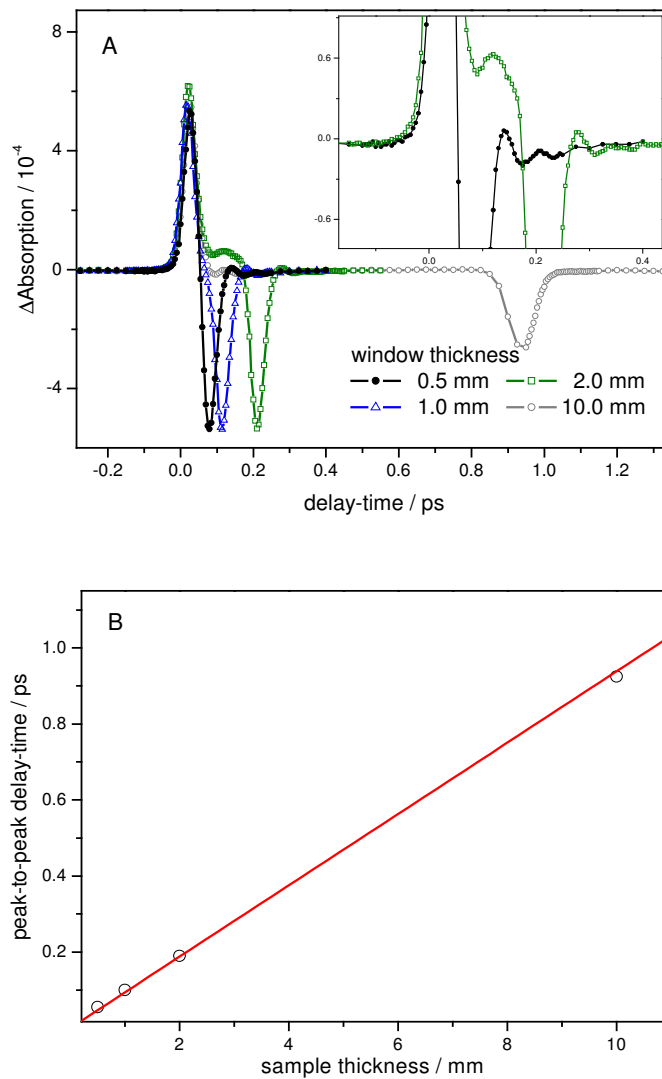


Figure 8.1: The figure displays coherent artifact signals taken integrating over the full spectral width of the probe-pulse centered at 1000 nm for various sample thickness (panel A). The samples were made of fused silica. The pump-pulse was centered at 505 nm and the temporal pulse widths as determined from pump-autocorrelation and cross-correlation measurements were 30 fs. Panel B shows the peak-to-peak distances extracted from the experimental traces in panel A (dots) together with the calculated values for the same pulse- color combination (solid line).

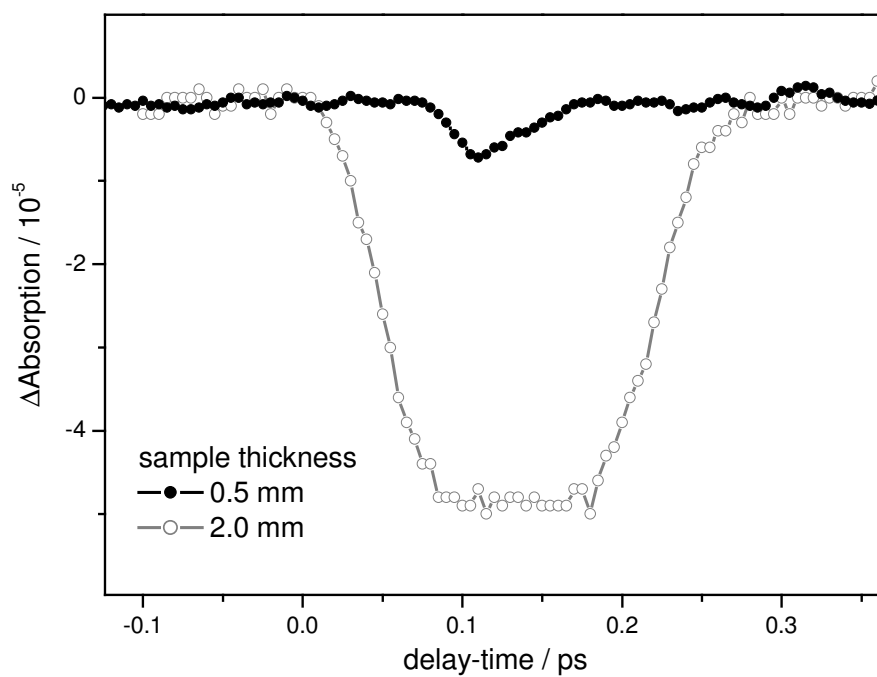


Figure 8.2: The coherent artifact signal measured with the probe-pulse being tuned to 870 nm with is shown, while all other experimental parameters kept identical to those employed in measuring the data depicted in figure 2. The solid dots represent the kinetic trace taken with the 0.5 mm thick fused silica window, while the data measured with the 2.0 mm quartz plate is shown as open circles.

8.1; nonetheless, it can be clearly detected due to the excellent signal-to-noise ratio of our experimental setup. Thus, changing the probe-wavelength from 1000 to 870 nm with otherwise unchanged experimental parameters drastically altered the overall signal shape instead of just reducing the peak-to-peak distance. Hence, a change in pulse-durations, in pump- or probe-power can be excluded to cause the fundamental changes observed in the artifact signal. Therefore, we suspect that the alterations are intrinsically related to the probe-color itself. This finding led us to a thorough examination of the detection scheme used in the experiments; the transient absorption changes are calculated from readings of photodiodes, which consist of silicon. These diodes typically show a sharp drop of photon-to-current conversion efficiency at wavelengths larger than about 950 nm [193], while their efficiency-curve is flat, i.e. parallel to the theoretically derived 100% efficiency conversion curve, over the spectral range of the probe-pulse when centered at 870 nm. Thus, the fundamental difference between the two experimental situations being compared is the fact, that when probing the non-resonant sample dynamics at 870 nm all probe photons are detected with the same efficiency regardless of their frequency, while detection at 1  $\mu\text{m}$  leads to a higher electronic signal for photons from the blue part of the probe-spectrum compared to photons from the low-frequency part of the pulse.

Taking this into account, the presence of a dispersion-shaped coherent artifact signal in an integrated detection scheme and the particular shape of the signal for thick samples might be understood on the basis of cross-phase modulation and group-velocity dispersion. Consider a delay-time that is chosen such that the probe-pulse overlaps with the leading edge of the pump-pulse on the entrance surface of the quartz window ( $\tau_1$  in figure 8.3). As the non-linear index,  $n_2$ , is positive for fused silica [194], this leads to a red-shift of the probe-pulse spectrum according to

$$\dot{\Phi}_{probe}(t) = \omega_0 - n_2 \cdot \frac{dI_{pump}(t)}{dt}. \quad (8.3)$$

In this equation  $\Phi_{probe}$  describes the time-dependent phase of the probe-field,  $n_2$  the lowest order non-linear refractive index of the material,  $\omega_0$  the central frequency of the pulse and  $I_{pump}(t)$  denotes the time-dependent pump-pulse intensity.

In the case of spectrally non-flat detection,  $\lambda_{probe} = 1 \text{ mm}$ , the red-shifted photons are less efficiently converted into an electronic signal due to the spectral sensitivity of the photo-diodes. Thus, for the delay-time  $\tau_1$  (see figure 8.3) the shift of the probe-spectrum

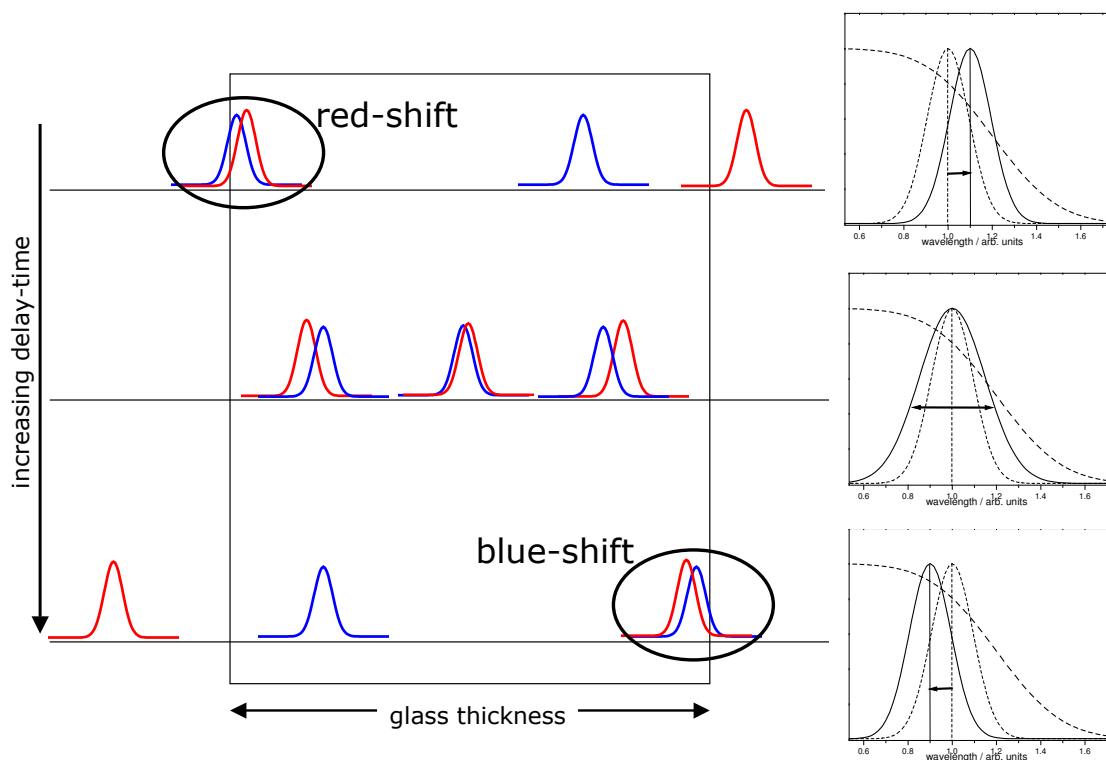


Figure 8.3: This figure schematically illustrates the emergence of the observed coherent artifact signal in an integrated detection scheme. On the left hand side the pulse overlap of pump- and probe-pulse propagating through the medium is shown for three characteristic delay-times. The column on the right hand side illustrates the effect of cross-phase modulation on the initial probe-pulse spectrum (dashed line). Depending on the delay-time the resulting probe-spectrum (solid line) emerges red-shifted ( $\tau_1$ ), blue-shifted ( $\tau_2$ ) or broadened from the sample.



induced by the simultaneous presence of the strong pump-beam leads to less photons being counted in the detector (despite of their actual presence) and thus to the observation of a positive differential absorption signal. In contrast, for the delay-time  $\tau_2$ , chosen such that the probe- catches up with the pump-pulse right before leaving the fused silica window and thus overlapping with the trailing edge of the pump, the blue-shifted probe-photons will be detected more efficiently by the spectrally non-flat photodiode and thus a negative absorption change is recorded. If the time-delay between the pulses is set such that the probe-pulse catches up with the pump in the bulk of the fused silica and leaves the material prior to the pump, cross-phase modulation results in a broadening of the probe-spectrum. [182,187] Therefore, the effects of more efficient detection of blue and less efficient detection of red photons cancel to a good approximation and the net differential absorption signal is zero. (The artifact signal detected in the non-flat-detection scheme for delay-times in between the delays corresponding to the two main peaks is found to be at least an order of magnitude smaller than the peaks but its exact amplitude is very much dependent on day-to-day fluctuations in the experimental setup. We assume that it is crucially dependent on the precise chirp of the pulses. Nevertheless, experiments to address this issue and its correlation to the presence of coherent artifact signals in the flat-detection scheme are pending.)

In order to test above assumption, we changed the spectral efficiency of our detection system at 870 nm in a controllable way by inserting color-filters into the passes of the probe- and the reference-beam after the sample before sending them into the photodiodes. Figure 8.4 displays the resultant kinetic transients taken for a 0.5 (panel A) and 10 mm fused silica window (panel B), while panel C depicts the unperturbed probe-spectrum together with the filter-transmission curves. The upper traces in panels A and B display the situation, in which a filter (NKC5) was inserted cutting the transmission of the probe-light on the red side of the spectrum (red-cutting detection), thus simulating the experimental conditions present when recording the data at 1000 nm. As can be seen clearly this approach leads to experimental traces in extremely good agreement with the kinetics displayed in figure 8.1. It should be noted, that the peak-to-peak distance is reduced compared to the data recorded at 1  $\mu\text{m}$ . This finding complies with our expectation that a reduction in group-velocity mismatch between the two pulses leads to a shortening of the artifact signal. The data with blue-cutting detection was recorded using the filter C3C26 and is shown in the lower trances of panels A and B. In this situation, the initial red-shift of the

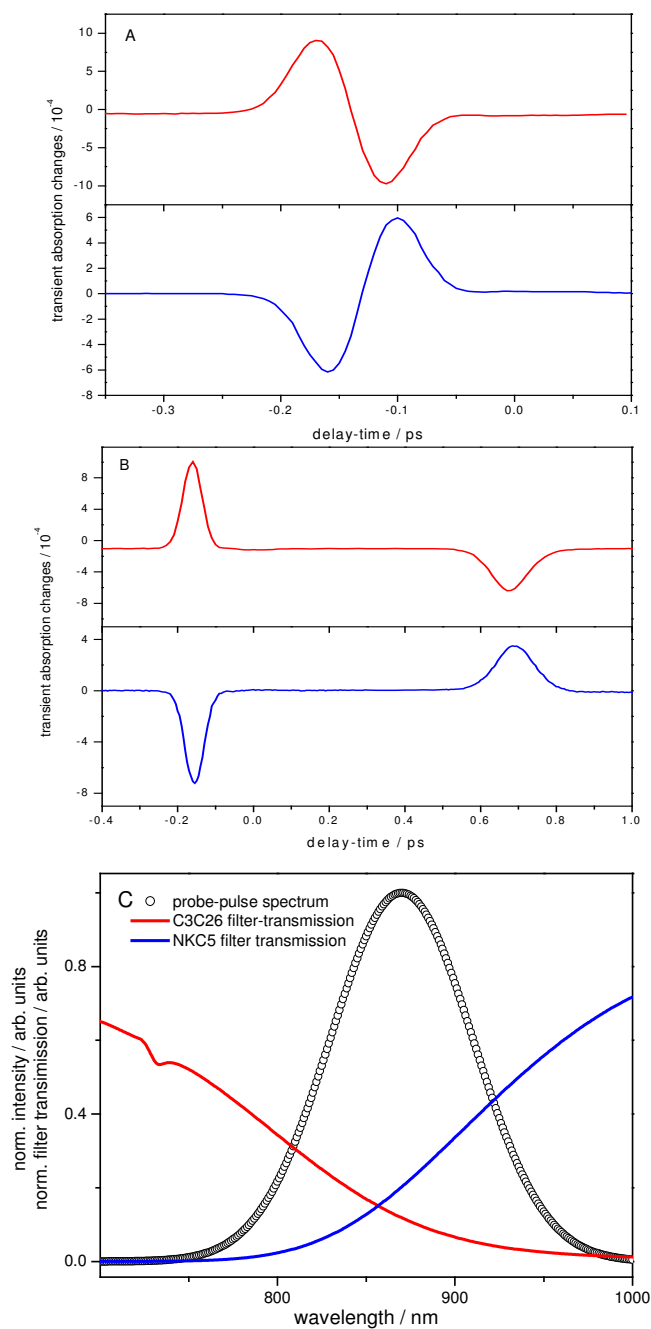


Figure 8.4: Panel A shows the coherent artifact signal in the 0.5 mm thick fused silica window observed with red-cutting detection (upper trace) and blue-cutting detection (lower trace). For details please see text. Pump- and probe-pulse have temporal widths of 30 fs and are centered at 505 and 870 nm, respectively. Panel B displays kinetic traces taken under identical experimental conditions with a 10.0 mm thick quartz plate, while panel B illustrates the spectral transmissions of the filters used for red- (red line) and blue-cutting detection (blue line). For comparison the initial probe-pulse spectrum is shown (dots).

probe-spectrum leads to more photons being detected and thus to a negative differential absorption signal for the delay-time  $\tau_1$  corresponding to the overlap of the pump- and the probe-pulse on the entrance surface of the quartz plate. The blue-shift of the spectrum, when the probe is overlapping with the trailing edge of the pump-pulse on the exit surface of the fused silica is seen as a loss of photons and thus as a positive absorption change in the blue-cutting detections scheme.

Having discussed the emergence of the overall two-peak-structure in the coherent artifact signal based on the process of cross-phase modulation, the presence of oscillations in our signals (see figure 8.1) remains to be explained. The signal is found to exhibit an oscillatory period of 65 fs (corresponding to  $513 \text{ cm}^{-1}$ ) and is completely damped very rapidly within about one ps. As the structure of the oscillations changes drastically when exchanging the fused silica with  $\text{CaF}_2$ , here the period of oscillations is about 104 fs ( $319 \text{ cm}^{-1}$ ) and the damping time in the order of 3 ps, the presence of the particular oscillations must be linked to the fused silica window. In agreement with other authors [38,185,195,196] we assign the oscillations to stimulated Raman scattering (SRS); a process, in which phonons are excited impulsively by the very short pump-pulse, i.e. with a pulse-duration shorter than or comparable to an oscillational period of the phonon. The impulsively excited phonons interact with the probe-pulse and modify its transmission. Depending on the delay-time the probe-pulse gains energy from the phonon and its spectrum appears blue-shifted or it loses energy to the sample and is red-shifted. [195,197] Therefore, no probe-photons are lost due to photo-induced absorption or gained (stimulated emission) nor occurs a bleach of a transition as the effect is observed in completely transparent media. Hence, impulsive stimulated Raman scattering is not visible in an integrated detection scheme and the appearance of the oscillations in our signals is intrinsically linked to the spectral discrimination imposed by the spectrally non-flat silicon detectors. [198]

Figure 8.5 shows the steady-state Raman spectra of our 2 mm fused silica and our  $\text{CaF}_2$  samples. The inset of panel A of figure 8.5 compares the Fourier transform of the SRS signal obtained for  $\text{CaF}_2$  with the steady state Raman spectra of the sample as recorded with a *Labram* Raman-spectrometer (*Horibo-Jobin-Yvon*) The agreement between the oscillatory wavenumbers of  $319 \text{ cm}^{-1}$  as obtained from the time-resolved measurement and  $320 \text{ cm}^{-1}$  from the steady-state data is excellent. The experimental data on the oscillatory part of the signal for delay-times, at which no cross-phase modulation contribution is observed any more, is shown for illustration in panel A. In contrast, the observed

105 fs oscillation period in fused silica (the experimental data is shown in figure 8.5 panel B) does not correspond directly to any of the observed Raman peaks. The corresponding Raman spectrum is displayed in the inset of panel B. But instead, the corresponding wavenumber of  $513 \text{ cm}^{-1}$  falls into the red flank of the strong Raman peak at  $483 \text{ cm}^{-1}$ , which would correspond to an oscillation with a period of 69 fs. This deviation might be due to the very limited number of oscillations observed in fused silica and thus the rather unprecise determination of the oscillation period. Nonetheless, it is remarkable to note, that our experimental setup is capable of resolving oscillations resulting in transient absorption changes as small as  $\pm 10^{-5}$  with a signal-to-noise ratio of about 10. This extraordinary experimental performance allows us to observe the features discussed in this publication with great detail and precision.

### Results of Numerical Simulations

Having discussed our experimental findings of dispersion-shaped coherent artifacts and oscillational contributions to the signals within an integrated detection scheme, a simple way of numerically modeling the detector-efficiency within the framework of XPM is presented. This approach is based on the analytical expression of the differential absorption signal derived by Ernsting and coworkers based on a response-function approach [38]. These authors derive a formula to describe the cross-phase modulation contribution in a thin sample, neglecting propagation effects and group-velocity dispersion, which reads for transform limited pulses (equation 30 of reference [38]):

$$\Delta Abs(\omega, \tau) \propto - \exp\left(\xi^4 T_{pump}^4 \frac{(\omega - \Omega)^2}{1 + 2\xi^2}\right) \cdot \exp\left(-\frac{\tau^2}{T_{pump}^2 \cdot (1 + 2\xi^2)}\right) \cdot \sin\left(\frac{2\xi^2}{1 + 2\xi^2} \cdot \tau \cdot (\omega - \Omega)\right), \quad (8.4)$$

where  $T_{pump}$  denotes the pump-pulse duration,  $\xi$  the ratio  $T_{probe}/T_{pump}$ ,  $\omega$  the detected probe-frequency,  $\Omega$  the central frequency of the probe-pulse and  $\tau$  the experimentally controlled delay-time. This formula displays the same functional form as the one derived by Kang et al. analytically solving the pulse-propagation equations [175] for transform limited pulses based on the non-linear refractive index as given in equation 8.1. Ekvall et al. [186] systematically compared the results obtained from their numerical integration of the pulse-propagation equations with the outcome of the analytical calculations by Ernsting

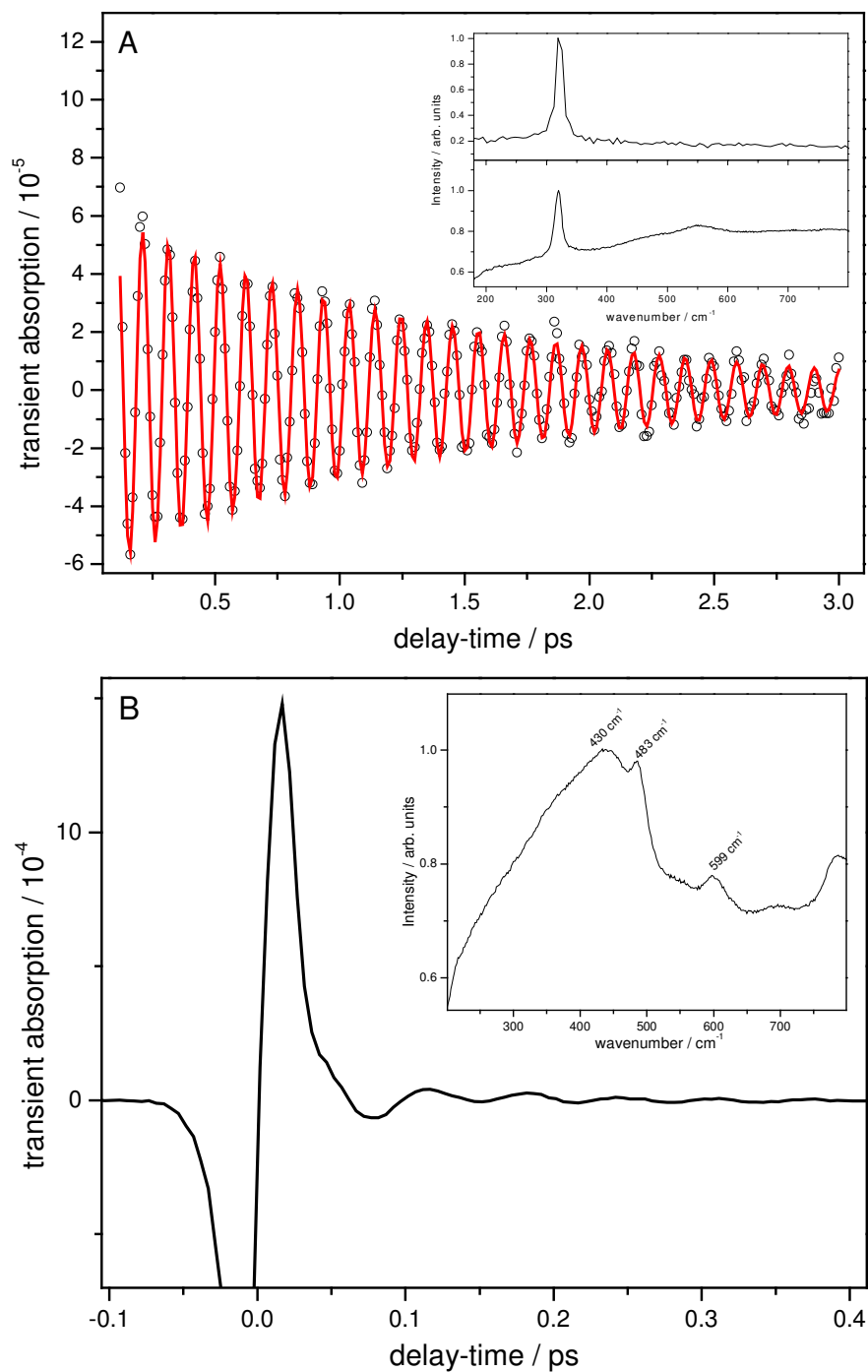


Figure 8.5: Panel A displays the oscillatory part of the signal of the 2 mm fused silica window and the  $\text{CaF}_2$ -sample (symbols refer to experimental data, while the solid line resembles the result of a least square fit). The results of the Fourier-transform of the signal is compared to the Raman-spectrum of the sample in the inset of the panel. Panel B shows the artifact signal taken in the 0.5 mm quartz sample and the inset gives corresponding the Raman-spectrum.

and coworkers. [38] Their finding of excellent agreement between the mathematically different approaches for situations, in which effects due to pulse propagation and group-velocity mismatch can be ignored, i.e. for thin samples, underpins the applicability of both methods to model experimental results.

In order to include the effect of detector efficiency into the model, the effect of XPM to the probe-pulse is calculated according to equation 8.4 multiplied by a function describing the initial spectral shape of the probe-pulse. Subsequently, the effect of photodiode detection is simulated by performing a summation of the individual kinetic traces over the range of the probe-pulse spectrum. To account for the spectrally dependent efficiency of the detector, the single-frequency kinetics are weighted by the normalized transmission of the cut-off filter used to introduce non-flat detection. The result of such calculations is shown in figure 8.6. Panel A displays the transmission curves of the filters *C3C26* and *NKC5* used in the experiments presented above superimposed to the spectrum of the 30 fs probe-pulse centered at 870 nm. The solid lines represent the analytical functions used to approximate the filter transmissions in our numerical simulations. The results of such calculations are shown in panel B. The upper trace corresponds to inserting *C3C26* into the probe-path and is compared to the experimental data obtained under the resulting red-cutting detection, while the lower trace shows the corresponding situation for blue-cutting employing the filter *NKC5* to modify the detector efficiency. The only free parameter in this calculation corresponds to the proportionality factor in equation 8.4 and is adjusted to match the amplitudes of the calculated traces to the experimental data. As can be seen, the overall features of the experimental traces can be very accurately reproduced even within this very simple approach. The fact that the measured kinetics shows a slightly larger peak-to-peak distance than the modeled data is attributed to neglecting of any propagation effects in the derivation of equation 30 in reference [38]. Though, the sample used here is only 500 nm thick, the value of  $\tau_{ptp} = 41$  fs for the given experimental conditions, as calculated based on the group-velocity mismatch of the pulses, is larger than the temporal width of the pump-pulse. Therefore, it is reasonable to expect equation 8.4 to result in slightly underestimated signal-widths.

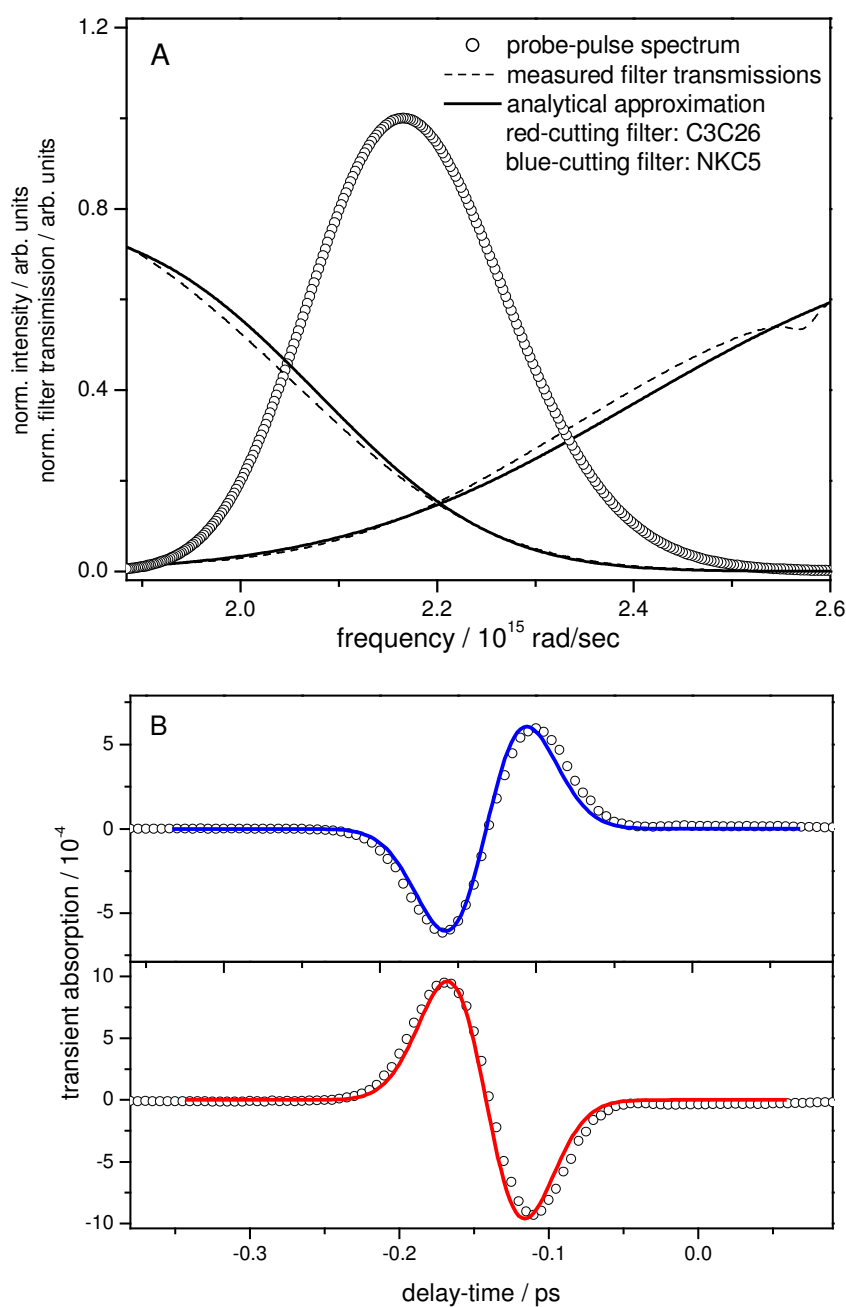


Figure 8.6: Panel A shows the spectral transmission of the filters NKC5 and C3C26 in the region of the probe-pulse spectrum (dashed lines). The solid lines represent the analytical approximations of the filter curves used in our calculations. The results of such calculations are displayed in panel B (solid lines) together with the measured data (dots). The upper trace corresponds to the insertion of filter C3C26 into the probe-beam and thus to red-cutting detection, while the lower trace compares the data taken under blue-cutting detection (insertion of NKC5) with the corresponding calculation.

### Sample-Induced Non-Flat Detection

In this section we extend our focus from single fused silica windows to quartz cuvettes with solvents and dyes, in order to point out an experimentally very important situation, in which strong coherent artifact signals can be observed - even when employing an integrated detection system and taking care of working in the spectrally flat region of the detector. Therefore, no strong contribution of cross-phase modulation either from the solvent or the cuvette itself is to be expected. Such a situation is chosen for measuring the transient shown in panel A of figure 8.7 reflecting the light-induced dynamics of uranin sample in a standard quartz cuvette, ethanol was used as solvent. The light-induced dynamics was initiated by a pump-pulse at 870 nm and interrogated by a probe tuned to 515 nm, the red flank of the ground-state absorption of uranin (see panel C of figure 8.7). Though, the photo-diodes used in the detection scheme show a flat efficiency in the region of the probe-spectrum and pumping at 870 nm should not excite any dye molecules, pronounced signals are observed. Removing the dye from and measuring the response of the cuvette with ethanol only leads to a signal reduced in amplitude by approximately an order of magnitude.

The outcome of a similar experiment is shown in panel B of figure 8.7; in this experiment the dye IR132 dissolved in DMSO was photo-excited at 515 nm and its stimulated emission was probed at 870 nm,  $520\text{ cm}^{-1}$  Stokes-shifted from the maximum of ground-state absorption at 832 nm. The inset of panel B shows the full transient up to delay-times of 200 ps. The stimulated emission kinetics exhibits strong oscillatory features superimposed to the overall rise of the signal for short delay-times. As in the case of uranin dissolved in ethanol - as discussed above - removing the solute from the solvent results in a drastically reduced signal amplitude.

The standard procedure of subtracting the solvent- from the sample-response taken under identical experimental conditions in both cases leads to kinetic traces displaying strong oscillatory contributions at short delay-times. As the effect of the solvent and the cuvette has to be taken care of in the subtraction process, it now has to be concluded that the oscillations observed are due to the presence of the dye molecules and thus it can be deduced that oscillational motions are excited in the dye molecules. This misleading argumentation does not take into account the spectral position of the probe-pulse with respect to the ground-state absorption of the investigated dyes. As can be seen from panels



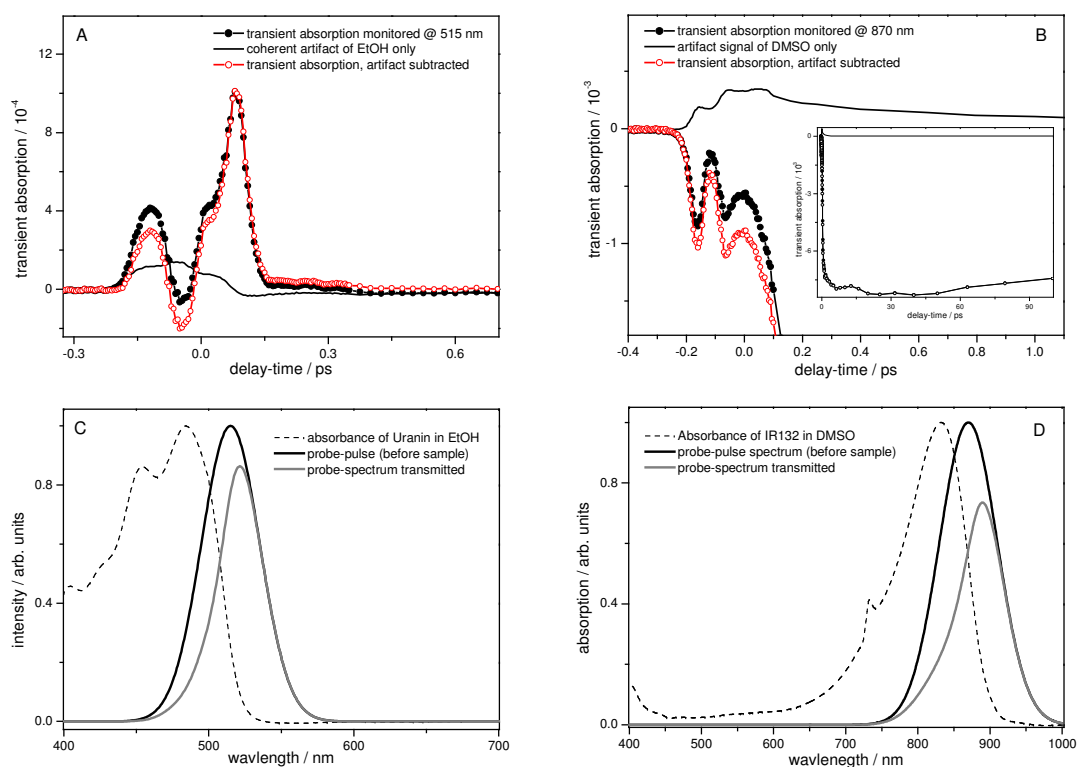


Figure 8.7: This figure summarizes the effect of the internal filter induced by the ground-state absorption of the sample placed in a cuvette on the coherent artifact signal of the front window of the cuvette. Panel A and B show coherent artifact signal of dyes in solution (solid dots) together with the experimental traces resulting in measuring the solvent response only (solid line) and the subtraction of both signals (open red circles). Panel C and D present the ground-state absorption spectra of the dyes in solution (dashed lines) in comparison with the probe-spectrum before entering the sample (black line) and the normalized transmitted probe-spectrum in the absence of cross-phase modulation (gray line). Panels A and C correspond to uranin dissolved in ethanol, while panels B and D summarize the data of IR132 dissolved in DMSO. For details please see text.

C and D of figure 8.7 the spectral position of the probe-beam is chosen such that it overlaps with the longwave-flank of the respective steady-state dye absorption. Therefore, the dye itself constitutes an *internal filter* that imposes a non-flat detection scheme and hence leads to the cross-phase modulation signal from the cuvette entrance-window and partially from the solvent showing up in the experimentally recorded traces. Though, the contribution of coherent artifacts due to a sample induced internal filter might be suppressed due to using tightly focused beams intersecting at a rather large angle, thus by restricting the actual pulse overlap to the sample, this might be extremely challenging for thin sample volumes.

### Estimation of the Artifact Cross-Section

The question remains to be asked for what kind of samples one should be especially aware of the possibility of having artifact signals superimposed to the kinetic traces aimed at. In other words: What is the *cross-section* of coherent artifacts? To address this question we estimated from our experimental parameters a typical photon-flux used in the experiments presented here. With an average energy per pulse of 10.4 mJ and a pump-area of  $9.6 \cdot 10^{-4} \text{ cm}^2$  in the focal plane we calculated the typical photon-flux in our experiments to be in the order of  $3 \cdot 10^{16} \text{ photons/cm}^2$  per pulse. Furthermore, let us call the cross-section of the artifact the empirical proportionality factor between the transient absorption changes due to the artifact  $\Delta A_{art}$  and the excitation energy before entering the cuvette  $I_{pump}$ . This gives rise to a cross-section of the artifact,  $\sigma_{art}$ , in the order of  $0.3 \cdot 10^{-19} \text{ cm}^2$ . In order to compare this number to signals expected from the sample, let us consider that the absorption changes due to the light induced processes in the sample can be written as

$$\Delta A_{samp} = 0.434 \cdot \Delta c \cdot (\sigma_{samp}^{PIA} - \sigma_{samp}^{GS}) \cdot d,$$

wherein  $d$  labels the sample thickness and  $\sigma^{PIA}$  and  $\sigma^{GS}$  refer to the cross-section of the photoinduced absorption and the ground-state absorption, respectively. Expressing the photoinduced concentration change of concentration of molecules in the excited state,  $\Delta c$ , as a function of the pump-intensity in the limit of low sample absorption at the pump-wavelength, e.g. small  $A_{exe}$ , leads to the following ratio of the absorption changes due to the sample and the artifact:

$$\frac{\Delta A_{samp}}{\Delta A_{art}} = 0.434 \cdot \frac{\sigma_{samp}^{PIA} - \sigma_{samp}^{GS}}{\sigma_{art}} \cdot (1 - \exp[-A_{exe}/0.434]). \quad (8.6)$$

---

For our initial experimental situation investigating the ultrafast processes in tetranuclear transition metal [(osmium)<sub>1</sub>(ruthenium)<sub>3</sub>] complexes, that triggered our interest in this subject, artifact absorption changes in the order of 10% of the total absorption changes were observed, thus  $\Delta A_{\text{samp}}/\Delta A_{\text{art}} = 10$ . In this case, the photoinduced absorption changes were recorded at 1000 nm, therefore the probe was far of resonance from the ground state absorption, which is centered at about 560 nm [151, 191]. Hence,  $\sigma_{\text{samp}}^{\text{GS}} = 0$  and assuming the excitation absorption to be 0.1, the excited state absorption cross-section can be estimated to be  $\sim 4 \cdot 10^{-18} \text{ cm}^2$ . In turn, this simple approach can be used to calculate the relative amplitude of the artifact and the signal contribution of the photoexcited sample. For doing so, we recommend to measure the pump-power dependence of the cross-phase modulation signal in the front cuvette used for the experiments and by this to determine the artifact cross-section as defined above. With this information and given the absorption of the sample at the pump-wavelength and estimations for the cross-sections of the ground and the excited state, it is possible to estimate relative contribution of the artifact to the observed short-time transient absorption signal. This should facilitate the correction of the experimental data for the coherent artifact contribution considerably and allow for a more precise characterization of the ultrafast processes observed.

From equation 8.6 it is obvious, that the contribution of the coherent artifact to the overall short time behavior of the transient signal can be quite dominating [173] especially for molecules with either small absorption at the pump-wavelength or when probing in a spectral region, in which the photoinduced absorption is spectrally very close to the ground state absorption. In the latter case  $\sigma_{\text{samp}}^{\text{PIA}} \approx \sigma_{\text{samp}}^{\text{GS}}$ , and therefore according to equation 8.6 strong artifact contributions can be observed. On the other hand as discussed above, in systems with large ground state absorption cross-sections such as carotenoids for example [199] the actual solute response by far dominates over any cross-phase modulation contribution. Nonetheless, the transition-metal complexes, that triggered our interest in coherent artifacts clearly belong to the class of systems that possess a small absorption cross-section at the pump-wavelength and show very rich ultrafast excited-state dynamics, thus making it crucial to account for the coherent artifacts in an appropriate and precise way [151, 191].

## Conclusions

The influence of the detector characteristics on the observation of coherent artifact signals in an integrated detection scheme is described. The presence of non-flat detection either because of employing probe-pulses spectrally centered in a region of non-flat photodiode sensitivity or due to the use of color filters, i.e. to filter pump-stray light out of the probe channel leads to an effective spectral resolution and thus to the observation of dispersion-shaped coherent artifact signals, which otherwise are expected to show up only in spectrally resolved detection. It has been shown, that special care has to be taken when the probe-spectrum overlaps with the dye spectrum in a region where the absorption of the dye changes drastically as a function of wavelength. In this case, the sample absorption itself results in an internal filter and hence leads to the observation of strong artifact signals. Under such experimental conditions, a simple subtraction of the kinetic trace obtained for the solvent only from the experimental data is not capable of accounting for the artifact signal. Thus, the cross-phase modulation contribution to the overall signal has to be fitted to a phenomenological model in order to include it into the fitting process. Under special experimental conditions, i.e. spectrally flat detection, residual artifact signals, usually one to two orders of magnitude smaller than for non-flat detection under otherwise identical experimental conditions, are observed. Despite the presence of these residual contribution, the combination of cross-phase modulation and detection efficiency is capable of accounting for the overall major features of coherent artifact signals in an integrated detection scheme in a qualitative and quantitative way.

# Bibliography

- [1] S. Claesson (Ed.). Fast reactions and primary processes in chemical kinetics. *Proceedings of the Fifth Nobel Symposium*, 1967.
- [2] The Nobel Foundation.
- [3] T.H. Maiman. *Nature*, **187**:493, 1960.
- [4] A.M. Prokhorov. *Sov. Phys. JETP*, **7**:1140, 1958.
- [5] A.L. Shawlow and C.H. Townes. *Phys. Rev.*, **112**:1940, 1958.
- [6] C. Rulliere, editor. *Femtosecond Laser Pulses*. Springer Verlag, Berlin, 1998.
- [7] M.Eigen. Immeasurable fast reactions. *Nobel lectures*, 1972.
- [8] J. Manz and L. Woeste, editors. *Femtosecond Chemistry*, volume I and II. Wiley-VCH, New York.
- [9] M. Chergui, editor. *Femtochemistry*. World Scientific, Singapore, 1997.
- [10] V. Sundstrom, editor. *Femtochemistry and Femtobiology*. World Scientific, Singapore, 1998.
- [11] N.A. Papadogiannis, B. Witzel, C. Kalpouzos, and D. Charalambidis. *Phys. Rev. Lett.*, **83**:4289, 1999.
- [12] M. Hentschel, R. Kienberger, Ch. Spielmann, G.A. Reider, N. Milosevic, T. Brabec, P. Corkum, U. Heinzmann, M. Drescher, and F. Krausz. *Nature*, **414**:509, 2001.
- [13] V. Sundstrom. *Prog. Quantum Electr.*
- [14] V. Sundstrom, T. Pullerits, and R. van Grondelle. *J. Phys. Chem. B*, **103**:2327, 1999.

- [15] V. Sundstrom, editor. *Femtochemistry and Femtobiology: Ultrafast reaction dynamics at Atomic-Scale Resolution*. Imperial College Press, London, 1997.
- [16] R. Ghanem, Y. Zu, J. Pan, T. Hoffman, J. Andersson, T. Polivka, T. Pascher, S. Styring, L. Sun, and V. Sundstrom. *Inorg. Chem.*, **41**:6258, 2002.
- [17] L. Banares, A.A. Heikel, and A.H. Zewail. *J. Phys. Chem.*, **96**:4127, 1992.
- [18] K. Ishii, S. Takeuchi, and T. Tahara. *Chem. Phys. Lett.*, **398**:400, 2004.
- [19] M. Bischoff, G. Hermann, S. Rentsch, D. Strehlow, s. Winter, and H. Chosrowjan. *J. Phys. Chem. B*, **104**:1810, 2000.
- [20] B. Dietzek, R. Maksimenka, G. Hermann, J. Popp, W. Kiefer, and M. Schmitt. *Chem. Phys. Chem.*, **5**:1171, 2004.
- [21] B. Dietzek, R. Maksimenka, G. Hermann, W. Kiefer, J. Popp, and M. Schmitt. *accepted for publication in Chem. Phys. Lett.*
- [22] A. Sautter, B.K. Kaletas, D.G. Schmid, R. Dobraawa, M. Zimine, G. Jung, I.H.M. van Stokkum, L. DeCola, R.M. Williams, and F. Würthner. *J. Am. Chem. Soc.*, **127**:6719, 2005.
- [23] F. Würthner, C.C. You, and C.R. Saha-Möller. *Chem. Soc. Rev.*, **33**:133, 2004.
- [24] O. Bossart, L. DeCola, S. Welter, and G. Calzaferri. *Chem. Eur. J.*, **10**:5771, 2004.
- [25] G. Calzaferri, S. Huber, H. Maas, and C. Minkowski. *Angew. Chem.*, **115**:3860, 2003.
- [26] M.L. Abrahamsson, H. Berglund Baudin, A. Tran, C. Philouze, K.E. Berg, M.K. Raymond-Johansson, L. Sun, B. Akermark, S. Styring, and L. Hammarstrom. *Inorg. Chem.*, **41**:1534, 2002.
- [27] S. Ott, M. Kritikos, B. Akermark, and L. Sun. *Angew. Chem. Int. Ed.*, **42**:3285, 2003.
- [28] S. Ott, M. Kritikos, B. Akermark, L. Sund, and R. Lomoth. *Ang. Chem. Int. Ed.*, **43**:1006, 2004.
- [29] J.T.M. Kennis, I.H.M. van Stokkum, S. Crosson, M. Gauden, K. Moffat, and R. van Grondelle. *J. Am. Chem. Soc.*, **126**:4512, 2004.

- [30] R.T.F. Jukes, V. Adamo, F. Hartl, P. Belser, and L. DeCola. *Coord. Chem. Rev.*, **249**:1327, 2005.
- [31] J.J.D. de Long, P.R. Hania, A. Pugzlys, L.N. Lucas, M. de Loos, R.M. Kellogg, B.L. Feringa, K. Duppen, and J.H. van Esch. *Ang. Chem. Int. Ed.*, **44**:2373, 2005.
- [32] T. Siebert, V. Engel, A. Materny, W. Kiefer, and M. Schmitt. *J. Phys. Chem. A*, **107**:8355, 2003.
- [33] T. Siebert, R. Maksimenka, A. Materny, V. Engel, W. Kiefer, and M. Schmitt. *J. Raman Spec.*, **33**:844, 2002.
- [34] T. Polivka and V. Sundstrom. *Chem. Rev.*, **104**:2021, 2004.
- [35] F. Schotte, M.H. Lim, T.A. Jackson, A.V. Smirnov, J. Soman, P.S Olson, G.N. Phillips, M. Wulff, and P.A. Anfinrud. *Science*, **300**:1944, 2003.
- [36] V. Blanchet, M.Z. Zgierski, T. Seideman, and A. Stolow. *Nature*, **401**:53, 1999.
- [37] S. Mukamel. *Ann. Rev. Phys. Chem.*, **41**:647, 1990.
- [38] S.A. Kovalenko, A.L. Dobryakov, J. Ruthmann, and N.P. Ernsting. *Phys. Rev. A*, **59**:2360, 1999.
- [39] J. Shah, editor. *Ultrafast Spectroscopy of Semiconductors and Semiconductor Nanostructures*. Springer, New York, 1996.
- [40] A. Myers. *J. Raman Spec.*, **28**:389, 1997.
- [41] R.G. Brewer and R.L. Shoemaker. *Phys. Rev. A*, **6**:2001, 1972.
- [42] N. Kohles, P. Aechter, and A. Laubereau. *Opt. Commun.*, **65**:391, 1988.
- [43] P.N. Butcher and D. Cotter, editors. *The elements of nonlinear optics*. Cambridge University Press, London, 1990.
- [44] C.H. Brito-Cruz, J.P. Gordon, P.C. Becker, R.L. Fork, and C.V. Shank. *IEEE J. Quant. Electr.*, **24**:261, 1998.
- [45] W.T. Pollard, S.Y Lee, and R.A. Mathies. *J. Chem. Phys.*, **92**:4012, 1990.

- [46] W.T. Pollard, C.H. Brito-Cruz, C.V. Shank, and R.A. Mathies. *J. Chem. Phys.*, **90**:199, 1989.
- [47] M. Bischoff. Femtosekundenspektroskopische untersuchungen an phytochromen. *Dissertation, Universitat Jena*, 2000.
- [48] C. Galli, K. Wynne, S.M. LeCours, and R.M. Hochstrasser. *Chem. Phys. Lett.*, **206**:493, 1993.
- [49] K. Ekvall, P. van der Meulen, C. Dhollande, L.E. Berg, S. Pommeret, R. Naskrecki, and J.C. Mialocq. *J. Appl. Phys.*, **87**:2340, 2000.
- [50] H.J. Eichler, P. Gunter, and D.W. Pohl, editors. *Laser-induced dynamical gratings*. Springer Verlag, Berlin, 1986.
- [51] M. Terazima. *Chem. Phys. Lett.*, **218**:574, 1994.
- [52] F.W. Deeg, J.J. Stankus, S.R. Greenfield, V.J. Newell, and M.D. Fayer. *J. Chem. Phys.*, **90**:6893, 1989.
- [53] L. Gomez-Jahn, J. Kasinski, and R.J.D. Miller. *Chem. Phys. Lett.*, **125**:500, 1986.
- [54] E. Vauthey and A. Henseler. *J. Chem. Phys.*, **100**:170, 1996.
- [55] T. Siebert, V. Engel, A. Materny, W. Kiefer, and M. Schmitt. *J. Phys. Chem. A*, **107**:8355, 2003.
- [56] B. Dietzek, R. Maksimenka, T. Siebert, E. Birckner, W. Kiefer, J. Popp, and M. Schmitt. *Chem. Phys. Lett.*, **397**:110, 2004.
- [57] S.H. Mukamel. *Principles of Nonlinear Optical Spectroscopy*. Oxford University Press, London, 1995.
- [58] C.J. Bardeen, S.J. Rosenthal, and C.V. Shank. *J. Phys. Chem. A*, **103**:10506, 1999.
- [59] O. Golonzka, M. Khalil, N. Demirdöven, and A. Tokmakoff. *J. Chem. Phys.*, **115**:10814, 2001.
- [60] M.D. Fayer. *Annu. Rev. Phys. Chem.*, **52**:315, 2001.



- [61] M.L. Cowan, B.D. Bruner, N. Huse, J.R. Dwyer, B. Chugh, E.T.J. Nibbering, T. El-sasser, and R.J.D. Miller. *Nature*, **434**:199, 2005.
- [62] T. Brixner, J. Stenger, H.M. Vaswani, M. Cho, R.E. Blankenship, and G.R. Fleming. *Nature*, **434**:625, 2005.
- [63] S. Meyer, M. Schmitt, A. Materny, W. Kiefer, and V. Engel. *Chem. Phys. Lett.*, **281**:332, 1997.
- [64] S. Meyer, M. Schmitt, A. Materny, W. Kiefer, and V. Engel. *Chem. Phys. Lett.*, **301**:248, 1999.
- [65] S. Meyer. Nichtlineare kurzzeitspektroskopie an kleinen molekülen. *Dissertation, Universität Würzburg*, 1999.
- [66] W. Demtroder. *Laserspektroskopie*. Springer Verlag, Berlin, 1993.
- [67] H.J. Eichler, P. Gunter, and D.W. Pohl, editors. *Laser Induced Dynamic Gratings*. Springer Verlag, Berlin, 1986.
- [68] J.A. Shirley, R.J. Hall, and A.C. Eckbreth. *Opt. Lett.*, **5**:380, 1980.
- [69] Y. Prior. *Appl. Opt.*, **19**:1741, 1980.
- [70] S. Maeda, T. Kamisuki, and Y. Adachi, editors. *Advances in Non-Linear Spectroscopy*. J. Wiley and Sons, New York, 1998.
- [71] K. Holloday, M. Croci, E. Vauthey, and U.P.Wild. *Phys. Rev. B*, **47**:14741, 1993.
- [72] P. Quail, M.T. Boylan, B.M. Parks, T.W. Short, Y. Xu, and D. Wanger. *Science*, **268**:675, 1995.
- [73] R.D. Vierstra. *Plant. Physiol.*, **103**:679, 1993.
- [74] G. Hermann. *Photophysikalische und photochemische Primäprozesse bei der Photo-transformation des Phytochroms von der Pr in die Pfr-Form*. Habilitation - Friedrich Schiller Universität Jena, Jena, 1993.
- [75] H. Falk, editor. *The chemistry of linear oligopyrroles and bile pigments*. Springer Verlag, Wien, 1998.

- [76] M. Betz. *Biol. Chem.*, **378**:167, 1997.
- [77] R. MacColl. *J. Struct. Biol.*, page 311, 1998.
- [78] N.T. de Marsac. *Photosynth. Res.*, **76**:197, 2003.
- [79] B. Knipp, M. Muller, N. Metzler-Nolte, T.S. Balaban, S.E. Braslavska, and K. Schaffner. *Helv. Chim. Acta*, **81**:881, 1998.
- [80] A.J. Wurzer, T. Wilhelm, J. Piel, and E. Riedle. *Chem. Phys. Lett.*, **299**:296, 1999.
- [81] M. Durring, G.B. Schmidt, and R. Huber. *J. Mol. Biol.*, **217**:577, 1997.
- [82] K. Brejc, R. Ricner, R. Huber, and S. Steinbacher. *J. Mol. Biol.*, **249**:633, 1995.
- [83] J. Matysik, P. Hildebrandt, W. Schlamann, S.E. Braslavsky, and K. Schaffner. *Biochemistry*, **34**:10497, 1995.
- [84] H. Foersterdorf, E. Mummert, E. Schaefer, H. Scheer, and F. Siebert. *Biochemistry*, **35**:10793, 1996.
- [85] F. Andel III, J.C. Lagarias, and R. Mathies. *Biochemistry*, **35**:15997, 1996.
- [86] M. Stanek and K. Grubmayr. *Chem. Eur. J.*, **4**:1653, 1998.
- [87] M. Stanek and K. Grubmayr. *Monatsh. Chemie*, **131**:879, 2000.
- [88] J.Y. Suzuki, D.W. Bolivar, and C.E. Bauer. *Annual. Rev. Genet.*, **31**:61, 1997.
- [89] S. Beale. *Photosynth. Res.*, **60**:43, 1999.
- [90] W.T. Griffinths. *FESB Lett.*, **49**:196, 1974.
- [91] K. Apel, H.J. Santel, T.E. Redlinger, and H. Falk. *Eur. J. Biochem.*, **111**:251, 1980.
- [92] N. Lebedev and M. Timko. *Photosynth. Res.*, **58**:5, 1998.
- [93] A.H. Zewail. *Angew. Chemie*, **112**:2587, 2000.
- [94] M.H. Vos and J.L. Martin and. *Biochim. Biophys. Acta*, **1411**:1, 1998.
- [95] D.J. Heynes, C.N. Hunter, I.H.M. van Stokkum, R. van Grondelle, and M.L. Groot. *Nat. Struct. Biol.*, **10**:491, 2003.

- [96] M. Gouterman in D. Dolphin (Ed.). The porphyrins. *Academic Press, New York*, page 1, 1978.
- [97] M. Nissum, J.M. Funk, and W. Kiefer. *J. Raman Spectrosc.*, **30**:605, 1999.
- [98] H.Z. Yu, J.S. Baskin, and A.H. Zewail. *J. Phys. Chem. A*, **106**:9845, 2002.
- [99] J. Rodruiguez, C. Kirmaier, and D. Holten. *J. Am. Chem. Soc.*, **111**:6500, 1989.
- [100] J. Rodruiguez, C. Kirmaier, and D. Holten. *J. Chem. Phys.*, **94**:6020, 1991.
- [101] H.A. Fererdea, J. Terspsta, and D.A. Wiersma. *J. Chem. Phys.*, **91**:3296, 1989.
- [102] J. Stenger, D. Madsen, J. Dreyer, P. Hamm, E.T.J. Nibbering, and T. Elsaesser. *Chem. Phys. Lett.*, **354**:256, 2002.
- [103] D.M. Mittleman, R.W. Schoenlein, J.J. Shiang, V.L. Colvin, A.P. Alivisatos, and C.V. Shank. *Phys. Rev. B*, **49**:14435, 1994.
- [104] Y. Nagasawa, S.A. Passino, T. Joo, and G.R. Fleming. *J. Chem. Phys.*, **106**:4840, 1997.
- [105] T. Gustavsson, G. Baldacchina, J.C. Mialocq, and S. Pommeret. *Chem. Phys. Lett.*, **236**:587, 1995.
- [106] T. Elsaesser and W. Kaiser. *Annu. Rev. Phys. Chem.*, **42**:83, 1991.
- [107] G.G. Gurzadyan, T.H. Tran-Thi, and T. Gustavsson. *J. Chem. Phys.*, **108**:385, 1998.
- [108] S. Akimoto, T. Yamazaki, I. Yamazaki, and A. Osuka. *Chem. Phys. Lett*, **309**:177, 2000.
- [109] J.S. Baskin, H.Z. Yu, and A.H. Zewail. *J. Phys. Chem. A*, **106**:9837, 2002.
- [110] B. Mysliwa-Kurdziel, J. Kruk, and K. Strzalka. *Photochem. Photobiol.*, **79**:62, 2004.
- [111] M. Enescu, K. Steenkeste, F. Tfibel, and M.P. Fontaine-Aupart. *Phys. Chem. Chem. Phys.*, **4**:6092, 2002.
- [112] P. Martinsson, J.A.I. Oksanen, M. Hilgendorff, P.H. Hynninen, V. Sundstrom, and E. Akesson. *Chem. Phys. Lett.*, **309**:386, 1999.

- [113] J.A.I. Oksanen, P. Martinsson, E. Akesson, P.H. Hynninen, and V. Sundstrom. *J. Phys. Chem. A*, **102**:4328, 1998.
- [114] S. Hess, E. Akesson, R.J. Coqdell, T. Pullerits, and V. Sundstrom. *Biophys. J.*, **69**:2211, 1995.
- [115] H. Klement, M. Helfrich, U. Oster, S. Schoch, and W. Rudiger. *Eur. J. Biochem.*, **265**:862, 1999.
- [116] H. Klement. *NADPH:Protochlorophyllid-Oxidoreduktase (POR): Untersuchungen zu einem Schlüsselenzym der Chlorophyll-Biosynthese in Angiospermen*. Dissertation - Ludwig Maximilians Universität München, München, 2001.
- [117] D. Zigmantas, T. Polivka, R.G. Hiller, A. Yartsev, and V. Sundstrom. *J. Phys. Chem. A*, **105**:10296, 2001.
- [118] J.A. Bautista, R.E. Connors, B.B. Raju, R.G. hiller, F.P. Sharples, D. Gosztola, M.R. Wasielewski, and H.A. Frank. *J. Phys. Chem. B*, **103**:8751, 1999.
- [119] H.A. Franck, J.A. Bautista, J. Josue, Z. Pendon, R.G. Hiller, F.P. Sharples, D. Gosztola, and M.R. Wasielewski. *J. Phys. Chem. B*, **104**:4569, 2000.
- [120] D. Zigmantas, R.G. Hiller, A. Yartsev, V. Sundstrom, and T. Polivka. *J. Phys. Chem. B*, **107**:5339, 2003.
- [121] H. Wilks and M. Timko. *Proc. Nat. Acad. Sci. USA*, **92**:724, 1995.
- [122] H. Satzger, C. Root, C. Renner, R. Behrendt, L. Moroder, J. Wachtveitl, and W. Zinth. *Chem. Phys. Lett.*, **396**:191, 2004.
- [123] D. Mandal, T. Tahara, and S.R. Meech. *J. Phys. Chem. B*, **108**:1102, 2004.
- [124] A. Yartsev, J.L. Alvarez, U. Aberg, and V. Sundstrom. *Chem. Phys. Lett.*, **243**:281, 1995.
- [125] M. Verngris, I.H.M. van Stokkum, X. He, A.F. Bell, P.J. Tonge, R. Van Grondelle, and D.S. Larsen. *J. Phys. Chem. A*, **108**:4587, 2004.
- [126] M. Chachisvilis and A.H. Zewail. *J. Phys. Chem. A*, **103**:7408, 1999.

- [127] S.V. Rao, N.K.M.N. Srinivas, D.N. Rao, L. Giribabu, B.G. Maiya, R. Philip, and G.R. Kumar. *Opt. Commun.*, **192**:123, 2001.
- [128] M.C. Yoon, D.H. Jeong, S. Cho, D. Kim, H. Rhee, and T. Joo. *J. Chem. Phys.*, **118**:164, 2003.
- [129] Min D, K, T. Joo, M.C. Yoon, C.M. Kim, Y.N. Hwang, D. Kim, N. Aratani, N. Yoshida, and A. Osuka. *J. Chem. Phys.*, **114**:6750, 2001.
- [130] H.S. Cho, N.W. Song, Y.H. Kim, S.C. Jeoung, S. Hahn, D. Kim, S.K. Kim, N. Yoshida, and A. Osuka. *J. Phys. Chem. A*, **104**:3287, 2000.
- [131] A.V. Gusev, E.O. Danilov, and M.A.J. Rodgers. *J. Phys. Chem. A*, **106**:1993, 2002.
- [132] G. Hermann J. Popp M. Schmitt B. Dietzek, W. Kiefer. *submitted to J.Phys.Chem.B*, 2005.
- [133] J.F.G.A. Jansen, E.M.M. de Brabander-van den Berg, and E.W. Meijer. *Science*, **266**:1226, 1994.
- [134] O.A. Matthews, A.N. Shipway, and J.F. Stoddart. *Prog. Polym. Sci.*, **23**:1, 1998.
- [135] T.H. Ghaddar, J.F. Wishart, D.W. Thompson, J.K. Whitesell, and M.A. Fox. *J. Am. Chem. Soc.*, **124**:8285, 2002.
- [136] L. Bottcher, J. Blumhoff, S. Schebesta, K. Lamm, H. Goerls, K. Schmuck, S. Rau, and D. Walther. *submitted to Eur. J. Inorg. Chem.*
- [137] B. O'Regan and M. Gratzel. *Nature*, **353**:737, 1991.
- [138] Supramolecular chemistry. *Wiley-VHC: Weinheim*, 1995.
- [139] V. Balzani, A. Credi, and M. Venturi. Supramolecular chemistry. *Wiley-VCH: Weinheim*, 2003.
- [140] C.N. Fleming, K.A. Maxwell, J.M. DeSimone, T.J. Meyer, and J. Papanikolas. *J. Am. Chem. Soc.*, **123**:10336, 2001.
- [141] A. Vlek and J. Heyrovsky in V. Balzani (Ed.). Electron transfer in chemistry vol. 2. *Wiley-VCH: Weinheim*, 2001.

- [142] F. Scandola, C. Chiorboli, M.T. Indelli, and M.A. Rampi in V. Balzani (Ed.). Electron transfer in chemistry vol. 3. *Wiley-VCH: Weinheim*, 2001.
- [143] H. Torieda, K. Nozaki, A. Yoshimura, and T. Ohno. *J. Phys. Chem. A*, **108**:4819, 2004.
- [144] N. Damrauer, G. Cerullo, A. Yeh, T.R. Boussie, C.V. Shank, and J.K. McCusker. *Science*, **275**:54, 1997.
- [145] A. Juris, V. Balzani, F. Barigeletti, S. Campagna, P. Belser, and A. von Zelewsky. *Coord. Chem. Rev.*, **84**:85, 1988.
- [146] P.C. Bradley, N. Kress, B.A. Hornberger, R.F. Dallinger, and W.H. Woodruff. *J. Am. Chem. Soc.*, **103**:7441, 1981.
- [147] L.F. Cooley, P. Bergquist, and D.F. Kelley. *J. Am. Chem. Soc.*, **112**:2612, 1990.
- [148] J. Monat and J.K. McCusker. *J. Am. Chem. Soc.*, **122**:4092, 2000.
- [149] J. Kallionen, G. Benko, V. Sundstrom, J.E.I. Korppi-Tommola, and A. Yartsev. *J. Phys. Chem. B*, **106**:4396, 2002.
- [150] W.R. Browne, G.C. Coates, C. Brady, P. Matousek, S.W. Botchway, A.W. Parker, J.G. Vos, and J.J. McGarvey. *J. Am. Chem. Soc.*, **125**:1706, 2003.
- [151] J. Andersson, F. Puntoriero, S. Serroni, A. Yartsev, T. Polivka, S. Campagna, and V. Sundstrom. *Chem. Phys. Lett.*, **386**:336, 2004.
- [152] F. Puntoriero, S. Serroni, M. Galletta, A. Juris, A. Licciardello, C. Chiorboli, S. Campagna, and F. Scandola. *Chem. Phys. Chem.*, **6**:129, 2005.
- [153] V. Balzani, A. Juris, M. Venturi, S. Campagna, and S. Serroni. *Chem. Rev.*, **96**:759, 1996.
- [154] S. Campagna, S. Serroni, F. Puntoriero, C. Di Pietro, and V. Ricevuto in V. Balzani (Ed.). Electron transfer in chemistry vol. 5. *Wiley-VCH: Weinheim*, 2001.
- [155] C.A. Bignozzi, J.R.Schoonover, and F. Scandola. *Prog. Inorg. Chem.*, **44**:1, 1995.

- [156] F. Barigeletti and L. Flamingi. *Chem. Soc. Res.*, **22**:163, 2000.
- [157] T.J. Meyer. *Acc. Chem. Res.*, **29**:1, 1989.
- [158] J.S. Hsiao, B.P. Krueger, R.W. Wagner, T.E. Johnson, J.K. Delaney, D.C. Mauzerall, G.R. Fleming, L.S. Lindsey, D.F. Bocian, and R.J. Donohoe. *J. Chem. Soc. Am.*, **118**:11181, 1996.
- [159] V.A. Durante and P.C. Ford. *J. Am. Chem. Soc.*, **97**:6898, 1975.
- [160] L. Flamigni, S. Encinas, F. Barigeletti, F.M. MacDonnell, K.J. Kim, F. Puntoniero, and S. Campagna. *Chem. Comm.*, **13**:1185, 2000.
- [161] C. Chiorboli, M.A.J. Rodgers, and F. Scandola. *J. Am. Chem. Soc.*, **125**:286, 2003.
- [162] T. Siebert, R. Maksimenka, V. Engel, A. Materny, W. Kiefer, and M. Schmitt. *J. Raman Spectr.*, **33**:844, 2003.
- [163] J. Blumhoff, S. Schebesta, K. Lamm, H. Goerls, K. Schmuck, D. Walther, S. Rau, L. Bottcher, and M. Stollenz. *Eur. J. Inorg. Chem.*, page 2800, 2002.
- [164] S. Rau, B. Schaefer, A. Gruessing, S. Schebesta, K. Lamm, J. Vieth, H. Goerls, D. Walther, m. Rudolph, U.W. Grummt, and E. Birckner. *Inorg. Chim. Acta*, **357**:4496, 2004.
- [165] M. Schmitt, G. Knopp, A. Materny, and W. Kiefer. *J. Phys. Chem. A*, **102**:4059, 1998.
- [166] G.B. Shaw, C.L.Grown, and P.M. Papanikolas. *J. Phys. Chem. A*, **106**:1483, 2002.
- [167] A.T. Yeh, C.V. Shank, and J.K. McCusker. *Science*, **289**:935, 2002.
- [168] G. Benko, J. Kallionen, P. Myllyperkio, F. Trif, J.E.I. Korppi-Tommola, A. Yartsev, and V. Sundstrom. *J. Phys. Chem. B*, **108**:2862, 2004.
- [169] J.N. Demas and G.A. Crosby. *J. Am. Chem. Soc.*, **93**:2841, 1971.
- [170] A.C. Bhasikuttan, M. Suzuki, S. Nakashima, and T. Okada. *J. Am. Chem. Soc.*, **124**:8389, 2002.
- [171] N. Damrauer and J.K. McCusker. *J. Phys. Chem. A*, volume=.

- [172] S. Rau, T. Buttner, C. Temme, M. Ruben, H. Goerls, D. Walther, M. Duati, S. Fanni, and J.G. Vos. *Inorg. Chem.*, **39**:1621, 2000.
- [173] M. Assel, R. Laenen, and A. Lauberau. *J. Phys. Chem. A*, **102**:2256, 1998.
- [174] M. Rasmusson, A.N. Tarnovsky, E. Akesson, and V. Sundstrom. *Chem. Phys. Lett.*, **335**:201, 2001.
- [175] T. Kang, T. Krauss, and F. Wise. *Opt. Lett.*, **22**:1077, 1997.
- [176] J.K. Wang, T.L. Chiu, C.H. Chi, and C.K. Sun. *J. Opt. Soc. Am. B*, **16**:651, 1999.
- [177] S.A. Kovalenko, N.P. Ernsting, and J. Ruthmann. *Chem. Phys. Lett.*, **258**:445, 1996.
- [178] T. Lian, Y. Kholodenko, B. Locke, and R.M. Hochstrasser. *J. Phys. Chem.*, **99**:7275, 1995.
- [179] B. Akhremitchev, C. Wang, and G.C. Walker. *Rev. Sci. Instr.*, **67**:3799, 1996.
- [180] T. Hattori, A. Terasaki, T. Kobayashi, T. Wada, A. Yamada, and H. Sasabe. *J. Chem. Phys.*, **95**:937, 1991.
- [181] K. Ekvall, C. Lundevall, and P. van der Meulen. *Opt. Lett.*, **26**:896, 2001.
- [182] J.F. Ripoche, B. Prade, M. Franco, G. Grillon, R. Lange, and A. Mysyrowisz. *Opt. Comm.*, **134**:165, 1997.
- [183] J.F. Ripoche, H.R. Lange, M.A. Franco, B.S. Prade, P. Rousseau, and A. Mysyrowisz. *IEEE J. Select. Top. Quant. Elect.*, **4**:301, 1998.
- [184] H.R. Lange, M.A. Franco, J.F. Ripoche, B.S. Prade, P. Rousseau, and A. Mysyrowisz. *IEEE J. Select. Top. Quant. Elect.*, **4**:295, 1998.
- [185] Q. Hong, J. Durrant, G. Hastings, G. Porter, and D.R. Klug. *Chem. Phys. Lett.*, **202**:183, 1995.
- [186] K. Ekvall, P. van der Meulen, C. Dhollande, L.E. Berg, S. Pommeret, R. Naskrecki, and J.C. Mialocq. *J. Appl. Phys.*, **87**:2340, 2000.
- [187] G.P. Agarwal, P.L. Baldeck, and R.R. Alfano. *Phys. Rev. A*, **40**:5063, 1989.



- 
- [188] R.R. Alfano, editor. *The supercontinuum Laser Source*. Springer Verlag, New York, 1989.
- [189] Y.R. Shen. The principles of nonlinear optics. *Wiley and Sons, New York*, , 1984.
- [190] R.R. Alfano and P.P. Ho. *IEEE J. Quant. Electr.*, **24**:351, 1981.
- [191] J. Andersson, F. Puntoriero, S. Serroni, A. Yartsev, T. Pascher, T. Polivka, S. Campagna, and V. Sundstrom. *Farraday Discuss.*, **127**:295, 2004.
- [192] J. Andersson. *Life of Excitons in Artificial Photosynthetic Antennas*. PhD Thesis - Lund University, Lund, 2005.
- [193] Hamamatsu Corp. Product information sheet. .
- [194] D. Milam. *Appl. Opt.*, **37**:546, 1998.
- [195] Y.X. Yan, E.B. Gamble, and K.A. Nelson. *J. Chem. Phys.*, **83**:5391, 83.
- [196] P. Vohringer and N.F. Scherer. *J. Phys. Chem.*, **99**:2684, 1995.
- [197] G. Korn, O. Duhr, and A. Nazarkin. *Phys. Rev. Lett.*, **81**:1215, 1998.
- [198] F. Rosca, D. Ionascu, A.T.N. Kumar, A.A. Demidov, and P.M. Champion. *Chem. Phys. Lett.*, **337**:107, 2001.
- [199] T. Polivka and V. Sundstrom. *Chem. Rev.*, **337**:2021, 2004.

# Acknowledgments - Danksagung

An erster Stelle möchte ich hier Herrn Prof. Kiefer für die Aufnahme in seine Arbeitsgruppe, für das spannende Thema, mit dem ich mich während meiner Arbeit beschäftigen durfte, die Möglichkeit, in seinen Laboren zu arbeiten, das ungebrochene Interesse an meiner Arbeit, die allzeit offene Tür und ein offenes Ohr für meine Fragen, für seine Anregungen, die Möglichkeit verschiedene Tagungen zu besuchen und drei Monate in Lund zu arbeiten und nicht zuletzt seine ermutigende Unterstützung bei der Suche nach Möglichkeiten für meinen weiteren Arbeitsweg herzlich danken.

Mein besonderer Dank gilt Dr. Michael Schmitt, der mit seiner Begeisterung für Femtosekunden-zeitaufgelöste Spektroskopie und die Chemie der angeregten Zustände begeistert hat, unter dessen Anleitung und Rat ich diese Arbeit erarbeiten durfte, der jederzeit ein offenes Ohr für Probleme, Sorgen und Ideen hatte. Danke Schmidti dafür, dass ich meine Ideen einbringen und verwirklichen durfte, danke für Hilfe im Labor, deine Motivationshilfen, deine Begeisterung über gelungene Experimente und deine Gelassenheit angesichts verrauschter Daten, deine ermutigende Unterstützung, das offene Diskutieren und die kollegiale Atmosphäre, die die Arbeit unter deiner unmittelbaren Anleitung nicht nur effektiv sondern in erster Linie begeisternd und bereichernd werden liess. Danke.

Dank sagen möchte ich einer Reihe von Personen in Jena. An erster Stelle Prof. Jürgen Popp für die Möglichkeit, eng mit seiner Gruppe zusammen zu arbeiten, von dem ich lernen durfte, der mir die Tür zu den Kooperationen geöffnet hat, die diese Arbeit erst möglich gemacht haben. Privatdozentin Hermann gilt mein Dank für eine exzellente Zusammenarbeit und dafür, dass sie mich die Begeisterung für Moleküle gelehrt hat, die für einen Physiker, der bis dato  $H_2^+$  für ein perfektes Molekül gehalten hat, riesenhafte Systeme darstellen. Herzlichen Dank an Prof. Walther und Dr. Rau dafür dass ich die von ihnen synthetisierten Übergangsmetallverbindungen untersuchen durfte.

Mein herzlicher Dank gilt Raman Maksimenka, der mich entscheidend in die praktischen Geheimnisse des Laboralltages eingewiesen hat, mit dem ich viele schaffensreiche und angenehme Stunden im Labor verbringen durfte. Danke Raman, ohne dich wäre diese Arbeit in ihrer jetzigen Form nicht möglich gewesen. Dies gilt auch für Belinda Böhm. Herzlichen Dank für nicht zu überschätzende Hilfe im Laboralltag, ungezählte Handgriffe und Reparaturen, die du mir abgenommen hast oder die wir gemeinsam durchgeführt haben, und zahlreiche Messungen, die ohne dich nicht so effektiv möglich gewesen wären.

Adriana, Bernd, Steffi, Raman und Belinda - Dank an euch für die gemeinsamen Pausen, Anregungen, Diskussionen, der Hilfe beim Durchleben von Praktikumsstunden und gelegentliche Phasen der Arbeitsfrustration. Ihr habt wesentlich zu einer Atmosphäre beigetragen, die freudiges und effektives Arbeiten ermöglicht hat.

Meinen Dank an Krisztina, Nicu und Nico, Katrin, Nele, Anne, Sebastian, Denis, Joachim, Marco, Phillip, Stefan, Wolfgang und Matthias für Gespräche, Anregungen und so manche nicht nur fachliche Diskussion.

Danken möchte ich Frau Müller für ihren unermüdlichen Kampf gegen die unsinnige Unibürokratie und Peter Popp für ungezählte, spontane Computerhilfsaktionen.

Dank an die Institutswerkstätten, die mich immer wieder unterstützend begeistert haben, indem sie aus teilweise recht unspezifischen Anforderungsprofilen funktionale und funktionierende Experimentbausteine gefertigt haben, ohne die meine Experimente nicht möglich gewesen wären.

Mein herzlicher Dank gilt Prof. Villy Sundstrom und Dr. Arkady Yartsev für die Möglichkeit, drei Monaten in ihrer Arbeitsgruppe arbeiten und lernen zu dürfen. Dank an alle Chemical Physics People in Lund, die mir meinen Aufenthalt in Schweden zu einem nicht nur fachlich bereichernden Erlebnis werden liessen.

Einen besonderen Dank möchte ich an Maren, meine Familie und meine Freunde richten, die mich in Phasen der Euphorie der Realität ausgesetzt und mir in Phasen der Unmotiviertheit immer wieder gezeigt haben, dass es anderes (und mitunter Wichtigeres) gibt als ein funktionierendes Lasersystem.

Dank an die Organisationen, die mich und meine Arbeit finanziell unterstützt haben: der Studienfonds der Chemischen Industrie, der Deutsche Akademische Austauschdienst und die DFG mit ihren Sonderforschungsbereichen 630 und 436.

# Lebenslauf

## Persönliche Daten:

Name: Benjamin Dietzek  
Geburtsdatum: 14.10.1977  
Geburtsort: Hildesheim  
Staatsangehörigkeit: deutsch  
Familienstand: verheiratet mit Maren Dietzek (geb. Strauch)

## Schulbildung:

1984–1988 Pestalozzi- Grundschule Einbeck  
1988–1990 Orientierungsstufe Einbeck  
1990–1997 Goetheschule (Gymnasium) Einbeck  
1997 Abschluss Allgemeine Hochschulreife

## Zivildienst:

1997–1998 Haus des Jugendrotkreuzes Einbeck

## Studium

1998–2001 Studium der Physik an der Bayerischen Julius Maximilians Universität Würzburg  
2001–2002 Studium der Physik an der State University of New York at Stony Brook und externe Diplomarbeit in der Arbeitsgruppe von Prof. H.J. Metcalf – Betreuung in Würzburg durch Prof. G. Gerber  
12/2002 Diplomprüfung im Fach Physik  
01/2003 Abschluss als Diplom-Physiker Univ.  
seit 02/2003 Promotion im Arbeitskreis von Prof. W. Kiefer  
03/2005–06/2005 Forschungsaufenthalt in der Arbeitsgruppe von Prof. V. Sundstrom am Department of Chemical Physics – Lund University, Schweden.